frontiers | Research Topics

Seafloor processes: Geomorphology, sediment-ocean interaction and natural resources

Edited by
Jiangxin Chen, Leonardo Azevedo, Wei Li and Min Luo

Coordinated by
Shaoru Yin

Published in
Frontiers in Marine Science

ISSN 1664-8714
ISBN 978-2-8325-3799-2
DOI 10.3389/978-2-8325-3799-2

About Frontiers

Frontiers is more than just an open access publisher of scholarly articles: it is a pioneering approach to the world of academia, radically improving the way scholarly research is managed. The grand vision of Frontiers is a world where all people have an equal opportunity to seek, share and generate knowledge. Frontiers provides immediate and permanent online open access to all its publications, but this alone is not enough to realize our grand goals.

Frontiers journal series

The Frontiers journal series is a multi-tier and interdisciplinary set of open-access, online journals, promising a paradigm shift from the current review, selection and dissemination processes in academic publishing. All Frontiers journals are driven by researchers for researchers; therefore, they constitute a service to the scholarly community. At the same time, the *Frontiers journal series* operates on a revolutionary invention, the tiered publishing system, initially addressing specific communities of scholars, and gradually climbing up to broader public understanding, thus serving the interests of the lay society, too.

Dedication to quality

Each Frontiers article is a landmark of the highest quality, thanks to genuinely collaborative interactions between authors and review editors, who include some of the world's best academicians. Research must be certified by peers before entering a stream of knowledge that may eventually reach the public - and shape society; therefore, Frontiers only applies the most rigorous and unbiased reviews. Frontiers revolutionizes research publishing by freely delivering the most outstanding research, evaluated with no bias from both the academic and social point of view. By applying the most advanced information technologies, Frontiers is catapulting scholarly publishing into a new generation.

What are Frontiers Research Topics?

Frontiers Research Topics are very popular trademarks of the *Frontiers journals series*: they are collections of at least ten articles, all centered on a particular subject. With their unique mix of varied contributions from Original Research to Review Articles, Frontiers Research Topics unify the most influential researchers, the latest key findings and historical advances in a hot research area.

Find out more on how to host your own Frontiers Research Topic or contribute to one as an author by contacting the Frontiers editorial office: frontiersin.org/about/contact

Seafloor processes: Geomorphology, sediment-ocean interaction and natural resources

Topic editors

Jiangxin Chen — Qingdao Institute of Marine Geology (QIMG), China

Leonardo Azevedo — University of Lisbon, Portugal

Wei Li — South China Sea Institute of Oceanology, Chinese Academy of Sciences (CAS), China

Min Luo — Shanghai Ocean University, China

Topic Coordinator

Shaoru Yin — Second Institute of Oceanography, Ministry of Natural Resources, China

Citation

Chen, J., Azevedo, L., Li, W., Luo, M., Yin, S., eds. (2023). *Seafloor processes: Geomorphology, sediment-ocean interaction and natural resources*. Lausanne: Frontiers Media SA. doi: 10.3389/978-2-8325-3799-2

Table of contents

frontiers | Frontiers in Marine Science

TYPE Editorial
PUBLISHED 12 October 2023
DOI 10.3389/fmars.2023.1282416

OPEN ACCESS

EDITED AND REVIEWED BY
Eric 'Pieter Achterberg,
Helmholtz Association of German Research Centres (HZ),
Germany

*CORRESPONDENCE
Jiangxin Chen
jiangxin_chen@sina.com

RECEIVED 24 August 2023
ACCEPTED 29 September 2023
PUBLISHED 12 October 2023

CITATION
Chen J, Li W, Luo M, Azevedo L and Yin S (2023) Editorial: Seafloor processes: geomorphology, sediment-ocean interaction and natural resources. *Front. Mar. Sci.* 10:1282416. doi: 10.3389/fmars.2023.1282416

Editorial: Seafloor processes: geomorphology, sediment-ocean interaction and natural resources

Jiangxin Chen[1,2]*, Wei Li[3,4], Min Luo[5], Leonardo Azevedo[6] and Shaoru Yin[7]

[1]Key Laboratory of Gas Hydrate, Ministry of Natural Resources, Qingdao Institute of Marine Geology, Qingdao, China, [2]Laboratory for Marine Mineral Resources, Qingdao National Laboratory for Marine Science and Technology, Qingdao, China, [3]CAS Key Laboratory of Ocean and Marginal Sea Geology, South China Sea Institute of Oceanology, Chinese Academy of Sciences, Guangzhou, China, [4]University of Chinese Academy of Sciences, Beijing, China, [5]College of Marine Sciences, Shanghai Ocean University, Shanghai, China, [6]DER/CERENA, Instituto Superior Técnico, Universidade de Lisboa, Lisboa, Portugal, [7]Key Laboratory of Submarine Geoscience, Second Institute of Oceanography, Ministry of Natural Resources, Hangzhou, China

KEYWORDS

seafloor process, gas hydrate, hydrodynamic interaction, submarine geomorphology, geological process, biological disturbance, fluid flow

Editorial on the Research Topic
Seafloor processes: geomorphology, sediment-ocean interaction and natural resources

Seafloor processes refer to the oceanic processes that take place near the seafloor, including physical, chemical, biological, and geological processes, which are related to submarine geomorphology, fluid dynamics, resources exploitation, and geotechnics, and are hard to fully describe due to the limitations of submarine detection technology and their interdisciplinary nature. Indeed, seafloor processes involve several scientific disciplines and fields, and require multi-level and multi-scale research. Moreover, the seafloor is interpreted as an essential interface between the lithosphere and hydrosphere, where substance circulation and energy exchange occur. The collection of works compiled in this Research Topic contributes to a deeper understanding, from multiple perspectives, of the study of seafloor processes.

In this Research Topic, Huang et al. indicate that approximately 98.9% of gold supplied in modern seafloor hydrothermal systems is transported into the depths of the global ocean, which is three to five orders of magnitude higher than what typically exists in deep ocean water.

Cold seeps are seafloor manifestations of methane-rich fluid migration from the sedimentary subsurface to the seabed and into the water column, accompanied by a series of biogeochemical reactions. Cen et al. infer that foraminiferal tests are extremely sensitive to alteration by methane-bearing fluids based on the elemental and stable carbon-oxygen isotopic compositions, and the elemental ratios of diagenetically altered tests are potentially reliable proxies for paleo-methane release events. Simultaneously, cold seeps are crucial for reconstructing the paleo-marine environment and tracing the origin of life and

the occurrence of minerals. The study of cold seeps in the southern South China Sea has demonstrated that cold seeps vary in time and space, and that fluid fluxes and tectonic settings have a significant impact on the sedimentary environment and geochemistry, resulting in obvious regional differences in the properties and activities of cold seeps (Chen et al.).

Seabed fluid flow is a constantly evolving dynamic process whose products can help complete a systematic understanding of seafloor evolution. For example, authigenic carbonates are direct records of past fluid flow near the seafloor. Feng et al. identify that the components of carbonates have a common trend among different seepage stages. Furthermore, this work infers that the temporal evolution of local fluid sources may play an essential role in determining carbonate isotope geochemistry. The small-scale event layers in the continental margin also contain abundant dynamic environmental information, and it is found that the changes in the ocean environment of the Late Quaternary, especially sea level and bottom water temperature, played a leading role in the occurrence of regional small-scale event layers (Li et al.).

The seafloor is rich in marine mineral resources with substantial economic and scientific research value. Ren et al. analyze the submarine ferromanganese (Fe-Mn) oxide precipitates from the South China Sea to form Fe-Mn polymetallic crusts and nodules. Moreover, they infer that it was formed in a short period of a sub-oxic environment and diagenetic process and would affect the enrichment of metals, such as Ni, during the growth process. Climate change and ocean evolution significantly impact the sedimentary processes in seamount regions. Tian et al. analyze the clay minerals, grain size, and ^{14}C ages of core SCS18-1 collected from the Beipo seamount in the northern South China Sea, and find that the relative content of EM1+EM2 and the illite chemical index, and the relative content of EM3 effectively indicate the changes in the intensity of East Asia summer monsoon winter monsoon, respectively.

Fresh submarine groundwater is a potentially untapped resource whose discharge impacts submarine morphology. However, the locations and extent of fresh submarine groundwater discharge and its impact on submarine morphology still need to be better understood. Hoffmann et al. use single and multibeam hydroacoustics and towfish (i.e., temperature, salinity, and turbidity) transects combined with remotely operated vehicle dives and sediment cores to better characterize submarine geomorphology. It is observed that there are a large number of seafloor depressions (pockmarks) caused by continuous seabed fluid flow.

The interaction between seawater and submarine topography caused by internal solitary waves will drive the disturbance of the benthic environment, but its impact on benthic organisms is less studied. Feng et al. perform *in-situ* observation in the Shenhu Canyon to determine the physical characteristics of internal solitary waves and the changes in benthic organisms. It is revealed that the abundance and density of benthic organisms were positively correlated with the time and intensity of interval solitary waves.

Seafloor processes still need to be wholly understood due to limitations in submarine detection technology and its spatial resolution. Because of the advantage of high spatial resolution, seismic reflection data has become a preferable tool to study and image seafloor processes. Han et al. combine fluid dynamics numerical simulation with seismic oceanography to discuss the formation mechanisms of the hair-like reflection configuration. As a consequence, it is deduced that the difference in seawater temperature and salinity can form a hair-like reflection configuration.

In this Research Topic, a comprehensive understanding of the patterns, mechanisms, and evolution of seafloor processes has been gained through multiple research methodologies. It has implications for submarine geomorphology, fluid dynamics, and natural resources, promoting the understanding of submarine biology and ecology, and marine geological activity and chemistry. Additionally, this Research Topic aims to demonstrate that multidisciplinary theories and approaches are required to address the interactions between the various seafloor processes, as well as the impact of natural and anthropogenic processes on the seafloor.

Author contributions

JC: Conceptualization, Writing – original draft, Writing – review & editing. WL: Writing – review & editing. ML: Writing – review & editing. LA: Writing – review & editing. SY: Writing – review & editing.

Conflict of interest

The authors declare that the research was conducted in the absence of any commercial or financial relationships that could be construed as a potential conflict of interest.

Publisher's note

frontiers | Frontiers in Marine Science

TYPE Original Research
PUBLISHED 07 February 2023
DOI 10.3389/fmars.2023.1110188

OPEN ACCESS

EDITED BY
Min Luo,
Shanghai Ocean University, China

REVIEWED BY
Xing Jian,
Xiamen University, China
Gábor Újvári,
Hungarian Academy of Sciences (MTA),
Hungary

*CORRESPONDENCE
Xilin Zhang
ouxzhxl@163.com
Fangjian Xu
xufangjiangg@163.com

SPECIALTY SECTION
This article was submitted to Marine Biogeochemistry, a section of the journal Frontiers in Marine Science

RECEIVED 28 November 2022
ACCEPTED 12 January 2023
PUBLISHED 07 February 2023

CITATION
Tian X, Zhang X, Wang J, Sun Z, Liu M, Zhao J, Zhang L, Fan D and Xu F (2023) Provenance and paleoenvironmental significance of sediments in the Beipo seamount of the northern South China Sea during the last deglaciation. *Front. Mar. Sci.* 10:1110188. doi: 10.3389/fmars.2023.1110188

Provenance and paleoenvironmental significance of sediments in the Beipo seamount of the northern South China Sea during the last deglaciation

Xu Tian[1], Xilin Zhang[2*], Jinli Wang[3], Zhilei Sun[2], Ming Liu[1], Jinhuan Zhao[2], Lin Zhang[4], Dejiang Fan[1] and Fangjian Xu[3*]

[1]College of Marine Geosciences, Ocean University of China, Qingdao, China, [2]Qingdao Institute of Marine Geology, Ministry of Natural Resources, Qingdao, China, [3]College of Marine Science, Hainan University, Haikou, China, [4]Haikou Center of Marine Geological Survey, China Geological Survey, Haikou, China

The sedimentary processes of seamount regions are closely related to climate change and ocean evolution. The clay minerals, grain size and ^{14}C ages of core SCS18-1, which was collected from the Beipo seamount in the northern South China Sea (SCS) were analyzed to discuss the provenance and paleoenvironmental conditions during the last deglaciation. The sediments of core SCS18-1 are dominated by clayey silt, which is mainly composed of illite (55.2~62.1%) and chlorite (17.1~22.5%), with subordinate kaolinite (9.5~12.6%) and smectite (7.3~15.1%). The illite chemical index and illite crystallinity indicate strong physical weathering conditions. The results of the end-member modeling algorithm (EMMA) suggest that the sediments of core SCS18-1 consist of three end-members containing EM1 (0.98 μm), EM2 (9.29 μm) and EM3 (44.19 μm), with average contents of 3%, 66% and 31%, respectively. The finest endmember represents fluvial mud, the middle and coarsest endmembers are considered fluvial fine silt and eolian dust, respectively. The mean grain size is mainly controlled by the coarser fraction EM3. Based on the clay minerals, grain size and SEM analysis, we can conclude that since the onset of the last deglaciation (16.1 ka BP), the sediments of core SCS18-1 mainly originate from fluvial input, and eolian material also contributed to the sediments. The clay mineral assemblages of core SCS18-1 are stable and originate mainly from Taiwan. Additionally, the Pearl River appears to be a secondary contributor of clay minerals. Further, the Luzon Islands only account for a small proportion. Major kaolinite and moderate illite and chlorite are thought to originate from the Pearl River, predominant illite and chlorite from Taiwan, and principal smectite from the Luzon Islands. Both the relative content of EM1+ EM2

and the illite chemical index effectively represent the variation of East Asia summer monsoon (EASM) strength. Meanwhile, the relative content of EM3 effectively represents the East Asian winter monsoon (EAWM) change. The material supply of core SCS18-1 is mainly controlled by solar radiation in the Northern Hemisphere.

KEYWORDS

grain size, clay minerals, provenance, the last deglaciation, South China Sea

1 Introduction

As part of the South China Sea (SCS), the largest marginal sea in the western Pacific, the northern SCS receives sediment derived from the Pearl River in South China, small mountainous rivers in southwestern Taiwan, and some rivers in Luzon (Boulay et al., 2005; Clift et al., 2014; Liu et al., 2016; Wan et al., 2017; Kissel et al., 2020), and its deposition processes are highly impacted by land-sea interactions, sea-level changes, East Asian monsoon (EAM), El Niño Southern Oscillation (ENSO), and other processes (Hu et al., 2012; Clift et al., 2014; Liu et al., 2016; Wan et al., 2017; Kissel et al., 2020). Currently, there are disagreements regarding the provenance of the sediments in the northern SCS. Most previous studies in the northern SCS have considered the Pearl River to be the main sediment (Clift et al., 2002; Boulay et al., 2003; Li et al., 2003). Growing evidence indicates that, due to the tectonic activity and monsoon/typhoon rainfall of Taiwan Island, the small mountainous rivers draining Taiwan Island supply 230–400 Mt/yr (Liu et al., 2008; Xu et al., 2021). Thus Taiwan is thought to be one of the highest sediment suppliers in the world. As a result, the Taiwan sediment provenance has become more important to the northern SCS, with only minor amounts transported from the Pearl River and Luzon rivers (Clift et al., 2014; Huang et al., 2016). However, our understanding of the sediment provenance of the continental slope in the northern SCS remains limited.

Seamounts are the most ubiquitous landforms on Earth but are unevenly distributed among ocean basins, and there are approximately 2500 seamounts with a height of more than 100 m in the world (Wessel et al., 2010). Seamount sediments are ideal recorders of ocean circulation, sediment deposition, sediment transportation and weathering of adjacent lands, so they are important for many disciplines, including such as geology, oceanography, biology, ecology, and possibly economics (considering future exploitation of mineral resources) (Staudigel and Clague, 2010; Staudigel and Koppers, 2015). Because the ocean is vast, research vessels have visited only a few thousand of these seamounts, with less than 0.1% of them being previously investigated (Zhou et al., 2020). In addition, due to the limitations of the marine survey equipment resolution, we know very little about seamounts; thus, the identification of seamounts may be arguably the last major frontier in geographic, geological, and ecological exploration on Earth (Staudigel and Koppers, 2015; Zhao et al., 2022). Growing evidence shown that seamounts not only affect the distribution of sediment and the path of sediment transport, but also influence the intensity and propagation path of deep-water dynamics, especially deep-water gravity and bottom currents (Zhang and Boyer, 1991; Chen et al., 2019). Thus, the source-to-sink mechanisms should be different between seamounts and other oceanic geomorphic units. However, most past studies have focused on the mineral resources (polymetallic nodules or Co-rich crusts) found in the seamounts in the northern SCS (Zhong et al., 2017). Work has seldom been done in relation to the provenance and paleoenvironment of seamounts; moreover, no research on the provenance and paleoenvironmental history of the sediments in the Beipo seamount of the northern SCS has been conducted.

Based on the accelerator mass spectrometry (AMS) ^{14}C ages, grain size compositions, and clay minerals of the core SCS18-1 sediments taken from the Beipo seamount on the continental slope of the northern SCS, the sediment provenances and paleoenvironmental of these marine sediments over the last deglaciation are discussed in this study.

2 Geological and oceanographic setting

The Beipo seamount is located on the continental slope of the northern SCS, southwest of Taiwan Island. According to the near-bottom observations of Jiaolong Dive 141 on the Dayang 38th voyage and Qianlong III on the 2018 Dayang Yihao comprehensive ocean expedition, large, irregular-shaped nodules with a hard substrate, low water content, and strong adhesion develop on the Beipo seamount and nearby areas (Dayang 38th voyage field report; 2018 Dayang Yihao comprehensive ocean expedition field report). A complex current system has developed in the northern SCS, including deep-water currents, Kuroshio and surface currents influenced by the EAM and the South China Offshore Current (Shaw and Chao, 1994; Huang et al., 2016; Liu et al., 2016; Liu et al., 2017). The summer and winter surface currents do not completely reverse with the shift of the monsoon direction; the surface currents only shift between the southwestward SCS Warm Current and the northeastward Guangdong Coastal Current on the northern shelf and upper land slope regions; the SCS branch of the Kuroshio current intruding from the Luzon Strait transforms northward into the SCS Warm Current and transforms southward into the northwest Luzon Cyclonic Eddy; the South China Offshore Current, Luzon Coastal Current and deepwater current do not show seasonal variations (Liu et al., 2010a).

The island of Taiwan is located at the tectonic collision boundary between the Philippine Sea Plate and the Eurasian. Given its steep

topographic gradients, less weather-resistant rocks (mainly composed of Tertiary metamorphic and sedimentary rocks), high tectonic activity, periodic typhoons and heavy rainfall, Taiwan is generally known to have one of the highest sediment yields in the world (Li et al., 2012). It is assumed that rivers in southwestern Taiwan contribute 187 × 10^6 t of suspended matter to the SCS annually (Liu et al., 2009). As the second largest river in our country, the Pearl River was formed by the uplift of the Tibetan Plateau in approximately 34 Ma. The basin covers an area of 453690 km^2 with a total annual runoff of 326 billion m^3. The Pearl River is an oligotrophic river that delivers 69 × 10^6 t of suspended sediment to the sea annually (Milliman and Syvitski, 1992). Luzon is dominated by basalt and andesite, with very developed volcanic activity. The tectonic movement and monsoon rainfall have a significant impact on the transport of terrigenous clastic sediments. The sediment transport of the Luzon rivers reached 16×10^6 t (Liu et al., 2009).

3 Materials and methods

Core SCS18-1 (118.06.22°E, 21.10.66°N, water depth 1750 m, total length 141 cm; Figure 1) was collected from the Beipo seamount in the northern SCS by gravity sampler in 2018. The core was described and subsampled at 1-cm intervals. The sediment of core SCS18-1 is mainly gray clay silt and contains numerous foraminifers.

The samples used for grain-size analysis were collected at 1-cm intervals. As to the pretreatment for grain size analysis, calcium carbonate and organic matter were carefully removed with excess 1

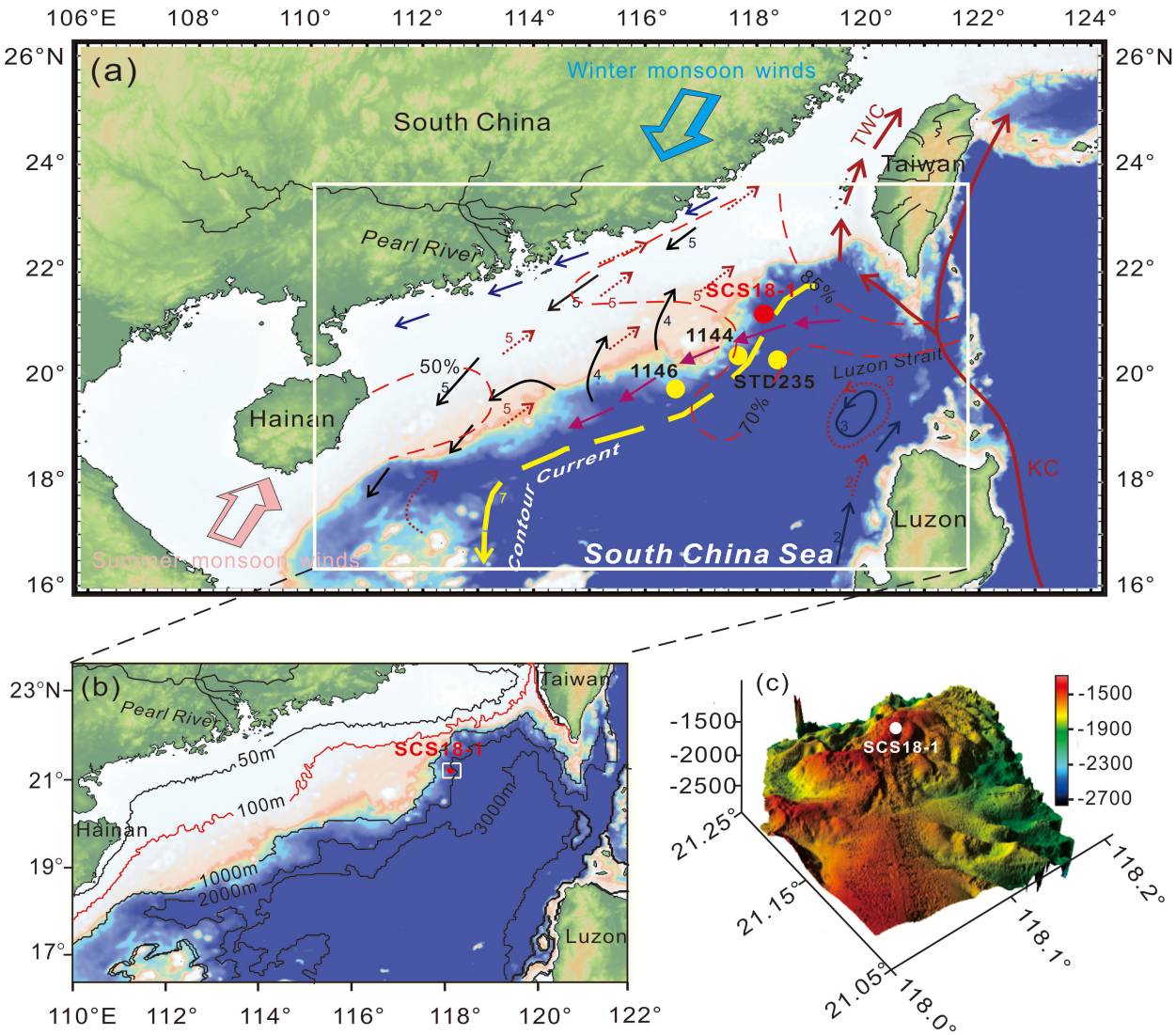

FIGURE 1
Map showing **(A)** the location of core SCS18-1 and the monsoon winds and current systems (modified from Liu et al., 2010b), **(B)** the submarine contour in the northern SCS, **(C)** the topography of the Beipo seamount. The location of cores ODP1144 (Liu et al., 2010b; Liu et al., 2013), ODP1146 (Wan et al., 2007b) and STD235 (Liu et al., 2018) are also shown. Southwesterly winds prevailing in summer (pink three-dimensional arrow) and northeasterly winds prevailing in winter (blue three-dimensional arrow); summer and winter surface currents (red dotted line arrow and black solid arrow, respectively); deep current (yellow dashed arrow); longshore current (blue solid arrow); Kuroshio current (KC); Taiwan current (TWC). Numbers for winter and summer surface currents: 1. SCS Branch of Kuroshio; 2. NW Luzon Coastal Current; 3. NW Luzon Cyclonic Eddy; 4. SCS Warm Current; 5. Guangdong Coastal Current.

mol/L HCl and 10% H_2O_2 for 24 h, respectively. After rinsing and centrifuging 3 times using deionized water, the residues were dispersed and homogenized using ultrasound and then analyzed using a Malvern Mastersizer 2000 instrument in Qingdao Sparta Analysis & Testing Co., Ltd. The analyses of each sample, which were repeated three times, show that the relative error is less than 2%, and the measurement range of this laser particle size analyzer is 0.02 to 2000 μm. According to the sediment sample characteristics and the instrument user manual, the grain size distributions (GSDs) were calculated using the Mie Theory, where the absorption coefficient and refractive index are 0.1 and 1.52, respectively. The grain size of the samples was divided into clay (< 4 μm), silt (4-63 μm) and sand (63-2000 μm) (Wentworth, 1922). The grain size data were simulated by the end-member model algorithm (EMMA), and the process of the simulation was generated by the software AnalySize embedded in MATLAB (Paterson and Heslop, 2015).

71 samples were used for clay mineral analyses. Samples were treated with 15% H_2O_2 and 1 mol/L HCl to remove organic matter and calcium carbonate and then centrifuged with deionized water three times. Clay mineral analyses were performed on the < 2 μm fraction, which was separated based on conventional Stokes' settling velocity principles. Each sample was transferred to two slides by wet smearing. Samples were then air-dried before X-ray diffraction (XRD) analysis (Liu et al., 2003; Wan et al., 2007a). The instrument is an X'Pert MPD Pro XRD diffractometer with CuKα radiation (40 kV and 100 mA) produced by Panako Company in the Netherlands. Natural and ethylene-glycol solvation samples were measured, and the scanning was completed done from 3° to 30° with a step size of 0.02°. Identification of clay minerals was made mainly according to the position of the (001) series of basal reflections on the two XRD spectra. Semi-quantitative estimation of clay mineral abundances is based on the peak areas of smectite (17Å), illite (10Å), and kaolinite/chlorite (7Å) on the glycolate curve using the Topas2p software. Relative proportions of kaolinite and chlorite were determined based on the ratio of the 3.57/3.54 Å peak areas. Relative clay mineral abundances are given in percentages. Biscaye weighting factors are used when calculating relative percentages of each clay mineral (Biscaye, 1965). In addition, the illite chemistry index (the ratio of illite 5Å and 10Å peak areas) and illite crystallinity (the full width at half maximum height (FWHM) of the illite 10 Å peak) were determined on the glycolate curve.

Five AMS^{14}C dating samples of the planktonic foraminifer *Globigerinoides ruber* (*G. ruber*) were analyzed by Beta Analytic Inc., USA for this core. The raw ^{14}C dates were converted into calendar years (yr BP) using CALIB 8.2.0 software and applying the Marine 20 program (http://calib.org/calib/calib.html), and the reservoir age correction values were -58 ± 43 a (Yoneda et al., 2007). Then, the downcore age uncertainty was modeled using the R-based statistical program Bacon 2.2, which is based on the calibrated ^{14}C dates and a Bayesian approach (Blaauw and Christen, 2011).

Micro-morphological examinations of two sediment samples (40 cm and 80 cm) from core SCS18-1 were performed using a Hitachi JSM-7610F scanning electronmicroscope (SEM) equipped with an energy dispersive X-ray spectrometer (EDS) at Qingdao marine equipment inspection & testing group Co., LTD. Organic matter and calcium carbonate were removed using 10% H_2O_2 and 15% HCl, respectively. The pretreated terrigenous grains were dispersed in ethanol by an ultrasonic cleaner and then carefully dropped on a cover glass slide. These grains were placed on a stub and coated in gold before examination under SEM. The chemical composition of selected grains was determined by EDS.

4 Results

4.1 Age model

The age model of core SCS18-1 is based on a total of 5 AMS ^{14}C dates. The sedimentation of core SCS18-1 is relatively continuous without age inversion, and the age at the bottom (141 cm) is approximately 16.1 ka BP (Table 1 and Figure 2).

4.2 Grain size characteristics and endmember analysis

The presence of trends in grain size composition changes significantly at 42 cm and 103 cm. The core can be divided into stages I, II, and III (Figure 3). For stage I (142-103 cm, 16.1-10.6 ka BP), the average contents of clay, silt, and sand are 19.0%, 72.4%, and 9.6%, respectively; for stage II (103-42 cm, 10.6-6.8 ka BP), the average contents of clay, silt, and sand are 19.8%, 74.7%, and 5.5%, respectively, and the average grain size gradually increases from bottom to top; for stage III (42-0 cm, 6.8-0 ka BP), the average contents of clay, silt, and sand are 17.1%, 74.1%, and 8.8%, respectively, and the average grain size changes slightly.

The coefficient of determination (R^2) and mean angular deviation (θ) were calculated to identify the minimal numbers of EMs necessary for a good statistical explanation of the grain size data. A relatively high R^2 and low θ indicate a better statistical fit (Paterson and Heslop, 2015).

TABLE 1 AMS^{14}C dates for core SCS18-1.

Laboratory number	Depth (cm)	Material	^{14}C age (a BP)	δ^{13}C (‰)	δ^{18}O (‰)	Calendar age (yr BP, 2σ)
Beta-526297	24-25	*G. ruber*	4320±30	+2.4	-1.4	4330 (4225-4429)
Beta-516707	44-45	*G. ruber*	6750±30	+1.4	-2.7	7119 (7029-7219)
Beta-521161	76-77	*G. ruber*	9090±30	+2.2	-1.7	9690 (9553-9777)
Beta-516708	109-110	*G. ruber*	9380±30	+1.8	-1.3	10108 (10016-10211)
Beta-516709	140-141	*G. ruber*	13950±40	+1.2	-1.6	16095 (15968-16225)

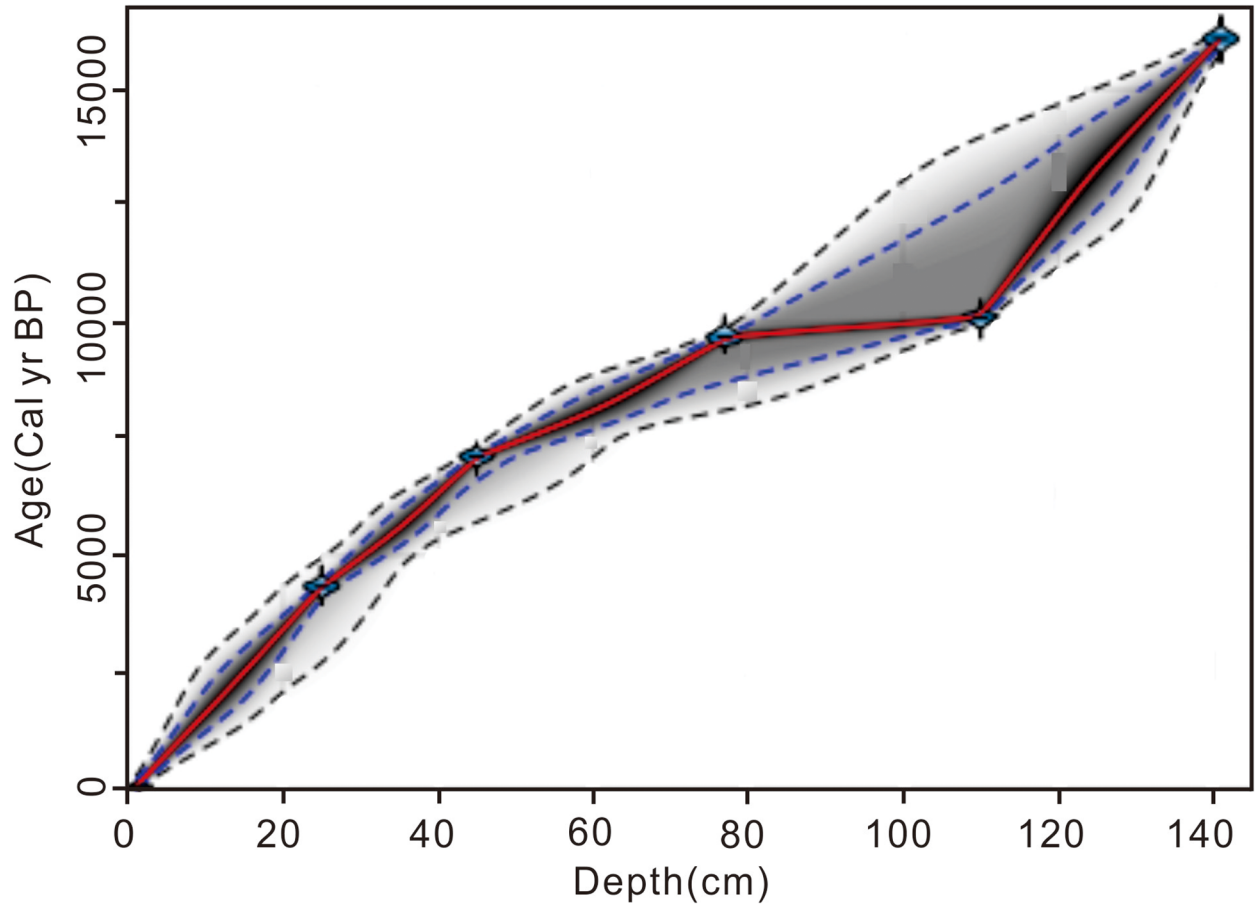

FIGURE 2
Age-depth model for core SCS18-1.

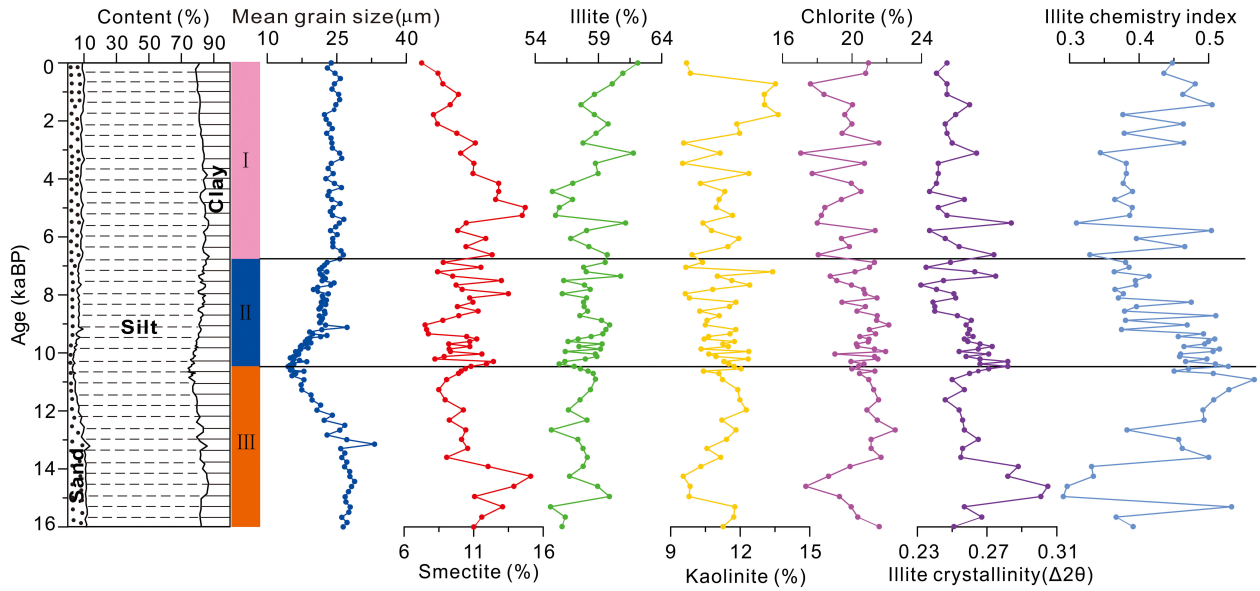

FIGURE 3
Lithology, mean grain size, clay mineral assemblages, crystallinity index, and chemical index of core SCS18-1.

The results show that EM number = 2 seems to be a turning point, where the value of R^2 becomes greater than 0.95 (Figure 4A), indicating that the fitting results reach the 95% confidence level; at higher numbers of EMs, R^2 is not significantly changed, indicating that the final EM number should be at least 2. To avoid overfitting, the correlation between the EMs should be as low as possible, and the EM correlation increases significantly when the EM number is ≥ 3 (Figure 4A); thus, the final EM number should be 2-3. The angle deviation (θ) is an index for evaluating the reliability of the EM model, where low θ value indicates a better statistical fit. To make the angle deviation (θ) as small as possible, the average angle deviation should be below 5°. When the EM number is 2, θ > 5° (Figure 4B); when the EM number is 3, θ < 5°. Therefore, when the final EM number is 3, a good fitting effect can be achieved, and the requirements of minimum EM number and maximum reproducibility are satisfied (Paterson and Heslop, 2015; Tanghe, 2016).

The grain size distribution curves of the simulated EMs (EM1, EM2, and EM3) exhibit an obvious single peak, which has a good corresponding relationship with the grain size distribution of the samples; the mode of the grain size is 0.98 μm, 9.29 μm, and 44.19 μm, respectively (Figure 4C). Figure 4D shows the relative contents of EM3 in core SCS18-1, and the contents of EM1, EM2, and EM3 vary from 1% to 5%, 53% to 83%, and 12% to 45%, with mean values of 3%, 66%, and 31%, respectively. The contents of EM1 and EM2 in the fine EMs follow the same trend, which is opposite to that of EM3. In the range of 103-141 cm, the contents of EM1 and EM2 increase significantly from bottom to top; in the range of 42-103 cm, they decrease; and above 42 cm, they increase. The trends of EM3 in these three stages are opposite.

The SEM results show that the coarse-grained components (30-100 μm) are quartz and feldspar, and the fine-grained components (less than 10 μm) are clay minerals (CMs) (Figure 5), which suggests that EM3 (mode of grain size: 44.19 μm) of core SCS18-1 corresponds to the coarse-grained quartz and feldspar, while EM1 (mode of grain size: 0.98 μm) and EM2 (mode of grain size: 9.29 μm) correspond to the CMs. These results agree well with the grain size analysis results at the adjacent ODP1146 site (Wan et al., 2007b).

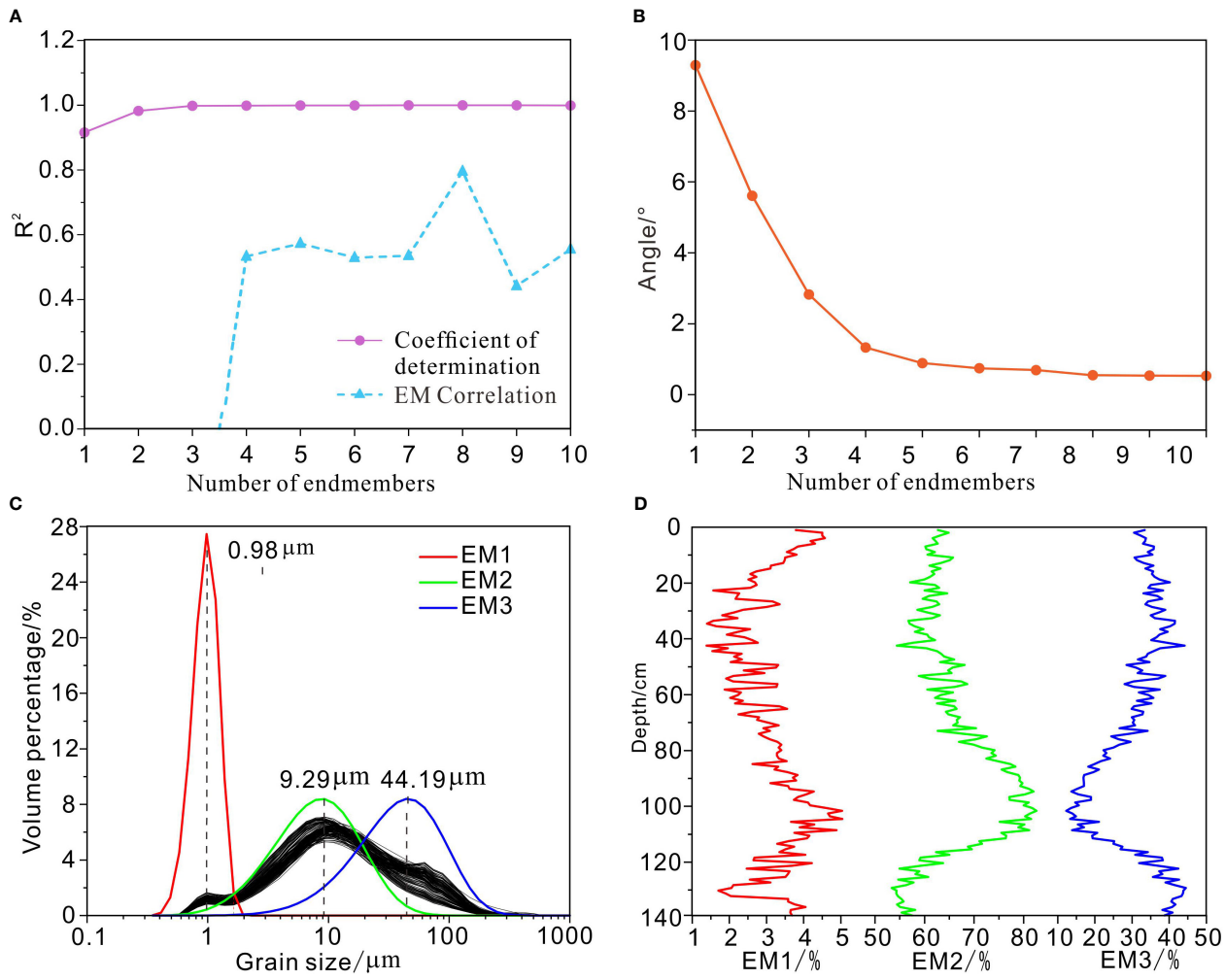

FIGURE 4
(A) Endmember analysis results of the sediment grain size data from core SCS18-1. Coefficients of determination (R^2) plotted against grain size for different endmember solutions, **(B)** mean angular deviation (θ) in the function of the number of endmembers for a lognormal endmember model, **(C)** grain size frequency distributions for the endmembers of the three-endmember solution, **(D)** variation in endmember contributions.

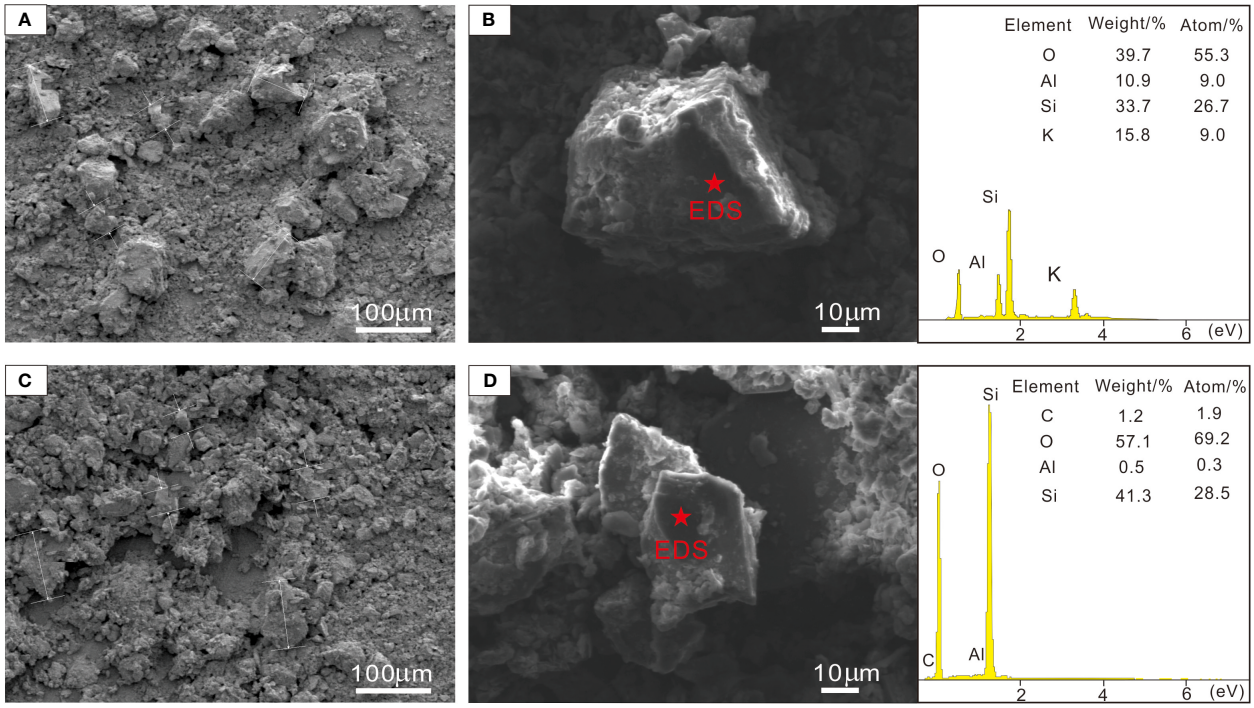

FIGURE 5
SEM and EDS images of sediments from core SCS18-1. **(A, B)** The SEM and EDS images sediments from core SCS18-1 at 40 cm depth. **(C, D)** SEM and EDS images of sediments from core SCS18-1 at 80 cm depth.

4.3 Clay minerals

The X-ray diffraction (XRD) analysis results show that the clay minerals of core SCS18-1 (< 2 μm) mainly comprise illite, chlorite, kaolinite, and smectite. The illite content is 55.2-62.1%, averaging 58.1%; the chlorite content is 17.1-22.5%, averaging 20.3%; the kaolinite content is 9.5-12.6%, averaging 11.2%; and the smectite content is 7.3-15.1%, averaging 10.5%. The illite chemistry index ranges from 0.29 to 0.57 (mean value: 0.43) and is usually less than 0.50, indicating that illite is rich in Fe–Mg (such as biotite and mica) and that it predominantly originated from physical erosion. The illite crystallinity ranges from 0.23 to 0.31°Δ2θ, averaging 0.26°Δ2θ, and the crystallinity is excellent, indicating strong physical weathering in the source area. As shown in Figure 3, smectite and illite exhibit opposite trends, however the trends of kaolinite and chlorite are not significantly correlated with the trends of other clay minerals.

5 Discussion

5.1 Material source and transport mechanism

Among the terrigenous clastic particles in oceans, clay minerals are the most important because they are widely distributed in almost all oceanic environments and record climate and environmental evolution information; therefore, they have been applied successfully to study sediment sources, oceanic current transport and paleoclimate evolution (Liu et al., 2010; Wan et al., 2012a). The clay minerals in core SCS18-1 are all terrigenous clastic sediments, and the influence of diagenesis can be ignored. Numerous studies have shown that the Pearl River, Taiwan, and Luzon are the main sources of terrigenous clastic sediments in the northern SCS (Liu et al., 2010b). The Mekong River materials and central Vietnamese river materials have difficulty reaching the northern continental shelf and continental slope area of the SCS (Liu et al., 2010c), and due to blocking by the island of Hainan, the detrital materials imported by the Red River are mainly deposited in the Beibu Gulf Basin, Yinggehai Basin, and Qiongdongnan Basin in the northwestern part of the SCS (Shao et al., 2013). In summary, the provenance regions of CMs in core SCS18-1 mainly include Taiwan, the Pearl River, and the Luzon rivers.

In the Taiwan sediments, the clay mineral assemblage consists mainly of illite (71%) and chlorite (26%) with very little kaolinite (3%) and almost no smectite. In the Pearl River sediment, the clay mineral assemblages have a high kaolinite content (35.7% on average) with illite, chlorite, and smectite contents of 41.6%, 21.0%, and 1.7%, respectively (Liu et al., 2007), while in the Luzon sediments, the clay mineral assemblage are mainly composed of smectite (75%) with a small amount of kaolinite (15%) and chlorite (7%) and almost no illite (3%) (Liu et al., 2010c).

The smectite–(illite+chlorite)–kaolinite triangle diagram (Figure 6) shows that the composition and contents of CMs in core SCS18-1 are essentially the same. Every sample from core SCS18-1 is distributed in the area between three potential sources (Taiwan, the Pearl River, and Luzon), suggesting a possible mix of the above three sources (Figure 6).

5.1.1 Smectite

The smectite content in core SCS18-1 is 7.3-15.1%, averaging 10.4% (Figure 3). For the provenance areas, the Pearl River and

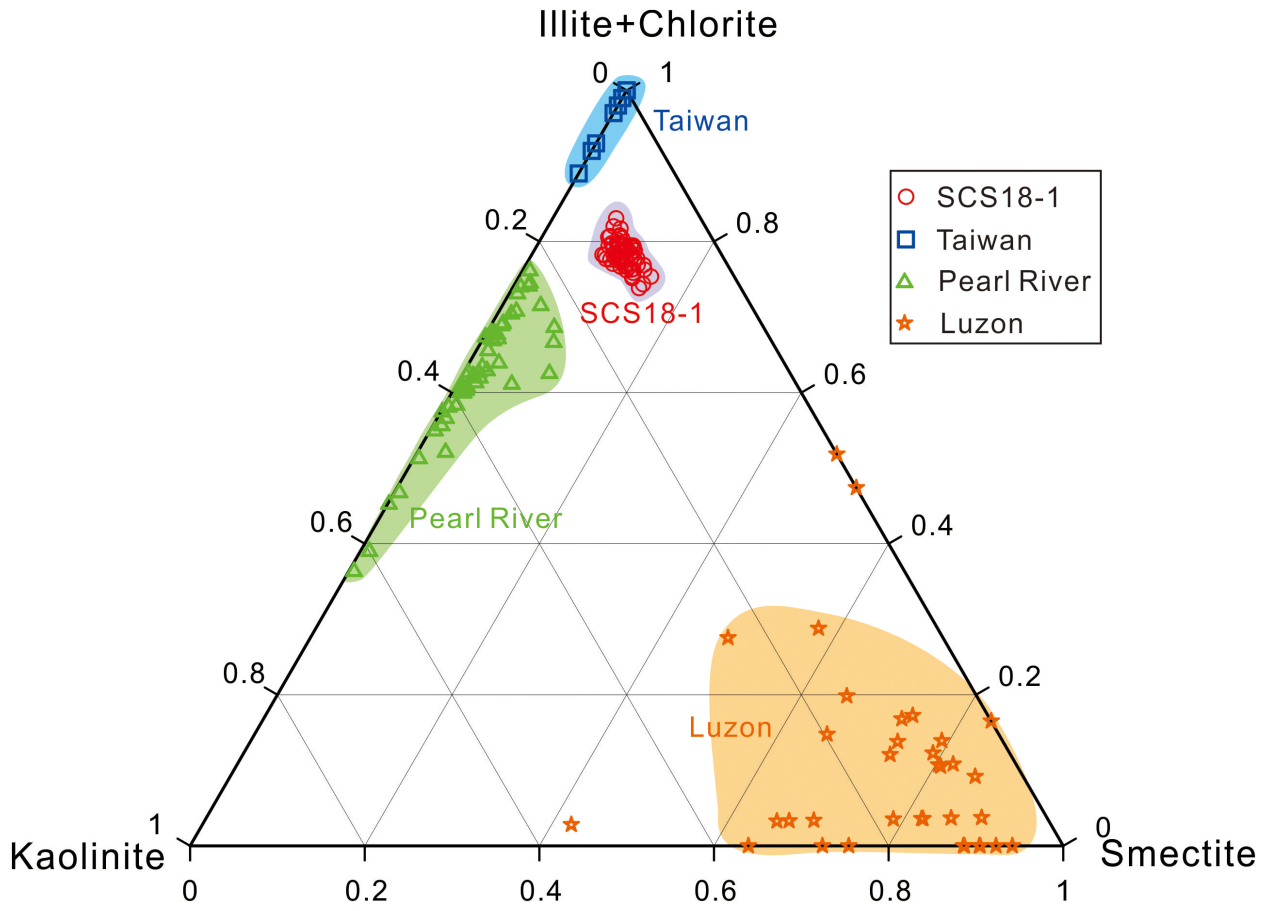

FIGURE 6
Ternary diagram of the major clay mineral groups illite+ chlorite, kaolinite, and smectite. Data of the Pearl River are from Liu et al. (2007); data of the Luzon rivers are from Liu et al. (2009); data of the Taiwan River are from Li et al. (2012); the referenced data have been converted according to Biscaye (1965).

Taiwan contain almost no or very low smectite (Liu et al., 2007; Li et al., 2012; Hu et al., 2014), while the smectite content in the Luzon river sediments is as high as 75% (Liu et al., 2009). The smectite of Luzon can be transported from south to north by the surface ocean current of the Kuroshio branch current in the SCS after the Kuroshio intrusion (Liu et al., 2010b), and concentrated subsidence occurs on the land slope and outer shelf in the northern part of the SCS due to topographic blockage (Liu and Li, 2011), thus providing smectite for core SCS18-1.

5.1.2 Kaolinite

The kaolinite content in core SCS18-1 is 9.5-12.6%, averaging 11.2%. Considering that the kaolinite content gradually decreases because of flocculation and sedimentation during the process of kaolinite entering the sea and transportation (Liu et al., 2007), the kaolinite content must be much higher in the provenance areas than in core SCS18-1. Among the three potential provenance areas, only the Pearl River has high kaolinite content. Therefore, the Pearl River may be the main provenance area of kaolinite in core SCS18-1, since the average kaolinite content in the Pearl River Basin is 35.7%, but additions from the Luzon river source cannot be excluded. Assuming that all kaolinite of the study area is from the Pearl River, then only the contribution of Pearl River contributes more than 31.4% to this area. The kaolinite of core SCS18-1 is 11.2%. The calculation is as follows: 31.4% (contribution percentage of Pearl River)×35.7% (the content of kaolinite in Pearl River) =11.2% (the content of kaolinite in SCS18-1).

The Pearl River material, after entering the sea, is mainly transported westward by the influence of the Guangdong coastal current and the SCS nearshore current and deposited within the coastal shelf between the mouth of the Pearl River and the northeast side of Hainan (water depth of less than 50 m) (Ge et al., 2014).

5.1.3 Illite+chlorite

The illite+chlorite in the northern part of the SCS is affected by the coastal current of Guangdong, the Kuroshio branch current in the SCS, and the deep current in winter and is transported southwestward at water depths of 100 m and 2000-2500 m. The spatial distribution of illite+chlorite content in the northern SCS displays a double tongue-shaped pattern extending from offshore Taiwan to the southwest (Liu et al., 2010c), indicating that Taiwan might be the main provenance area of illite and chlorite in the northern SCS. The illite+chlorite content in core SCS18-1 is as high as 78.3%, and only Taiwan (with an average illite+chlorite content of 96%) could provide such a high content of illite and chlorite, indicating that the illite and chlorite in core SCS18-1 sediments are mainly from Taiwan, which is consistent

with the results of Cao et al. (2018) and Liu et al. (2010b). In addition, after conversion using the method in Biscaye (1965), the content of illite and chlorite in the Pearl River is approximately 62.6%, so the possibility that the Pearl River could provide illite and chlorite to the study area cannot be excluded.

The illite crystallinity and illite chemistry index have also been widely used to indicate weathering intensity and trace sources (Wan et al., 2012b; Wang and Yang, 2013). An illite chemistry index of less than 0.5 represents Fe–Mg-rich illite, which results from physical erosion, and an illite chemistry index greater than 0.5 represents Al-rich illite, which represents strong hydrolysis. Low illite crystallinity indicates high crystallinity, indicating weak hydrolysis of the terrestrial provenance area in a dry and cold climate, and vice versa (Hu et al., 2014). The Pearl River illite has a high illite chemistry index from 0.43 to 0.8, averaging 0.59, due to long exposure to warm, humid climatic conditions and strong chemical weathering (Liu et al., 2007). The physical weathering or mechanical denudation of Taiwan is very strong because of tectonic activity and monsoon/typhoon rainfall; thus, the illite of Taiwan has a low chemistry index that ranges from 0.4 to 0.63 (the average is 0.5) (Li et al., 2012). To further clarify the material source of illite in core SCS18-1, the illite crystallinity and chemical index of core SCS18-1 are compared with those of two potential provenance areas in Taiwan and the Pearl River, and the results show that the most likely source is Taiwan (Figure 7A), followed by the Pearl River. Since illite and chlorite in the northern SCS have the same material source (Chen, 1978; Liu et al., 2003; Liu et al., 2016), it can be inferred that the illite and chlorite in the CMs of core SCS18-1 are mainly from Taiwan, followed by the Pearl River.

Kaolinite is generally formed through chemical weathering, while illite and chlorite are mainly formed by the physical weathering of the parent rock. Therefore, the ratio of kaolinite/(illite+chlorite) can be used to indicate the type of weathering, the higher the ratio is, the stronger the chemical weathering and the weaker the physical weathering, and vice versa (Huang et al., 2011; Alizai et al., 2012; Hu et al., 2014). Illite+chlorite and kaolinite are characteristic minerals of the rivers in southwestern Taiwan and the Pearl River, respectively (Liu et al., 2008). Therefore, the ratio of kaolinite/(illite +chlorite) can be used to determine the main contributions of these two source EMs to the CMs at the research station (Wan et al., 2010). Comparing illite crystallinity and kaolinite/(illite+chlorite) (Figure 7B) shows that core SCS18-1 is located between the Taiwanese rivers and the Pearl River and is closer to Taiwan, indicating that the CMs of the sediments in core SCS18-1 are mainly from Taiwan: however, a Pearl River contribution cannot be dismissed. The results of studies on the material sources of the adjacent ODP1144 (Liu et al., 2010b; Liu et al., 2013) and STD235 stations (Liu et al., 2018) also suggest that the Pearl River material has a relatively small impact in the northeastern region of the SCS.

According to the data and figure illustrations, the vertical variations(Figure 3) of illite crystallinity and chemical index values (and the clay mineral assemblages) might indicate temporal changes in contributions from different source terranes. Which may be caused by sea-level changes, climate changes, and other factors. While the vertical variations of clay mineral assemblages are inapparent, the distribution of core SCS18-1 in the ternary diagram is relatively concentrated (Figure 6), indicating that the provenance regions of the core sediments were relatively stable and experienced no major changes since the last deglaciation.

In summary, since the last deglaciation, the sources of sediments in core SCS18-1 have remained relatively stable; the sediments are mainly from Taiwan, followed by the Pearl River, and the contribution of Luzon is low. Among them, kaolinite mainly comes

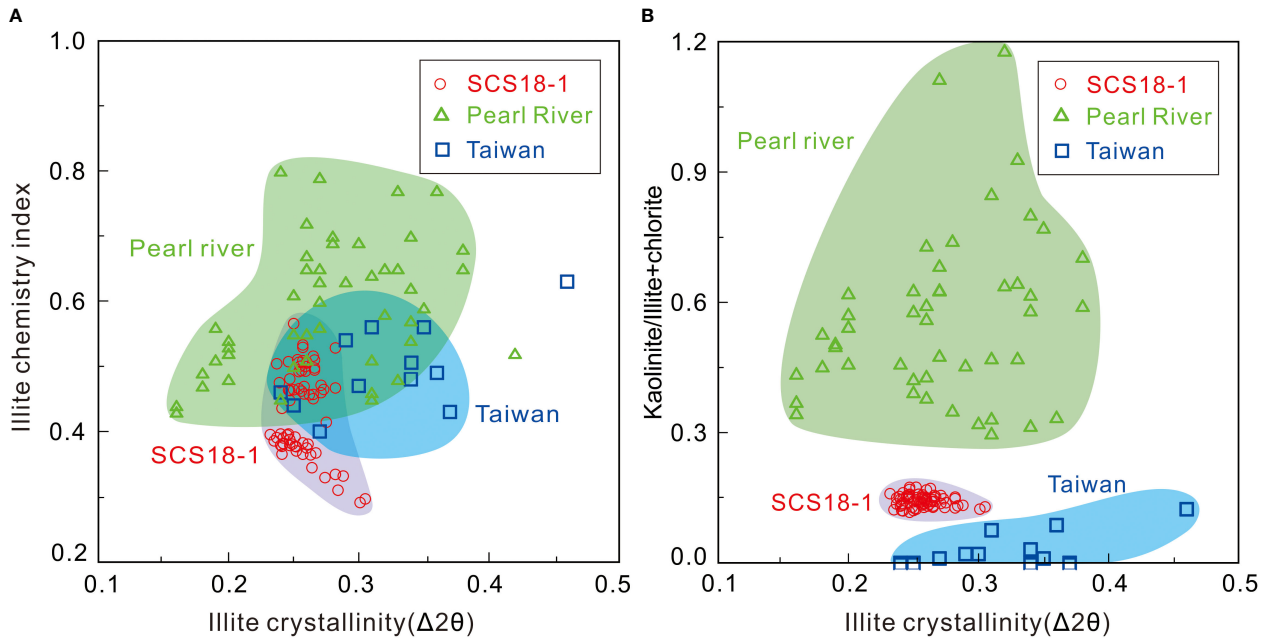

FIGURE 7
Correlation of illite crystallinity with the **(A)** illite chemical index and **(B)** kaolinite/illite+chlorite ratio in argillaceous sediments from core SCS18-1. River sediments from Taiwan rivers (Li et al., 2012), the Pearl River (Liu et al., 2007), and Luzon (Liu et al., 2009); the referenced data have been converted according to Biscaye (1965).

from the Pearl River, illite and chlorite mainly come from Taiwan, and smectite mainly originated from Luzon, with a possible certain contribution from the Pearl River.

5.2 Relevance of grain size EM components

Many studies on clay minerals, Nd isotopes, and grain size have shown that the river sediments near the SCS are the primary material source (Boulay et al., 2005; Wan et al., 2007a; Boulay et al., 2007; Shao et al., 2009; Liu et al., 2010b). The contribution of aeolian dust is small but often mentioned by some researchers (Wehausen and Brumsack, 2002; Boulay et al., 2003; Wan et al., 2007b). Numerical simulations have shown that the average contribution of aeolian dust in the northern SCS to the total terrigenous matter can reach 20% (Wan et al., 2007a). Notably, the content of quartz and feldspar in aeolian dust can reach 60-80%, which is far higher than the value of 30% in a river suspension (Li, 1997). Based on the grain size EM and SEM analysis, we conclude that aeolian dust and river sediments contribute to the quartz and feldspar in this study area, and the CMs are mainly related to fluvial input.

Previous studies have found that the "coarse eolian dust" can be transported over long distances from the land to the ocean; the coarsest component is interpreted as aeolian dust, and the finest component is interpreted as mud input by the rivers (Betzer et al., 1988; Stuut et al., 2002; Weltje and Prins, 2003; Stuut et al., 2005). Moreover, for the adjacent station ODP1146, Wan et al. (2007b) interpreted the coarse-grained EMs (mainly quartz and feldspar) as aeolian dust and the fine- and medium-grained EMs (mainly CMs) as fluvial mud and fluvial fines. The modes of the finest and medium-grained EMs are 7.5 μm and 2 μm, respectively, which agree well with the modes for EM2 (mode: 9.29 μm) and EM1 (mode: 0.98 μm) in this paper. Therefore, for core SCS18-1, the coarse-grained EM, i.e., EM3 with quartz and feldspar as the main components, is from the aeolian dust, while the fine-grained and medium-grained EMs, i.e., EM1 and EM2 with CMs as the main component, are from muddy and fine silt sediments of fluvial input, respectively.

5.3 Relevance of environmental indicators

It is generally believed that the CMs in the sediments of the northern SCS mainly come from the river input, and the river input intensity can to some extent indicate the EASM intensity (Liu et al., 2003; Wan et al., 2007b). The illite chemistry index in the CMs indicates chemical weathering in the provenance areas; therefore, the EASM also has a certain influence. On the other hand, a stronger EASM can bring more coarse-grained aeolian dust from the Asian inland or the bare, shallow sea shelf area during a low sea-level period, which could increase the contribution of coarse-grained EMs. Therefore, in this paper, the simulated coarse-grained EM3, characterizes the intensity change in the winter monsoon, and EM1 +EM2, which represents the terrigenous river material, indicates the intensity change in the summer monsoon.

In core SCS18-1, the changes in the relative content of EM1+EM2 and the illite chemistry index are identical. The relative content of EM1+EM2 and the illite chemistry index increased rapidly after 16.1 ka BP, reached a maximum value at 10.6 ka BP, and then rapidly decreased. From 6.8 ka BP to the present, the two slightly increase, and the relative content of EM3 has the opposite trend.

In stage I (16.1-10.6 ka BP), the sea level gradually increased by nearly 100 m (Figure 8F), and the estuary of the Pearl River left the study area, precluding the transport of Pearl River material to the study site. However, during stage I, EM1+EM2, which represents fluvial material, increases (Figure 8A), and the sedimentation rate of core SCS18-1 significantly increase, indicating an increase in fluvial material input, which in turn indicates that the Pearl River is not the main provenance area at this study location. Because of the narrow Taiwan shelf, a 100 m sea-level rise cannot significantly affect the location of the estuary (Figure 1B); therefore, the sea-level change since 16.1 ka BP has a slight effect on the distance between the river estuary in Taiwan and core SCS18-1, which indicates that the material from core SCS18-1 is mainly from Taiwan, not from the Pearl River. Since the last deglaciation, the EASM (Figures 8C, D) and the solar radiation in the Northern Hemisphere have gradually become stronger (Figure 8H). By the early Holocene, the East Asian monsoon reached its peak (Dykoski et al., 2005), and the strong summer monsoon inevitably brought heavy rainfall and enhanced river supply capacity, which, together with the increased typhoon events during this period, led to increased soil erosion in Taiwan (Huang et al., 2015). As a result, for core SCS18-1, the total amount of terrigenous detrital material from Taiwan increased, i.e., the relative content of EM1+EM2, representing fluvial material, increased (Figure 8A), and the sedimentation rate reached a maximum near 10.6 ka BP (Figure 8I). At the same time, because of the sea-level rise, many shallow marine areas from the west of Taiwan to the Zhongsha Islands were submerged, resulting in the transport of land-derived clastic sediments over longer distances. Thus, although the terrestrial material increased, the sediment particles became finer (Figure 8G). In addition, the global warming at the beginning of the Holocene and the strengthening of the EASM (Figures 8C, D) correspond well to the enhanced illite chemistry index of core SCS18-1 (Figure 8B). Notably, the winter monsoon index was augmented (Figure 8E), and in general, the EM3 content, which represents the contribution of aeolian dust, should also increase, but the relative EM3 content tended to decrease at this stage (Figure 4D). By combining this result with the increase in sedimentation rate at this stage (Figure 8I), we speculate that the decrease in EM3 content is caused far more by the increase in the amount of river input than by the increase in the amount of aeolian dust input.

In stage II (10.6-6.8 ka BP), during the Holocene, the global climate changed to warm, hot, and humid; vegetation was extensively developed; the range of weathering and denudation decreased, and the amount of terrigenous material suddenly decreased; the sea level rose (Figure 8F); the shoreline was pushed landward; and the sediment supply was drastically reduced (Huang et al., 2013). As a result, the sedimentation rate of core SCS18-1 decreased (Figure 8I), and the contribution of EM1+EM2, representing the river material, decreased (Figure 8A). Overall, the illite chemistry index of core SCS18-1 also decreased during this stage, which corresponds well to the gradual weakening of the EASM (Figures 8C, D).

In stage III (6.8-0 ka BP), since the Holocene (6.8 ka BP), the sea level has been stable at its highest level, and the outcropping area of the continental shelf is small; meanwhile, because of the weakening of

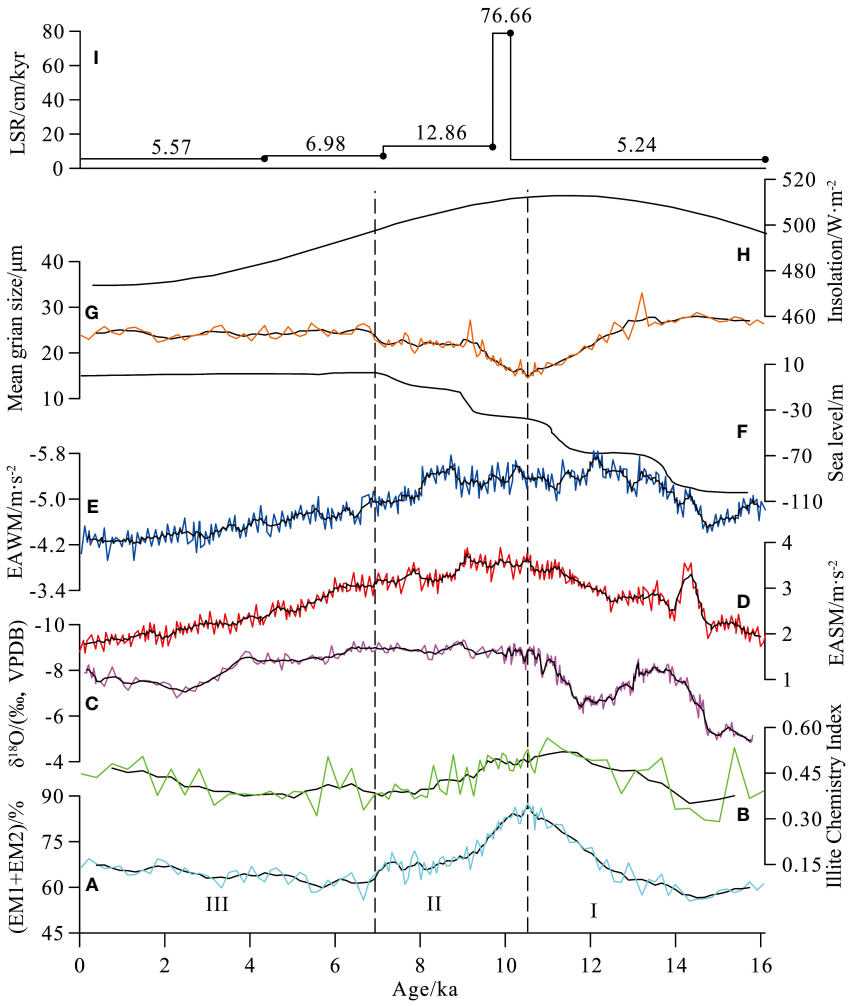

FIGURE 8
Temporal variations in **(A)** EM1+EM2 in core SCS18-1, **(B)** illite chemistry index in core SCS18-1, **(C)** $\delta^{18}O$ values of Dongge Cave stalagmites (Yuan et al., 2004), **(D)** EASM wind indices in TRACE21 (Wen et al., 2016), **(E)** EAWM wind indices in TRACE21 (Wen et al., 2016), **(F)** sea level (Liu et al., 2004; Zong, 2004), **(G)** mean grain size in core SCS18-1, **(H)** 30°N insolation (Berger and Loutre, 1991), and **(I)** linear sedimentation rate (LSR) of core SCS18-1. The thick solid lines are several points of the moving average curve.

the summer and winter monsoons (Figures 8D, E), the transport capacity of rivers and winds is reduced; therefore, the sedimentation rate of core SCS18-1 is low and has slightly decreased since 6.8 ka BP. Notably, the relative contribution of EM1+EM2 at core SCS18-1, representing riverine material, has weakly increased since 6.8 ka BP, but this trend may be caused by a relatively large reduction in the contribution of the aeolian dust (EM3).

In summary, the sedimentation process of core SCS18-1 is relatively continuous, and information on the material source and environmental evolution in the north slope of the SCS since the last deglaciation is well recorded. The relative content of EM1+EM2 and the illite chemistry index, representing riverine material, can effectively reflect the change of the EASM, and the relative content of EM3, representing aeolian dust, can effectively reflect the change of the EAWM. Thus, this study reconstructed the intensity changes of EASM and EAWM since the last deglaciation. During stage I (16.1-10.6 ka BP), the EASM and EAWM grew stronger, while since 10.6 ka BP, the EASM and EAWM have exhibited a weakening trend. Furthermore, these proxies could also reflect the variations in ocean currents. On the orbital scale, the change in East Asian summer and winter monsoon intensities is closely related to the solar radiation in the Northern Hemisphere (Figure 8H) (Wang et al., 2008; Wen et al., 2016). Therefore, the amount of supplied material in core SCS18-1 may be closely related to changing solar radiation in the Northern Hemisphere.

6 Conclusions

The grain size information of core SCS18-1 was analyzed by endmember modeling analysis, and combined with clay mineralogical methods, the provenances of the sediment in the Beipo seamount of the SCS since the last deglaciation and its paleoenvironmental conditions were explored. The following conclusions were drawn:

1. The grain size of core SCS18-1 can be divided into three endmembers, EM1, EM2, and EM3, among which fine-grained EM1 and medium-coarse-grained EM2 are mainly fluvial mud and fluvial fine silt, and the coarse-grained EM3 is mainly aeolian dust. The average grain size of core SCS18-1

is predominantly controlled by the coarse-grained EM3 with quartz and feldspar as the major components.

2. Since the last deglaciation, the sediments of core SCS18-1 have been mainly derived from fluvial input, with some contributions from aeolian input. Its clay minerals mainly originate from Taiwan, followed by the Pearl River, and Luzon Island contributes less. Among these minerals, kaolinite is mainly from the Pearl River; illite and chlorite are mainly from Taiwan, with some contribution from the Pearl River; and smectite is mainly from Luzon Island.
3. The sediments of core SCS18-1 provide a complete record of the provenance and paleoenvironmental evolution of the Beipo seamount since the last glaciation. The fluvial materials, represented by the relative content of EM1+EM2, and the illite chemical index can effectively reflect the changes in the East Asian summer monsoon. The aeolian materials, represented by the relative content of EM3, can effectively reflect the changes in the EAWM. The material supply of core SCS18-1 is mainly controlled by the amount of solar radiation in the Northern Hemisphere.

Data availability statement

The original contributions presented in the study are included in the article/supplementary material. Further inquiries can be directed to the corresponding authors.

Author contributions

XT: Conceptualization, Methodology, Validation, Formal analysis, Investigation, Resources, Writing–original draft, Writing–review and editing. XZ: Conceptualization, Methodology, Validation, Writing–review and editing, Supervision, Funding acquisition. JW: Conceptualization, Data curation, Writing–review and editing. ZS: Data curation, Writing–review and editing. ML: Conceptualization, Methodology, Data curation. JZ: Conceptualization, Methodology, Writing–review and editing, Supervision. LZ: Conceptualization, Writing–review & editing. DF: Conceptualization, Methodology, Data curation, Supervision. FX: Conceptualization, Methodology, Validation, Writing – review and editing, Supervision, Funding acquisition. All authors contributed to the article and approved the submitted version.

Funding

This study was jointly supported by the Shandong Provincial Natural Science Foundation of China (ZR2020MD062), the National Key Research and Development Program of China (2016YFA0600904), the Project of the China. Geological Survey (DD20221701), the National Natural Science Foundation of China (42176057), and a Central Government-Led Local Science andTechnology Development Foundation (ZY2021HN04).

Acknowledgments

We would like to thank Editor ML, XJ and GÚ for their constructive comments and reviews of the earlier versions of this paper.

Conflict of interest

The authors declare that the research was conducted in the absence of any commercial or financial relationships that could be construed as a potential conflict of interest.

Publisher's note

References

Alizai, A., Hillier, S., Clift, P. D., Giosan, L., Hurst, A., VanLaningham, S., et al. (2012). Clay mineral variations in Holocene terrestrial sediments from the indus basin. *Quaternary Res.* 77 (3), 368–381. doi: 10.1016/j.yqres.2012.01.008

Berger, A., and Loutre, M. F. (1991). Insolation values for the climate of the last 10 million years. *Quaternary Sci. Rev.* 10 (4), 297–317. doi: 10.1016/0277-3791(91)90033-Q

Betzer, P. R., Carder, K. L., Duce, R. A., Merrill, J. T., Tindale, N. W., Uematsu, M., et al. (1988). Long-range transport of giant mineral aerosol particles. *Nature.* 336 (6199), 568–571. doi: 10.1038/336568a0

Biscaye, P. E. (1965). Mineralogy and sedimentation of recent deep-sea clay in the Atlantic ocean and adjacent seas and oceans. *Geological Soc. America Bulletin.* 76 (7), 803–832. doi: 10.1130/0016-7606(1965)76[803:MASORD]2.0.CO;2

Blaauw, M., and Christen, J. A. (2011). Flexible paleoclimate age-depth models using an autoregressive gamma process. *Bayesian Anal.* 6 (3), 457–474. doi: 10.1214/ba/1339616472

Boulay, S., Blum, P., Christophe, C., Alain, T., Wang, P. X., Pluquet, F., et al. (2003). Mineralogy and sedimentology of pleistocene sediment in the south China Sea (ODP site 1144). *Proc. Ocean Drilling Program: Sci. Results.* 184 (211), 1–21. doi: 10.2973/odp.proc.sr.184.211.2003

Boulay, S., Colin, C., Trentesaux, A., Frank, N., and Liu, Z. F. (2005). Sediment sources and East Asian monsoon intensity over the last 450 ky. mineralogical and geochemical investigations on south China Sea sediments. *Paleogeogr Palaeoclimatol Palaeoecol.* 228 (3-4), 260–277. doi: 10.1016/j.palaeo.2005.06.005

Boulay, S., Colin, C., Trentesaux, A., Stéphane, C., Liu, Z. F., and Christine, L. L. (2007). Sedimentary responses to the pleistocene climatic variations recorded in the south China Sea. *Quaternary Res.* 68 (1), 162–172. doi: 10.1016/j.yqres.2007.03.004

Cao, L., Liu, J. G., He, W., and MD, H. R. K. (2018). Clay mineral assemblage features of major rivers along the south China coast and their contributions to the northern south China Sea. *Earth Sci.* 43 (Suppl. 2), 192–202. doi: 10.3799/dqkx.2018.189

Chen, P. Y. (1978). Minerals in bottom sediments of the south China Sea, geological. *Soc. America Bulletin.* 89 (2), 211–222. doi: 10.1130/0016-7606(1978)89<211:MIBSOT>2.0.CO;2

Chen, H., Zhang, W., Xie, X., and Ren, J. Y. (2019). Sediment dynamics driven by contour currents and mesoscale eddies along continental slope: A case study of the northern south China Sea. *Mar. Geol* 409, 48–66. doi: 10.1016/j.margeo.2018.12.012

Clift, P. D., Lee, J. I., Clark, M. K., and Blusztajn, J. (2002). Erosional response of south China to arc rifting and monsoonal strengthening; a record from the south China Sea. *Mar. Geol.* 184 (3-4), 207–226. doi: 10.1016/S0025-3227(01)00301-2

Clift, P. D., Wan, S. M., and Blusztajn, J. (2014). Reconstructing chemical weathering, physical erosion and monsoon intensity since 25 ma in the northern south China Sea: a review of competing proxies. *Earth-Science Rev.* 130, 86–102. doi: 10.1016/j.earscirev.2014.01.002

Dykoski, C. A., Edwards, R. L., Cheng, H., Yuan, D. X., Cai, Y. J., Zhang, M. L., et al. (2005). A high-resolution, absolute-dated Holocene and deglacial Asian monsoon record from dongge cave, China. *Earth Planetary Sci. Letters.* 233 (1-2), 71–86. doi: 10.1016/j.epsl.2005.01.036

Ge, Q., Liu, J. P., Xue, Z., and Chu, F. Y. (2014). Dispersal of the zhujiang river (Pearl river) derived sediment in the Holocene. *Acta Oceanologica Sinica.* 33 (8), 1–9. doi: 10.1007/s13131-014-0407-8

Huang, J., Li, A. C., and Wan, S. M. (2011). Sensitive grain-size records of Holocene East Asian summer monsoon in sediments of northern south China Sea slope. *Quaternary Res.* 75 (3), 734–744. doi: 10.1016/j.yqres.2011.03.002

Huang, E. Q., Tian, J., Qiao, P. J., Wan, S., Xie, X., and Yang, W. G. (2015). Early interglacial carbonate-dilution events in the south China Sea: Implications for strengthened typhoon activities over subtropical East Asia. *Quaternary Sci. Rev.* 125, 61–77. doi: 10.1016/j.quascirev.2015.08.007

Huang, J., Li, A. C., Wan, S. M., Xu, F. J., and Meng, Q. Y. (2013). Terrigenous input to the northern slope of the south China Sea and its controlling factor since the last phase of the last glacial maximum. *Oceanologia et Limnologia Sinica* 44 (4), 882–889. doi: 10.11693/hyhz201304009009

Huang, J., Wan, S. M., Xiong, Z. F., Zhao, D. B., Liu, X. T., Li, A. C., et al. (2016). Geochemical records of Taiwan-sourced sediments in the south China Sea linked to Holocene climate changes. *Paleogeogr Palaeoclimatol Palaeoecol.* 441 (4), 871–881. doi: 10.1016/j.palaeo.2015.10.036

Hu, D. K., Böning, P., Köhler, C. M., Hillier, S., Pressling, N., Wan, S. M., et al. (2012). Deep sea records of the continental weathering and erosion response to East Asian monsoon intensification since 14 ka in the south China Sea. *Chem. Geol.* 326-327, 1–18. doi: 10.1016/j.chemgeo.2012.07.024

Hu, B. Q., Li, J., Cui, R. Y., Wei, H. L., Zhao, J. T., Li, G. G., et al. (2014). Clay mineralogy of the riverine sediments of hainan island, south China Sea: Implications for weathering and provenance. *J. Asian Earth Sci.* 96, 84–92. doi: 10.1016/j.jseaes.2014.08.036

Kissel, C., Laj, C., Jian, Z., Wang, P., Wandres, C., and Rebolledo-Vieyra, M. (2020). Past environmental and circulation changes in the south China Sea: Input from the magnetic properties of deep-sea sediments. *Quaternary Sci. Rev.* 236, 106263. doi: 10.1016/j.quascirev.2020.106263

Li, A. C. (1997). *The flux and composition of mineral aerosols over the East China sea. PhD dissertation* (Qingdao: Institute of Oceanology of the Chinese Academy of Sciences), 46–70.

Li, C. S., Shi, X. F., Kao, S. J., Chen, M. T., Liu, Y. G., Fang, X. S., et al. (2012). Clay mineral composition and their sources for the fluvial sediments of Taiwanese rivers. *Chin. Sci. Bull.* 57 (6), 673–681. doi: 10.1007/s11434-011-4824-1

Liu, Z. F. (2010). Clay mineral assemblages in sediments of the south China Sea: East Asian monsoon evolution proxies? *Acta Sedimentological Sin.* 28 (5), 1012–1019.

Liu, J. G., Chen, Z., Chen, M. H., Yan, W., Xiang, R., and Tang, X. Z. (2010a). Magnetic susceptibility variations and provenance of surface sediments in the south China Sea. *Sedimentary geol* 230 (1/2), 77–85. doi: 10.1016/j.sedgeo.2010.07.001

Liu, Z. F., Colin, C., Huang, W., Chen, Z., Alain, T., and Chen, J. (2007). Clay minerals in surface sediments of the pearl river drainage basin and their contribution to the south China Sea. *Chin. Sci. Bulletin.* 52 (8), 1101–1111. doi: 10.1007/s11434-007-0161-9

Liu, Z. F., Colin, C., Li, X. J., Zhao, Y. L., Tuo, S. T., Chen, Z., et al. (2010c). Clay mineral distribution in surface sediments of the northeastern south China Sea and surrounding fluvial drainage basins: Source and transport. *Mar. Geol.* 277 (1-4), 48–60. doi: 10.1016/j.margeo.2010.08.010

Liu, Z. F., Colin, C., Trentesaux, A., Blamart, D., Bassinot, F., Siani, G., et al. (2004). Erosional history of the eastern Tibetan plateau over the past 190 kyr: Clay mineralogical and geochemical investigations from the southwestern south China Sea. *Mar. Geol.* 209 (1), 1–18. doi: 10.1016/j.margeo.2004.06.004

Liu, Z. F., and Li, X. J. (2011). Discussion on smectite formation in south China Sea sediments. *Quaternary Sci.* 31 (2), 199–206. doi: 10.3969/j.issn.1001-7410.2011.02.01

Liu, Z. F., Li, X. J., Colin, C., and Ge, H. M. (2010b). A high-resolution clay mineralogical record in the northern south China Sea since the last glacial maximum, and its time series provenance analysis. *Chin. Sci. Bull.* 55 (29), 2852–2862. doi: 10.1007/s11434-010-4149-5

Liu, J. G., Steinke, S., Vogt, C., Mohtadi, M., Pol-Holz, R. D., and Hebbeln, D. (2017). Temporal and spatial patterns of sediment deposition in the northern south China Sea over the last 50,000 years. *Paleogeogr Palaeoclimatol Palaeoecol.* 465 (Part A), 212–224. doi: 10.1016/j.palaeo.2016.10.033

Liu, Z. F., Trentesaux, A., Clemens, S. C., Colin, C., Wang, P. X., Huang, B. Q., et al. (2003). Clay mineral assemblages in the northern south China Sea: Implications for East Asian monsoon evolution over the past 2 million years. *Mar. Geol.* 201 (1), 133–146. doi: 10.1016/S0025-3227(03)00213-5

Liu, Z. F., Tuo, S. T., Colin, C., Liu, J. T., Huang, C. Y., Chen, C. T. A., et al. (2008). Detrital fine-grained sediment contribution from Taiwan to the northern south China Sea and its relation to regional ocean circulation. *Mar. Geol.* 255 (3-4), 149–155. doi: 10.1016/j.margeo.2008.08.003

Liu, J. G., Xiang, R., Chen, Z., Chen, M. H., Yan, W., Zhang, L. L., et al. (2013). Sources, transport and deposition of surface sediments from the south China Sea. *Deep Sea Res. Part I: Oceanographic Res. Papers.* 71, 92–102. doi: 10.3969/j.issn.1001-7410.2011.02.01

Liu, F., Yang, C. P., Chang, X. H., and Liao, Z. W. (2018). Sedimentary geochemistry properties of rare earth elements from the continental lower slope of the northeastern south China Sea over the last 20 ka and its implication for provenance. *Acta Oceanologica Sinica.* 40 (9), 148–158. doi: 10.3969/j.issn.0253-4193.2018.09.013

Liu, Z. F., Zhao, Y. L., Colin, C., Siringan, F. P., and Wu, Q. (2009). Chemical weathering in Luzon, Philippines from clay mineralogy and major-element geochemistry of river sediments. *Appl. Geochem.* 24 (11), 2195–2205. doi: 10.1016/j.apgeochem.2009.09.025

Liu, Z. F., Zhao, L. Y., Colin, C., Stattegger, K., Wiesner, M. G., Huh, C. A., et al. (2016). Source-to-sink transport processes of fluvial sediments in the south China Sea. *Earth-Science Rev.* 153, 238–273. doi: 10.1016/j.earscirev.2015.08.005

Li, X. H., Wei, G. J., Shao, L., Liu, Y., Liang, X. R., Jian, Z. M., et al. (2003). Geochemical and Nd isotopic variations in sediments of the south China Sea: A response to Cenozoic tectonism in SE Asia. *Earth Planetary Sci. Letters.* 211 (3), 207–220. doi: 10.1016/S0012-821X(03)00229-2

Milliman, J. D., and Syvitski, J. P. M. (1992). Geomorphic/tectonic control of sediment discharge to the ocean: The importance of small mountainous rivers. *J. Geol.* 100 (5), 525–544. doi: 10.1086/629606

Paterson, G. A., and Heslop, D. (2015). New methods for unmixing sediment grain size data. *Geochem Geophysics Geosystems.* 16 (12), 4494–4506. doi: 10.1002/2015GC006070

Shao, L., Qiao, P. J., Pang, X., Wei, G. J., Li, Q. Y., Miao, W. L., et al. (2009). Nd Isotopic variations and its implications in the recent sediments from the northern south China Sea. *Chin. Sci. Bulletin.* 54 (2), 311–317. doi: 10.1007/s11434-008-0453-8

Shao, L., Zhao, M., Qiao, P. J., Pang, X., and Wu, M. S. (2013). Sediment characteristics in the northern south China Sea and their response to the evolution of the pearl river. *Quaternary Res.* 33 (4), 760–770. doi: 10.3969/j.issn.1001-7410.2013.04.13

Shaw, P. T., and Chao, S. Y. (1994). Surface circulation in the south China Sea. *Oceanographic Res. Papers.* 41 (11-12), 1663–1683. doi: 10.1016/0967-0637(94)90067-1

Staudigel, H., and Clague, D. A. (2010). The geological history of deep-sea volcanoes: Biosphere, hydrosphere, and lithosphere interactions. *Oceanography.* 23 (1), 58–71. doi: 10.5670/oceanog.2010.62

Staudigel, H., and Koppers, A. A. P. (2015). "Seamounts and island building," in *The encyclopedia of volcanoes* (Amsterdam: Elsevier), 405–421.

Stuut, J. B. W., Prins, M. A., Schneider, R. R., Weltje, G. J., Jansen, J. H. F., and Postma, G. (2002). A 300-kyr record of aridity and wind strength in southwestern Africa: inferences from grain-size distributions of sediments on Walvis ridge, SE Atlantic. *Mar. Geol.* 180 (1-4), 221–233. doi: 10.1016/S0025-3227(01)00215-8

Stuut, J. B., Zabel, M., Ratmeyer, V., Helmke, P., Schefuß, E., Lavik, G., et al. (2005). Provenance of present-day eolian dust collected off NW Africa. *J. Geophysical Research: Atmospheres* 110 (D04202). doi: 10.1029/2004JD005161

Tanghe, N. (2016). *The palaeo-environmental history of equatorial East Africa: Implications from mineralogy and particle-size distributions (Master's thesis)* (Belgium: Universiteit Gent).

Wan, S. M., Clift, P. D., Li, A. C., Yu, Z. J., Li, T. G., and Hu, D. K. (2012a). Tectonic and climatic controls on long-term silicate weathering in Asia since 5 ma. *Geophysical Res. Lett.* 39 (15), L15611. doi: 10.1029/2012GL052377

Wan, S. M., Clift, P. D., Zhao, D. B., Hovius, N., Munhoven, G., France-Lanord, C., et al. (2017). Enhanced silicate weathering of tropical shelf sediments exposed during glacial lowstands: a sink for atmospheric CO_2. *Geochimical Cosmochimica Acta* 200, 123–144. doi: 10.1016/j.gca.2016.12.010

Wang, Y. J., Cheng, H., Edwards, R. L., Kong, X. G., Shao, X. H., Chen, S., et al. (2008). Millennial-and orbital-scale changes in the East Asian monsoon over the past 224,000 years. *Nature.* 451 (7182), 1090–1093. doi: 10.1038/nature06692

Wang, Q., and Yang, S. Y. (2013). Clay mineralogy indicates the Holocene monsoon climate in the changjiang (Yangtze river) catchment, China. *Appl. Clay Science.* 74, 28–36. doi: 10.1016/j.clay.2012.08.011

Wan, S. M., Li, A. C., Clift, P. D., and Stuut, J. B. W. (2007a). Development of the East Asian monsoon: mineralogical and sedimentologic records in the northern south China Sea since 20 ma. *Palaeogeogr Palaeoclimatol Palaeoecol.* 254 (3-4), 561–582. doi: 10.1016/j.palaeo.2007.07.009

Wan, S. M., Li, A. C., Clift, P. D., Wu, S. G., Xu, K. H., and Li, T. G. (2010). Increased contribution of terrigenous supply from Taiwan to the northern south China Sea since 3 ma. *Mar. Geol.* 278 (1-4), 115–121. doi: 10.1016/j.margeo.2010.09.008

Wan, S. M., Li, A. C., Jan-Berend, W. S., and Xu, F. J. (2007b). Grain-size records at ODP site 1146 from the northern south China Sea: Implications on the East Asian monsoon evolution since 20 ma. *Sci. China Ser. D: Earth Sci.* 50 (10), 1536–1547. doi: 10.1007/s11430-007-0082-0

Wan, S. M., Yu, Z. J., Clift, P. D., Sun, H. J., Li, A. C., and Li, T. G. (2012b). History of Asian eolian input to the West Philippine Sea over the last one million years. *Paleogeogr Palaeoclimatol Palaeoecol.* 326-328, 152–159. doi: 10.1016/j.palaeo.2012.02.015

Wehausen, R., and Brumsack, H. J. (2002). Astronomical forcing of the East Asian monsoon mirrored by the composition of pliocene south China Sea sediments. *Earth Planetary Sci. Letters.* 201 (3-4), 621–636. doi: 10.1016/S0012-821X(02)00746-X

Weltje, G. J., and Prins, M. A. (2003). Muddled or mixed? *Inferring palaeoclimate size distributions deep-sea classtics. Sedimentary Geol.* 162 (1-2), 39–62. doi: 10.1016/S0037-0738(03)00235-5

Wen, X. Y., Liu, Z. Y., Wang, S. W., and Chen, J. (2016). Correlation and anti-correlation of the East Asian summer and winter monsoons during the last 21,000 years. *Nat. Commun.* 7 (1), 1–7. doi: 10.1038/ncomms11999

Wentworth, C. K. (1922). A scale of grade and class terms for clastic sediments. *J. Geol.* 30 (5), 377–392. doi: 10.1086/622910

Wessel, P., Sandwell, D. T., and Kim, S. S. (2010). The global seamount census. *Oceanography.* 23 (1), 24–33. doi: 10.5670/oceanog.2010.60

Xu, F. J., Hu, B. Q., Zhao, J. T., Liu, X. T., Xu, K. H., Xiong, Z. F., et al. (2021). Provenance and weathering of sediments in the deep basin of the northern south China Sea during the last 38 kyr. *Mar. Geol.* 440, 106602. doi: 10.1016/j.margeo.2021.106602

Yoneda, M., Uno, H., Shibata, Y., Suzuki, R., Kumamoto, Y., Yoshida, K., et al. (2007). Radiocarbon marine reservoir ages in the western pacific estimated by pre-bomb molluscan shells. *Nucl. Instruments Methods Phys. Res. Section B: Beam Interact. Materials Atoms.* 259 (1), 432–437. doi: 10.1016/j.nimb.2007.01.184

Yuan, D. X., Cheng, H., Edwards, R. L., Dykoski, C. A., Kelly, M. J., Zhang, M. L., et al. (2004). Timing, duration, and transitions of the last interglacial Asian monsoon. *Science.* 304 (5670), 575–578.

Zhang, X., and Boyer, D. L. (1991). Current deflections in the vicinity of multiple seamounts. *J. Phys. Oceanogr* 21 (8), 1122–1138. doi: 10.1175/1520-0485(1991)021<1122:CDITVO>2.0.CO;2

Zhao, B., Lü, W. H., He, G. W., Zhang, J. B., Wei, Z. Q., Ning, Z. J., et al. (2022). Sedimentary processes of weijia guyot and implications for western pacific seamount evolution. *Earth Sci.* 47 (1), 357–367. doi: 10.3799/dqkx.2020.291

Zhong, Y., Chen, Z., González, F. J., Hein, J. R., Zheng, X. F., Li, G., et al. (2017). Composition and genesis of ferromanganese deposits from the northern south China Sea. *J. Asian Earth Sci.* 138, 110–128. doi: 10.1016/j.jseaes.2017.02.015

Zhou, H. Y., Zhu, Q. K., Ji, F. W., and Yang, Q. H. (2020). Discoveries about seamounts in deep basin of south China Sea. *Sci. Technol. Rev.* 38 (18), 83–88. doi: 10.3981/j.issn.1000-7857.2020.18.013

Zong, Y. Q. (2004). Mid-Holocene sea-level highstand along the southeast coast of China. *Quaternary Int.* 117 (1), 55–67. doi: 10.1016/S1040-6182(03)00116-2

frontiers | Frontiers in Marine Science

TYPE Original Research
PUBLISHED 24 February 2023
DOI 10.3389/fmars.2023.1141926

OPEN ACCESS

EDITED BY
Wei Li,
South China Sea Institute of Oceanology (CAS), China

REVIEWED BY
Jingbo Nan,
Southern University of Science and Technology, China
Yazhou Fu,
Institute of Geochemistry (CAS), China

*CORRESPONDENCE
Yao Guan
guanyao@mail2.sysu.edu.cn
Xiaoming Sun
eessxm@mail.sysu.edu.cn

†These authors have contributed equally to this work

SPECIALTY SECTION
This article was submitted to Marine Biogeochemistry, a section of the journal Frontiers in Marine Science

RECEIVED 11 January 2023
ACCEPTED 10 February 2023
PUBLISHED 24 February 2023

CITATION
Ren Y, Guan Y, Sun X, Xu L, Xiao Z, Deng Y and He W (2023) Nano-mineralogy and growth environment of Fe-Mn polymetallic crusts and nodules from the South China Sea. *Front. Mar. Sci.* 10:1141926. doi: 10.3389/fmars.2023.1141926

Nano-mineralogy and growth environment of Fe-Mn polymetallic crusts and nodules from the South China Sea

Yingzhi Ren[1,2†], Yao Guan[3,4*†], Xiaoming Sun[1*], Li Xu[1], Zhenglian Xiao[5], Yuqi Deng[4] and Wentao He[4]

[1]School of Marine Sciences, Guangdong Provincial Key Laboratory of Marine Resources and Coastal Engineering, Sun Yat-sen University, Guangzhou, China, [2]Key Laboratory of Marine Mineral Resources, Guangzhou Marine Geological Survey, Guangzhou, China, [3]Key Laboratory of Tropical Marine Ecosystem and Bioresource, Fourth Institute of Oceanography, Ministry of Natural Resources, Beihai, China, [4]Guangxi Key Laboratory of Beibu Gulf Marine Resources, Environment and Sustainable Development, Fourth Institute of Oceanography, Ministry of Natural Resources, Beihai, China, [5]Southern Marine Science and Engineering Guangdong Laboratory (Zhuhai), Zhuhai, China

Fe-Mn polymetallic crusts and nodules from the South China Sea (SCS) consist of submarine ferromanganese (Fe-Mn) oxide precipitates, and represent important marine mineral resource with substantial economic and scientific research value. Previous studies on the SCS polymetallic crusts and nodules were mainly focused on their bulk mineralogy and geochemistry, whilst research on their nanomineralogy is still lacking. In this study, transmission electron microscopy (TEM), Raman spectroscopic mapping, and in-situ micro X-ray diffraction (XRD) analysis were conducted on the nano-mineralogy of the SCS polymetallic crusts and nodules. It is found that the SCS polymetallic crusts and nodules consist mainly of layered/columnar/mottled nano-phase Fe-Mn minerals and detritus such as quartz, feldspar, and clays. Also, an independent Ti mineral phase has been documented, and the mineralogical analysis reveals the transformation from vernadite to birnessite and todorokite. Titanium forms colloidal minerals in seawater and precipitates into the crusts and nodules with other colloids, such as FeOOH and Si-Al. Vernadite and birnessite can be transformed to todorokite with stable structure under sub-oxic conditions. Therefore, the SCS polymetallic crusts and nodules were formed in a short period of sub-oxic environment and diagenetic process, and the transformation can influence the enrichment of Ni and other metals during the crust/nodule growth.

KEYWORDS

nano-mineralogy, high resolution transmission electron microscope (HRTEM) analysis, growth environment, polymetallic crusts and nodules, South China Sea

1 Introduction

Marine Fe-Mn ferromanganese (Fe-Mn) oxide precipitates are mainly formed by direct precipitation from the ambient cold seawater (hydrogenetic-type), sediment pore water (diagenetic-type), or seafloor hydrothermal fluids (hydrothermal-type) (Hein et al., 1997; Hein et al., 2013; Bau et al., 2014). According to the deposition environments, marine Fe-Mn precipitates are classified into crusts, nodules, and hydrothermal Fe-Mn deposits. Fe-Mn (or Co-rich) polymetallic crusts are commonly deposited on substrates without sediment cover, e.g., on the outer margin of seamount summits and marine platforms or saddle structures (Halbach et al., 2017; Usui et al., 2017), whilst Fe-Mn polymetallic nodules are deposited on intermountain basins or abyssal plains with more sediment cover, and tend to grow around a core. All the Fe-Mn polymetallic crusts, nodules, and hydrothermal deposits are important marine mineral resource and host critical metals such as Co, Ni, Cu, Tl, Te, Nb, and rare earth elements plus yttrium (REY) (Hein et al., 2013), and have received much research and exploration interest.

In recent years, the Fe-Mn polymetallic crusts and nodules in marginal seas have received increasing attention, esp. those in the Baltic Sea (Grigoriev et al., 2013; Yli-Hemminki et al., 2016) and the California continental margin (Hein, 2005; Conrad et al., 2017). Several mineralogical and geochemical studies on the Fe-Mn crusts and nodules in the South China Sea (SCS) have also been carried out (Li and Zhang, 1990; Bao and Li, 1993; Lin et al., 2003; Zhang and Weng, 2005; Zhang et al., 2009; Wang and Zhang, 2011; Zhang et al., 2013; Zhong et al., 2017; Guan et al., 2017a; Guan et al., 2017b; Guan et al., 2017c; Guan et al., 2019; Jiang et al., 2019; Zhou et al., 2021; Konstantinova et al., 2022).

Polymetallic crusts and nodules are widely distributed on the SCS seafloor (Li and Zhang, 1990; Zhong et al., 2017), including in the northern continental slope (around the Dongsha (Pratas) Islands), the northwestern continental margin (around the Zhongjian (Trition) Island), the central sea basin [around the Huangyan Island (Scarborough Shoal)], and around the Nansha Islands (Spratly islands). The SCS polymetallic crusts and nodules were developed mainly on the terraces and seamounts of continental slope at 472 to 3570 m water depth. The Fe-Mn encrustation is generally thin (few mm to cm). Previously, the SCS polymetallic crusts and nodules are generally considered to have a hydrogenetic origin (Zhang et al., 2013; Guan et al., 2017b), but later studies also suggested major involvement from gas hydrate release (Zhong et al., 2017) and biogenesis (Jiang et al., 2019). Microzonal analysis revealed that the northern SCS nodules may have had a mixed hydrogenetic-diagenetic genesis (Guan et al., 2019; Zhong et al., 2019).

Analyzing the growth structure and mineralogy of polymetallic crusts and nodules is essential for studying this kind of marine mineralization, and techniques such as XRD, *in-situ* XRD, synchrotron XRD, and transmission electron microscopy (TEM) are widely used, as minerals from polymetallic crusts and nodules are generally poorly crystalline (Bai et al., 2002; Kashiwabara et al., 2013; Manceau et al., 2014; Marcus et al., 2015; Atkins et al., 2016; Lee et al., 2016; Lee and Xu, 2016a, b; Shiraishi et al., 2016; Konstantinova et al., 2017). Mineralogical studies on the SCS polymetallic crusts and nodules were focused mainly on whole-rock mineral phase characterization, whereas in-depth studies on *in-situ* mineralogical characterization and nano-minerals are still inadequate (Zhong et al., 2017; Guan et al., 2017b).

Previous studies have shown that micro-structures in the SCS polymetallic crusts and nodules are mainly growth structures and intermittent structures. Common growth structures include mottled, stacked, laminated, columnar and palisade structures. These structures are composed mainly of Fe-vernadite, todorokite (10 Å manganite), birnessite, amorphous Fe-oxides/hydroxides, quartz, and feldspars (Guan et al., 2017b; Guan et al., 2019). Zhong et al. (2017) found that the northwestern SCS nodules contain large amount of pyrite, asbolite and apatite. The SCS polymetallic crusts and nodules are mainly composed of poorly-crystallized Fe-Mn hydroxides, and manganese oxides. The poor crystallization often leads to complex mineral identification, esp. for some Fe-phase minerals (often amorphous), which cannot be determined with XRD. Therefore, the TEM analyses would allow accurate identification of multiple mineral phases in these polymetallic crusts and nodules.

As mentioned above, the SCS polymetallic crusts and nodules contain kinds of minerals and metallic minerals have poor crytallinity, which makes them ideal samples for nano-mineralogy research. Furthermore, the nano Fe-Mn minerals have strong surface chemical activity and selective adsorption capacity, which is of great significance to the selective enrichment of ore-forming elements in the polymetallic crusts and nodules (Guan et al., 2017b). And the study of nano-minerals is beneficial in revealing the mechanism of element enrichment and mineralization of the polymetallic crusts and nodules.

2 Geological setting

The SCS lies at the intersection of the Eurasian, Indo-Australian, and Philippine Sea plates. It is a marginal sea located south of South China, with an area of ~3.50×10^4 km^2 (Figure 1). Regional surveys suggested that the SCS slopes in a stepwise manner from the margin to the center with increasing water depth (200-3800 m), with the development of undulatory topography comprising continental shelf and slope, island shelf and slope, and marginal sea basin (Yang et al., 2015). Isobath of the northern continental shelf is relatively straight, and the width decreases from west to east. Meanwhile, water depth of the northern continental shelf increases gradually from northwest to southeast, whilst the gradient first increases and then decreases. Gradient of the western continental shelf is narrow and steep; the water depth of the western continental shelf varies greatly, the topography is undulating and complex, with the development of sea platforms, terraces, ridges, and troughs. The eastern island slope is located west of the Philippine Islands, with a maximum water depth of 4,000 m and an average gradient of 1.4°. The topography is obviously undulating, with geographical entities such as ridges, troughs, slopes, and deep-water terraces. The SCS basin is located in the central, developing deep-sea plains, seamount chains, and seamount groups,

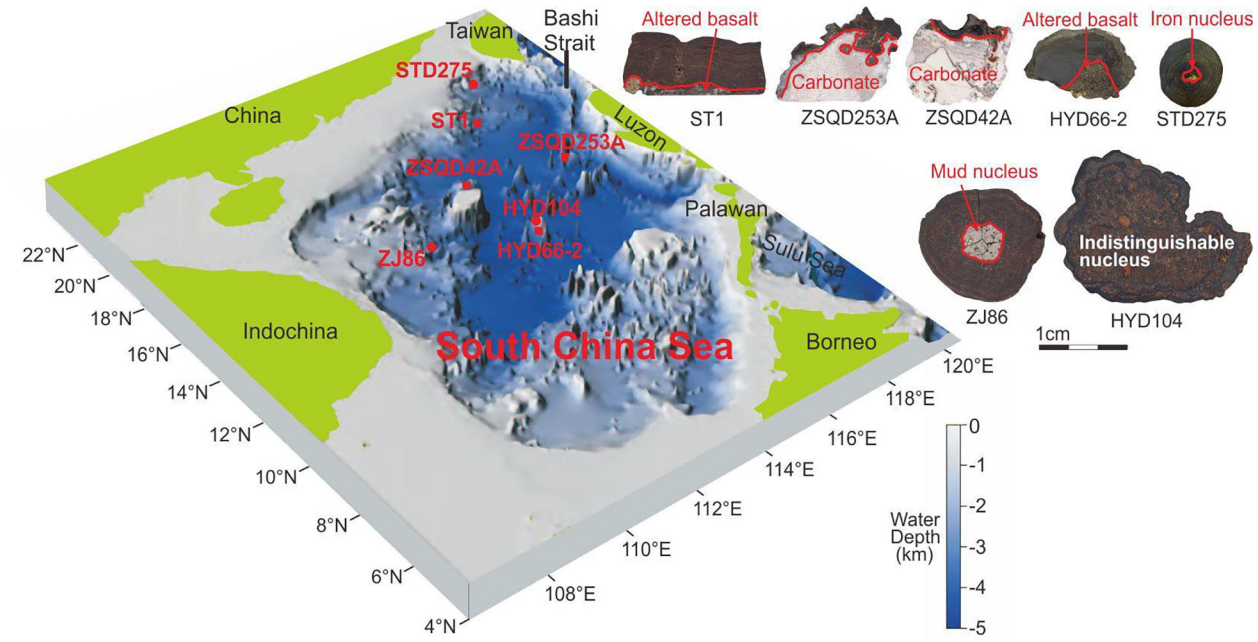

FIGURE 1
Location and topographic map of the South China Sea (Wang and Li, 2009).

etc. The water depth is between 4000-4500 m. The topography is generally flat, but the elevation difference of seamounts is large (> 3000 m). Therefore, the tectonic and geological background of the SCS and the good water exchange capacity are both favorable for the growth and mineralization of the polymetallic crusts and nodules.

3 Samples and analytical methods

3.1 Samples

Our samples of the SCS crusts and nodules were collected by seafloor trawling on the Guangzhou Marine Geological Survey research vessel "Haiyangsihao" during the 2011-2012 SCS survey. Detailed information of the samples is given in Guan et al. (2017b). Polymetallic crust samples (ST1, ZSQD251A, ZSQD253A, ZSQD42A, and HYD66-2) have platy or crustal Fe-Mn encrustations and hard substrate of altered basalt and carbonates (e.g., reef limestone). Most samples have friable thin (0.1-1.9 cm) Fe-Mn encrustations and are (dark) brown or black. Polymetallic nodule samples (STD275, ZJ86, and HYD104) are spherical, ellipsoidal, elongate, conodont, or irregular. They have Fe-Mn encrustations around the cores (iron oxides, clayey, muddy, or altered basalt). The nodules grow on top or surrounded by coarse sandy to clayey sediments (Table 1).

3.2 Petrographic analysis

The samples are cut along the growth profile to make polished thick sections (thickness ~100 μm), and then observed with a ZEISS Imager and an A2m optical microscope (reflected light). Photographs were processed with the Axio Vision 4.8 software.

3.3 Laser Raman spectroscopy

The analysis was conducted at the School of Marine Science, Sun Yat-sen University (SYSU), using a ThermoFisher DXR2xi laser Raman micro-spectrometer equipped with a 532 nm argon ion laser and edge filters. Both spot analysis and mapping were performed. The map was formed by multiple line analyses. The analysis conditions include 3 mW laser energy, 6 μm beam size, 0.2 s exposure time, 10 scans, 600 × 600 μm sweep range, and 8 μm mapping resolution. Data processing utilized the ThermoFisher's OMSNICxi and OMSNIC software.

3.4 XRD analysis

The analysis were conducted at the School of Marine Science, SYSU, using a Rigaku D/max Rapid II micro-area X-ray diffractometer (Japan). In the XRD analysis of bulk samples, the crusts and nodules were washed with ultrapure water and dried in a blower for 24 h (drying temperature set at 30°C), then ground to 200-mesh using an agate mortar. In the *in-situ* micro XRD analysis, particle samples with a diameter of <3 mm were observed with an optical microscope equipped on the X-ray diffractometer, and then adjust the selected microarea to the center of the field of view.

The instrument parameters include Mo target and 0.1 mm collimator, 50 kV voltage, 30 mA current, and XRD data acquisition on a 2-D image plate detector. All samples were

TABLE 1 Sample descriptions and bulk mineralogy of Fe-Mn crusts and nodules from the South China Sea.

Sample	Type	Locations	Water depth (m)	Substrate/Nucleus	Major minerals
ST1	crust	117.9104°E 20.4674°N	1600	Altered basalt	δ-MnO2, quartz and anorthite
ZSQD253A	crust	118.6061°E 16.7664°N	1150	Carbonate	δ-MnO2, quartz, anorthite and calcite
ZSQD42A	crust	114.8172°E 16.8493°N	1230	Carbonate	δ-MnO2, quartz, anorthite and calcite
HYD66-2	crust	115.2729°E 13.6789°N	1378	Altered basalt	δ-MnO2, todorokite, quartz and anorthite
STD275	nodule	118.2791°E 21.6915°N	1548	Iron nucleus	δ-MnO2, quartz and anorthite (with goethite and feroxyhyte in the nucleus)
ZJ86	nodule	112.5245°E 15.3421°N	1945	Mud nucleus	δ-MnO2, todorokite, quartz and anorthite
HYD104	nodule	116.1818°E 15.5635°N	815	Undiscernible or no nucleus	δ-MnO2, todorokite, birnessite, quartz and clinochlore

analyzed twice under the same conditions, and the signals were combined to improve the signal-to-noise ratio. The 2-D data were then converted to 1-D spectra using Rigaku's 2DP software. Identification of the major minerals was done with the PDXL2 software.

3.5 TEM analysis

The high-resolution TEM (HRTEM) imaging and selected-area electron diffraction (SAED) analyses were completed at the Analysis Center of SYSU on a JEOL JEM-2010 transmission electron microscope (Japan), and at the Guangzhou Institute of Geochemistry, Chinese Academy of Sciences, on a FEI Talos F200S transmission electron microscope (USA).

(1) JEM-2010: The powder sample (200-mesh) was dispersed in alcohol and dropped onto a Cu grid (with a carbon film microgrid), using a disposable dropper and then allowed to dry naturally. The TEM operating voltage is 200 kV, and the instrument is equipped with an INCA energy spectrum. The analysis site was selected first under microscope at low magnification, and observed with energy-dispersive X-ray spectroscopy (EDS) at higher magnification, followed by high resolution phase analysis at ultra-high magnification.

(2) Talos F200S: The samples were made by secondary embedding-ultra-thin sectioning. Each sample was dispersed in ultrapure water by ultrasound, which was then dropped onto the pre-consolidated resin, dried with a blower, and re-embedded in resin afterward. The resin was heated with a blower, solidified, and cut with a Leica ultrathin microtome (USA), and then placed on a Cu mesh (with carbon-coated film) and dried. The instrument operates at 200 kV with maximum 1.5M× magnification and ≤ 0.25 nm resolution. The instrument is equipped with an EDAX energy spectrum with ≤ 136 eV energy resolution. Fast Fourier transform (FFT) and other TEM image processing were performed with the TIA TEM Imaging and Analysis software (version 4.15).

4 Results

4.1 Microscopic structure characteristics

The encrustations of the SCS polymetallic crusts and nodules contain light and dark Fe-Mn mineral layers, with medium-coarse crystalline silicates and bioclasts being cemented or encapsulated by Fe-Mn minerals (Figures 2, 3). Microstructural features of the samples are very similar, with primary growth structures being lamellar, columnar, or mottled, and secondary ones being concentric or dendritic.

By comparing the Raman spectra (Mn-O peak signal) maps and microscopic photographs, we find that the Mn-O peak intensity correlates positively to the density of growth structure (Figure 4). The Mn-O peak intensity is similar to the light and dark changes of the growth layer, which indicates that the changes in the growth structure and the growth layer of the crust (core) are the alternating changes in the mineral composition.

4.2 Mineral compositions

Previous studies have shown that Fe-Mn crusts and nodules consists mainly of Mn (Fe-vernadite and todorokite) and Fe (goethite, lepidocrocite, amorphous ferrihydrite) phase minerals, together with minor clay minerals, calcite, apatite and detrital quartz and feldspars (Rajani et al., 2005; Pattan and Parthiban,

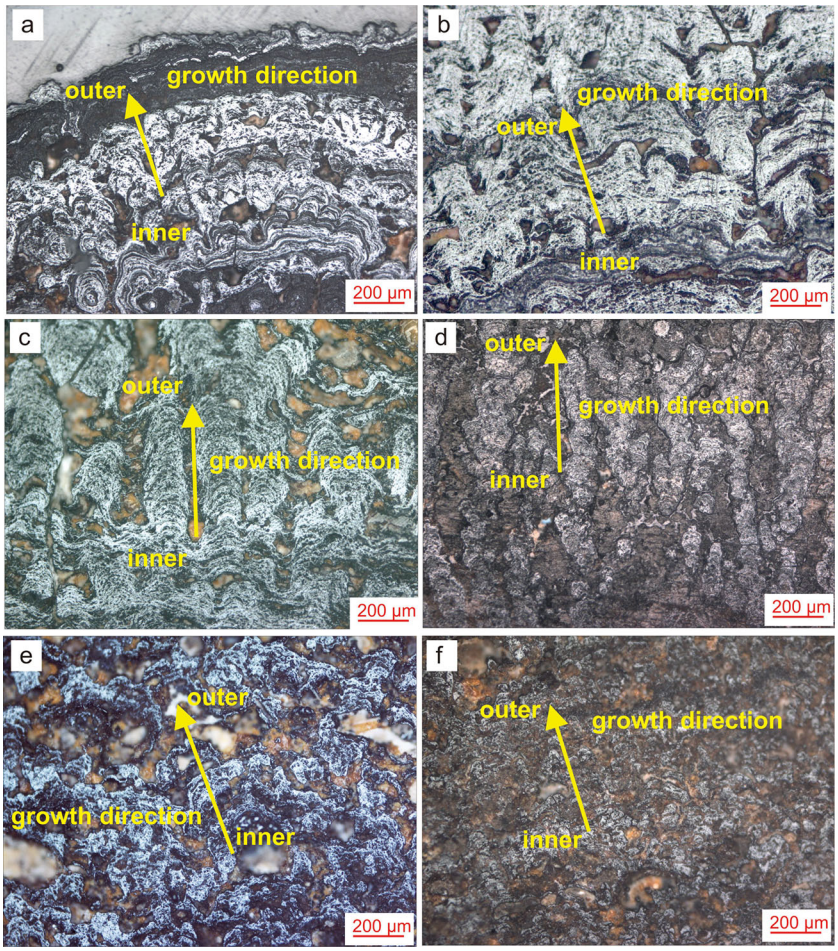

FIGURE 2
Photos of main growth structure of the SCS polymetallic crusts and nodules **(A, B)** laminated structure, **(C, D)** columnar, structure, **(E, F)** taxitic structure).

2007; Xu, 2013; Zhou, 2016; Zhong et al., 2017). Characteristic XRD peaks of different Mn minerals in our samples include (Figure 5): 0.239 and 0.140 nm (vernadite), 0.72, 0.35 and 0.24 nm (birnessite), and 0.97, 0.48, 0.24 and 0.14 nm (todorokite and buserite). The characteristic diffraction peaks of todorokite are at 9.56 Å (100) and 4.78 Å (covering (200) and (002)). Meanwhile, the 4.26 Å $(100)_{quartz}$, 3.34 Å $(011)_{quartz}$, 2.45 Å $(110)_{quartz}$, and 1.37 Å $(203)_{quartz}$ diffraction peaks represent the better-crystallized quartz, whilst the 3.84 Å $(104)_{calcite}$, 3.02 Å $(113)_{calcite}$, 2.08 Å $(202)_{calcite}$, 1.90 Å $(018)_{calcite}$, and 1.86 Å $(116)_{calcite}$ diffraction peaks represent Mg-calcite, which is mainly derived from biological detritus (mainly foraminifera). Most samples have an undulating background peak with peaks centered at ca. 2.4 and 1.4 Å. This background represents the presence of amorphous ferrihydrite (Lee et al., 2016). Our results show that the SCS polymetallic crusts and nodules comprise mainly Fe-vernadite (δ-MnO_2), quartz, feldspars, and amorphous ferrihydrite. This is consistent with the findings by Guan et al. (2017b), although some minerals (e.g., apatite) reported by that study were not found here.

Under the microscope, the SCS polymetallic crusts and nodules display black Fe-Mn encrustations with grape-like or massive structure. *In situ* micro-XRD analysis results indicate that the Fe-Mn crusts are mainly composed of Fe-vernadite and todorokite, with many light-colored minerals (mainly quartz and feldspars) interspersed among the Fe-Mn minerals (Figure 6).

4.3 Nano-mineralogy

In the TEM dark field, there are numerous nano-particles in the samples (Figure 7). Based on the XRD results, we further analyze the SAED patterns and the TEM-EDS data, and the major minerals in the samples are recognized. In particular, the form and composition of birnessite and todorokite are very similar, so it will be confirmed by SAED pattern after each EDS analysis (Figures 7, 8). In samples ST1 and ZSQD253A (Figures 7A–C), there are numerous nano-particles of quartz, thin clay mineral layers, network of Fe-vernadite (δ-MnO_2), and amorphous flocs of FeOOH. Sample ZJ86 contains birnessite and todorokite as well (Figures 7F–H). The EDS results show that the birnessite is mainly associated with Na, K, Ca, and Ni, while todorokite is mainly associated with Ca and Ni.

We found that independent Ti minerals are common in the SCS crusts and nodules (Figure 8). In the TEM dark field, Ti minerals exist

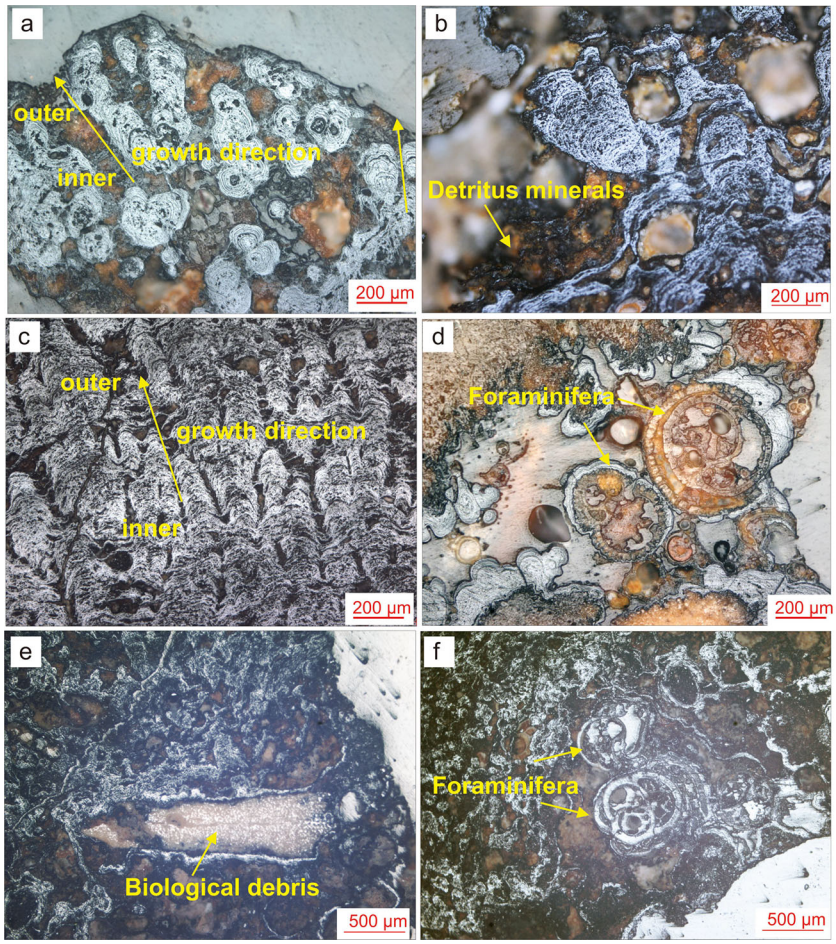

FIGURE 3
Photos of secondary growth structures of the SCS polymetallic crusts and nodules **(A)** concentric circle micro-nodules and columnar structure; **(B)** palmar-print structure; **(C)** dendritic structure; **(D–F)** biological debris and foraminifera in the encrustations).

in a flocculent form, which is very similar to the colloidal morphology of amorphous FeOOH and Si-Al hydrate. Meanwhile, Ti minerals occur in the form of nanofragments in the high-resolution bright field. The EDS results show that the flocculent Ti minerals contain certain Fe and Si. Its high-resolution photograph and the FFT results show [_37_4] the crystallographic stripes in (_403), (111), and (51_2) under the crystallographic band axis, and the measured crystallographic spacing under the Z-axis is 3.58 Å. Therefore, the Ti minerals were determined as hydrated Ti oxide (e.g. $H_2Ti_3O_7$, Kataoka et al., 2013).

5 Discussion

5.1 Microstructure and hydrodynamic environment

In this study, the growth profiles of the SCS polymetallic crusts and nodules were found to contain different microstructure assemblages (Figure 9). Xu (2013) summarized that the growth structures of the crusts and nodules can be divided into primary and secondary ones, while different structure assemblages representing different growth rates and bottom currents. The alternating growth of different Fe-Mn layers implies fluctuations in the growing conditions, which may reflect periodic changes of seawater environment in the South China Sea.

Based on the growth structure characteristics, we suggest that the SCS polymetallic crusts and nodules may have formed in four growth stages (Figure 9). Columnar, palisade, and dendritic structures are predominant in the early growth stage. In this stage, the dendritic structure indicates the inconsistent growth rates at various locations on the same growth surface, while the formation of columnar structure indicates a low hydrodynamic growth environment and a higher formation growth rate (Xu, 2013). The second growth stage developed mainly lamellar (and some mottled) structures, which indicates that the bottom current and oxidation conditions are weak (Xu, 2013). The third growth stage mainly developed mottled structures, which reflects strong bottom current and turbulent seawater environment (Xu, 2013; Guan et al., 2017b). Laminar and mottled structures are mainly developed in the fourth growth stage, indicating that the bottom current and oxidation environment in this stage are more reduced than the previous stage (Guan et al., 2017b).

We also found that the SCS polymetallic crusts and nodules from near the continental margin contain mainly mottled structures. This indicates that they were grown in a more turbulent depositional

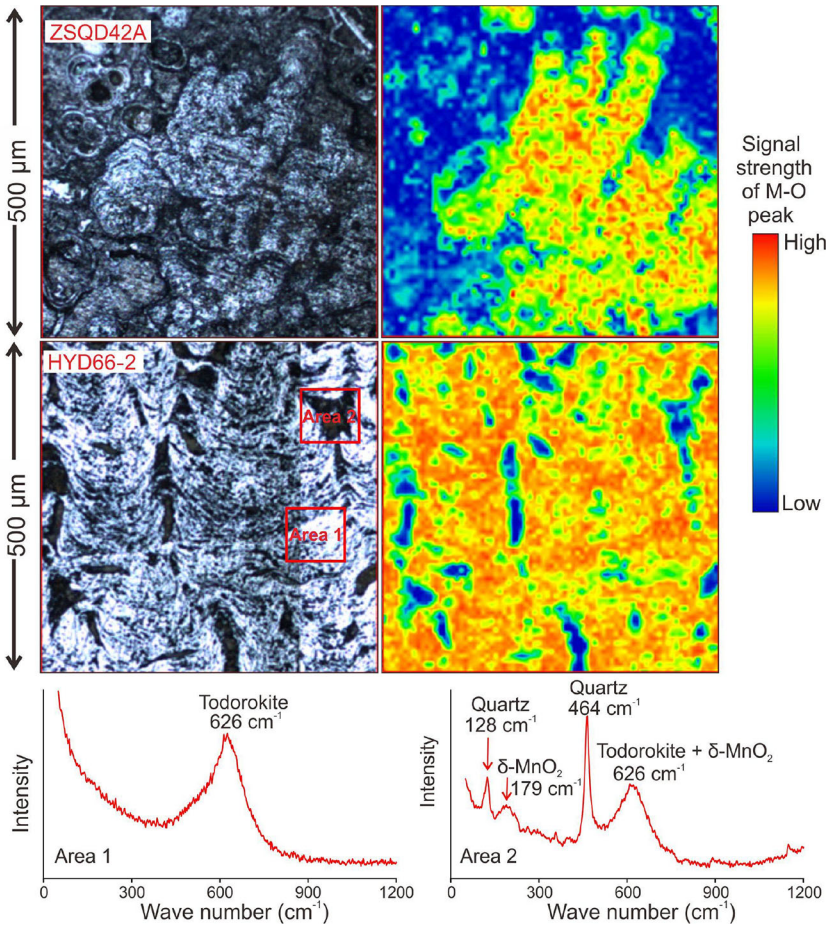

FIGURE 4
Raman mapping results of the selected area in the samples ZSQD42A and HYD66-2.

environment, and were strongly influenced by coastal currents and terrestrial debris (Zhong et al., 2017). In contrast, polymetallic crusts and nodules near the central basin (e.g., HYD66-2 and HYD104) mostly develop laminae and columnar structures. This indicates that they grew in a more stable bottom flow, and were less influenced by terrestrial input (Zhong et al., 2017).

5.2 Mineral composition and depositional environment

Mineralogical characteristics are important in determining the genetic type of Fe-Mn crusts and nodules (Bau et al., 2014) and the ore-metal enrichment mechanism. The XRD spectral peaks of Mn minerals are all broad, indicating poor crystallization, and the presence of todorokite suggests that the SCS polymetallic crusts and nodules may have grown in a short period of sub-oxic seawater environment (Conrad et al., 2017).

According to the intensity of XRD (Figure 5) and chemical composition (Guan et al., 2017b), samples from the northern SCS samples (e.g., ST1, STD275) have large amount of detrital quartz and feldspar. This suggests that these SCS crusts and nodules obtain many terrestrial materials. Samples ZSQD42A, and ZSQD253 from around the Zhongsha Island areas contain large amounts of calcite and biological debris (Table 1), suggesting input from marine organisms on the polymetallic crust/nodule mineralization. In contrast, samples near the central basin (e.g., HYD66-2 and HYD104) contain significant amounts of Mn minerals and less detrital minerals (quartz and feldspar, Figure 5), consistent with their columnar and dendritic growth structures that suggest a stable growth environment and insignificant terrestrial input. Todorokite in crust samples HYD66-2 (Figure 5) and ST1 (Figure 6) indicates the prevalence of todorokite in the SCS polymetallic crusts and nodules, yet its content is likely very low (undetected by XRD). Todorokite in crusts and nodules usually forms in suboxic condition (Conrad et al., 2017), the low content of todorokite in the SCS polymetallic crusts and nodules suggested that they have experienced suboxic environment. As mentioned above, the SCS crusts and nodules are of hydrogenetic origin. Therefore, we propose that the SCS crusts and nodules have been exposed a suboxic environment (Guan et al., 2019), but the process may have been of short duration or not suboxic enough to affect their overall hydrogenetic signatures. According to Figure 6, the SCS crusts contain a low content of todorokite expect for HYD66-2. The reason for more todorokite in HYD66-2 is that the location of this sample grows near the central basin and more possible to be exposed to a suboxic environment.

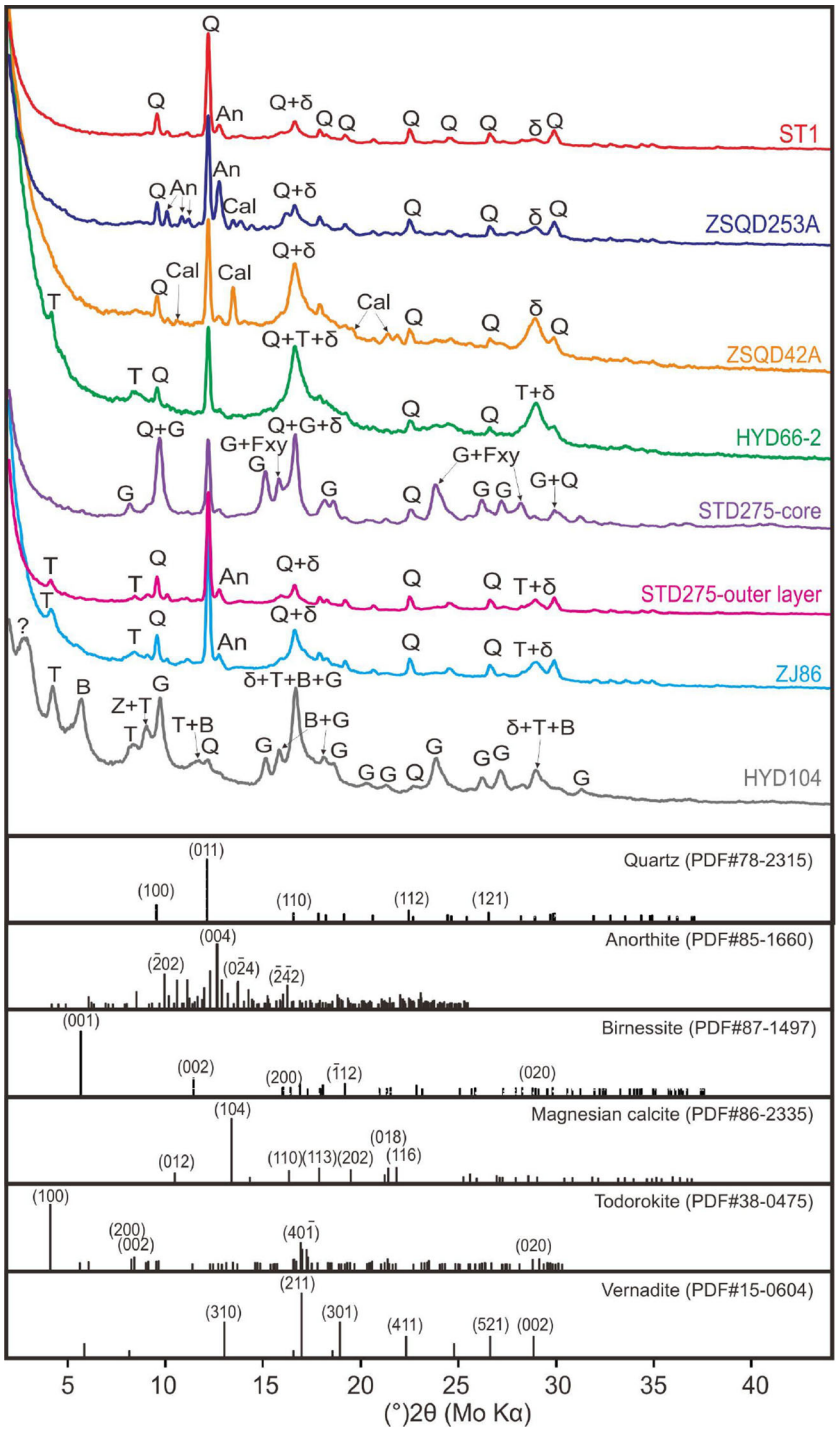

FIGURE 5
XRD patterns of the SCS polymetallic crusts and nodules (Q, quartz; An, Anorthite; Cal, calcite; T, todorokite; G, goethite; B, birnessite; Z, Chloro zeolite).

5.3 The existing phase of Si, Ti, Fe hydroxides

Silicon can precipitate directly into the polymetallic crusts and nodules as quartz and clay minerals, and occur in seawater in colloidal precipitates or as anion complexes (Akagi, 2013; Tréguer and de la Rocha, 2013). EDS spectra of Si is present in all the samples (Figure 7), which indicates good supply of Si during the crust/nodule growth and accompanied by the precipitation of Fe-Mn oxides into the crusts and nodules, and the layered clay minerals often coexist with the Mn minerals. This may be due to the similar layered structure of vernadite and birnessite (both clay minerals). In addition, the mineral interlayers of birnessite are negatively charged (Halbach et al., 2017) and can accommodate

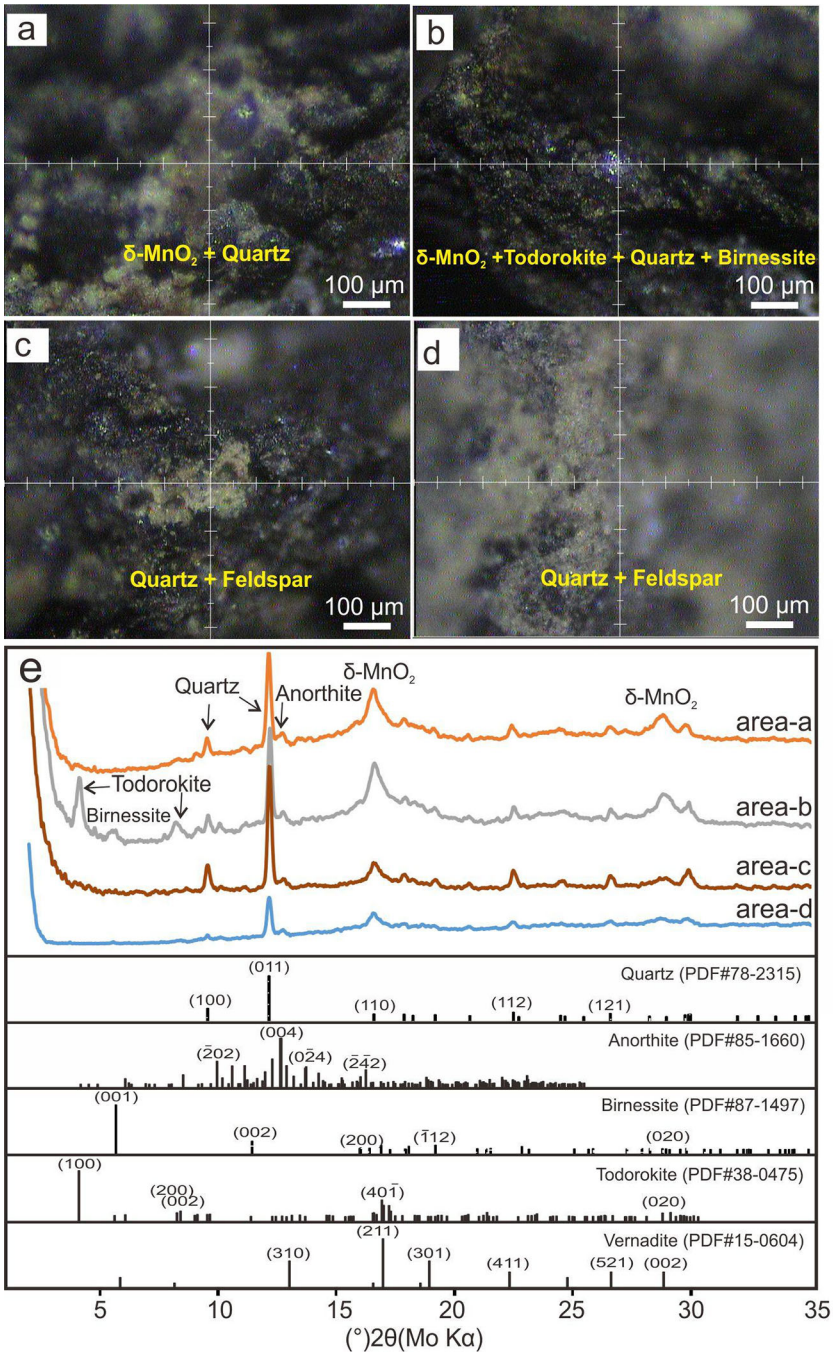

FIGURE 6
In-situ micro-XRD patterns of sample ST1. **(A, B)** Mn minerals including δ-MnO_2 and todorokite. **(C, D)** light-colored minerals including quartz and feldspar. **(E)** XRD patterns of area a-d.

cations (e.g., K^+, Ca^+) and even water molecules (Manceau et al., 2014; Lee and Xu, 2016b). This shows strong adsorption properties similar to those of clay minerals. In addition to the layered minerals, many flocculent minerals can be seen in the TEM dark-field phase, which are mostly colloidal minerals of Si, Al and FeOOH.

The hydrated oxide of Ti ($H_2Ti_3O_7$) was first reported by Izawa et al. (1985), and its crystal structure determined by Kataoka et al. (2013). $H_2Ti_3O_7$ is a hydrate of TiO_2, and occurs mainly in colloidal form in aqueous solution. In this study, we first observed Ti minerals in the SCS polymetallic crusts and nodules, and the EDS result shows that these Ti minerals mainly contained Ti and O. However, the SAED pattern could not match any Ti-O minerals data. Nevertheless, the evidences in this study were not enough to support the proposal of a newfound Ti mineral. Because the nodules and crusts grow in the seabed environment, and previous studies have already suggested that Ti entered the nodules in a colloidal chemical way (Koschinsky and Hein, 2003). We speculate that these independent Ti minerals might be a kind of Ti hydroxide, which

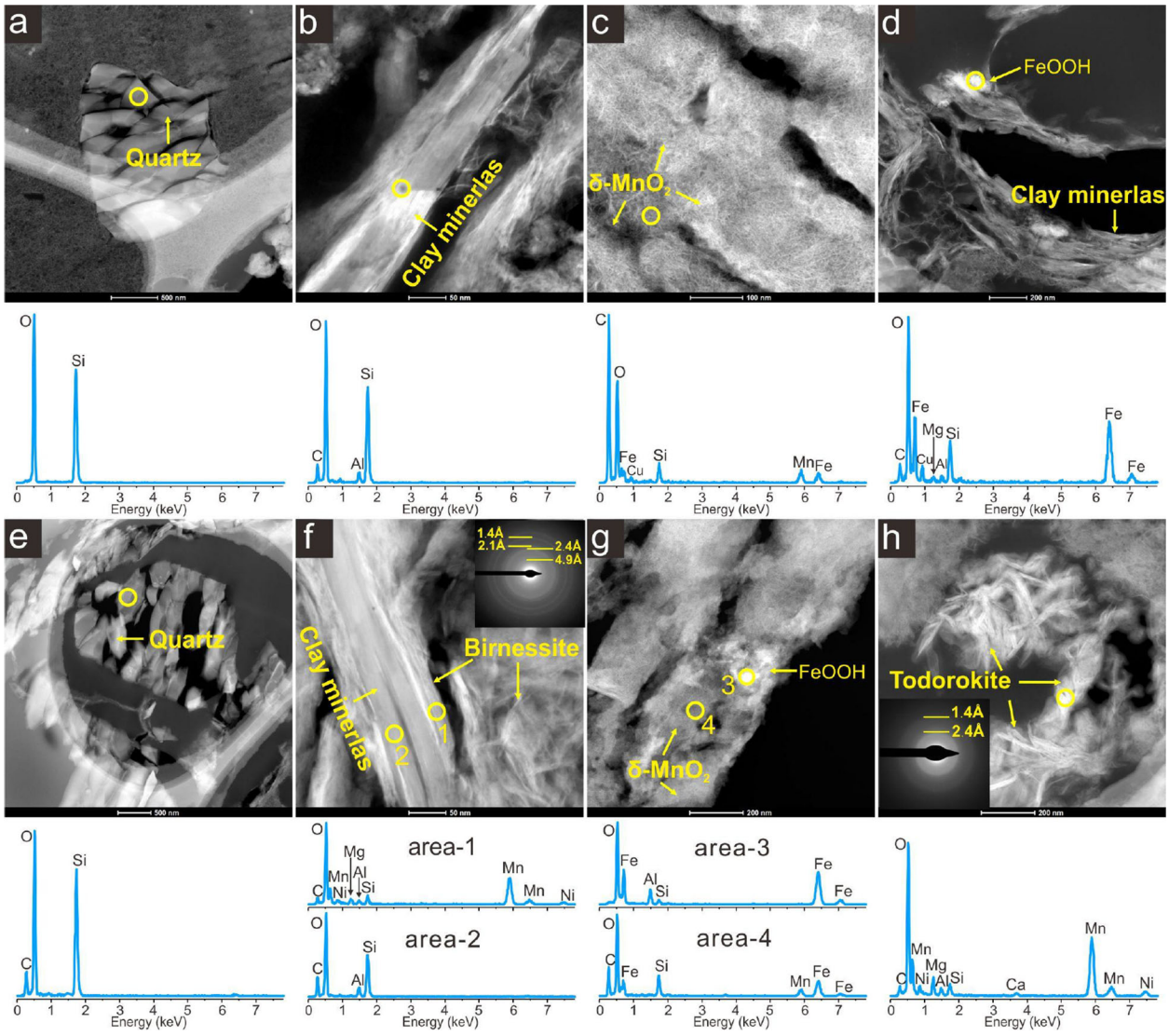

FIGURE 7
TEM photos and micro-*in-situ* EDS patterns of samples ST1 **(A–C)**, ZSQD253A **(D, E)**, and ZJ86 **(F–H)** in the TEM dark field.

was temporarily indicated by $TiO_2{\cdot}xH_2O$ in this study. These Ti minerals perhaps indicated that Ti could form colloidal minerals in seawater and enter directly into the crusts and nodules.

The surface of hydrated FeOOH and Ti oxides is positively charged in seawater, which facilitates selective adsorption of some seawater anions or anion complexes (Koschinsky and Hein, 2003; Jiang et al., 2011). In addition, colloids can aggregate (through covalent bonds) and eventually co-precipitate (Bruland et al., 2014). In this study, we inferred that these colloidal hydrated Ti and Fe oxides were concentrated into the polymetallic crusts and nodules (together with colloidal aggregates, incl. $SiO_2{\cdot}xH_2O$ or $Al_2O_3{\cdot}xH_2O$ in seawater), as evidenced by the widespread presence of colloidal flocs of Fe, Ti, Si, and Al in the samples (Koschinsky and Halbach, 1995). Fluvial and aeolian input can carry substantial terrestrial substance (incl. Si and Al) to the South China Sea, which dissolves rapidly and forms colloids in the seawater, and then re-precipitates in Fe-Mn oxides/hydroxides. Therefore, terrestrial influence on mineral composition of the SCS polymetallic crusts and nodules includes not only the direct detrital input, but also the later re-precipitation of dissolved materials or colloids.

5.4 Mn-phase minerals and their intraconversion

Previous studies have shown that vernadite, birnessite, and todorokite are the three major Mn-phase minerals in marine Fe-Mn crusts and nodules (Usui et al., 1989; Bodeï et al., 2007). In general, vernadite (δ-MnO_2) is a good indicator mineral for hydrogenetic origin, while todorokite and 10 Å phyllomanganate often occur in diagenetic and hydrothermal origins respectively (Takahashi et al., 2007; Manceau et al., 2014; Pelleter et al., 2017). For example, some Fe-Mn growth layers at the bottom of oceanic polymetallic nodules (buried in sediments) were subjected to early

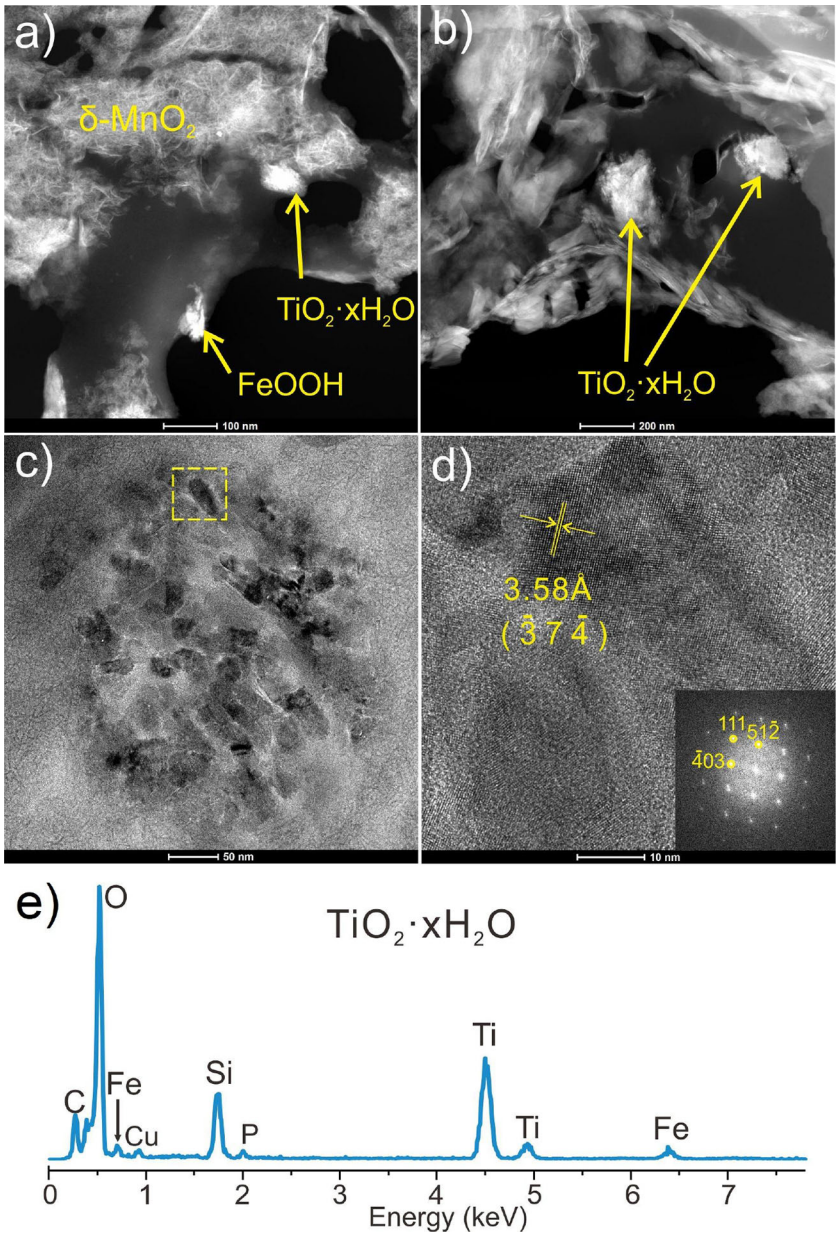

FIGURE 8
TEM photos, SAED and EDS patterns of nano-minerals in samples ST1 and ZJ86. **(A, B)** under the TEM dark field. **(C)** under bright field. **(D)**, high resolution image of the yellow dotted-line frame. **(E)** the energy spectra of the area inside the yellow dotted-line frame.

diagenesis to form todorokite, as reported in the Pacific and Atlantic Fe-Mn nodules and crusts (Marino et al., 2018). The Mn minerals in the SCS crusts and nodules are mainly disordered vernadite (δ-MnO_2) with minor birnessite and buserite. This result suggests that the SCS polymetallic crusts and nodules are mainly of hydrogenetic origin, with some Fe-Mn growth layers possibly affected by diagenesis (Guan et al., 2019).

Under the TEM bright field, we found direct evidence for the conversion of vernadite (δ-MnO_2) to birnessite and todorokite (Figure 10). Vernadite (δ-MnO_2) is an amorphous phyllomanganate that is randomly stacked in the c-axis. This series of δ-MnO_2 minerals is mainly divided into three species (Halbach et al., 2017): (1) 7 Å vernadite with [001] and [002] crystal plane spacing of ca. 7 and 3.5 Å, respectively; (2) 10 Å vernadite with [001] and [002] crystal plane spacing of ca. 10 and 5 Å, respectively; (3) Fe-vernadite (δ-MnO_2) without crystalline surface spacing, which is most common in the SCS polymetallic crusts and nodules (referred to as Fe-vernadite hereafter).

Birnessite are ordered, layered, well-crystallized δ-MnO_2 (Giovanoli, 1980). Since there are two species of 7 Å and 10 Å vernadite, the ordered birnessite is divided into 7 Å birnessite and 10 Å buserite. Birnessite is structurally more stable and occurs mostly in diagenetic (or mixed hydrogenetic-diagenetic) Fe-Mn crusts and nodules, which are often used as precursors in experiments on synthetic todorokite (Liu et al., 2005; Atkins et al., 2016). 10 Å buserite is more common in diagenetic Fe-Mn

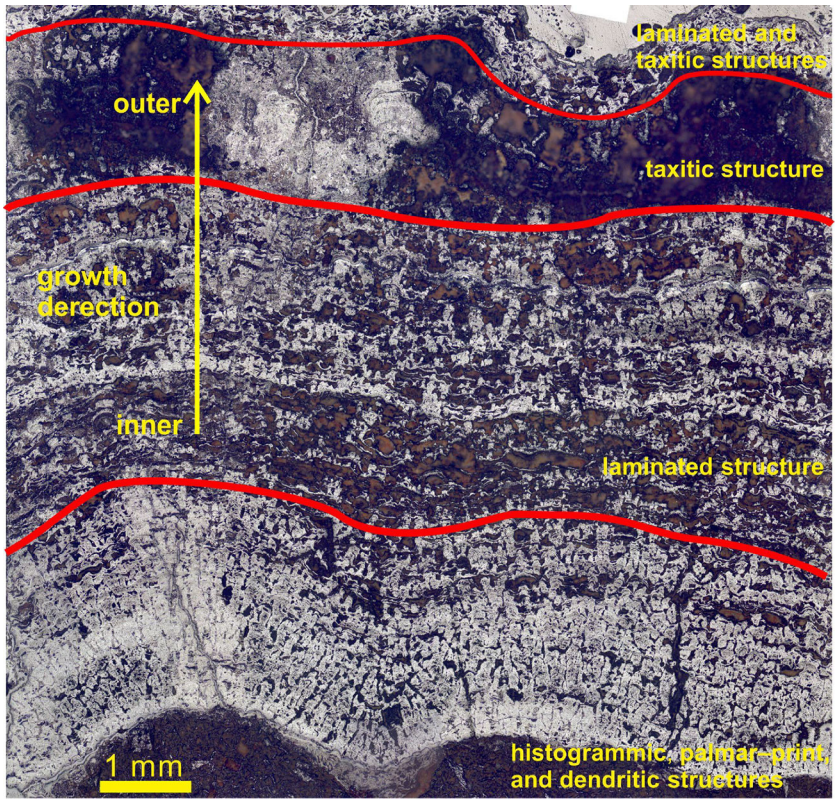

FIGURE 9
Microstructure growth of sample HYD66-1.

nodules, and can be used as a precursor (Bai et al., 2002) or intermediate transition phase (Bodeï et al., 2007) in experimental synthesis of the structurally less-stable todorokite.

The ideal todorokite has a 3-D tunnel structure, consisting of three M-O octahedra (arranged as tunnel) and three M-O octahedra (arranged as tunnel bottom) at common angles, with the tunnel and tunnel bottom oriented along the a-axis and c-axis, respectively (Yu, 1979; Cui et al., 2009; Qiao et al., 2016). Its [001] and [002] crystal plane spacing is ~9.7 Å and ~4.8 Å, respectively, and its diffraction pattern has a strong peak at ~2.4 Å and weak peaks at ~2.2 Å and ~1.7 Å.

As shown in Figure 10, Region 1 of the sample is a random stack of Mn oxides, whose diffraction patterns show two broad rings at ca. 2.4 and 1.4 Å, which indicates that δ-MnO_2 is weakly crystallized. In contrast, the minerals in Region 2 have a bamboo-leaf shape, and their diffraction patterns show four broad rings at ~4.9 Å, ~2.4 Å, ~2.1 Å, and ~1.4 Å, indicating that the nano-minerals in this region are relatively well crystallized. The HRTEM photos show clearer crystal plane stripes (Figures 10C, D), with crystal plane spacing of ca. 6.2 and 7.4 Å (birnessite) and 4.9 and 9.8 Å (todorokite).

To elucidate the transformation processes between these different Mn minerals, we combined our trace element data with published ones (Golden et al., 1987; Cui et al., 2005; Cui et al., 2006; Cui et al., 2010; Atkins et al., 2014; Lee and Xu, 2016b), and proposed a phase transformation model for Mn minerals in the SCS polymetallic crusts and nodules (Figure 11): the interlayer space of 7 Å birnessite contains single H_2O molecules and/or cations (e.g., Na^+, K^+, Mg^{2+}, Ca^{2+}, Ni^{2+}) (Manceau et al., 2014; Lee and Xu, 2016b; Halbach et al., 2017). Some cations (e.g., Ni^{2+}) can increase the layer spacing of birnessite after entering the layers of birnessite, which eventually leads to the conversion of 7 Å birnessite to todorokite (Golden et al., 1987; Atkins et al., 2016). This transformation process was also reported from Fe-Mn nodules in freshwater lakes (Lee and Xu, 2016b). Previous studies have shown that synthetic phyllomanganate mineral phases can be converted to todorokite by atmospheric reflux, hydrothermal treatment, or aging treatments (Cui et al., 2005; Cui et al., 2006; Cui et al., 2010; Atkins et al., 2016), and can be promoted by neutral-alkaline and reducing conditions and the presence of clay minerals. Since todorokite crystallization in the SCS polymetallic crusts and nodules is poor, we suggested that the SCS crusts and nodules were subjected to short period of suboxic conditions and diagenetic process.

The TEM-EDS results show that both birnessite and todorokite contain high Ni content, while vernadite (δ-MnO_2) contains only low trace element contents, which can be explained by their crystal structures. In the birnessite structure, some divalent cations (e.g., Co^{2+}, Ni^{2+}, Zn^{2+}, Fe^{2+}, Cu^{2+}) can replace Mn^{4+} to enter the Mn mineral interlayer (Halbach et al., 2017). In the todorokite, Mg^{2+}, Ca^{2+}, Co^{2+}, or Ba^{2+} are the main cations in the crystal lattice (Post, 1999; Manceau et al., 2014), while other cations are bound to the lamellar sites of Mn (incl. co-hexagonal, co-bilateral, co-trilateral, co-dual, and co-trigonal with Mn-O octahedra) (Cui et al., 2009; Qiao et al., 2016). In addition, vernadite has negative charge in seawater (Koschinsky and Hein, 2003), which facilitate its

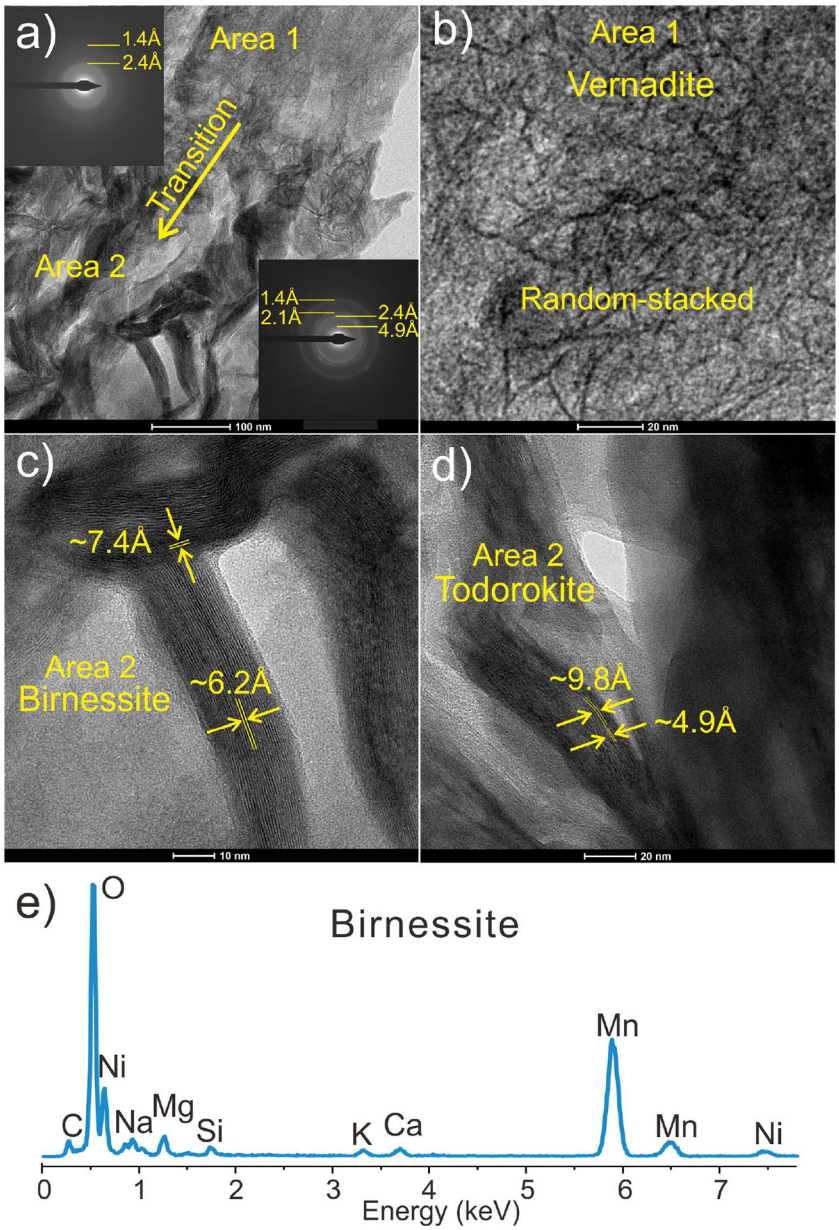

FIGURE 10
SAED patterns **(A)**, high resolution image **(B–D)**, and EDS pattern **(E)** of nano-minerals of sample ZJ86.

adsorption of free cations and cation complexes (e.g., VO^{2+}) from the seawater (Wehrli and Stumm, 1989).

6 Conclusions

(1) Growth structures of the SCS polymetallic crusts and nodules are mainly laminar, columnar, and mottled. The minerals include mainly vernadite (δ-MnO_2), quartz, feldspar, and amorphous FeOOH, as well as minor birnessite, todorokite, and clay minerals. Nano-minerals include mainly vernadite (δ-MnO_2), clay minerals, amorphous FeOOH, $H_2Ti_3O_7$, birnessite, and todorokite.

(2) Different mineral compositions and growth structures represent different growth environments. The growth environment of crusts and nodules from near the continental margin is relatively turbulent with significant terrigenous source influence. Meanwhile, the growth environment of crusts and nodules from near the central basin is more stable and less affected by terrigenous source.

(3) Titanium can form colloidal minerals in the seawater, and precipitate into the crusts and nodules with colloids such as FeOOH and Si-Al.

(4) Vernadite (δ-MnO_2) and birnessite can be transformed into the structurally more stable todorokite in suboxic environment. The SCS polymetallic crusts and nodules may have been in a short period of suboxic growth environment and diagenetic process.

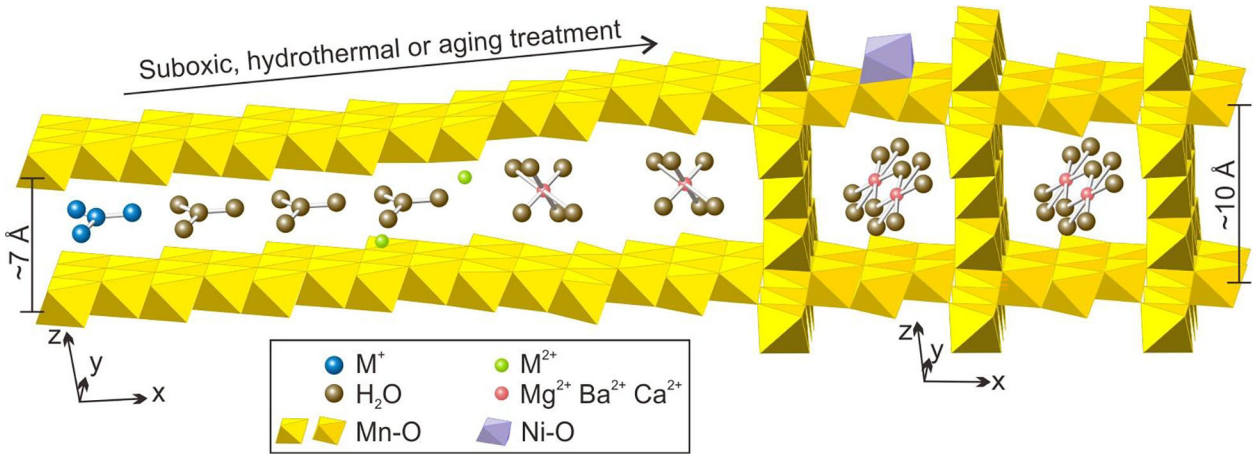

FIGURE 11
Schematic model of the Mn-oxides transformation in the SCS polymetallic crusts and nodules.

Data availability statement

The raw data supporting the conclusions of this article will be made available by the authors, without undue reservation.

Author contributions

YR, YG, and ZX conceived the experiments. YR analyzed the data and wrote this paper. YG participated in the writing of this paper. XS substantially revised the manuscript. LX, YD and WH analyzed the data and revised this paper. All authors contributed to the article and approved the submitted version.

Funding

This work is financially supported by National Natural Science Foundation of China (42003040, 92262304), Guangxi Natural Science Foundation Youth Science Foundation (2019GXNSFBA185030), and the Guangdong Provincial Key Laboratory of Marine Resources and Coastal Engineering Research Fund.

Acknowledgments

We thank the Guangzhou Marine Geological Survey for supplying the samples, and the Guangzhou Institute of Geochemistry, Chinese Academy of Sciences for helping with the mineralogical analysis. Many thanks to the editor and reviewers for their valuable advice.

Conflict of interest

The authors declare that the research was conducted in the absence of any commercial or financial relationships that could be construed as a potential conflict of interest.

Publisher's note

References

Akagi, T. (2013). Rare earth element (REE)-silicic acid complexes in seawater to explain the incorporation of REEs in opal and the "leftover" REEs in surface water: New interpretation of dissolved REE distribution profiles. *Geochim. Cosmochim. Acta* 113, 174–192. doi: 10.1016/j.gca.2013.03.014

Atkins, A. L., Shaw, S., and Peacock, C. L. (2014). Nucleation and growth of todorokite from birnessite: Implications for trace-metal cycling in marine sediments. *Geochim. Cosmochim. Acta* 144, 109–125. doi: 10.1016/j.gca.2014.08.014

Atkins, A. L., Shaw, S., and Peacock, C. L. (2016). Release of Ni from birnessite during transformation of birnessite to todorokite: Implications for Ni cycling in marine sediments. *Geochim. Cosmochim. Acta* 189, 158–183. doi: 10.1016/j.gca.2016.06.007

Bai, Z., Yin, C., Jiang, X., Liu, X., and Wang, S. (2002). Nanometer properties of oceanic polymetallic nodules and cobalt-rich crusts. *Chin. Sci. Bull.* 47, 15. doi: 10.1360/02tb9290

Bao, G., and Li, Q. (1993). Geochemistry of rare earth elements in ferromanganese nodules (crusts) of the south China Sea. *Oceanol. Limnol. Sin.* 24 (3), 304–313. doi: 10.3321/j.issn:0029-814X.1993.03.013

Bau, M., Schmidt, K., Koschinsky, A., Hein, J., Kuhn, T., and Usui, A. (2014). Discriminating between different genetic types of marine ferro-manganese crusts and nodules based on rare earth elements and yttrium. *Chem. Geol.* 381, 1–9. doi: 10.1016/j.chemgeo.2014.05.004

Bodeï, S., Manceau, A., Geoffroy, N., Baronnet, A., and Buatier, M. (2007). Formation of todorokite from vernadite in Ni-rich hemipelagic sediments. *Geochim. Cosmochim. Acta* 71, 5698–5716. doi: 10.1016/j.gca.2007.07.020

Bruland, K. W., Middag, R., and Lohan, M. C. (2014). "Controls of trace metals in seawater," in *Treatise on geochemistry (Second edition)*. Eds. H. D. Holland and K. K. Turekian (Oxford: Elsevier Ltd), 19–51.

Conrad, T., Hein, J. R., Paytan, A., and Clague, D. A. (2017). Formation of fe-Mn crusts within a continental margin environment. *Ore Geol. Rev.* 87, 25–40. doi: 10.1016/j.oregeorev.2016.09.010

Cui, H., Feng, X., He, J., Tan, W., and Liu, F. (2006). Effects of reaction conditions on the formation of todorokite at atmospheric pressure. *Clays Clay Minerals* 54, 605–615. doi: 10.1346/CCMN.2006.0540507

Cui, H., Feng, X., Liu, F., Tan, W., and He, J. (2005). Factors governing formation of todorokite at atmospheric pressure. *Sci. China—Series D: Earth Sci.* 48 (10), 1678–1689. doi: 10.1360/01yd0550

Cui, H., Feng, X., Liu, F., Tan, W., Qiu, G., and Chen, X. (2009). Progress in the study of todorokite. *Adv. Earth Sci.* 24 (10), 1085–1093. doi: 10.3321/j.issn:1001-8166.2009.10.003

Cui, H., Liu, F., Feng, X., Tan, W., and Wang, M. K. (2010). Aging promotes todorokite formation from layered manganese oxide at near-surface conditions. *J. Soils Sediments* 10, 1540–1547. doi: 10.1007/s11368-010-0261-z

Giovanoli, R. (1980). On natural and synthetic manganese nodules. *Geol. Geochem. Manganese* 1, 159–202.

Golden, D. C., Chen, C. C., and Dixon, J. B. (1987). Transformation of birnessite to buserite, todorokite, and manganite under mild hydrothermal treatment. *Clays Clay Minerals* 35, 271–280. doi: 10.1346/CCMN.1987.0350404

Grigoriev, A. G., Zhamoida, V. A., Gruzdov, K. A., and Krymsky, R. S. (2013). Age and growth rates of ferromanganese concretions from the gulf of Finland derived from 210Pb measurements. *Oceanology* 53 (3), 345–351. doi: 10.1134/S0001437013030041

Guan, Y., Ren, Z., Sun, X., Xiao, Z., and Huang, Y. (2019). Fine scale study of major and trace elements in the fe-Mn nodules from the south China Sea and their metallogenic constraints. *Mar. Geol.* 416, 105978. doi: 10.1016/j.margeo.2019.105978

Guan, Y., Sun, X., Jiang, X., Sa, R., Zhou, L., Huang, Y., et al. (2017a). The effect of fe-Mn minerals and seawater interface and enrichment mechanism of ore-forming elements of polymetallic crusts and nodules from the south China Sea. *Acta Oceanol. Sin.* 36 (6), 34–46. doi: 10.1007/s13131-017-1004-4

Guan, Y., Sun, X., Ren, Y., and Jiang, X. (2017b). Mineralogy, geochemistry and genesis of the polymetallic crusts and nodules from the south China Sea. *Ore Geol. Rev.* 89, 206–227. doi: 10.1016/j.oregeorev.2017.06.020

Guan, Y., Sun, X., Shi, G., Jiang, X., and Lu, H. (2017c). Rare earth elements composition and constraint on the genesis of the polymetallic crusts and nodules in the south China Sea. *Acta Geol. Sin. (English Edition)* 91 (5), 1751–1766. doi: 10.1111/1755-6724.13409

Halbach, P. E., Jahn, A., and Cherkashov, G. (2017). "Marine Co-rich ferromanganese crust deposits: Description and formation, occurrences and distribution, estimated world-wide resources," in *Deep-Sea minerals: Distribution characteristics and their resource potential*. Ed. R. Sharma (Switzerland: Springer Nature), 65–140.

Hein, J. R. (2005). Mercury- and silver-rich ferromanganese oxides, southern California borderland: Deposit model and environmental implications. *Economic Geol.* 100 (6), 1151–1168. doi: 10.2113/gsecongeo.100.6.1151

Hein, J. R., Koschinsky, A., Halbach, P., Manheim, F. T., and Bau, M. (1997). Iron and manganese oxide mineralization in the pacific. *Geol. Soc. London Special Publicat.* 119 (1), 123–138. doi: 10.1144/GSL.SP.1997.119.01.09

Hein, J. R., Mizell, K., Koschinsky, A., and Conrad, T. A. (2013). Deep-ocean mineral deposits as a source of critical metals for high- and green-technology applications: Comparison with land-based resources. *Ore Geol. Rev.* 51, 1–14. doi: 10.1016/j.oregeorev.2012.12.001

Izawa, H., Yasuda, F, ., Kikkawa, S., and Koizumi, M. (1985). Lithium ion titration of layered titanic acid, H2Ti3O7. *Chem. Lett.* 14, 1775–1778. doi: 10.1246/cl.1985.1775

Jiang, X., Lin, X., Yao, D., and Guo, W. (2011). Enrichment mechanisms of rare earth elements in marine hydrogenic ferromanganese crusts. *Sci. China Earth Sci.* 54 (2), 197–203. doi: 10.1007/s11430-010-4070-4

Jiang, X., Sun, X., and Guan, Y. (2019). Biogenic mineralization in the ferromanganese nodules and crusts from the south China Sea. *J. Asian Earth Sci.* 171, 46–59. doi: 10.1016/j.jseaes.2017.07.050

Kashiwabara, T., Takahashi, Y., Marcus, M. A., Uruga, T., Tanida, H., Terada, Y., et al. (2013). Tungsten species in natural ferromanganese oxides related to its different behavior from molybdenum in oxic ocean. *Geochim. Cosmochim. Acta* 106, 364–378. doi: 10.1016/j.gca.2012.12.026

Kataoka, K., Kijima, N., and Akimoto, J. (2013). Ion-exchange synthesis, crystal structure, and physical properties of hydrogen titanium oxide $H_2Ti_3O_7$. *Inorganic Chem.* 52, 13861–13864. doi: 10.1021/ic401144k

Konstantinova, N., Cherkashov, G., Hein, J. R., Mirão, J., Dias, L., Madureira, P., et al. (2017). Composition and characteristics of the ferromanganese crusts from the western Arctic ocean. *Ore Geol. Rev.* 87, 88–99. doi: 10.1016/j.oregeorev.2016.09.011

Konstantinova, N., Son, V. T., Thang, L. A., Trung, T. T., Giang, V. T., Dung, N. T. T., et al. (2022). Ferromanganese crusts of the Vietnam margin, central south China Sea: Composition and genesis. *Mar. Geol.* 453, 106911. doi: 10.1016/j.margeo.2022.106911

Koschinsky, A., and Halbach, P. (1995). Sequential leaching of marine ferromanganese precipitates: Genetic implications. *Geochim. Cosmochim. Acta* 59 (24), 5113–5132. doi: 10.1016/0016-7037(95)00358-4

Koschinsky, A., and Hein, J. R. (2003). Uptake of elements from seawater by ferromanganese crusts: Solid-phase associations and seawater speciation. *Mar. Geol.* 198 (3-4), 331–351. doi: 10.1016/S0025-3227(03)00122-1

Lee, S., Shen, Z., and Xu, H. (2016). Study on nanophase iron oxyhydroxides in freshwater ferromanganese nodules from green bay, lake Michigan, with implications for the adsorption of as and heavy metals. *Am. Mineral.* 101, 1986–1995. doi: 10.2138/am-2016-5729

Lee, S., and Xu, H. (2016a). Size-dependent phase map and phase transformation kinetics for nanometric iron(III) oxides ($\gamma \rightarrow \epsilon \rightarrow \alpha$ pathway). *J. Phys. Chem. C* 120 (24), 13316–13322. doi: 10.1021/acs.jpcc.6b05287

Lee, S., and Xu, H. (2016b). XRD and TEM studies on nanophase manganese oxides in freshwater ferromanganese nodules from green bay, lake Michigan. *Clays Clay Minerals* 64 (5), 523–536. doi: 10.1346/CCMN.2016.064032

Li, Z., and Zhang, F. (1990). Geochemical of elements in ferromanganese particles at depths of south Sea. *Mar. Sci. Bull.* 9 (6), 41–50.

Lin, Z., Ji, F., Zhang, F., Lin, X., and Shi, Z. (2003). Characteristics and origin of ferromanganese nodules from the northeastern continental slope of the south China Sea. *Mar. Geol. Quater. Geol.* 23 (1), 7–12.

Liu, Z.h., Kang, L., Ooi, K., Makita, Y., and Feng, Q. (2005). Studies on the formation of todorokite-type manganese oxide with different crystalline birnessites by Mg2+-templating reaction. *J. Colloid Interface Sci.* 285, 239–246. doi: 10.1016/j.jcis.2004.11.021

Manceau, A., Lanson, M., and Takahashi, Y. (2014). Mineralogy and crystal chemistry of Mn, fe, Co, Ni, and Cu in a deep-sea pacific polymetallic nodule. *Am. Mineral.* 99 (10), 2068–2083. doi: 10.2138/am-2014-4742

Marcus, M. A., Edwards, K. J., Gueguen, B., Fakra, S. C., Horn, G., Jelinski, N. A., et al. (2015). Iron mineral structure, reactivity, and isotopic composition in a south pacific gyre ferromanganese nodule over 4 ma. *Geochim. Cosmochim. Acta* 171, 61–79. doi: 10.1016/j.gca.2015.08.021

Marino, E., González, F. J., Lunar, R., Reyes, J., Medialdea, T., Castillo-Carrión, M., et al. (2018). High-resolution analysis of critical minerals and elements in fe-Mn crusts from the canary island seamount province (Atlantic ocean). *Minerals* 8 (7), 285. doi: 10.3390/min8070285

Pattan, J. N., and Parthiban, G. (2007). Do manganese nodules grow or dissolve after burial? results from the central Indian ocean basin. *J. Asian Earth Sci.* 30 (5-6), 696–705. doi: 10.1016/j.jseaes.2007.03.003

Pelleter, E., Fouquet, Y., Etoubleau, J., Cheron, S., Labanieh, S., Josso, P., et al. (2017). Ni-Cu-Co-rich hydrothermal manganese mineralization in the Wallis and Futuna back-arc environment (SW pacific). *Ore Geol. Rev.* 87, 126–146. doi: 10.1016/j.oregeorev.2016.09.014

Post, J. E. (1999). Manganese oxide minerals: Crystal structures and economic and environmental significance. *Proc. Natl. Acad. Sci.* 96 (7), 3447–3454. doi: 10.1073/pnas.96.7.3447

Qiao, Z., Tu, X., and Zhou, H. (2016). Microscopic characteristics of manganates in deep sea ferromanganese nodules. *Chin. J. Nat.* 38 (4), 1–8. doi: 10.3969/j.issn.0253-9608.2016.04.006

Rajani, R. P., Banakar, V. K., Parthiban, G., Mudholkar, A. V., and Chodankar, A. R. (2005). Compositional variation and genesis of ferromanganese crusts of the afanasiy–nikitin seamount, equatorial Indian ocean. *J. Earth System Sci.* 114 (1), 51–61. doi: 10.1007/BF02702008

Shiraishi, F., Mitsunobu, S., Suzuki, K., Hoshino, T., Morono, Y., and Inagaki, F. (2016). Dense microbial community on a ferromanganese nodule from the ultra-oligotrophic south pacific gyre: Implications for biogeochemical cycles. *Earth Planet. Sci. Lett.* 447, 10–20. doi: 10.1016/j.epsl.2016.04.021

Takahashi, Y., Manceau, A., Geoffroy, N., Marcus, M. A., and Usui, A. (2007). Chemical and structural control of the partitioning of Co, ce, and Pb in marine ferromanganese oxides. *Geochim. Cosmochim. Acta* 71 (4), 984–1008. doi: 10.1016/j.gca.2006.11.016

Tréguer, P. J., and de la Rocha, C. L. (2013). The world ocean silica cycle. *Annu. Rev. Mar. Sci.* 5 (5), 477–501. doi: 10.1146/annurev-marine-121211-172346

Usui, A., Mellin, T. A., Nohara, M., and Yuasa, M. (1989). Structural stability of marine 10Å manganates from the ogasawara (Bonin) arc: Implication for low-temperature hydrothermal activity. *Mar. Geol.* 86, 41–56. doi: 10.1016/0025-3227(89)90017-0

Usui, A., Nishi, K., Sato, H., Nakasato, Y., Thornton, B., Kashiwabara, T., et al. (2017). Continuous growth of hydrogenetic ferromanganese crusts since 17 myr ago on takuyo-daigo seamount, NW pacific, at water depths of 800-5500 m. *Ore Geol. Rev.* 87, 71–87. doi: 10.1016/j.oregeorev.2016.09.032

Wang, P., and Li, Q. (2009). "The south China Sea," in *The south China Sea*. Eds. P. Wang and Q. Li (Berlin: Springer), 28–56.

Wang, Y., and Zhang, Z. (2011). Internal microstructure characteristics and geological significance of polymetallic nodules from the northern continental margin of the south China Sea. *J. North China Univ. Sci. Technol. (Natural Sci. Edition)* 33 (4), 5–8. doi: 10.3969/j.issn.1674-0262.2011.04.002

Wehrli, B., and Stumm, W. (1989). Vanadyl in natural waters: Adsorption and hydrolysis promote oxygenation. *Geochim. Cosmochim. Acta* 53, 69–77. doi: 10.1016/0016-7037(89)90273-1

Xu, D. (2013). *Ocean mineral geology* (Beijing: Ocean Press).

Yang, S., Qiu, Y., and Zhu, B. (2015). *Atlas of geology and geophysics of the south China Sea* (Tianjin: China Navigation Publications).

Yli-Hemminki, P., Sara-Aho, T., Jørgensen, K. S., and Lehtoranta, J. (2016). Iron–manganese concretions contribute to benthic release of phosphorus and arsenic in anoxic conditions in the Baltic Sea. *J. Soils Sediments* 16 (8), 2138–2152. doi: 10.1007/s11368-016-1426-1

Yu, X. (1979). Mineral structure of deep-sea manganese nodules. *Mar. Sci.* 3 (2), 44–50.

Zhang, Z., Du, Y., Wu, C., Fang, N., Yang, S., Liu, J., et al. (2013). Growth of a polymetallic nodule from northwestern continental margin of the south China Sea and its response to changes in paleoceanographical environment of the late Cenozoic. *Sci. China: Earth Sci.* 56, 453–463. doi: 10.1007/s11430-012-4535-8

Zhang, Z., Fang, N., Du, Y., Gao, L., Yang, S., Liu, J., et al. (2009). Geochemical characteristics and their causative mechanism of polymetallic nodules from the northwest continental margin of the south China Sea. *Earth Sci.* 34 (6), 955–962. doi: 10.3321/j.issn:1000-2383.2009.06.010

Zhang, X., and Weng, H. (2005). Deposit record of iron and manganese in northeast continental slope of the south China Sea and its indication to environmental changes. *Haiyang Xuebao* 27 (1), 93–100. doi: 10.3321/j.issn:0253-4193.2005.01.013

Zhong, Y., Chen, Z., González, F. J., Hein, J. R., Zheng, X., Li, G., et al. (2017). Composition and genesis of ferromanganese deposits from the northern south China Sea. *J. Asian Earth Sci.* 138, 110–128. doi: 10.1016/j.jseaes.2017.02.015

Zhong, Y., Liu, Q., Chen, Z., Gonzáleze, F. J., Hein, J. R., Zhang, J., et al. (2019). Tectonic and paleoceanographic conditions during the formation of ferromanganese nodules from the northern south China Sea based on the high-resolution geochemistry, mineralogy and isotopes. *Mar. Geol.* 410, 146–163. doi: 10.1016/j.margeo.2018.12.006

Zhou, H. (2016). Metallogenetic mystery of deep sea ferromanganese nodules. *Chin. J. Nat.* 37 (6), 397–404. doi: 10.3969/j.issn:0253-9608.2015.06.001

Zhou, J., Cai, P. J., Yang, C. P., Li, X. J., Gao, H. F., Cai, G. Q., et al. (2021). Geochemical characteristics and genesis of polymetallic crusts in the seamount chain of the Eastern subsean basin, south China Sea. *Earth Sci.* 47 (7), 2586–2601. doi: 10.3799/dqkx.2021.093

frontiers | Frontiers in Marine Science

TYPE Original Research
PUBLISHED 03 March 2023
DOI 10.3389/fmars.2023.1147751

OPEN ACCESS

EDITED BY
Wei Li,
South China Sea Institute of Oceanology (CAS), China

REVIEWED BY
Entao Liu,
China University of Geosciences Wuhan, China
Feng Huaiwei,
Weifang University of Science and Technology, China
Li Cao,
Shandong Provincial Research Institute of Coal Geology Planning and Exploration, China

*CORRESPONDENCE
Jiangong Wei
weijiangong007@163.com
Xiuli Feng
fengxiuli@ouc.edu.cn

SPECIALTY SECTION
This article was submitted to Marine Biogeochemistry, a section of the journal Frontiers in Marine Science

RECEIVED 19 January 2023
ACCEPTED 20 February 2023
PUBLISHED 03 March 2023

CITATION
Li J, Miao X, Feng X, Jiang R, Zhao M, Dan X, Xiao Q and Wei J (2023) Pulsed turbidite and methane seep records in the north western South China Sea since the last glacial maximum.
Front. Mar. Sci. 10:1147751.
doi: 10.3389/fmars.2023.1147751

Pulsed turbidite and methane seep records in the north western South China Sea since the last glacial maximum

Jingrui Li[1], Xiaoming Miao[2], Xiuli Feng[2]*, Rui Jiang[1], Mengwei Zhao[3], Xiaopeng Dan[2], Qianwen Xiao[2] and Jiangong Wei[4,5,6,7]*

[1]Deep-sea Multidisciplinary Research Center & Laboratory for Marine Geology, Laoshan Laboratory, Qingdao, China, [2]Key Laboratory of Submarine Geosciences and Prospecting, College of Marine Geosciences, Ocean University of China, Qingdao, China, [3]Center for Isotope Geochemistry and Geochronology, Laoshan Laboratory, Qingdao, China, [4]Key Laboratory of Marine Mineral Resources, Guangzhou Marine Geological Survey, Ministry of Natural Resources, Guangzhou, China, [5]Sanya Institute of South China Sea Geology, Guangzhou Marine Geological Survey, Sanya, China, [6]Academy of South China Sea Geological Science, China Geological Survey, Sanya, China, [7]Southern Marine Science and Engineering Guangdong Laboratory, Guangzhou, China

The small-scale event layers in the continental margin contain abundant dynamic environment information, and pose a challenge to the interpretation of continuous sedimentary records, giving geological significance to their accurate identify and possible genesis. Here, pulsed turbidite layers since the last glacial maximum (LGM) in a gravity core in the northwestern South China Sea (SCS) was analyzed to investigate the precisely identification, possible causes and the role of marine environmental change during the late Quaternary in formation of these small-scale event layers in the SCS. Eight potential pulsed turbidite layers, according to the petrographic characteristics, grain size parameters and element geochemistry, were identified. Meanwhile, indicators including total sulfur (TS)/total organic carbon (TOC) ratio, $CaCO_3$ content, and chromium-reducible sulfur (CRS) revealed these horizons were mostly related to methane seep events. Constrained by foraminifera shells AMS^{14}C results, these events were determined to have occurred from the LGM to early Holocene, Similar records in the northern and southern slopes suggests the universal occurrence of these small-scale layers in the SCS. The comprehensive analysis showed that the development of these event layers over the past 25 ka can be divided into three stages, 25-15.5 ka, 15.5-7 ka and 7 ka to present. Late Quaternary Ocean environment changes, especially sea level and bottom water temperature, controlled the occurrence of regional small-scale event layers in the SCS. The regional scale mechanism is that the pressure and temperature change affect the stability of hydrate and the methane seepage, and thus the strata stability. Corresponding to the lowest, the rapid increase and the highest levels of the sea level and bottom water temperature, the temporal evolution pattern of small-scale event layers in the SCS showed a highest, decreased and lowest

frequency, respectively. The linkage between the late Quaternary marine environmental change and turbidite deposition through gas activities in this study can act as a useful reference for further understanding the continental margin sedimentary process.

KEYWORDS

turbidite deposition, methane seep, sea-level, bottom water temperature, South China Sea

1 Introduction

The continental margin experiences active sedimentation and is a transit station for the transportation of materials from land to deep ocean. As a geomorphic unit connecting the shallow continental shelf and deep ocean basin, the continental slope contains various sedimentary types, e.g. hemipelagic, gravity-flow, and contourite depositions. The turbidity current, a gravity flow composed of sediment and water with a density greater than that of the surrounding water, is a characteristic geological agent of sediment transport and deposition in the slope Sedimentologists have struggled to decipher the environmental signals contained in the strata due to the unsteady environment resulting from frequent turbidity currents. Therefore, extracting information for the continuous evolution of the geological environment from instantaneously triggered deep-sea turbidite deposition is an challenge in deep-sea sedimentology (Zaragosi et al., 2006; Toucanne et al., 2008; Pouderoux et al., 2012; Lombo Tombo et al., 2015; Yu et al., 2017; Li et al., 2021a). The occurrence of deep-sea turbidity currents is closely related to strata collapse, which presents hidden dangers to engineering safety. Large-scale strata collapse can result in the formation of a tsunami (Nisbet and Piper, 1998), thereby posing danger to residents. In addition, the coarse-grained sedimentary strata formed under the turbidite environment are good reservoirs of deep-sea oil and gas hydrate, which is of great significance for the exploration of deep-sea resources (Rothwell et al., 1998; Mienert et al., 2005; Liang et al., 2017; Liu et al., 2020).

The area around the South China Sea (SCS) contains developed river systems draining basins with active erosion. In the northern SCS margin, currents include different layers of western boundary currents (Wang et al., 2011; Zhou et al., 2017; Zhu et al., 2019), Guangdong Coastal Current and the SCS Warm Current (Guan and Fang, 2006). Additionaly, frequent typhoons and strong internal waves (Alford et al., 2015; Zhang et al., 2018a) combined with the supply of a large number of terrigenous materials lead to frequent turbidity currents on the northern slope of the SCS. Many turbidite layers have been identified in the core samples of the SCS continental slope area in recent decades using geophysics, sedimentology, geochemistry, and mineralogy proxies (Zhao et al., 2011; Jiang et al., 2014; Yu et al., 2017; Li et al., 2019; Liu et al., 2020). This revealed that turbidites with a water depth of 1,000–4,500 m from the slope to the basin have been widely distributed since the last glacial period. Most previous studies focused on medium- to large-scale turbidity activities, with discussion on large-scale collapse or enormous terrestrial materials input. In contrast, there have been relatively few studies on records of small -scale pulsed turbidite events contained in core samples. On the other hand, the proposed complex and diverse turbidity current triggering mechanisms have remained controversial, and include typhoons, earthquakes, floods, etc (Lombo Tombo et al., 2015; Zhang et al., 2018a; Maloney et al., 2020). Proposed mechanisms regulating long term turbidity currents include tectonic activity, sea-level fluctuation, and climate related periodic high sediment supply pulse (Maslin et al., 1998; Ducassou et al., 2009; Lombo Tombo et al., 2015). The hydrate dissociation is a characteristic geological agent in the continental slope that has attracted extensive attention in recent years. Methane leakage can induce collapse and disastrous turbidity current over large scales (Paull et al., 1991; Nisbet and Piper, 1998). For example, the extremely thick turbidite layer of the Mediterranean is related to strata instability induced by methane leakage generated by hydrate decomposition (Rothwell et al., 1998). The enormous collapse of the Norwegian continental margin is also related to the reduction of gas hydrate stability (Mienert et al., 2005; Crémière et al., 2016), and even triggered a tsunami (Bondevik et al., 2005). The SCS is one of the most important gas hydrate reservoirs. Bottom simulating reflectors, mud volcanoes, mud diapirs and gas chimneys have all been found in ashes associated with natural gas hydrates. In addition, due to the unstable state of hydrate, methane seepage is common in the SCS slope. Recent studies showed widespread methane leakage in the SCS slope. However, most leaks are of a small scale and weak intensity. No catastrophic collapse resulting from large-scale leakage is contained in geological records. Therefore, various uncertainties remain, including: (1) How could we identify the deep-sea turbidite layers in the SCS precisely; (2) whether such the small-scale coarse-grained event layers commonly existing in the SCS slope are related to methane leakage activities; (3) the role of marine environmental change during the late Quaternary in formation of these small-scale event layers. The present study selected a gravity core from the “Haima” seep area in the northwestern SCS, comprehensively compared with the records of other cores taken from the southern and northern slopes of the SCS to discuss the possible relationship between turbidite records and methane leakage and control mechanism in the SCS since the LGM.

2 Materials and methods

2.1 Materials

The core Q6 (water depth: 1,400 m; length: 2.72 m) used in the present study was collected by the Guangzhou Marine Geological Survey using the Haiyang-6 vessel between April and May, 2019 (Figure 1). The core site is on the north western continental slope of the SCS. In general, the core shows relatively homogeneous silty-clay deposition, besides for three obviously coarsened sand layers (Figure 2). The potential pulsed turbidite layers of the core were identified using petrography, sedimentology, and geochemistry proxies. The layers significantly affected by methane leakage were identified using geochemistry proxies. Eight layers were chosen for AMS^{14}C ages measurements (Figure 2) using planktonic foraminifera *Globorotilia menardii* shells in BETA laboratory (U.S.), and the results has been reported in our previous work (Miao et al., 2021a).

2.2 Grain-size analyses

Solutions of 15 mL 30% H_2O_2 and 5 mL 3 mol/L HCl were added to remove organic matter and carbonate. All samples were fully desalted and dispersed before measurements. The samples were analyzed using a Mastersizer 2000 instrument (range: 0.02–2,000 μm; resolution: 0.01Φ) at the Key Laboratory of Submarine Geosciences and Prospecting, Ministry of Education, China. The error based on repeated measurements was estimated to be less than 3%.

2.3 Geochemical element analyses

Prior to the analyses, 0.05 g freeze-dried sample was dissolved twice in HF-HNO_3 (1:1) and dried again at 190°C for 48 h. Approximately ~50 g of the mixture was then prepared and

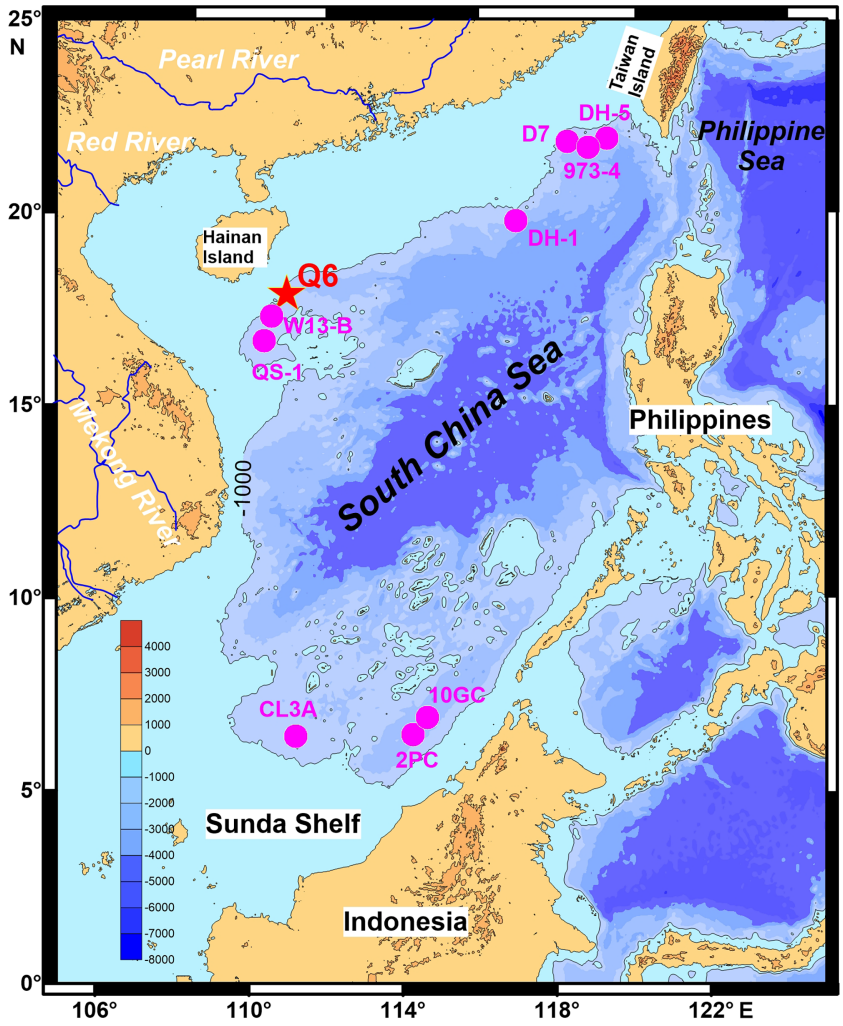

FIGURE 1
Map showing the study area in the SCS. The red star indicates the sampling location of Q6 and the magenta cycles indicate referenced cores in this study.

10.3389/fmars.2023.1147751

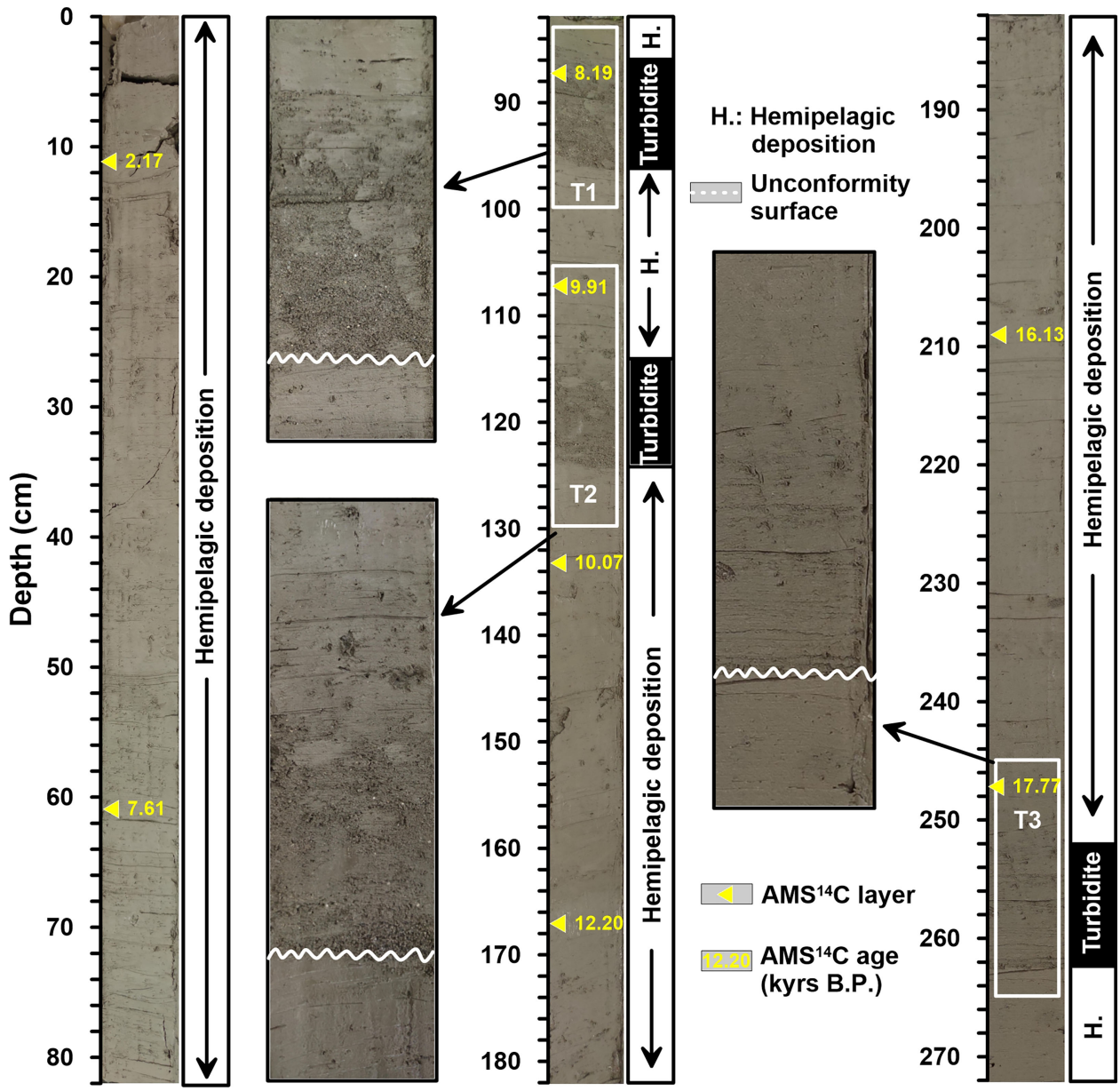

FIGURE 2
Photographs and lithological description of the core Q6.

measured. Nearly 10% of these samples were analyzed in replicates to determine the measurement error, and the elemental compositions of a GSD-9 reference standard were measured to confirm the accuracy of the analyses. The geochemical element analysis, including the measurement of major and trace elements was conducted by the Experiment-Testing Center of Marine Geology, Ministry of Land and Resources. The major elements in the sediments were analyzed using inductively coupled plasma atomic emission spectroscopy (ICP-AES), and the standard deviation of these measurements was < 1%. The trace elements in the sediments were analyzed by ICP mass spectrometry (ICP-MS), and the standard deviation of these measurements was < 5%.

2.4 Total organic carbon analyses

Accurately weigh about 1g of freeze-dried sediment and ground to 200 mesh. Approximately 2 mL of 1 mol/L HCl was then added, and the sample was soaked and submitted to ultrasound to remove inorganic carbon. The sample was then placed on a low-temperature electric heating plate for 12 h to volatilize HCl. After drying, 50 mg of sediment was placed in an elemental analyzer (Elementar Vario ELIII, Germany) and organic carbon (TOC) was determined in the CN mode. The sediment was dried under low temperature, after which 50 mg was extracted and placed directly on the elemental analyzer for the determination of total carbon (TC). A

standard sample GSD-9 and 10% parallel sample were analyzed concurrently during the test. The standard deviations of TC and TOC were 0.004% and 0.006%, respectively. The measurement was completed in the Key Laboratory of Marine Geology and Metallogeny, First Institute of Oceanography, Ministry of Natural Resources. $CaCO_3$ content was calculated as:

$$CaCO_3(\%) = (TC - TOC) \times 8.33 \quad (1)$$

2.5 Chromium reducible sulfur analyses

Chromium-reducible sulfur (CRS) was analyzed according to the method described by Canfield et al. (1986). The bulk sediments were dried and grounded to homogeneous powders of 200 mesh size. Then, pyrite extraction was carried out by weighing 50–200 mg samples. CRS was reduced using 1.0 M $CrCl_2$-0.5 M HCl and 3N HCl solutions under a continuous flow of nitrogen for 2 h at 200–250°C. The liberated H_2S was trapped in an $AgNO_3$-NH_4OH solution and converted into Ag_2S precipitates. The percentage of pyrite could be calculated by the amount of Ag_2S extracted.

3 Results and discussion

3.1 Identification of turbidite layers

The turbidite layer often produces obvious unconformity in comparison with stable and continuous hemipelagic sediments. This is due to the significant scouring of the underlying strata by the high concentration of suspended sediment, resulting in significant variation in grain size (including higher sand content, coarser mean grain size or median grain size, and a finer positive sequence from bottom to top), higher coarse-grained detrital minerals, such as quartz and zircon, and higher Si/Al, Si/Fe, and Zr/Rb ratios (Fournier et al., 2016; Fauquembergue et al., 2019; Di et al., 2021; Liu et al., 2021; Li et al., 2021a). Core Q6 contains three layers with obvious coarsening grain size at 88–96 cm, 116–128 cm, and 254–260 cm, respectively. These layers are in obvious unconforming contact with the underlying strata, of which the sand particles in the 88–96 cm and 116–128 cm layers are clearly visible by the naked eye (Figure 2). The characteristic grain size end-members were extracted using the inversion model (Dobigeon et al., 2009; Schmidt et al., 2010; Joussain et al., 2016) (Figure 3) to further identify the possible small-scale pulsed turbidite layers not visible by the naked eye and to limit the dynamic changes of the deposition process. The first three fractions explained ~96.3% of all variations, and covered almost all the core data. Therefore, three end-members were chosen to explain data variation. End-member 1 (EM 1) varied between 1 μm–30 μm, with a peak of 5 μm; End-member 2 (EM 2) varied between 1 μm–40 μm, with a peak of 6 μm; End-member 3 (EM 3) showed the widest range of between 1 μm–300 μm, with a peak of 30 μm. EM 3 showed similar trends with sand fraction content and median grain size (Figure 4). Therefore, this end member was the key to regulating variations in grain size. EM 3 also showed several obvious pulse peaks, which were a good indication of the above three potential turbidite layers and in good agreement with the local peak records of Si/Al, Si/Fe and Zr/Rb ratios. Based on the above evidence, eight possible turbidite layers were identified: 88–96 cm, 116–128 cm, 140–148 cm, 160–162 cm, 212–214 cm, 230 cm, 238–240 cm, and 254–260 cm. Particle size distribution curves for these layers show obvious bimodal distribution with an additional coarse-grained peak than the hemipelagic layers (Figure 3). The C-M diagram based on the sediment cumulative frequencies of 1% (coarsest component) and 50% (median grain size) contents were used to assess the dynamic deposition environment through different sediment transport dynamics (Passega, 1957; Passega, 1977). Here, turbidite deposition was parallel to the C=M line. The C-M diagram of these eight potential turbidite layers was used to determine that the distributions of the 88–96 cm, 116–128 cm, and 254–260 cm layers were roughly parallel to the C=M line (Figure 5A), which is a typical turbidite deposition feature. In contrast, the distributions of the 140–148 cm, 160–162 cm, 212–214 cm, 230 cm, and 238–240 cm layers were roughly parallel to the horizontal axis (Figure 5B). Since these distributions were consistent with the distribution characteristics of other hemipelagic layers (Figure 5C), the genesis could not yet be determined. Some layers may contain coarser particles in a limited range due to hydrodynamic factors such as bottom current enhancement. Alternatively, some layers may show small-scale turbidite deposition resulting from gas hydrate dissociation environment (to be analyzed below). The samples did not show typical turbidite characteristics due to their small number. It should be noted that there was no clear positive grain sequence structure of turbidite layers, which may be transformed by later hydrodynamic forces. The hydrodynamics of the northern slope of the SCS is complex and includes a highly active contour current activity (Chen et al., 2014; Zhao et al., 2015). The northwestern slope encounters the anticyclonic intermediate water circulation of the SCS (Chen et al., 2014), which is likely to transform the existing sediments. However, no obvious sedimentological evidence exists at present, calling for the need for further analyzes in combination with more data. Although the geochemical indices of the 212–214 cm and 230 cm layers were high, there was no indication of EM 3 (Figure 4). This result could possibly be attributed by the increase in the content of authigenic minerals, such as opal.

3.2 Identification of methane seep events

The sediments of the methane seep environment usually show abnormal enrichment of authigenic carbonate and pyrite due to the existence of sulfate-driven anaerobic oxidation of methane (SD-AOM) (Jørgensen et al., 2004; Peckmann et al., 2004; Bayon et al., 2007; Bayon et al., 2013; Han et al., 2014; Crémière et al., 2016; Lin et al., 2016; Liu et al., 2020). This eventually leads to clear changes in sediment geochemical characteristics, such as the CRS, TS/TOC ratio and $CaCO_3$ (Peketi et al., 2012; Sato et al., 2012; Li et al., 2018; Miao et al., 2021a; Miao et al., 2021b; Miao et al., 2022). Under a normal environment without methane seepage, labile organic matter is gradually degraded by sulfate-reducing bacteria *via* organoclastic sulfate reduction (OSR) and this biogeochemical

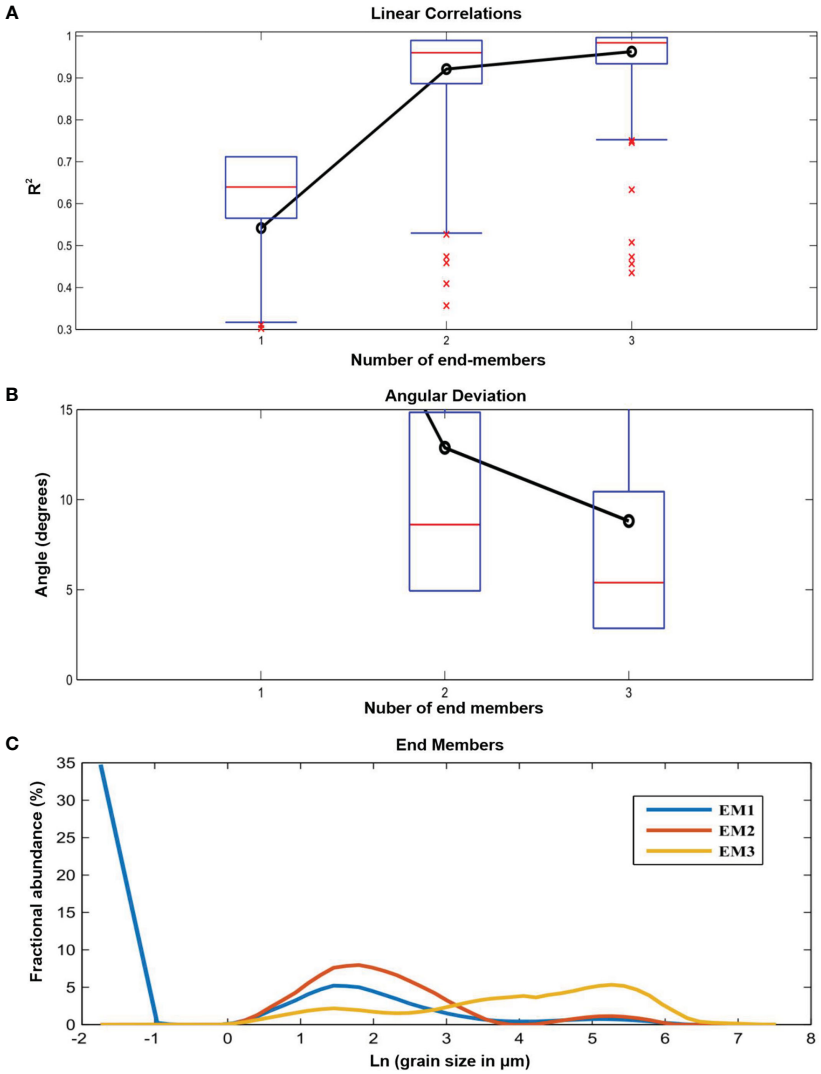

FIGURE 3
(A) Fraction of data variance explained by the unmixing model vs. number of end-members. **(B)** Volume percent vs. grain size (μm) diagram of the three end- members (EM1, EM2, and EM3) identified in core Q6 **(C)**.

process would produce H_2S (Jørgensen, 1982; Lim et al., 2011). Hydrogen sulfide eventually mixes with iron ions in the environment to form pyrite (Jørgensen, 1982). At this time, there is a significant positive correlation between TS and TOC, and the ratio of TS/TOC fluctuates between 0.1 and 0.5 (average of ~0.36) (Berner, 1982; Wei and Algeo, 2020). However, SD-AOM resulting from the methane seep provides a large quantity of additional hydrogen sulfide for the pyrite formation process, promotes the enrichment of authigenic pyrite in the methane anaerobic oxidation zone (SMTZ), and leads to an increase in the CRS content and TS/TOC ratio (Boetius et al., 2000; Peketi et al., 2012). In addition, the additional H_2S input destroys the positive relationship between TOC and TS (Sato et al., 2012; Li et al., 2018; Miao et al., 2021b).The TS/TOC ratio in the core Q6 mostly exceeded 0.36 and the organic matter content was low (generally < 1.4%), inconsistent with the sulfate reduction of organic debris. In particular, the TS/TOC ratios of layers 88–96 cm, 116–128 cm, 160–162 cm, 212–214 cm, 230 cm, 238–240 cm, and 254-260 cm increased significantly, and were generally all above 0.5. The exceptions were those of layers 88–96 cm, 116–128 cm, 160–162 cm, and 254–260 cm, which were > 1.0 (Figures 6B, D). Furthermore, we further analyzed the correlation between TOC and TS and CRS (Figure 7). We found a significant positive between CRS and TS (R^2 = 0.94), indicating that TS mainly consists of pyrite and other inorganic sulfur. At the same time, CRS and TS have no significant correlation with TOC (R^2 = 0.13 and R^2 = 0.04, respectively), which indicates that pyrite generation has little relationship with TOC. Moreover, SD-AOM-pyrite usually has a heavy sulfur isotope value, which is also considered to be an important marker for identifying methane seepage activities (Jørgensen et al., 2004; Lin et al., 2016). In the previous work, we also found the phenomenon of increasing sulfur isotope value of pyrite in these horizons (Miao et al., 2021b). Therefore, this result showed that pyrite is obviously enriched in these layers in the core Q6 and is affected by SD-AOM (Figures 6B, G–I). In addition, SD-AOM also makes the environment more alkaline and produces large amounts of carbonates (Peckmann et al., 2004; Bayon et al.,

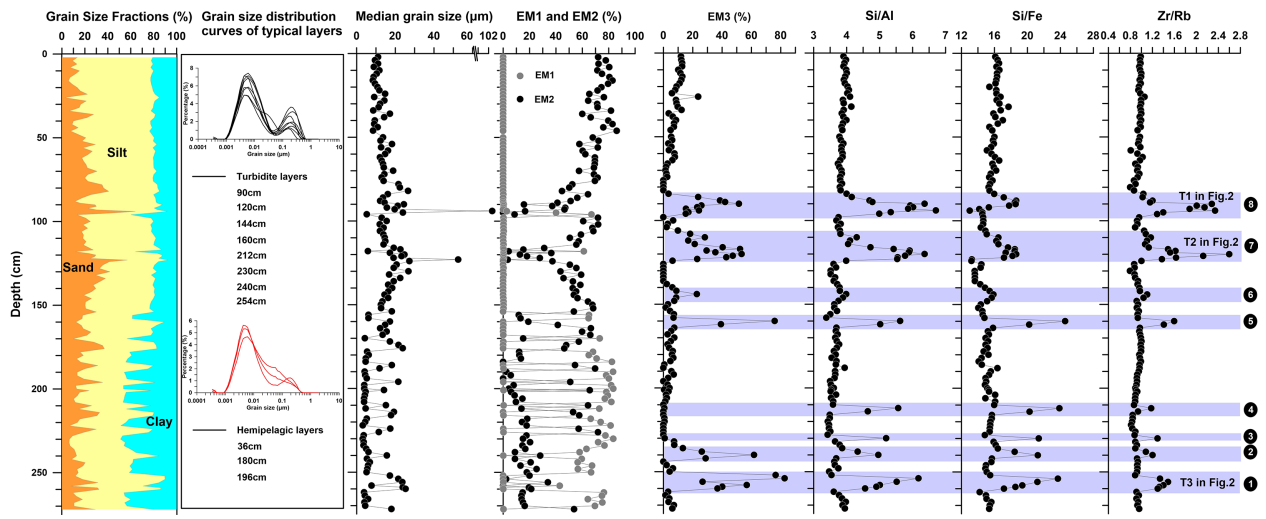

FIGURE 4
Potential turbidite layers identification proxies of grain-size and element ratios.

2007; Bayon et al., 2013). In Q6, it is found that $CaCO_3$ content also increases in pyrite enriched horizons. The $CaCO_3$ content was significantly higher than that of other hemi-pelagic layers. Similar phenomena have been observed in other hydrate areas, such as the Bay of Bengal (Peketi et al., 2012) and the Beikang Basin (Li et al., 2018). Therefore, we can believe that the above layers are obviously affected by methane seep.

3.3 Pulsed turbidite and methane seep events: Sea-level and bottom temperature forcing

The factors that induce strata instability and result in turbidity current include occasional earthquakes, typhoons, volcanic activity, instantaneous pulse of high sediment supply, sea level fluctuation, gas hydrate decomposition, and leakage (Masson, 1996; Maslin et al., 1998; Prins and Postma, 2000; Ducassou et al., 2009; Lombo Tombo et al., 2015; Crémière et al., 2016; Zhang et al., 2018b; Maloney et al., 2020; Li et al., 2021a). The instantaneous pulse of high sediment supply is generally related to a sharp increase in the quantity of erosion material. This is regulated by regional climate conditions or the rapid entry of a large quantity of sediment into the ocean caused by flood events (Ducassou et al., 2009). Lower precipitation occurred both in the the East Asian summer monsoon and Indian summer monsoon regimes during the LGM period, whereas pulsed turbidite events occurred frequently in many regions of the SCS (Hu et al., 2017; Li et al., 2017; Liu et al., 2020; Di et al., 2021; Feng et al., 2021; Li et al., 2021b). Clearly, these observations cannot be explained by strata instability caused by the increase in the instantaneous sediment supply in the source area alone. There has been no record of such high-frequency volcanic eruptions around the SCS since the LGM. Sea level fluctuation regulates the accumulation of sediment and controls the strata pressure by changing the accommodation space, which may affect the hydrate dissociation and induce strata instability. Examples include the Amazon fan, the southern Carolina rise, and the inner Blake Ridge, etc (Paull et al., 1996; Maslin et al., 1998). As instantaneous triggering factors, occasional earthquakes and typhoons are difficult to identify at a geological scale and may

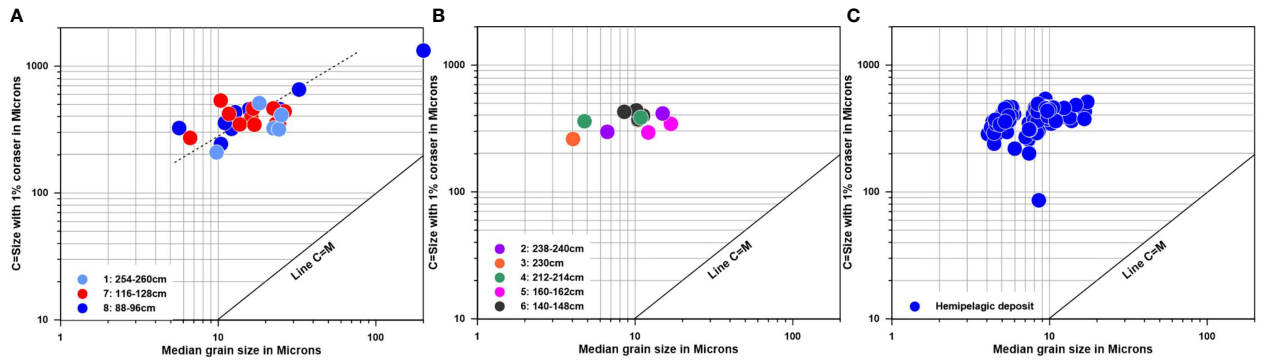

FIGURE 5
C-M diagram of potential turbidite and hemi-pelagic layers. **(A)** Layers T1, T7 and T8; **(B)** Layers T2-T6; **(C)** Hemipelagic Layers.

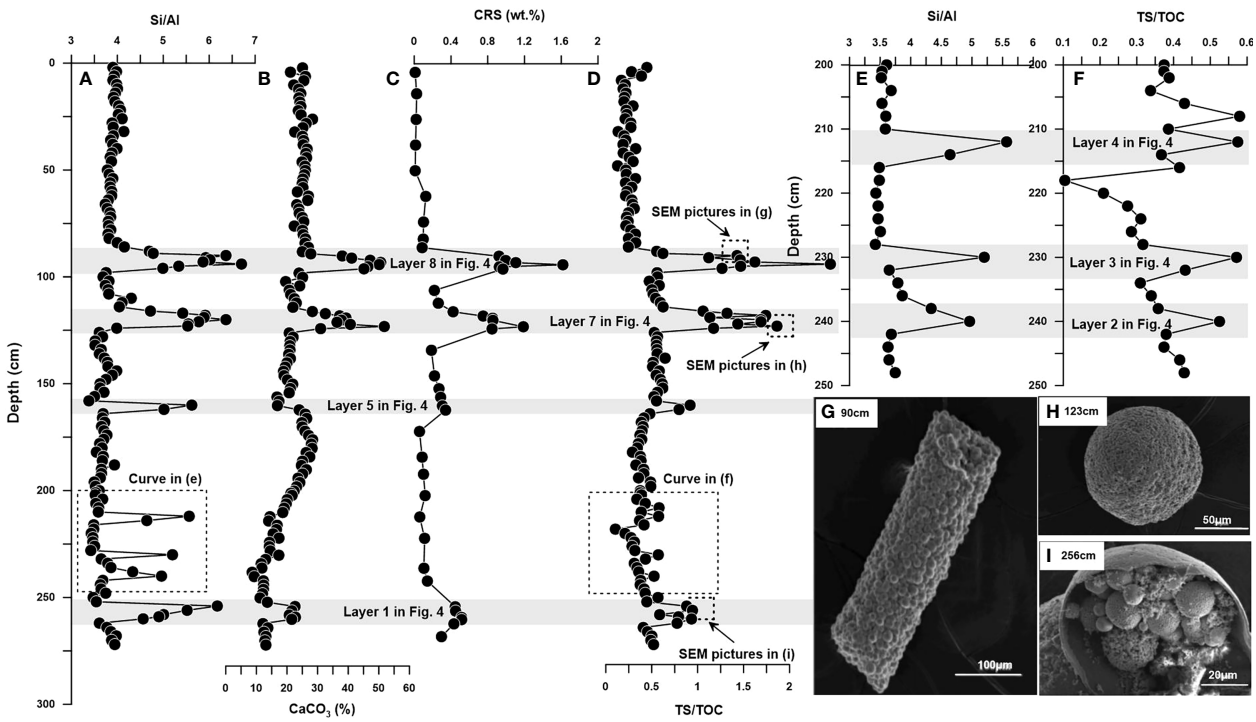

FIGURE 6
Identification proxies for methane release layers. **(A)** Si/Al; **(B)** $CaCO_3$(%); **(C)** CRS (wt.%); **(D)** TS/TOC; **(E)** Si/Al between 200-250cm; **(F)** TS/TOC between 200-250cm; **(G–I)** Scanning electron microscopy (SEM) pictures of pyrite aggregates in samples. TS/TOC and SEM pictures according to Miao et al. (2021b).

need to be comprehensively analyzed in combination with other factors.

Gas hydrate dissociation is common in the continental slope area and is generally considered to occur due to changes in temperature and pressure (Phrampus and Hornbach, 2012; Tong et al., 2013; Crémière et al., 2016). A low temperature and high-pressure environment are suitable for hydrate storage, whereas the opposite is conducive to hydrate dissociation. The sea level and bottom water temperature of the SCS have increased significantly since the LGM (Shackleton, 1987; Fairbanks, 1989; Waelbroecka et al., 2002; Lisiecki and Raymo, 2005; Bates et al., 2014; Wan and Jian, 2014) (Figure 8). Therefore, the changes in pressure and temperature during this process can play a key role in the hydrate dissociation. The present study integrated the hydrate dissociation records of several cores in the northwestern slope, northeastern slope, central northern slope, and southern slope areas of the SCS (Figure 8). The results showed that the dissociation of hydrate could be roughly divided into three stages according to the characteristics of sea level and bottom water temperature: (1) 25–15.5 ka, characterized by a low sea level (low pressure) and low temperature stage during which methane leakage was common; (2) 15.5–7 ka, characterized by rising trends in sea level and temperature and in which methane leakage activity was common and continuous, although this activity stopped during the latter part of this stage; (3) 7 ka to the present, characterized by a low activity of methane leakage at a high sea level (high pressure) and high

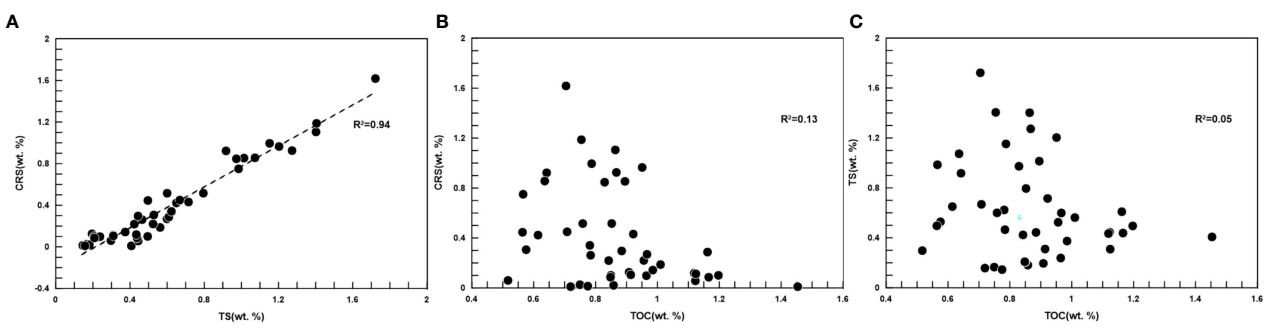

FIGURE 7
CRS-TS-TOC diagram. **(A)** CRS *vs* TS; **(B)** CRS *vs* TOC; **(C)** TS *vs* TOC.

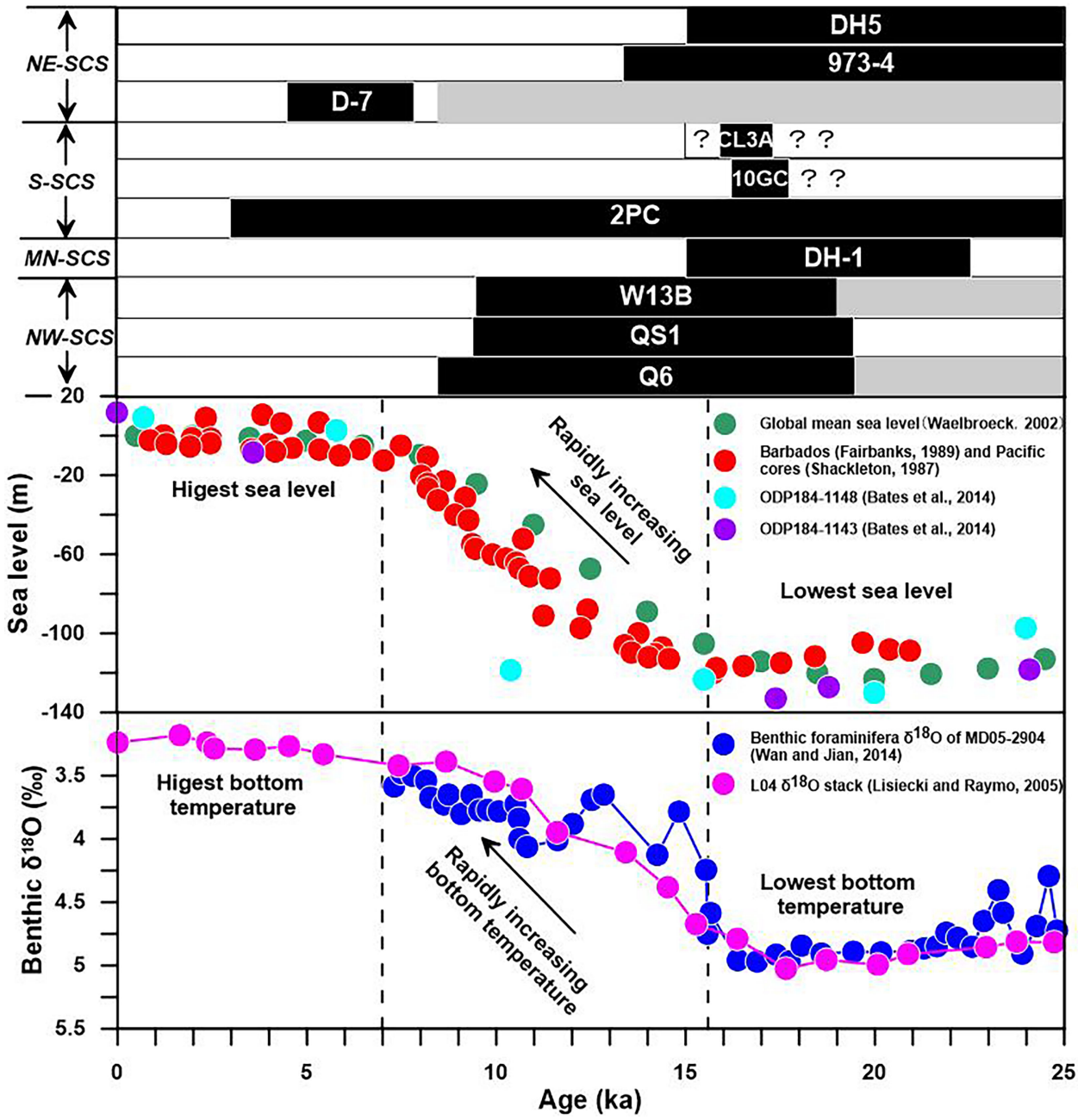

FIGURE 8
Comparison of methane leakage records in the South China Sea and reconstruction results of sea level and bottom water temperature. NE-SCS, northeastern South China Sea; S-SCS, southern South China Sea; MN-SCS, middle-northern South China Sea; NW-SCS, northwestern South China Sea. The black, grey and white rectangular bars show time ranges of methane release events, data absence and normal hemipelagic layers with no methane release events, respectively. The interrogation mark show records with no accurate age points. Data sources: DH5, W13B and 2PC (Li et al., 2021b); CL3A (Feng et al., 2021); DH-1 (Li et al., 2017); D-7 (Hu et al., 2017); QS1 (Liu et al., 2020); 10GC (Di et al., 2021); 973-4 (Zhang et al., 2018b); Q6 (This study). Sea-level reconstruction results are from global mean (Waelbroecka et al., 2002), Barbados (Fairbanks, 1989), Pacific cores (Shackleton, 1987), ODP184-1143 and ODP184-1143 (Bates et al., 2014). Bottom temperature results: Benthic foraminifera $\delta^{18}O$ of core MD05-2904 (Wan and Jian, 2014) and the LR04 stack (Lisiecki and Raymo, 2005).

temperature. The effects of sea level and bottom water temperature on gas hydrate were opposite in each stage.

The sea level dropped by over 100 m during the regression of the late Pleistocene, resulting in a decrease in the pressure on the seabed by 1,000 kPa (Wang et al., 2004). The reduction in total pressure resulted in the dissociation of natural gas hydrate, the release of large quantities of methane and water, and an increase in slope instability. These changes occurred globally, and resulted in nearly 200 landslides on the continental margin of the Atlantic in the United States, the continental slope of Southwest Africa, the continental margin of Norway, the continental margins of the Beaufort Sea, the Caspian Sea, the north Panama continental shelf and Newfoundland. The Amazon submarine landslide is attributed to the rapid decline in sea level. This is because the drop in sea level

induced an instability in natural gas hydrate and to the sliding of overlying sediments (Maslin et al., 1998). The sea level decreased significantly during the last glacial period, particularly in the LGM, during which the sea level was 120 m below the current level in the SCS. The strata pressure overlying the gas hydrate decreased significantly, inducing dissociation leakage, which was recorded widely in slope areas of the SCS (Hu et al., 2017; Li et al., 2017; Zhang et al., 2018b; Liu et al., 2020; Di et al., 2021; Feng et al., 2021; Li et al., 2021b) (Figure 8). Although the low temperature during this period was suitable for maintaining the stability of hydrate, the significant reduction in pressure dominated the release of gas hydrate. The factors triggering strata instability may include an occasional earthquake, typhoon, or flood. For example, observations of a submarine canyon in the northern SCS confirmed that typhoon triggered turbidity currents (Zhang et al., 2018a). At the initiation of a landslide, free gas under the hydrate layer rises along the crack, and the hydrate in the original metastable state will decompose and release methane gas. This release of gas will have a significant impact on the seabed redox environment, such as deep-water oxygen consumption (Bayon et al., 2013) and seawater sulfate concentration (Crémière et al., 2013; Kiel, 2015). These processes explain the significant increases in CRS, TS/TOC, $CaCO_3$ and pyrite (Figure 6).

There were rapid increases in the sea level and bottom water temperature between 15.5–7 ka. Gas hydrate leakage records continued to be recorded in almost all areas, and significantly decreased or stagnated during this period (Figure 8). This result indicated that leakage activity continued concurrent with the significant pressurization and heating of the storage environment. Leakage activity then almost stagnated under pressure after a period. The rapid rise in bottom water temperature since 15.5 ka likely promoted the dissociation of gas hydrate, offset the inhibition of hydrate dissociation resulting from sea-level rise-induced pressure increase to a certain extent, and maintained the occurrence of methane leakage until the early Holocene. This mechanism is similar to the hydrate dissociation and release of a large quantity of methane gas from many continental margins globally during the Quaternary glacial-interglacial transition period, which is often attributed to the rise of bottom water temperature (Dean et al., 2015; Himmler et al., 2019; Kennett James et al., 2000; Reagan and Moridis, 2007). Hydrate decomposition events have been identified in the transition periods of MIS10/9 (Tong et al., 2013)、 MIS6/5(Chen et al., 2019; Deng et al., 2021)、MIS4/3 (Han et al., 2014; Yang et al., 2018)、 MIS2/1(Feng and Chen, 2015; Wei et al., 2020; Deng et al., 2021) in the SCS. These events indicate that the significant change in temperature was indeed conducive to hydrate dissociation. Although there was no obvious change in bottom water temperature since the early Holocene, the sea level continued to rise rapidly. The increasing overlying sea water pressure maintained the stable state of hydrate. Hydrate begins to form in large quantities once the appropriate conditions are met and dissociation is halted.

The highest sea level and bottom water temperature have occurred since 7 ka, and the records indicate significant decreases in gas hydrate dissociation in various regions of the SCS (Figure 8). Although modern seafloor observations show continued methane gas leakage (Zhang et al., 2020), the stratigraphic records show no turbidite layer formed by strata instability resulting from methane leakage.

4 Conclusions

According to multi-disciplinary indicators, the small-scale deep-sea turbidite and methane seep event layers in a gravity core in the northwestern SCS were identified, and the role of the changes in the sea level and paleoceanography environment during the late Quaternary in the formation of the above layers was discussed, and the following understanding was formed:

(1) Based on the petrographic characteristics, grain size parameters and element geochemistry indicators, eight potential pulsed turbidite layers were identified. Meanwhile, indicators including TS/TOC ratio, $CaCO_3$ content, and CRS revealed these horizons were mostly related to methane seep events.

(2) These event layers mainly occurred from the LGM to early Holocene, when low sea level and transgression were universal to the SCS continental slope, indicating a high incidence of small-scale turbidite layers and methane seepage events.

(3) Development of these small-scale pulsed turbidite and methane seep events could be divided into three stages: 25–15.5 ka, 15.5–7 ka and 7 ka. The variations in strata pressure over hydrate resulting from the changes in sea level and bottom water temperature were suggested the main factors regulating methane seepage, which affected strata stability of the continental slope and the occurrence of pulsed turbidite events.

Data availability statement

The original contributions presented in the study are included in the article/Supplementary Material. Further inquiries can be directed to the corresponding author.

Author contributions

JL, XF and JW: Conceived the project, write and correct the manuscript. XM, RJ and MZ: Participated in scientific interpretation and editing. XD and QX: Carried out sample pretreatment and measurements. All the authors contributed to the data interpretation and writing of the paper. All authors contributed to the article and approved the submitted version.

Funding

This research was funded by Guangdong Province Marine Economic Development (Six Major Marine Industries) Special Fund Project ([2021] No. 58), Qingdao National Laboratory for Marine Science and Technology Basic Scientific Research Projects

Special Fund (JCZX202003) and the National Key R&D Program of China (2017YFC0306703).

Acknowledgments

We would like to thank the scientists and crew from the Guangzhou Marine Geological Survey and the Haiyang-6 vessel for their hard work in collecting the core samples.

Conflict of interest

The authors declare that the research was conducted in the absence of any commercial or financial relationships that could be construed as a potential conflict of interest.

Publisher's note

Supplementary material

The Supplementary Material for this article can be found online at: https://www.frontiersin.org/articles/10.3389/fmars.2023.1147751/full#supplementary-material

References

Alford, M. H., Peacock, T., MacKinnon, J. A., Nash, J. D., Buijsman, M. C., Centuroni, L. R., et al. (2015). The formation and fate of internal waves in the south China Sea. *Nature* 521, 65–69. doi: 10.1038/nature14399

Bates, S. L., Siddall, M., and Waelbroeck, C. (2014). Hydrographic variations in deep ocean temperature over the mid-pleistocene transition. *Quaternary Sci. Rev.* 88, 147–158. doi: 10.1016/j.quascirev.2014.01.020

Bayon, G., Dupré, S., Ponzevera, E., Etoubleau, J., Chéron, S., Pierre, C., et al. (2013). Formation of carbonate chimneys in the Mediterranean Sea linked to deep-water oxygen depletion. *Nat. Geosci.* 6, 755–760. doi: 10.1038/ngeo1888

Bayon, G., Pierre, C., Etoubleau, J., Voisset, M., Cauquil, E., Marsset, T., et al. (2007). Sr/Ca and Mg/Ca ratios in Niger delta sediments: Implications for authigenic carbonate genesis in cold seep environments. *Mar. Geol.* 241, 93–109. doi: 10.1016/j.margeo.2007.03.007

Berner, R. A. (1982). Burial of organic carbon and pyrite sulfur in the modern ocean; its geochemical and environmental significance. *Am. J. Sci.* 282, 451. doi: 10.2475/ajs.282.4.451

Boetius, A., Ravenschlag, K., Schubert, C. J., Rickert, D., Widdel, F., Gieseke, A., et al. (2000). A marine microbial consortium apparently mediating anaerobic oxidation of methane. *Nature* 407, 623–626. doi: 10.1038/35036572

Bondevik, S., Mangerud, J., Dawson, S., Dawson, A., and Lohne, Ø. (2005). Evidence for three north Sea tsunamis at the Shetland islands between 8000 and 1500 years ago. *Quaternary Sci. Rev.* 24, 1757–1775. doi: 10.1016/j.quascirev.2004.10.018

Canfield, D. E., Raiswell, R., Westrich, J. T., Reaves, C. M., and Berner, R. A. (1986). The use of chromium reduction in the analysis of reduced inorganic sulfur in sediments and shales. *Chem. Geol.* 54, 149–155. doi: 10.1016/0009-2541(86)90078-1

Chen, F., Wang, X., Li, N., Cao, J., Bayon, G., Peckmann, J., et al. (2019). Gas hydrate dissociation during Sea-level highstand inferred from U/Th dating of seep carbonate from the south China Sea. *Geophys. Res. Lett.* 46, 13928–13938. doi: 10.1029/2019GL085643

Chen, H., Xie, X., Van Rooij, D., Vandorpe, T., Su, M., and Wang, D. (2014). Depositional characteristics and processes of alongslope currents related to a seamount on the northwestern margin of the Northwest Sub-basin, south China Sea. *Mar. Geol.* 355, 36–53. doi: 10.1016/j.margeo.2014.05.008

Crémière, A., Bayon, G., Ponzevera, E., and Pierre, C. (2013). Paleo-environmental controls on cold seep carbonate authigenesis in the Sea of marmara. *Earth Planetary Sci. Lett.* 376, 200–211. doi: 10.1016/j.epsl.2013.06.029

Crémière, A., Lepland, A., Chand, S., Sahy, D., Condon, D. J., Noble, S. R., et al. (2016). Timescales of methane seepage on the Norwegian margin following collapse of the Scandinavian ice sheet. *Nat. Commun.* 7, 11509. doi: 10.1038/ncomms11509

Dean, W. E., Kennett, J. P., Behl, R. J., Nicholson, C., and Sorlien, C. C. (2015). Abrupt termination of marine isotope stage 16 (Termination VII) at 631.5 ka in Santa Barbara basin, California. *Paleoceanography* 30, 1373–1390. doi: 10.1002/2014PA002756

Deng, Y., Chen, F., Guo, Q., Hu, Y., Chen, D., Yang, S., et al. (2021). Possible links between methane seepages and glacial-interglacial transitions in the south China Sea. *Geophys. Res. Lett.* 48, e2020GL091429. doi: 10.1029/2020GL091429

Di, P., Yang, X., Rashid, H., Zhou, Y., Wang, H., Li, N., et al. (2021). Enhanced sulfidization in a sedimentary turbidite layer from the nansha trough in the southern south China Sea. *Sedimentary Geol.* 421, 105955. doi: 10.1016/j.sedgeo.2021.105955

Dobigeon, N., Moussaoui, Saïd, Tourneret, J., and Carteret, Cédric (2009). Bayesian Separation of spectral sources under non-negativity and full additivity constraints. *Signal Process.* 89, 2657–2669. doi: 10.1016/j.sigpro.2009.05.005

Ducassou, E., Migeon, S., Mulder, T., Murat, A., Capotondi, L., Bernasconi, S. M., et al. (2009). Evolution of the Nile deep-sea turbidite system during the late quaternary: influence of climate change on fan sedimentation. *Sedimentology* 56, 2061–2090. doi: 10.1111/j.1365-3091.2009.01070.x

Fairbanks, R. G. (1989). A 17,000-year glacio-eustatic sea level record: influence of glacial melting rates on the younger dryas event and deep-ocean circulation. *Nature* 342, 637–642. doi: 10.1038/342637a0

Fauquembergue, K., Fournier, L., Zaragosi, S., Bassinot, F., Kissel, C., Malaizé, B., et al. (2019). Factors controlling frequency of turbidites in the Bengal fan during the last 248 kyr cal BP: Clues from a presently inactive channel. *Mar. Geol.* 415, 105965. doi: 10.1016/j.margeo.2019.105965

Feng, D., and Chen, D. (2015). Authigenic carbonates from an active cold seep of the northern south China Sea: New insights into fluid sources and past seepage activity. *Deep Sea Res. Part II: Topical Stud. Oceanogr.* 122, 74–83. doi: 10.1016/j.dsr2.2015.02.003

Feng, J., Li, N., Liang, J., Shang, J., Yang, S., and Wang, H. (2021). Using multi-proxy approach to constrain temporal variations of methane flux in methane-rich sediments of the southern south China Sea. *Mar. Petroleum Geol.* 132, 105152. doi: 10.1016/j.marpetgeo.2021.105152

Fournier, L., Fauquembergue, K., Zaragosi, S., Zorzi, C., Malaizé, B., Bassinot, F., et al. (2016). The Bengal fan: External controls on the Holocene active channel turbidite activity. *Holocene* 27, 900–913. doi: 10.1177/0959683616675938

Guan, B., and Fang, G. (2006). Winter counter-wind currents off the southeastern China coast: A review. *J. Oceanogr.* 62, 1–24. doi: 10.1007/s10872-006-0028-8

Han, X., Suess, E., Liebetrau, V., Eisenhauer, A., and Huang, Y. (2014). Past methane release events and environmental conditions at the upper continental slope of the south China Sea: constraints by seep carbonates. *Int. J. Earth Sci.* 103, 1873–1887. doi: 10.1007/s00531-014-1018-5

Himmler, T., Sahy, D., Martma, T., Bohrmann, G., Plaza-Faverola, A., Bünz, S., et al (2019). A 160,000-year-old history of tectonically controlled methane seepage in the Arctic. *Sci. Adv.* 5, eaaw1450. doi: 10.1126/sciadv.aaw1450

Hu, Y., Chen, L., Feng, D., Liang, Q., Xia, Z., and Chen, D. (2017). Geochemical record of methane seepage in authigenic carbonates and surrounding host sediments: A case study from the south China Sea. *J. Asian Earth Sci.* 138, 51–61. doi: 10.1016/j.jseaes.2017.02.004

Jørgensen, B. B. (1982). Mineralization of organic matter in the sea bed-the role of sulphate reduction. *Nature* 296, 643–645. doi: 10.1038/296643a0

Jørgensen, B. B., Böttcher, M. E., Lüschen, H., Neretin, L. N., and Volkov, I. I. (2004). Anaerobic methane oxidation and a deep H2S sink generate isotopically heavy sulfides in black Sea sediments 1 1Associate editor: D. e. canfield. *Geochimica Cosmochimica Acta* 68, 2095–2118. doi: 10.1016/j.gca.2003.07.017

Jiang, T., Zhang, Y., Tang, S., Zhang, D., Zuo, Q., Lin, W., et al. (2014). CFD simulation on the generation of turbidites in deepwater areas: a case study of turbidity current processes in qiongdongnan basin, northern south China Sea. *Acta Oceanologica Sin.* 33, 127–137. doi: 10.1007/s13131-014-0582-7

Joussain, R., Colin, C., Liu, Z., Meynadier, L., Fournier, L., Fauquembergue, K., et al. (2016). Climatic control of sediment transport from the Himalayas to the proximal NE Bengal fan during the last glacial-interglacial cycle. *Quaternary Sci. Rev.* 148, 1–16. doi: 10.1016/j.quascirev.2016.06.016

Kennett James, P., Cannariato Kevin, G., Hendy Ingrid, L., and Behl Richard, J. (2000). Carbon isotopic evidence for methane hydrate instability during quaternary interstadials. *Science* 288, 128–133. doi: 10.1126/science.288.5463.128

Kiel, S. (2015). Did shifting seawater sulfate concentrations drive the evolution of deep-sea methane-seep ecosystems? *Proc. R. Soc. B: Biol. Sci.* 282, 20142908. doi: 10.1098/rspb.2014.2908

Li, N., Feng, D., Chen, L., Wang, H., and Chen, D. (2017). Compositions of foraminifera-rich turbidite sediments from the shenhu area on the northern slope of the south China Sea: Implication for the presence of deep water bottom currents. *J. Asian Earth Sci.* 138, 148–160. doi: 10.1016/j.jseaes.2017.02.010

Li, M., Ouyang, T., Tian, C., Zhu, Z., Peng, S., Tang, Z., et al. (2019). Sedimentary responses to the East Asian monsoon and sea level variations recorded in the northern south China Sea over the past 36 kyr. *J. Asian Earth Sci.* 171, 213–224. doi: 10.1016/j.jseaes.2018.01.001

Li, J., Shi, X., Liu, S., Qiao, S., Zhang, H., Wu, K., et al. (2021a). Frequency of deep-sea turbidity as an important component of the response of a source-to-sink system to climate: A case study in the eastern middle Bengal fan since 32 ka. *Mar. Geol.* 441, 106603. doi: 10.1016/j.margeo.2021.106603

Li, N., Yang, X., Peckmann, J., Zhou, Y., Wang, H., Chen, D., et al. (2021b). Persistent oxygen depletion of bottom waters caused by methane seepage: Evidence from the south China Sea. *Ore Geol. Rev.* 129, 103949. doi: 10.1016/j.oregeorev.2020.103949

Li, N., Yang, X., Peng, J., Zhou, Q., and Chen, D. (2018). Paleo-cold seep activity in the southern south China Sea: Evidence from the geochemical and geophysical records of sediments. *J. Asian Earth Sci.* 168, 106–111. doi: 10.1016/j.jseaes.2017.10.022

Liang, Q., Hu, Y., Feng, D., Peckmann, J., Chen, L., Yang, S., et al. (2017). Authigenic carbonates from newly discovered active cold seeps on the northwestern slope of the south China Sea: Constraints on fluid sources, formation environments, and seepage dynamics. *Deep Sea Res. Part I: Oceanographic Res. Papers* 124, 31–41. doi: 10.1016/j.dsr.2017.04.015

Lim, Y. C., Lin, S., Yang, T. F., Chen, Y. G., and Liu, C. S. (2011). Variations of methane induced pyrite formation in the accretionary wedge sediments offshore southwestern Taiwan. *Mar. Petrology Geol.* 28, 1829–1837. doi: 10.1016/j.marpetgeo.2011.04.004

Lin, Q., Wang, J., Taladay, K., Lu, H., Hu, G., Sun, F., et al. (2016). Coupled pyrite concentration and sulfur isotopic insight into the paleo sulfate–methane transition zone (SMTZ) in the northern south China Sea. *J. Asian Earth Sci.* 115, 547–556. doi: 10.1016/j.jseaes.2015.11.001

Lisiecki, L. E., and Raymo, M. E. (2005). A pliocene-pleistocene stack of 57 globally distributed benthic δ18O records. *Paleoceanography* 20. doi: 10.1029/2004PA001071

Liu, S., Feng, X., Feng, Z., Xiao, X., and Feng, L. (2020). Geochemical evidence of methane seepage in the sediments of the qiongdongnan basin, south China Sea. *Chem. Geol.* 543, 119588. doi: 10.1016/j.chemgeo.2020.119588

Liu, E. T., Wang, H., Pan, S. Q., Qin, C. Y., Jiang, P., Chen, S., et al. (2021). Architecture and depositional processes of sublacustrine fan systems in structurally active settings: An example from weixinan depression, northern south China Sea. *Mar. Petroleum Geol.* 134, 105380. doi: 10.1016/j.marpetgeo.2021.105380

Lombo Tombo, S., Dennielou, B., Berné, S., Bassetti, M. A., Toucanne, S., Jorry, S. J., et al. (2015). Sea-Level control on turbidite activity in the Rhone canyon and the upper fan during the last glacial maximum and early deglacial. *Sedimentary Geol.* 323, 148–166. doi: 10.1016/j.sedgeo.2015.04.009

Maloney, J. M., Bentley, S. J., Xu, K., Obelcz, J., Georgiou, I. Y., Jafari, N. H., et al. (2020). Mass wasting on the Mississippi river subaqueous delta. *Earth-Science Rev.* 200, 103001. doi: 10.1016/j.earscirev.2019.103001

Maslin, M., Mikkelsen, N., Vilela, C., and Haq, B. (1998). Sea-Level –and gas-hydrate–controlled catastrophic sediment failures of the Amazon fan. *Geology* 26, 1107–1110. doi: 10.1130/0091-7613(1998)0262.3.CO;2

Masson, D. G. (1996). Catastrophic collapse of the volcanic island of hierro 15 ka ago and the history of landslides in the canary islands. *Geology* 24, 231–234. doi: 10.1130/0091-7613(1996)0242.3.CO;2

Miao, X., Feng, X., Li, J., and Lin, L. (2021a). Tracing the paleo-methane seepage activity over the past 20,000 years in the sediments of qiongdongnan basin, northwestern south China Sea. *Chem. Geol.* 559, 119956. doi: 10.1016/j.chemgeo.2020.119956

Miao, X., Feng, X., Li, J., Liu, X., Liang, J., Feng, J., et al. (2022). Enrichment mechanism of trace elements in pyrite under methane seepage. *Geochem. Perspect. Lett.* 21, 18–22. doi: 10.7185/geochemlet.2211

Miao, X., Feng, X., Liu, X., Li, J., and Wei, J. (2021b). Effects of methane seepage activity on the morphology and geochemistry of authigenic pyrite. *Mar. Petroleum Geol.* 133, 105231. doi: 10.1016/j.marpetgeo.2021.105231

Mienert, J., Vanneste, M., Bünz, S., Andreassen, K., Haflidason, H., and Sejrup, H. P. (2005). Ocean warming and gas hydrate stability on the mid-Norwegian margin at the storegga slide. *Mar. Petroleum Geol.* 22, 233–244. doi: 10.1016/j.marpetgeo.2004.10.018

Nisbet, E. G., and Piper, D. J. W. (1998). Giant submarine landslides. *Nature* 392, 329–330. doi: 10.1038/32765

Passega, R. (1957). Texture as characteristic of clastic deposition. *AAPG Bull.* 41, 1952–1984. doi: 10.1306/0BDA594E-16BD-11D7-8645000102C1865D

Passega, R. (1977). Significance of CM diagrams of sediments deposited by suspensions. *Sedimentology* 24, 723–733. doi: 10.1111/j.1365-3091.1977.tb00267.x

Paull, C. K., Buelow, W. J., Ussler, W., and Borowski, W. S. (1996). Increased continental-margin slumping frequency during sea-level lowstands above gas hydrate–bearing sediments. *Geology* 24, 143–146. doi: 10.1130/0091-7613(1996)024<0143:ICMSFD>2.3.CO;2

Paull, C. K., Ussler Iii, W., and Dillon, W. P. (1991). Is the extent of glaciation limited by marine gas-hydrates? *Geophys. Res. Lett.* 18, 432–434. doi: 10.1029/91GL00351

Peckmann, J., Thiel, V., Reitner, J., Taviani, M., Aharon, P., and Michaelis, W. (2004). A microbial mat of a Large sulfur bacterium preserved in a Miocene methane-seep limestone. *Geomicrobiol. J.* 21, 247–255. doi: 10.1080/01490450490438757

Peketi, A., Mazumdar, A., Joshi, R. K., Patil, D. J., Srinivas, P. L., and Dayal, A. M. (2012). Tracing the paleo sulfate-methane transition zones and H2S seepage events in marine sediments: An application of c-S-Mo systematics. *Geochem. Geophys. Geosystems* 13. doi: 10.1029/2012GC004288

Phrampus, B. J., and Hornbach, M. J. (2012). Recent changes to the gulf stream causing widespread gas hydrate destabilization. *Nature* 490, 527–530. doi: 10.1038/nature11528

Pouderoux, H., Proust, J.-N., Lamarche, G., Orpin, A., and Neil, H. (2012). Postglacial (after 18ka) deep-sea sedimentation along the hikurangi subduction margin (New zealand): Characterisation, timing and origin of turbidites. *Mar. Geol.* 295-298, 51–76. doi: 10.1016/j.margeo.2011.11.002

Prins, M. A., and Postma, G. (2000). Effects of climate, sea level, and tectonics unraveled for last deglaciation turbidite records of the Arabian Sea. *Geology* 28, 4. doi: 10.1130/0091-7613(2000)282.0.CO;2

Reagan, M. T., and Moridis, G. J. (2007). Oceanic gas hydrate instability and dissociation under climate change scenarios. *Geophys. Res. Lett.* 34. doi: 10.1029/2007GL031671

Rothwell, R. G., Thomson, J., and Kähler, G. (1998). Low-sea-level emplacement of a very large late pleistocene 'megaturbidite' in the western Mediterranean Sea. *Nature* 392, 377–380. doi: 10.1038/32871

Sato, H., Hayashi, K., Ogawa, Y., and Kawamura, K. (2012). Geochemistry of deep sea sediments at cold seep sites in the nankai trough: Insights into the effect of anaerobic oxidation of methane. *Mar. Geol.* 323-325, 47–55. doi: 10.1016/j.margeo.2012.07.013

Schmidt, F., Schmidt, A., Treguier, E., Guiheneuf, M., Moussaoui, S., and Dobigeon, N. (2010). Implementation strategies for hyperspectral unmixing using Bayesian source separation. *IEEE Trans. Geosci. Remote Sens.* 48, 4003–4013. doi: 10.1109/TGRS.2010.2062190

Shackleton, N. J. (1987). Oxygen isotopes, ice volume and sea level. *Quaternary Sci. Rev.* 6, 183–190. doi: 10.1016/0277-3791(87)90003-5

Tong, H., Feng, D., Cheng, H., Yang, S., Wang, H., Min, A. G., et al. (2013). Authigenic carbonates from seeps on the northern continental slope of the south China Sea: New insights into fluid sources and geochronology. *Mar. Petroleum Geol.* 43, 260–271. doi: 10.1016/j.marpetgeo.2013.01.011

Toucanne, S., Zaragosi, S., Bourillet, J. F., Naughton, F., Cremer, M., Eynaud, F., et al. (2008). Activity of the turbidite levees of the celtic–armorican margin (Bay of Biscay) during the last 30,000 years: Imprints of the last European deglaciation and Heinrich events. *Mar. Geol.* 247, 84–103. doi: 10.1016/j.margeo.2007.08.006

Waelbroecka, C., Labeyrie, L., Michel, E., Duplessy, J. C., McManus, J. F., Lambeck, K., et al. (2002). Sea-Level and deep water temperature changes derived from benthic foraminifera isotopic records.pdf. *Quaternary Sci. Rev.* 21, 11. doi: 10.1016/S0277-3791(01)00101-9

Wan, S., and Jian, Z. (2014). Deep water exchanges between the south China Sea and the pacific since the last glacial period. *Paleoceanography* 29, 1162–1178. doi: 10.1002/2013PA002578

Wang, G., Xie, S.-P., Qu, T., and Huang, R. X. (2011). Deep south China Sea circulation. *Geophys. Res. Lett.* 38, L05601. doi: 10.1029/2010GL046626

Wang, S. H., Song, H. B., and Yan, W. (2004). Environmental effects of natural gas hydrate. *Bulletin of Mineralogy Petrology and Geochemistry* 23 (2), 160–165. doi: 10.1038/nature14399

Wei, W., and Algeo, T. J. (2020). Elemental proxies for paleosalinity analysis of ancient shales and mudrocks. *Geochimica Cosmochimica Acta* 287, 341–366. doi: 10.1016/j.gca.2019.06.034

Wei, J., Wu, T., Zhang, W., Deng, Y., Xie, R., Feng, J., et al. (2020). Deeply buried authigenic carbonates in the qiongdongnan basin, south China Sea: Implications for ancient cold seep activities. *Minerals* 10. doi: 10.3390/min10121135

Yang, K., Chu, F., Zhu, Z., Dong, Y., Yu, X., Zhang, W., et al. (2018). Formation of methane-derived carbonates during the last glacial period on the northern slope of the south China Sea. *J. Asian Earth Sci.* 168, 173–185. doi: 10.1016/j.jseaes.2018.01.022

Yu, S.-W., Tsai, L. L., Talling, P. J., Lin, A. T., Mii, H.-S., Chung, S.-H., et al. (2017). Sea Level and climatic controls on turbidite occurrence for the past 26kyr on the flank of the gaoping canyon off SW Taiwan. *Mar. Geol.* 392, 140–150. doi: 10.1016/j.margeo.2017.08.011

Zaragosi, S., Bourillet, J.-F., Eynaud, F., Toucanne, S., Denhard, B., Van Toer, A., et al. (2006). The impact of the last European deglaciation on the deep-sea turbidite systems of the celtic-armorican margin (Bay of Biscay). *Geo-Marine Lett.* 26, 317–329. doi: 10.1007/s00367-006-0048-9

Zhang, J., Lei, H., Chen, Y., Kong, Y., Kandasamy, S., Ou, W., et al. (2018b). Carbon and oxygen isotope composition of carbonate in bulk sediment in the southwest Taiwan basin, south China Sea: Methane hydrate decomposition history and its link to mud volcano eruption. *Mar. Petroleum Geol.* 98, 687–696. doi: 10.1016/j.marpetgeo.2018.08.031

Zhang, Y., Liu, Z., Zhao, Y., Colin, C., Zhang, X., Wang, M., et al. (2018a). Long-term *in situ* observations on typhoon-triggered turbidity currents in the deep sea. *Geology* 46, 675–678. doi: 10.1130/G45178.1

Zhang, K., Song, H., Tao, J., Wang, H., and Geng, M. (2020). A preliminary study on the active cold seeps flow field in the qiongdongnan Sea area, the northern south China Sea. *Chin. Sci. Bull.* 65, 1130–1140. doi: 10.1360/TB-2019-0582

Zhao, Y., Liu, Z., Colin, C., Xie, X., and Wu, Q. (2011). Turbidite deposition in the southern south China Sea during the last glacial: Evidence from grain-size and major elements records. *Chin. Sci. Bull.* 56, 3558–3565. doi: 10.1007/s11434-011-4685-7

Zhao, Y., Liu, Z., Zhang, Y., Li, J., Wang, M., Wang, W., et al. (2015). *In situ* observation of contour currents in the northern south China Sea: Applications for deepwater sediment transport. *Earth Planetary Sci. Lett.* 430, 477–485. doi: 10.1016/j.epsl.2015.09.008

Zhou, C., Zhao, W., Tian, J., Zhao, X., Zhu, Y., Yang, Q., et al. (2017). Deep Western boundary current in the south China Sea. *Sci. Rep.* 7, 9303. doi: 10.1038/s41598-017-09436-2

Zhu, Y., Sun, J., Wang, Y., Li, S., Xu, T., Wei, Z., et al. (2019). Overview of the multi-layer circulation in the south China Sea. *Prog. Oceanogr.* 175, 171–182. doi: 10.1016/j.pocean.2019.04.001

frontiers | Frontiers in Marine Science

TYPE Original Research
PUBLISHED 28 March 2023
DOI 10.3389/fmars.2023.1166305

OPEN ACCESS

EDITED BY
Min Luo,
Shanghai Ocean University, China

REVIEWED BY
Xiaoming Sun,
Sun Yat-sen University, China
Giuliana Panieri,
UiT the Arctic University of Norway, Norway

*CORRESPONDENCE
Jiasheng Wang
js-wang@cug.edu.cn

SPECIALTY SECTION
This article was submitted to Marine Biogeochemistry, a section of the journal Frontiers in Marine Science

RECEIVED 15 February 2023
ACCEPTED 16 March 2023
PUBLISHED 28 March 2023

CITATION
Cen Y, Wang J, Algeo TJ, Wang Z, Ma X and Chen C (2023) Methane release effects on foraminiferal tests in northern South China Sea.
Front. Mar. Sci. 10:1166305.
doi: 10.3389/fmars.2023.1166305

Methane release effects on foraminiferal tests in northern South China Sea

Yue Cen[1,2], Jiasheng Wang[1,2]*, Thomas J. Algeo[1,3,4], Zhou Wang[1,2,5], Xiaochen Ma[1,2] and Can Chen[1,2]

[1]Hubei Key Laboratory of Marine Geological Resources in College of Marine Science and Technology, China University of Geosciences, Wuhan, Hubei, China, [2]State Key Laboratory of Biogeology and Environment Geology, China University of Geosciences, Wuhan, Hubei, China, [3]State Key Laboratory of Geological Processes and Mineral Resources, China University of Geosciences, Wuhan, Hubei, China, [4]Department of Geosciences, University of Cincinnati, Cincinnati, OH, United States, [5]State Key Laboratory of Marine Geology, Tongji University, Shanghai, China

Upward diffusing methane in gas hydrate geological systems is consumed in the sediment and water column by a series of biogeochemical reactions, which not only affect living foraminifera but also lead to early diagenetic alteration of buried foraminiferal tests. Previous studies of the impact of methane release events on fossil foraminifera focused mainly on carbon and oxygen isotopes, with little attention given to other geochemical proxies to date. Here, we examine the test wall microstructure and analyze the elemental and stable carbon-oxygen isotopic compositions of buried foraminifera from gas hydrate-bearing sediments at Site GMGS2-16 in the northern South China Sea. Our results show that diagenetic alteration of foraminiferal tests at Site GMGS2-16 is mainly linked to high-Mg calcite overgrowths. Test $\delta^{13}C$ covaries negatively with the degree of diagenetic alteration (based on petrographic characteristics) but positively with Mg/Ca ratios. With increasing diagenetic alteration, Ba/Ca, Mn/Ca, Fe/Ca, Mo/Ca, U/Ca, V/Ca, Ni/Ca and Co/Ca also generally increase, but Sr/Ca and Cu/Ca exhibit variable changes. We infer that foraminiferal tests are highly susceptible to alteration by methane-bearing fluids, and that the elemental ratios of diagenetically altered tests are potentially reliable proxies for paleo-methane release events. At Site GMGS2-16, the overall pattern of diagenetic alteration of foraminiferal tests records frequent vertical fluctuations of the sulfate-methane transition zone (SMTZ) caused by variable fluid flux and methane release rates, with two discrete large-scale methane release events having maximum ages of ~0.47 ka and ~170 ka.

KEYWORDS

carbon isotopes, oxygen isotopes, early diagenesis, LA-ICP-MS, trace elements, gas hydrates

1 Introduction

A large amount of methane is trapped as methane hydrates, dissolved methane and free gas reservoirs in continental margin sediments worldwide. Methane-rich fluids can migrate upwards along faults and fractures, emitting methane back into the hydrosphere and atmosphere, which can have serious impacts on global climate and the biosphere (Dickens et al., 1997; Retallack et al., 1998; Them et al., 2018). Hence, it is of considerable importance to evaluate the character, timing, and drivers of natural past methane release events and explore how to avoid consequent climatic and biotic effects (Miao et al., 2021). Methane-derived authigenic carbonate (MDAC) is regarded as a reliable archive of information about paleo-methane release events, past fluid composition and circulation, and sedimentary redox processes (Peckmann and Thiel, 2004; Feng et al., 2009; Hu et al., 2015; Crémière et al., 2016; Liang et al., 2017; Zhu et al., 2019; Bayon et al., 2020; Schier et al., 2021; Liu et al., 2022). During the upward migration of methane-bearing fluids, steep chemical gradients provide ecological niches for microbial communities mediating the anaerobic oxidation of methane (AOM, $CH_4 + SO_4^{2-} \rightarrow HCO_3^- + HS^- + H_2O$) in the sulfate-methane transition zone (SMTZ). The production of bicarbonate results in increased pore-fluid alkalinity, inducing precipitation of MDAC at timescales typically in the range of centuries to millennia (Schneider, 2018). Therefore, some short duration paleo-methane release events may fail to leave a carbonate record.

Diagenetically altered foraminifera have been found to preserve post-depositional signals similar to those in MDAC (Torres et al., 2010), and the wider distribution of the former therefore has the potential to yield higher-resolution records of paleo-methane release events. Organic matter in marine sediments is subject to a succession of heterotrophic microbial metabolisms that utilize a depth sequence of electron acceptors, largely in accordance with Gibbs free energy yield: NO_3^-, Mn(IV), Fe(III), and SO_4^{2-} (Jørgensen, 2021). When all energetically more favorable terminal electron acceptors have been depleted, organic carbon is mineralized *via* methanogenesis, causing the accumulation of methane in deeper sediments. Upward diffusing methane will meet the zone of sulfate reduction and AOM occurs. The diagenetic processes not only affect living benthic foraminifera but also lead to diagenetic alteration of buried foraminiferal tests (Millo et al., 2005a; Torres et al., 2010; Panieri et al., 2017; Schneider et al., 2017; Cen et al., 2022). To date, most studies investigating the effect of methane release events on foraminiferal tests have focused on their stable carbon isotopic compositions (Hill et al., 2004; Millo et al., 2005b; Martin et al., 2007; Panieri et al., 2014; Schneider et al., 2017; Sztybor and Rasmussen, 2017; Wan et al., 2018). Additionally, their elemental compositions (e.g., Mg/Ca, Sr/Ca, Ba/Ca, Mn/Ca, Fe/Ca, U/Ca, and Al/Ca) (Torres et al., 2010; Schneider et al., 2017; Fontanier et al., 2018; Detlef et al., 2020) may also be influenced by MDAC precipitation. Borrelli et al. (2020) proposed benthic foraminiferal $\delta^{34}S$ as a novel tool to identify methane release events in geological records and to indirectly date fossil seeps. Nonetheless, a comprehensive understanding of the influence of early diagenetic processes on the elemental composition of foraminifera awaits the analysis of a full suite of elemental ratios in a suitably designed study.

Here, we undertook a suite of petrographic and geochemical analyses including reflected light microscopy, scanning electron microscope (SEM) imaging, oxygen and carbon isotopic measurements, laser ablation inductively coupled plasma mass spectrometry (LA-ICP-MS), and electron probe microanalysis (EPMA) elemental mapping on foraminiferal tests with varying degrees of diagenetic alteration from gas hydrate-bearing sediments of the northern South China Sea. Our main goal was to investigate the effects of methane release on diagenetic alteration of foraminiferal tests and to refine multiple proxies for recognition of paleo-methane release events in gas hydrate geosystems.

2 Geological setting

The South China Sea (SCS) is one of the largest marginal seas in the western Pacific Ocean (Taylor and Hayes, 1980). On account of the interactive and complex collision among the Eurasian, Pacific and Indian-Australian plates, a series of sedimentary basins, e.g., the Qiongdongnan Basin and Pearl River Mouth Basin, were developed along the northern continental margin of the SCS (Zhu et al., 2009; Morley, 2012). During June to September in 2013, the gas hydrate drilling expedition GMGS2 was conducted by the Chinese Geological Survey (CGS) incorporating with Fugro and Geotek to accurately quantify gas hydrate in the sediment cores and to determine the nature and distribution of gas hydrate within the sedimentary sequence in the Pearl River Mouth Basin (Zhang et al., 2015). The drilling area of expedition GMGS2 was located in the eastern Pearl River Mouth Basin, along the crest of two prominent seafloor ridges (Figure 1), where bottom simulating reflectors and other seismic indicators for widespread gas hydrate and seepage had been recognized (Zhang et al., 2015).

The study site (GMGS2-16), which is located on the eastern ridge (Figure 1) at a water depth of 871 m, yielded a 230-m-long core. The age framework for site GMGS2-16 was established by combining calcareous nannofossil and planktonic foraminifer datums (Chen et al., 2016a). The oldest sediments recovered are

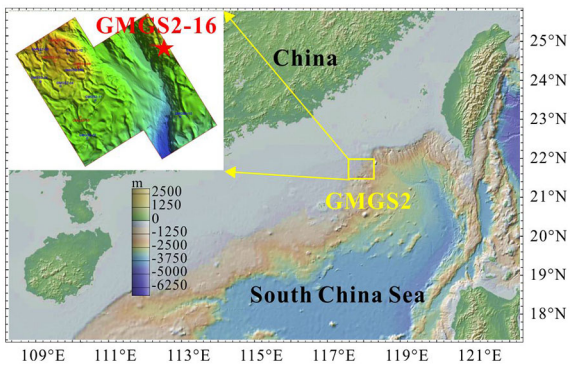

FIGURE 1
Location of the study site (GMGS2-16) in the eastern Pearl River Mouth Basin, South China Sea (modified after Zhang et al., 2015).

of middle Pleistocene age, younger than ~500 ka. Sedimentation rates since 440 ka have varied from 28 to 62.3 cm/kyr, with a mean rate of 47.4 cm/kyr (Chen et al., 2016a). The logging-while-drilling data indicated the existence of two layers of gas hydrate: an upper hydrate layer, characterized by nodules and fracture-filling hydrates, at a shallow depth (13-29 mbsf), and a lower pore-filling hydrate layer near the bottom simulating reflector (BSR) at depths of 192-222 mbsf (Feng et al., 2015). At this site, porewater sulfate concentrations decline to zero at 13.69 mbsf, indicating a high upward methane flux and a shallow SMTZ (Kuang et al., 2018).

3 Materials and methods

3.1 Sample description and processing

The dominant lithologies of the sediments in this core are dark-green, unconsolidated clayey silt and silty clay. Authigenic minerals including carbonate, pyrite, and gypsum were observed at multiple levels (Gong et al., 2017; Lin et al., 2018; Zhao et al., 2021). For this study, sediment samples were collected from the curated core at the GMGS laboratory in Guangzhou and processed in the State Key Laboratory of Biogeology and Environmental Geology (BGEG) at China University of Geosciences in Wuhan (CUG). Fifty-seven core samples, each representing a quarter-section of the drillcore having a volume of 10-15 cm^3, were collected, weighed, and stored in a freezer prior to analysis. For each sample, a ~10 cm^3 aliquot was dried at 40 °C for 24 hours in an air-dry oven and re-weighed to determine moisture-free sample weight. This aliquot was then rinsed using distilled water, sieved through 150 μm, 65 μm and 30.8 μm sifters. In the process of sieving, the sample was ultrasonicated in distilled water for 30 s to remove clay minerals and detrital materials sticking to the foraminiferal tests. For each sample, the three size fractions were air dried at a temperature of 40 °C, and then stored separately after weighing.

3.2 Petrography

All particles with size of larger than 150 μm were examined using a binocular microscope (Carl Zeiss Stemi 2000-C). Foraminiferal samples were grouped into four classes (pristine, weakly altered, moderately altered, and strongly altered; Figure 2) according to their degree of diagenetic alteration following the approach of Schneider et al. (2017). Well-preserved pristine tests are optically smooth with high reflectance and transparency, and primary test features such as chambers, sutures and pores are easily observed. Weakly altered tests are translucent or white in color with decreased reflectance and transparency, but still have prominent morphological features. Moderately altered tests appear white or yellow with both translucent and opaque areas. Strongly altered tests appear yellow to dark brown in color, low reflectance and transparency with an opaque test wall, a 'frosty' texture, and obscured morphological features. In order to determine the frequencies of the various diagenetic alteration stages, all foraminiferal specimens larger than 150 μm in each core sample were assigned to one of these four categories and tallied. Given their relatively greater abundance, three foraminiferal species were chosen for geochemical measurements: the planktic taxa *Globorotalia menardii* and *Neogloboquadrina dutertrei*, and the benthic taxon *Uvigerina peregrina*.

3.3 Scanning electron microscopy

Representative foraminiferal tests of each species (i.e., *G. menardii*, *N. dutertrei*, and *U. peregrina*) at each diagenetic alteration stage (as determined by reflected-light microscopy) were selected from seven core samples and further tested using SEM and elemental analysis (Table 1). The seven core samples cover the intervals containing authigenic carbonate nodules above (GMGS2-16B-1H-1a, 0.23 mbsf), within (GMGS2-16D-2H-1, 10.83 mbsf), and below (GMGS2-16F-6H-1, 50.47 mbsf; GMGS2-16D-8H-1, 92.32 mbsf; GMGS2-16H-4H-1b, 164.68 mbsf) the current SMTZ (the bottom boundary is at 13.69 mbsf) (Kuang et al., 2018), as well as some intervals where no authigenic carbonate nodules are present (GMGS2-16F-2P-CC, 20.52 mbsf; GMGS2-16F-5H-2, 40.92 mbsf), with the aim of achieving a comprehensive understanding of the influence of diagenetic processes on foraminiferal geochemistry.

We selected foraminiferal tests of the same species that had approximately equal shell size in order to limit the size dependency of the shell chemistry (Friedrich et al., 2012). The selected specimens were then cleaned ultrasonically with methanol for 10 s to remove clay minerals and other particles, with repeated rinses performed until visible discoloration was absent. Then each specimen was mounted in epoxy resin and polished down to yield a cross-section view for the purpose of studying its internal structure. SEM observation and imaging were conducted on whole and polished specimens of tests using a Hitachi SU8010 SEM in high-vacuum mode, with a beam voltage of 10-20 kV, at the State Key Laboratory of BGEG (CUG-Wuhan).

3.4 Geochemical analyses

Foraminiferal $\delta^{13}C$ and $\delta^{18}O$ were measured using a Gas Bench coupled with a Thermo Finnigan MAT 253 at the Oxy-Anion Stable Isotope Consortium (OASIC) in the Department of Geology & Geophysics, Louisiana State University. Each isotopic sample contained 2-3 foraminiferal tests to generate sufficient material for measurement. Samples were loaded into 12 mL Labco Exetainer vials and left in an oven for 12-24 h at 75 °C, then were sealed with Labco septa and flushed with 99.999% helium and manually acidified at 72°C. The carbon dioxide analytic gas was isolated *via* gas chromatography, and water was removed using a Nafion trap prior to introduction into the stable isotope mass spectrometer fitted with a continuous flow interface. Isotopic results are expressed in the delta notation as per mille (‰) deviations from the Vienna-Pee Dee Belemnite (VPDB) standard. Precision was routinely < 0.06 ‰ for $\delta^{13}C$ and < 0.08 ‰ for $\delta^{18}O$.

10.3389/fmars.2023.1166305

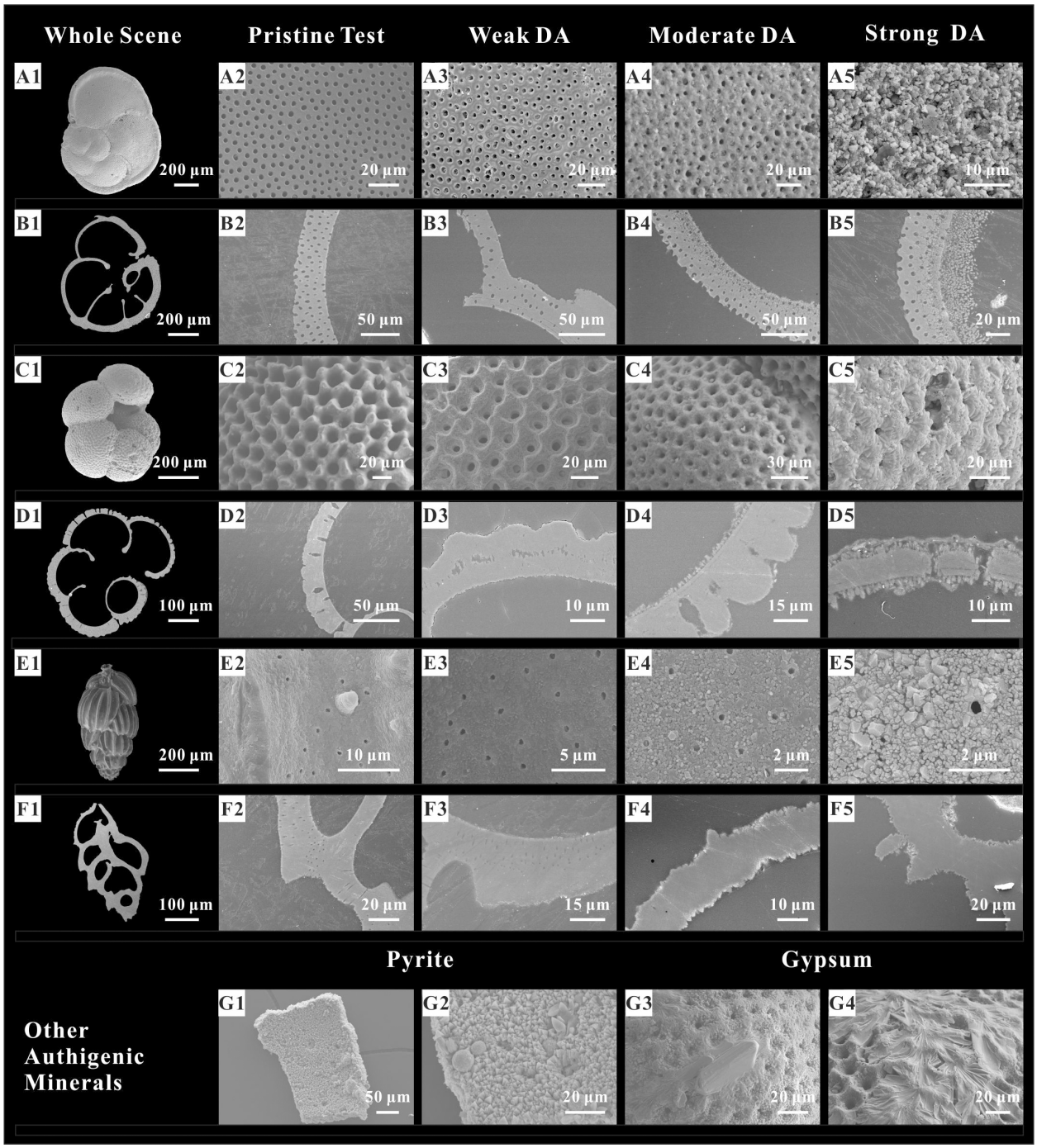

FIGURE 2
SEM images of foraminiferal tests representing a range of diagenetic alteration (DA) stages. Whole test, exterior wall, and wall cross-section views for *G. menardii* (**A**1-**B**5), *N. dutertrei* (**C**1-**D**5), and *U. peregrina* (**E**1-**F**5). Authigenic pyrite framboids inside the test chamber (**G** 1-2), and authigenic gypsum growing on the exterior wall (**G**3-4).

LA-ICP-MS was performed on polished cross-sections of the selected tests. The isotopes of ^{24}Mg, ^{27}Al, ^{43}Ca, ^{51}V, ^{55}Mn, ^{57}Fe, ^{59}Co, ^{60}Ni, ^{63}Cu, ^{88}Sr, ^{97}Mo, ^{137}Ba, ^{238}U were measured along the laser profile tracks. Analyses were measured using an integrated *in situ* laser ablation (COMPexPro 102 ArF 193 nm excimer laser; Coherent GeoLasPro) and ICP-MS (Agilent 7900) system at the Sample-Solution Analytical Technology Co. in Wuhan, China. The spot size and frequency of the laser were set to 44 µm and 5 Hz, respectively. Internal standard-independent calibrations followed the procedure of Chen et al. (2011). Each test session analyzed 50 sample spots, with measurement of a standard (NIST 610) for drift correction after every fifth sample. A series of standard materials were

10.3389/fmars.2023.1166305

TABLE 1 Overview of the analytical techniques for each sample.

Sample ID	Depth (mbsf)	Foraminiferal taxon	Degree of diagenetic alteration (DA)	Methodology			
				SEM	EPMA	$\delta^{13}C$ and $\delta^{18}O$	LA-ICP-MS
GMGS2-16B-1H-1a	0.23	*G. menardii*	Pristine test	√		√	√
			Weak DA	√		√	√
			Moderate DA	√		√	√
			Strong DA	√		√	√
		N. dutertrei	Pristine test	√		√	√
			Weak DA	√		√	√
			Moderate DA	√		√	√
			Strong DA	√		√	√
		U. peregrina	Pristine test	√		√	√
			Weak DA	√		√	√
			Moderate DA	√		√	√
			Strong DA	√		√	√
GMGS2-16D-2H-1	10.83	*G. menardii*	Pristine test			√	√
			Weak DA	√		√	√
			Moderate DA	√		√	√
			Strong DA	√	√	√	√
		N. dutertrei	Pristine test			√	√
			Weak DA	√		√	√
			Moderate DA	√		√	√
			Strong DA	√	√	√	√
		U. peregrina	Pristine test			√	√
			Weak DA	√		√	√
			Moderate DA	√		√	√
			Strong DA	√	√	√	√
GMGS2-16F-2P-CC	20.52	*G. menardii*	Pristine test	√		√	√
		N. dutertrei	Pristine test	√		√	√
		U. peregrina	Pristine test	√		√	√
GMGS2-16F-5H-2	40.92	*G. menardii*	Pristine test			√	√
		N. dutertrei	Pristine test			√	√
		U. peregrina	Pristine test			√	√
GMGS2-16F-6H-1	50.47	*G. menardii*	Pristine test			√	√
			Weak DA	√		√	√
			Moderate DA	√		√	√
		N. dutertrei	Pristine test			√	√
			Weak DA	√		√	√
			Moderate DA	√		√	√
		U. peregrina	Pristine test			√	√

(Continued)

10.3389/fmars.2023.1166305

TABLE 1 Continued

Sample ID	Depth (mbsf)	Foraminiferal taxon	Degree of diagenetic alteration (DA)	Methodology			
				SEM	EPMA	$\delta^{13}C$ and $\delta^{18}O$	LA-ICP-MS
			Weak DA	√		√	√
			Moderate DA	√		√	√
GMGS2-16D-8H-1	92.32	*G. menardii*	Pristine test			√	√
			Weak DA			√	√
			Moderate DA			√	√
			Strong DA			√	√
		N. dutertrei	Pristine test			√	√
			Weak DA			√	√
			Moderate DA			√	√
			Strong DA			√	√
		U. peregrina	Pristine test			√	√
			Weak DA			√	√
			Moderate DA			√	√
			Strong DA			√	√
GMGS2-16H-4H-1b	164.68	*G. menardii*	Pristine test				√
			Weak DA				√
			Moderate DA				√
			Strong DA				√
		N. dutertrei	Pristine test				√
			Weak DA				√
			Moderate DA				√
			Strong DA				√
		U. peregrina	Pristine test				√
			Weak DA				√
			Moderate DA				√
			Strong DA				√

measured before (NIST610, BHVO-2G, BIR-1G, BCR-2G, MACS-3, and MACS-3 in order) and after (same measured in reverse order) the session to set a calibration curve. Each spot analysis incorporated an initial <5 s wash-out time then ~20 s background acquisition, followed by a ~50 s sample-data acquisition interval. ICPMSDataCal (version 10.8) software was used to calculate and calibrate off-line data (Liu et al., 2008). For each sample, the reported Element/Ca ratios were calculated by averaging 15-25 measurements (5 laser spots per specimen, 3-5 specimens per sample) to reduce the impact of natural geochemical heterogeneity in foraminiferal tests (Rathmann et al., 2004). The signals of Mn and Al were used to monitor clay contamination, and any specimens with values above 1 mmol/mol (Mn/Ca) or 0.25 mmol/mol (Al/Ca) were removed from the dataset (Skinner et al., 2019).

To study the spatial cross-sectional distribution of Mg in the altered specimens, EPMA elemental mapping were obtained with a JEOL JXA-8230 electron microprobe at the Sample-Solution Analytical Technology Co. in Wuhan, China. Operation conditions were 15 kV acceleration voltage and 20 nA beam current with 1 μm beam diameter. Standards were natural minerals from international suppliers. Before measuring elemental concentrations, optical microscope and SEM images were taken to assess diagenetic alteration and assist in selecting sampling points.

Pairwise correlations among foraminiferal elemental proxies measured by LA-ICP-MS were tested using Pearson correlation coefficients. To test differences in the mean elemental contents of foraminiferal tests, a Student's *t*-test was performed for sample pairs.

4 Results

4.1 Foraminiferal preservation and petrography

Petrographic observation of the core samples using reflected light microscopy revealed that both planktonic and benthic foraminiferal tests exhibit diagenetic alteration features. Each foraminiferal specimen was assigned to one of four categories: pristine, weakly altered, moderately altered, or strong altered (Figure 2). For each core sample, the number of tests assigned to each category was tabulated (Appendix 1). Altered foraminiferal tests are present through nearly the full drillcore, at depths ranging from 0.23 to 205.82 mbsf. The samples yielding the highest percentage of altered tests (>30%) are at depths of 10.83 and 92.32 mbsf, but a larger number of samples contain at least 10% altered tests, including those at 16.65, 22.08, 50.47, and 164.68 mbsf. The samples containing the fewest altered foram tests (<1%) are at 25.73, 29.91, 59.48, 109.75, 148.63-154.63, 172.93, 179.67, 192.46, and 205.82 mbsf. The intensity of diagenetic alteration is variable, e.g., the sample at 10.83 mbsf is dominated by moderately altered tests and the sample at 22.08 mbsf by weakly altered tests. There is no systematic downhole increase in the intensity of diagenetic alteration at site GMGS2-16, challenging the conventional view that diagenetic intensity correlates with burial depth (Schlanger and Douglas, 1974).

SEM microscopy was used to identify various alteration features, including dissolution, overgrowth, and recrystallization (Edgar et al., 2015). SEM imaging reveals that the foraminiferal tests exhibit a range of diagenetic features, including overgrowths of coarse inorganic crystallites, without recrystallization and dissolution. As shown in Figure 2, the internal and external wall surfaces of pristine tests are smooth and free of infilling and overgrowths, pores are unplugged, and wall cross sections are homogeneous with a well-defined outline (Figures 2A2–F2). In contrast to pristine tests, altered tests reveal a fine (~1-30 μm thick) layer of calcite crystals on the tests (Figures 2A 3–F5). The secondary calcite crystals encrust interior and/or exterior test surfaces as well as fill in pores, resulting in a reduction in pore size until complete infilling is achieved. The euhedral crystals grow perpendicular to test walls and are typically much larger than primary foraminiferal biogenic crystals, making them easily identified by SEM. Furthermore, authigenic pyrite (Figures 2G1–2) and gypsum (Figures 2G3–4) were also found inside and outside test chambers.

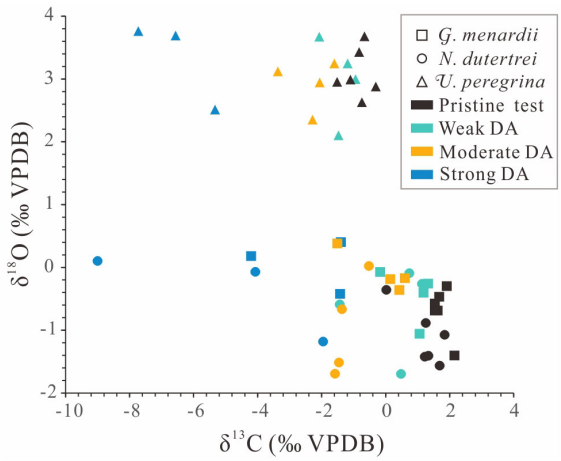

FIGURE 3
Carbon and oxygen stable isotopes of foraminiferal tests at variable diagenetic alteration stages. The squares, circles, and triangles represent the taxa *G. menardii*, *N. dutertrei* and *U. peregrina*, respectively; black, green, orange and blue represent pristine, weakly altered, moderately altered, and strongly altered tests, respectively.

4.2 Stable isotopic compositions

The pristine and altered tests exhibit significantly different carbon isotopic compositions. The pristine tests of *G. menardii*, *N. dutertrei* and *U. peregrina* exhibit $\delta^{13}C$ values ranging from +1.53 ‰ to +1.66 ‰, +1.21 ‰ to +1.83 ‰, and −0.75 ‰ to −0.31 ‰, respectively (Figure 3, Table 2, Appendix 2). In contrast, foraminiferal tests of *G. menardii*, *N. dutertrei* and *U. peregrina* with variable diagenetic alteration stages have $\delta^{13}C$ values ranging

TABLE 2 Overall range and average value of carbon and oxygen stable isotopes for samples with weak, moderate, and strong diagenetic alteration.

	Degree of diagenetic alteration (DA)	*G. menardii*			*N. dutertrei*			*U. peregrina*		
		min	max	average	min	max	average	min	max	average
$\delta^{13}C$ (‰ VPDB)	Pristine test	+1.52	+2.14	+1.73	+0.01	+1.83	+1.21	−1.52	−0.31	−0.87
	Weak DA	−0.18	+1.31	+0.84	−1.44	+1.12	+0.22	−2.08	−0.95	−1.43
	Moderate DA	−1.52	+0.59	−0.10	−1.59	−0.53	−0.96	−3.37	−1.61	−2.33
	Strong DA	−4.21	−1.40	−2.35	−8.99	−1.96	−5.01	−7.72	−5.33	−6.54
$\delta^{18}O$ (‰ VPDB)	Pristine test	−1.41	−0.30	−0.69	−1.57	−0.36	−1.12	+2.63	+3.68	+3.09
	Weak DA	−1.06	−0.08	−0.45	−1.70	−0.09	−0.66	+2.10	+3.67	+3.00
	Moderate DA	−0.36	+0.38	−0.09	−1.69	+0.02	−0.96	+2.35	+3.25	+2.91
	Strong DA	−0.42	+0.40	+0.05	−1.18	+0.10	−0.38	+2.51	+3.76	+3.32

from –1.52 ‰ to +1.59 ‰, –8.99 ‰ to +1.32 ‰ and –7.72 ‰ to –0.95 ‰, respectively. As can be seen from Figure 3 and Table 2, with the increase of diagenetic alteration, the range of carbon isotopes tends to be wider and the boundary values of the range as well as the average $\delta^{13}C$ value of both planktonic and benthic foraminiferal tends to be more negative.

The oxygen isotopic compositions of the pristine and altered tests do not differ as significantly as the carbon isotopic composition. The $\delta^{18}O$ values of pristine tests are less variable ranging from –0.57 ‰ to –0.30 ‰ for planktonic foraminifera (*G. menardii* and *N. dutertrei*) and +2.63 ‰ to +3.68 ‰ for benthic foraminifera (*U. peregrina*) (Table 2). On the other hand, the foraminiferal tests of planktonic and benthic foraminifera with variable diagenetic alteration stages have $\delta^{18}O$ values ranging from –1.70 ‰ to +0.40 ‰ and +2.10 ‰ to +3.76 ‰, respectively. With the increase of diagenetic alteration, the average values of $\delta^{18}O_{planktonic}$ reveal a slight positive bias, while the average values of $\delta^{18}O_{benthic}$ exhibit no significant variation.

4.3 Elemental compositions

EPMA maps of *G. menardii* and *N. dutertrei* serve to investigate the spatial variability of Mg/Ca in strongly altered tests (Figure 4). SEM images of a single sample reveal isolated calcite crystal overgrowth on the test wall cross-section (Figures 4A–C). The EPMA maps demonstrate clear Mg enrichment in the authigenic overgrowths. The highest Mg concentrations of the carbonate crystals encrusting on the outside and/or inside of the foraminiferal tests can reach up to 4.8 wt%, which is 4-10 times higher than the Mg content of the biogenic low-Mg calcite of the original test (Figures 4B–D).

In addition, LA-ICP-MS analyses were utilized to determine the elemental compositions of foraminiferal tests Appendix 3. Boxplots reveal the overall distributions of elemental ratios of foraminiferal tests at each diagenetic alteration stage (Figure 5). In general, Mg/Ca, V/Ca, Mn/Ca, Fe/Ca, Co/Ca, Cu/Ca, Ba/Ca, and U/Ca ratios increase strongly with the degree of diagenesis, Al/Ca, Ni/Ca, and Mo/Ca ratios increase moderately, and there is no significant change in Ni/Ca, Sr/Ca, and Cd/Ca ratios. Particularly noteworthy is the order-of-magnitude increase in Mg concentrations (Figure 5), yielding Mg/Ca values ranging from 0.85 for unaltered tests to 69.8 mmol/mol for strongly altered tests. For comparison, an earlier study reported Mg/Ca of 0.5 to 5 mmol/mol and 0.5 to 10 mmol/mol in pristine planktonic and benthic foraminifera, respectively (Lea, 2003).

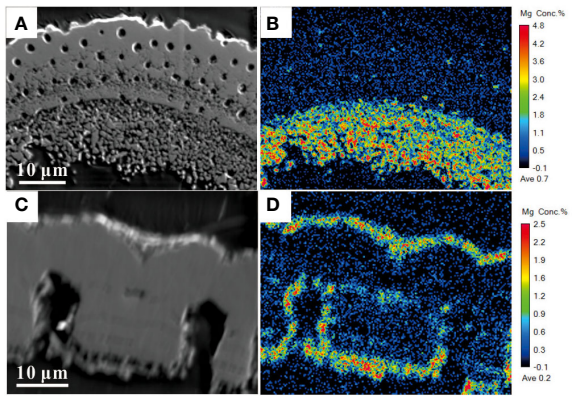

FIGURE 4
SEM images of foraminiferal wall cross-section and Mg (intensity) EPMA map of *G menardii* **(A, B)** and *N. dutertrei* **(C, D)**.

5 Discussion

5.1 Influence of diagenesis on foraminiferal tests

Based on petrographic evidence, diagenetic alteration of foraminiferal tests at Site GMGS2-16 is mostly due to calcite overgrowths (Figure 2). The secondary calcite crystals encrust test surfaces and fill test pores, leading to changes in the visual characteristics of the tests. With increased amounts of secondary calcite deposited on internal and/or external test surfaces and within pores, the color of foraminiferal tests changes to yellow or gray, the reflectance and transparency of the tests are reduced, and test walls start to display a 'frosty' texture.

Precipitation of inorganic calcite can alter the original geochemical composition of a foraminiferal test (Edgar et al., 2015). In a methane release environment, authigenic carbonate acquires substantial carbon from methane, which has a strongly ^{13}C-depleted signature (–110 ‰ to –50 ‰ for biogenic methane, and –50 ‰ to –30 ‰ for thermogenic methane), resulting in extremely low $\delta^{13}C$ values for MDAC (Whiticar, 1999; Chen et al., 2016b; Liang et al., 2017). MDAC precipitation can overprint the isotope signal of the pristine biogenic test, leading to bulk-test $\delta^{13}C$ values of –10 ‰ or lower (Torres et al., 2010). The authigenic carbonates of the study site precipitated in irregular clumps having extremely negative $\delta^{13}C$ (–37.3 ‰ to –51.7 ‰) and positive $\delta^{18}O$ values (+3.13 ‰ to +4.95 ‰), which is typical of MDAC (Zhao et al., 2018). We infer that methane release also caused secondary calcite precipitation on foraminiferal tests, leading to strongly negative $\delta^{13}C$ values (as low as –8.99‰) and weakly positive $\delta^{18}O$ values. Compared with the planktonic foraminiferal taxa, the $\delta^{18}O$ of the benthic taxon *U. peregrina* was less affected by MDAC precipitation, probably because the original oxygen isotopic composition of *U. peregrina* tests was similar to that of the secondary calcite.

Elemental compositions also provide evidence of diagenetic alteration due to methane release. Mg-rich carbonates having low $\delta^{13}C$ values are known to dominate in cold-seep settings (Schneider et al., 2017). In the vicinity of methane seeps, the Mg/Ca ratio of carbonate overgrowths on foraminiferal test walls can be as high as 220 mmol/mol, while the Mg/Ca ratio of the original test calcite is <10 mmol/mol (Panieri et al., 2017). As the degree of diagenetic alteration increases, Mg/Ca ratios rise and $\delta^{13}C$ declines, providing evidence of concurrent incorporation of Mg and ^{13}C-depleted carbon into secondary precipitates. This pattern is observed in the present study, in which Mg/Ca ratios are significantly negatively correlated with $\delta^{13}C$ ($R^2 = 0.32$, $p < 0.001$, $n = 51$) (Figure 6A).

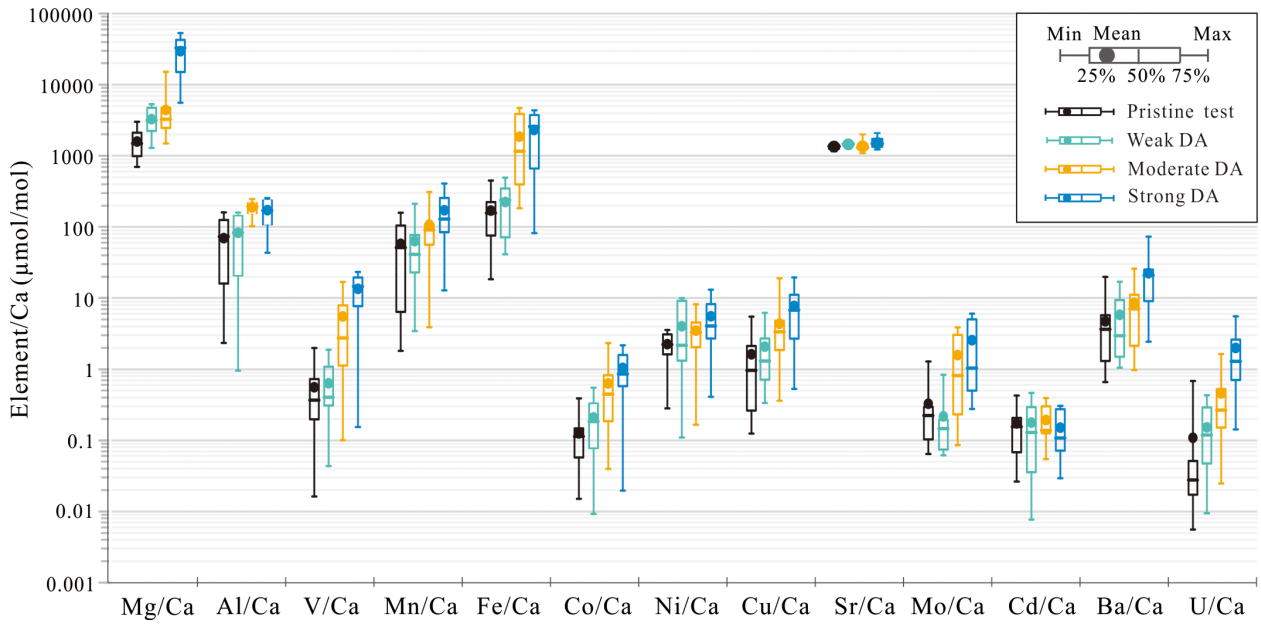

FIGURE 5
Boxplots of Element/Ca of foraminiferal specimens measured by LA-ICP-MS and tabulated according to degree of diagenetic alteration: pristine (black), weakly altered (green), moderately altered (orange), and strongly altered (blue).

Authigenic carbonate minerals precipitated in cold-seep systems include high-Mg calcite, aragonite, and dolomite (Greinert et al., 2013). The mineralogy of carbonate assemblages can be recognized by Sr/Ca versus Mg/Ca covariation patterns, as shown for Niger Delta sediments influenced by methane seepage (Figure 6B; Bayon et al., 2007). In the present study, pristine foraminiferal samples yield Sr/Ca and Mg/Ca ratios typical of biogenic calcite, whereas altered tests yield signals reflecting a mixture of biogenic calcite and high-Mg calcite (Figure 6B). With increasing diagenetic alteration, the average composition of the tests more closely approaches that of high-Mg calcite, indicating that it is the dominant secondary phase. Panieri et al. (2017) found that foraminiferal calcite and authigenic Mg-calcite crystals have identical lattice fringes, and, therefore, that foraminifera can serve as a nucleation template for authigenic Mg-calcite overgrowths.

The stratigraphic distribution of diagenetically altered foraminiferal tests at Site GMGS2-16 does not follow a regular pattern of increasing intensity with depth. Rather, there is a close association between intensely altered tests and authigenic carbonate nodules, which are present at 4.68, 10.83, 92.32, 140.18, 148.63, 149.67, 164.68, 192.46, and 205.8 mbsf (Figure 7). The percentage of altered foraminifera is obviously correlated with the content of carbonate nodules in these core samples (Zhao et al., 2018) ($y = 1.18x + 17.39$, $R^2 = 0.35$, $p = 0.04$, $n = 11$). The most likely explanation for this relationship is that formation of MDAC nodules and high-Mg calcite overgrowths on foraminifera was triggered by the same cause, i.e., a methane release event. However, diagenetically altered foraminifera are also present in intervals without authigenic carbonate nodules, such as at 50.47-69.68, 120.81-144.18, and 180.96-189.66 mbsf (Figure 7). We infer that this pattern is due to the high sensitivity of foraminiferal tests to methane, leading to secondary overgrowths at lower methane concentrations and/or during shorter periods of peak methane flow compared to MDAC precipitation.

Compared to the Sr/Ca of pristine foraminiferal tests (1.1-1.5 mmol/mol), the altered tests yield slightly higher values (1.1-2.1 mmol/mol), suggesting a limited increase in response to diagenetic alteration (Figure 6B). For primary carbonate phases, aragonite is typically enriched in Sr by a factor of 3-10× relative to calcite (Katz et al., 1972). In the methane release environment, aragonite is more inclined to precipitate near the sediment-water interface while calcite tends to form at greater depth, because the sulfate inhibition effect on calcite is stronger than on aragonite (Luff and Wallmann, 2003; Goetschl et al., 2019; Jin et al., 2021). Although cold seeps with high methane fluxes and, thus, shallow SMTZs are commonly characterized by aragonite precipitation (Burton, 1993; Bayon et al., 2007; Peckmann et al., 2009; Nöthen and Kasten, 2011), increases in both the Mg and Sr content of the study samples suggest precipitation of a secondary Mg-calcite phase that is enriched in Sr. During early diagenesis, aragonite can be replaced by more stable carbonate species, leading to Sr/Ca ratios above typical values for pristine calcite tests (Detlef et al., 2020). Sr enrichment may also be related to distortion of the calcite crystal lattice due to incorporation of Mg^{2+}, generating more space for relatively large Sr^{2+} cations (Mucci and Morse, 1983).

Cu was co-enriched with Mg, as shown by its positive correlation with Mg/Ca ($R^2 = 0.38$, $p < 0.001$, $n = 60$; Figure 8A). It is well known that Cu plays a central role in the metabolism of aerobic methane-oxidizing bacteria. When Cu is abundant, methanotrophic bacteria produce a membrane-bound Cu-containing enzyme (particulate methane mono-oxygenase) that catalyzes the oxidation of methane to methanol (Glass and

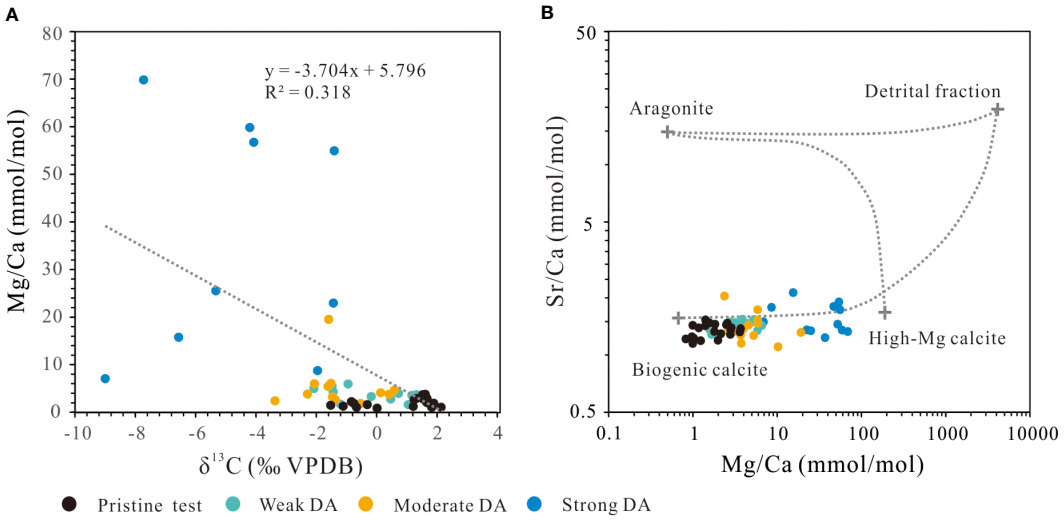

FIGURE 6
(A) Mg/Ca vs. $\delta^{13}C$ for various diagenetic alteration stages. **(B)** Sr/Ca vs. Mg/Ca for various diagenetic alteration stages. Endmember compositions of aragonite, high Mg-calcite, biogenic calcite, and the detrital fraction (black crosses), along with mixing trends (dashed curves) from Bayon et al. (2007).

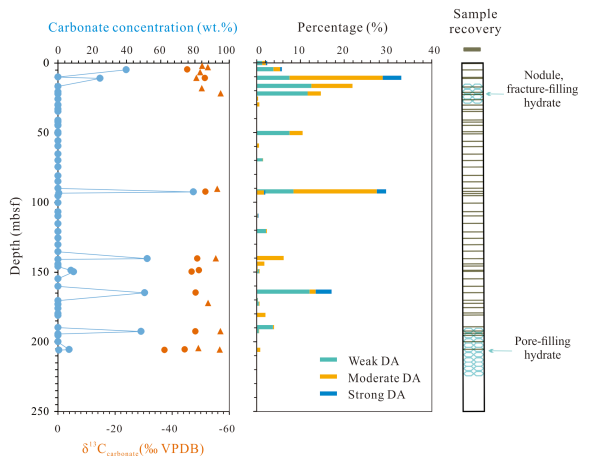

FIGURE 7
The distribution of foraminiferal tests by degree of diagenetic alteration (DA; this study), compared with the distribution and carbon isotope of carbonate nodules (Zhao et al., 2018) at Site GMGS2-16.

Orphan, 2012). Near the sediment-water interface, methane oxidation can be catalyzed by Cu-dependent aerobic methane-oxidizing bacteria, which may account for the high Cu contents of a few Sr-rich foraminiferal tests (e.g., the diagenetically altered test of *U. peregrina* from sample GMGS2-16B-1H-1a).

Foraminiferal Ba/Ca is positively correlated with Mg/Ca ratios (R^2 = 0.55, p < 0.001, n = 63) (Figure 8B). In the methane release environment, porewater Ba concentrations increase below the depth of sulfate depletion, and the consequent upward flux of dissolved Ba is almost quantitatively precipitated as authigenic barite at the SMTZ (Torres et al., 2002; Snyder et al., 2007). Carbonate samples from the Oregon Margin and foraminiferal samples from fossil methane seeps exposed from Oregon to Vancouver Island also show a trend of increasing Mg and Ba, consistent with barium incorporation into Mg-carbonates formed in methane-charged sediments (Torres et al., 2009; Torres et al., 2010).

Mn/Ca and Fe/Ca ratios also exhibit distinct increases from pristine to strongly altered tests. In the latter, Fe is the second most abundant cation with the Fe/Ca ratios of up to 4.6 mmol/mol, while Mn/Ca ratios are up to 0.49 mmol/mol. LA-ICP-MS results show a significant difference in the median values of Mn/Ca and Fe/Ca ratios in the moderate and strongly altered foraminifera compared with the pristine tests and positive correlations of Mn/Ca and Fe/Ca with Mg/Ca (R^2 = 0.31, p < 0.001, n = 63; R^2 = 0.25, p < 0.001, n = 63, respectively) (Figures 8D, E). However, the presence of Fe-Mn-oxides and pyrite in foraminiferal tests can bias LA-ICP-MS analyses of Mn/Ca and Fe/Ca. Since the cleaning process applied in this study may not completely eliminate detrital materials, Al/Ca and Mn/Ca were monitored to identify possible contamination from clays, silicate minerals, and Mn-Fe-oxide coatings (Lea, 2003). Specimens with values above 1 mmol/mol Mn/Ca or 0.25 mmol/mol Al/Ca (n.b., thresholds from Skinner et al., 2019) were removed from the dataset before statistical calculations to avoid potential effects linked to clay contamination. In the screened dataset, Al/Ca shows little correlation with Mg/Ca (R^2 = 0.08, p < 0.001, n = 63) (Figure 8C), supporting our inference of limited effects from detrital materials. On the other hand, if all foraminiferal Mn was derived from Mn-Fe-oxides, a Mn/Mg ratio close to that of global-ocean Mn-Fe-oxide crusts/nodules of 5 mol/mol would be expected (de

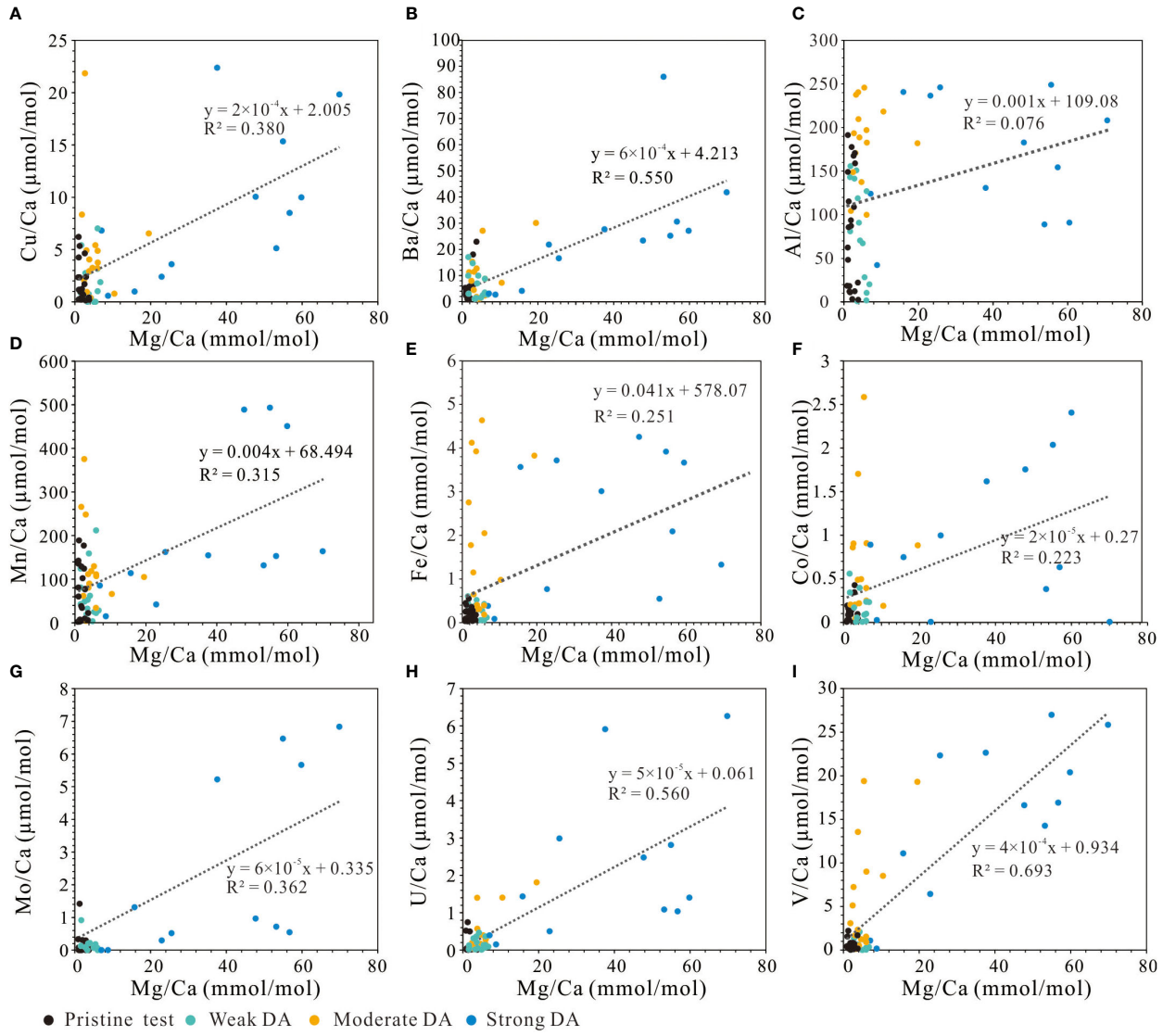

FIGURE 8
(A–I) Correlations of LA-ICP-MS foraminiferal elemental ratios. The samples are coded according to diagenetic alteration stage: pristine (black), weakly altered (green), moderately altered (orange), and strongly altered (blue).

Lange et al., 1992; Pattan, 1993). However, all of the study specimens have much lower Mn/Mg ratios (0.7-155 mmol/mol), suggesting that Mn-Fe-oxides are not an important contaminant phase.

SEM images of foraminifera from both above and below the SMTZ at Site GMGS2-16 demonstrate the presence of pyrite framboids within the foraminiferal tests, suggesting co-precipitation of authigenic carbonates and pyrite. The AOM reaction can lead to the production of pyrite (Lin et al., 2016). Authigenic pyrite framboids form in the spaces between calcite microcrystals of the overgrowths (Figures 2G1–2) and are not easily removed during cleaning processes, resulting in Fe contamination. Moreover, in the AOM process, anaerobic methanotrophic archaea (ANME) require large amounts of iron (Glass and Orphan, 2012), which can lead to further Fe enrichment of diagenetically altered foraminiferal tests.

The concentrations of trace elements such as Mo, U, V, Ni, Cd and Co are very sensitive to environmental conditions in siliciclastic depositional systems (Tribovillard et al., 2006; Guo et al., 2013; Wang et al., 2018). At Site GMGS2-16, significant differences in the medians of Mo/Ca, U/Ca, V/Ca, and Co/Ca are observed between moderately and strongly altered foraminifera (Figure 5). In addition, these Element/Ca ratios are significantly positively correlated with Mg/Ca (R^2 = 0.36, n = 50; R^2 = 0.56, n = 63; R^2 = 0.69, n = 62; R^2 = 0.22, n = 57, respectively; all $p < 0.001$) (Figures 8F–I). On the other hand, Ni/Ca and Cd/Ca show little relationship to the degree of diagenetic alteration, although this might be related to the lack of data for more than half of the samples in which the trace-element content is below the detection limit. The enrichment of these redox-sensitive elements in methane-derived carbonates compared to other types of marine carbonates has previously been ascribed to the ubiquitous presence of anoxic

conditions in the methane release environment (Tribovillard et al., 2006; Palomares et al., 2012; Sato et al., 2012; Hu et al., 2015; Chen et al., 2016b). Moreover, in addition to iron, other transition metals (Co, V, Mo) have been identified in proteins and enzymes involved in the metabolism of sulfate-reducing bacteria or methanogenic and methanotrophic archaea (Scheller et al., 2010; Glass and Orphan, 2012; Glass et al., 2014; Glass et al., 2018), which may account for the enrichment of these elements in the sediment.

5.2 Diagenetic processes and implications for paleo-methane release events

In this study, our results show that stable carbon and oxygen isotopes as well as elemental ratios (Mg/Ca, Sr/Ca, Ba/Ca, Mn/Ca, Fe/Ca, Mo/Ca, U/Ca, V/Ca, Ni/Ca, Co/Ca and Cu/Ca) measured in the foraminiferal tests are consistent with those of MDAC reported in earlier studies (see Section 5.1). Changes in geochemical compositions can provide valuable information, as they record fluid sources and biogeochemical processes during and after methane release.

Dissolved inorganic carbon (DIC) produced during AOM is typically characterized by highly ^{13}C-depleted carbon derived from methane (Haese et al., 2003; Yoshinaga et al., 2014), yielding extremely low δ^{13}C values. Variation in the elemental compositions of MDAC formed in various depositional environments is closely related to the dynamics of methane release (Feng et al., 2009).

Diagenetically altered foraminiferal tests from sample GMGS2-16B-1H-1a (0.23 mbsf), record extremely negative δ^{13}C values and enrichments in Mg/Ca, Sr/Ca, Ba/Ca, Mn/Ca, Fe/Ca, Mo/Ca, U/Ca, V/Ca, Ni/Ca, Co/Ca and Cu/Ca (Figure 9). This sample is located near the sediment-water interface, above the present SMTZ. In this sample, gypsum occurs on the exterior wall of foraminiferal test (Figure 2G3), indicating downward migration of the SMTZ, a process that caused anaerobic pyrite oxidation and gypsum formation at the previous (higher) level of the SMTZ. As mentioned above, aragonite precipitation is favored when the SMTZ is located at shallower depths, in response to a methane release event having high flow rates (Peckmann et al., 2001; Moore et al., 2004; Gieskes et al., 2005; Nöthen and Kasten, 2011; Hu et al., 2015; Jin et al., 2021). Overgrowth of Sr-enriched Mg-calcite possibly reflects recrystallization of primary aragonitic phases. Near the sediment-water interface, methane oxidation can be catalyzed by Cu-dependent aerobic methane-oxidizing bacteria, resulting in a concomitant increase in the contents of both Sr and Cu (Glass and Orphan, 2012). The foraminifera from sample GMGS2-16D-8H-1 (92.32 mbsf) have similar geochemical compositions (Figure 9) and contain gypsum (Figure 2G4), which may be evidence of another methane release event from near the sediment-water interface. Samples GMGS2-16D-2H-1 (10.83 mbsf), GMGS2-16F-6H-1 (50.47 mbsf) and GMGS2-16H-4H-1b (164.68 mbsf) show similar extremely negative δ^{13}C values and enrichments in Mg/Ca, Ba/Ca, Mn/Ca, Fe/Ca, Mo/Ca, U/Ca, V/Ca, Ni/Ca and Co/Ca, suggesting that a high-Mg calcite contaminant formed in the deeper SMTZ in association with low rates of methane-bearing fluid flow (Luff and Wallmann, 2003; Feng et al., 2009).

We infer that Mg enrichment of diagenetically altered foraminifera coupled with increases in Sr/Ca, Ba/Ca, Mn/Ca, Fe/Ca, Mo/Ca, U/Ca, V/Ca, Ni/Ca, Co/Ca and Cu/Ca ratios are potentially reliable indicators of paleo-methane release events. Furthermore, the main differences in elemental compositions of authigenic carbonate formed near the seafloor versus in deeper anoxic porewaters are higher concentrations of Cu and Sr in the former. For this reason, enrichments of Cu/Ca and Sr/Ca in diagenetically altered foraminiferal tests may be used to recognize intense upward methane fluxes within the sediment column.

Determining the timing of methane release events using stratigraphic data is difficult because the SMTZ can migrate vertically through the sediment column, leading to precipitation of MDAC overgrowths on foraminiferal tests at times younger than their stratigraphic ages. When a high methane flux produces a shallow SMTZ, the formation of secondary overgrowths can be considered quasi-synsedimentary, but otherwise the stratigraphic age of MDAC represents a maximum formation age. At the study site, stratigraphic ages were calculated by linear interpolation from the age framework established by Chen et al., 2016a. The two documented methane release events at 0.23 mbsf and 92.32 mbsf thus have maximum ages of ~0.47 ka and ~170 ka, respectively.

Based on the observations and analyses of foraminifera from Site GMGS2-16, a potential mechanism for diagenetic alteration of buried foraminiferal tests linked to the gas hydrate geosystem is proposed (Figure 10). When gas hydrates are in a stable state, there is no unusual methane emission, and the geochemical compositions of foraminifera record the original (i.e., unaltered) signal of normal marine conditions (Figure 10A; sample GMGS2-16F-2P-CC and GMGS2-16F-5H-2). During a high methane flux event, methane is transported further towards the sediment-water interface, shifting the SMTZ upward and compressing it into the uppermost sediment column (Figure 10B; sample GMGS2-16B-1H-1a and GMGS2-16D-8H-1). The authigenic carbonates (mainly Sr-enriched Mg-calcite) with extremely negative δ^{13}C values and enrichments in Mg/Ca, Sr/Ca, Ba/Ca, Mn/Ca, Fe/Ca, Mo/Ca, U/Ca, V/Ca, Ni/Ca, Co/Ca and Cu/Ca, are co-precipitated with pyrite in the SMTZ near the seafloor. When the methane flux is subsequently reduced, the SMTZ migrates back downward to a greater depth in the sediment column (e.g., similar to the depth of the current SMTZ at the study site). In this scenario, authigenic pyrites and carbonates (mainly high-Mg calcite) formed in anoxic porewaters are characterized by extremely negative δ^{13}C values and enrichments in Mg/Ca, Ba/Ca, Mn/Ca, Fe/Ca, Mo/Ca, U/Ca, V/Ca, Ni/Ca and Co/Ca. In the upper part of the sediment column, carbonate and pyrite precipitated before the downward shift of the SMTZ are converted to authigenic gypsum through anaerobic pyrite oxidation (Figure 10C; samples GMGS2-16D-2H-1, GMGS2-16F-6H-1, and GMGS2-16H-4H-1b).

6 Conclusions

In this study, we used a suite of petrographic and geochemical analyses (including reflected light microscopy, SEM imaging,

10.3389/fmars.2023.1166305

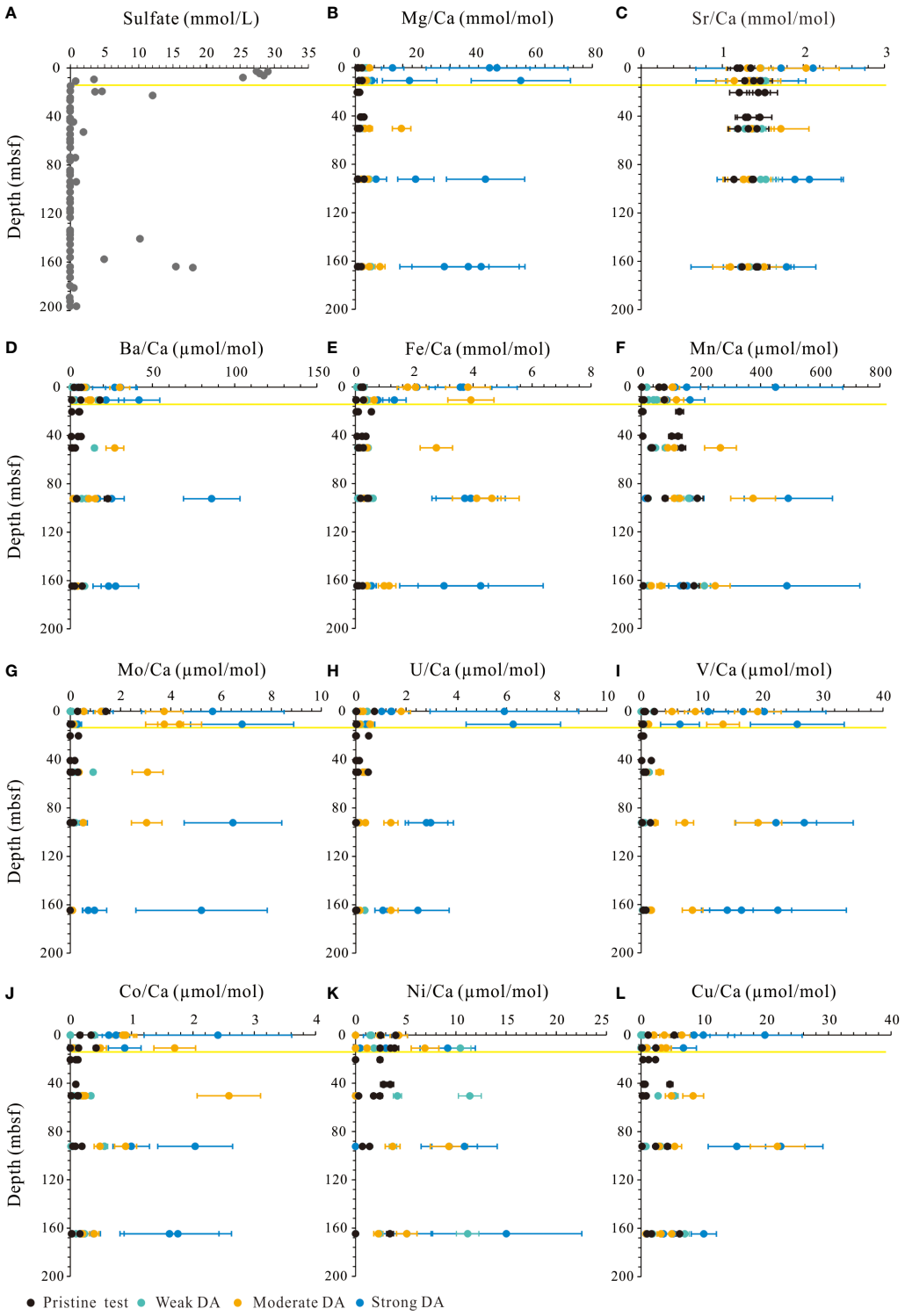

FIGURE 9
Sulfate **(A)** (Kuang et al., 2018) and elemental-ratio **(B–L)** profiles for Site GMGS2-16. The samples are coded according to diagenetic alteration stage: pristine (black), weakly altered (green), moderately altered (orange), and strongly altered (blue). Error bars represent one standard deviation. The yellow lines show the depth of the current sulfate-methane interface (SMI; i.e., where porewater sulfate declines to zero).

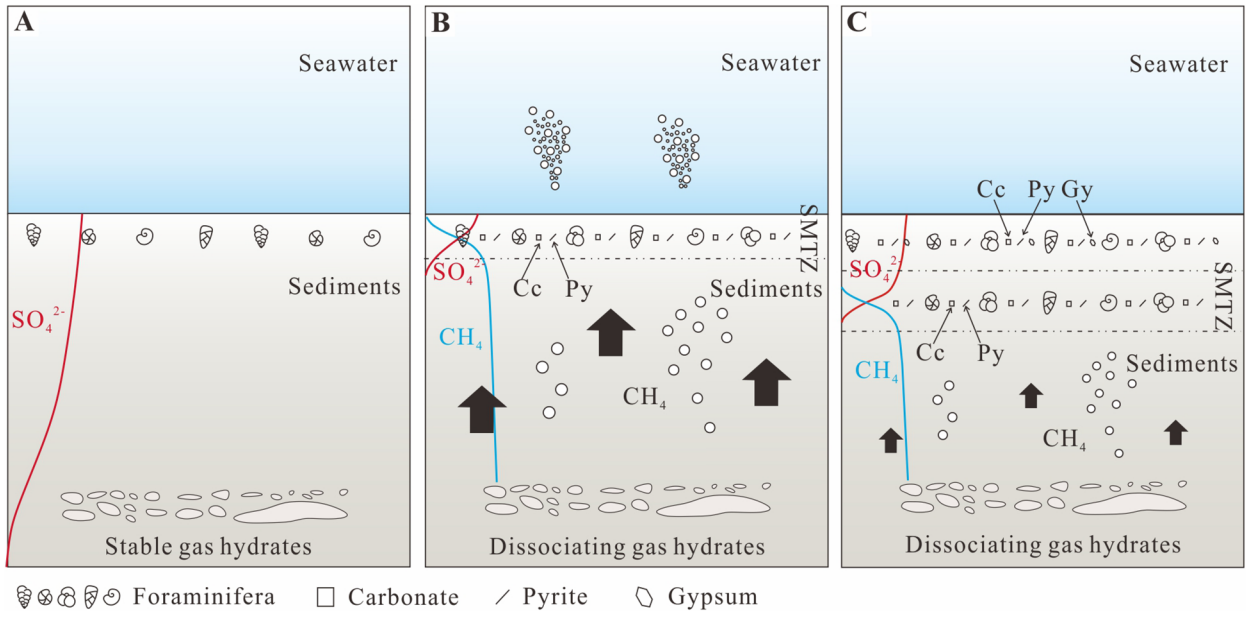

FIGURE 10
Schematic of post-depositional alteration of buried foraminiferal tests in a gas hydrate geosystem (modified from Kennett et al., 2000). **(A)** Gas hydrates are in a stable state, and the geochemical compositions of foraminifera record the original signal of the normal marine conditions. **(B)** During a high methane flux event, methane is transported further toward the sediment-water interface, shifting the SMTZ upward and compressing it into the uppermost sediment column. Authigenic carbonates are co-precipitated with pyrite in the SMTZ near the seafloor, causing foraminiferal shells buried in this interval to be coated with MDAC, along with some framboidal pyrite interspersed between carbonate crystals. **(C)** Subsequent reduction of the methane flux causes the SMTZ to migrate back downward within the sediment column. Authigenic pyrite and carbonate form in the active SMTZ, whereas pyrite precipitated in the upper part of the sediment column before the downward SMTZ shift are converted to authigenic gypsum through anaerobic pyrite oxidation, which also leaves traces on foraminiferal shells. Cc, carbonate; Py, pyrite; Gy, gypsum.

oxygen and carbon isotopic measurements, LA-ICP-MS, and EPMA elemental mapping) to study foraminiferal tests from gas hydrate-bearing sediments of the northern South China Sea that exhibit varying degrees of diagenetic alteration. Our goals were to make inferences on the post-burial alteration processes affecting foraminiferal calcite caused by methane release. Our results are consistent with diagenetically altered foraminiferal tests acting as a template for MDAC precipitation. The $\delta^{13}C$ values and Mg/Ca ratios of tests are susceptible to diagenetic alteration. There is a negative correlation between $\delta^{13}C$ values and the degree of diagenetic alteration, but a positive correlation with Mg/Ca ratios. This may be related to the relative contribution of Mg-calcite, which has a strongly negative $\delta^{13}C$ value, to bulk foraminiferal carbonate. The elemental content of diagenetically altered foraminifera can be used to reconstruct methane release history. We infer that enrichments in Mg along with increased Ba/Ca, Mn/Ca, Fe/Ca, Mo/Ca, U/Ca, V/Ca, Ni/Ca and Co/Ca ratios are potentially reliable indicators of paleo-methane release events. Furthermore, enrichments of Cu/Ca and Sr/Ca may be used to recognize episodes of intense methane flux. Reconstruction of the methane release history of Site GMGS2-16 reveals that diagenetically altered foraminifera record frequent fluctuations of the SMTZ, indicating a variable methane flux intensity. Notably, the methane release events have maximum ages of ~0.47 ka and ~170 ka.

Data availability statement

The original contributions presented in the study are included in the article/Supplementary Material. Further inquiries can be directed to the corresponding author.

Author contributions

YC and JW designed the study. YC and JW collected the samples. YC, ZW, XM, and CC have carried out the laboratory work and analyzed the data. YC, JW, and TA wrote the manuscript. All authors contributed to the article and approved the submitted version.

Funding

This research was supported by the National Natural Science Foundation of China (No. 42276068), China National Gas Hydrate Project (Grant No. DD20160211) and State Key Laboratory of Marine Geology, Tongji University (No. MGK202206).

Acknowledgments

We would like to acknowledge the crew and scientists of the GMGS2 expedition for their supports in sediment samples and analyses. We are grateful to Profs. Huiming Bao and Yongbo Peng for technical support in stable isotope analysis and Hongfang Chen for support in the LA-ICP-MS and EPMA analysis. We acknowledge the editors and reviewers for their constructive reviews.

Conflict of interest

The authors declare that the research was conducted in the absence of any commercial or financial relationships that could be construed as a potential conflict of interest.

Publisher's note

Supplementary material

The Supplementary Material for this article can be found online at: https://www.frontiersin.org/articles/10.3389/fmars.2023.1166305/full#supplementary-material

References

Bayon, G., Lemaitre, N., Barrat, J.-A., Wang, X., Feng, D., and Duperron, S. (2020). Microbial utilization of rare earth elements at cold seeps related to aerobic methane oxidation. *Chem. Geology* 555, 119832. doi: 10.1016/j.chemgeo.2020.119832

Bayon, G., Pierre, C., Etoubleau, J., Voisset, M., Cauquil, E., Marsset, T., et al. (2007). Sr/Ca and Mg/Ca ratios in Niger delta sediments: Implications for authigenic carbonate genesis in cold seep environments. *Mar. Geology* 241, 93–109. doi: 10.1016/j.margeo.2007.03.007

Borrelli, C., Gabitov, R. I., Liu, M.-C., Hertwig, A. T., and Panieri, G. (2020). The benthic foraminiferal $\delta^{34}S$ records flux and timing of paleo methane emissions. *Sci. Rep.* 10, 1304. doi: 10.1038/s41598-020-58353-4

Burton, E. A. (1993). Controls on marine carbonate cement mineralogy: review and reassessment. *Chem. Geology* 105, 163–179. doi: 10.1016/0009-2541(93)90124-2

Cen, Y., Wang, J., Ding, X., Stow, D., Wang, Z., Chen, C., et al. (2022). Tracing the methane events by stable carbon isotopes of benthic foraminifera at glacial periods in the Andaman Sea. *J. Earth Sci.* 33 (6), 1571–1582. doi: 10.1007/s12583-022-1750-x

Chen, F., Hu, Y., Feng, D., Zhang, X., Cheng, S., Cao, J., et al. (2016b). Evidence of intense methane seepages from molybdenum enrichments in gas hydrate-bearing sediments of the northern south China Sea. *Chem. Geology* 443, 173–181. doi: 10.1016/j.chemgeo.2016.09.029

Chen, L., Liu, Y. S., Hu, Z. C., Gao, S., Zong, K. Q., and Chen, H. (2011). Accurate determinations of fifty-four major and trace elements in carbonate by LA-ICP-MS using normalization strategy of bulk components as 100%. *Chem. Geology* 284, 283–295. doi: 10.1016/j.chemgeo.2011.03.007

Chen, F., Zhuang, C., Zhou, Y., Su, X., Duan, J., Liu, G. H., et al. (2016a). Calcareous nannofossils and foraminifera biostratigraphy on the northeastern slope of the south China Sea and variation in sedimentation rates. *Earth Sci.* 41 (3), 416–424. doi: 10.3799/dqkx.2016.033

Crémière, A., Lepland, A., Chand, S., Sahy, D., Condon, D. J., Noble, S. R., et al. (2016). Timescales of methane seepage on the Norwegian margin following collapse of the Scandinavian ice sheet. *Nat. Commun.* 7, 11509. doi: 10.1038/ncomms11509

de Lange, G. J., van Os, B., and Poorter, R. (1992). Geochemical composition and inferred accretion rates of sediments and managanese nodules from a submarine hill in the Madeira abyssal plain, eastern north Atlantic. *Mar. Geology* 109, 171–194. doi: 10.1016/0025-3227(92)90227-9

Detlef, H., Sosdian, S. M., Kender, S., Lear, C. H., and Hall, I. R. (2020). Multi-elemental composition of authigenic carbonates in benthic foraminifera from the eastern Bering Sea continental margin (International ocean discovery program site U1343). *Geochimica Cosmochimica Acta* 268, 1–21. doi: 10.1016/j.gca.2019.09.025

Dickens, G. R., Castillo, M. M., and Walker, J. C. G. (1997). A blast of gas in the latest Paleocene: Simulating first-order effects of massive dissociation of oceanic methane hydrate. *Geology* 25, 259–262. doi: 10.1130/0091-7613(1997)025<0259:ABOGIT>2.3.CO;2

Edgar, K. M., Anagnostou, E., Pearson, P. N., and Foster, G. L. (2015). Assessing the impact of diagenesis on $\delta^{11}B$, $\delta^{13}C$, $\delta^{18}O$, Sr/Ca and B/Ca values in fossil planktic foraminiferal calcite. *Geochimica Cosmochimica Acta* 166, 189–209. doi: 10.1016/j.gca.2015.06.018

Feng, D., Chen, D., and Roberts, H. H. (2009). Petrographic and geochemical characterization of seep carbonate from bush hill (GC 185) gas vent and hydrate site of the gulf of Mexico. *Mar. Petroleum Geology* 26, 1190–1198. doi: 10.1016/j.marpetgeo.2008.07.001

Feng, J.-C., Wang, Y., Li, X.-S., Li, G., Zhang, Y., and Chen, Z.-Y. (2015). Production performance of gas hydrate accumulation at the GMGS2-site 16 of the pearl river mouth basin in the south China Sea. *J. Natural Gas Sci. Eng.* 27, 306–320. doi: 10.1016/j.jngse.2015.08.071

Fontanier, C., Dissard, D., Ruffine, L., Mamo, B., Ponzevera, E., Pelleter, E., et al. (2018). Living (stained) deep-sea foraminifera from the Sea of marmara: A preliminary study. *Deep Sea Res. Part II: Topical Stud. Oceanography* 153, 61–78. doi: 10.1016/j.dsr2.2017.12.011

Friedrich, O., Schiebel, R., Wilson, P. A., Weldeab, S., Beer, C. J., Cooper, M. J., et al. (2012). Influence of test size, water depth, and ecology on Mg/Ca, Sr/Ca, $\delta^{18}O$ and $\delta^{13}C$ in nine modern species of planktic foraminifers. *Earth Planetary Sci. Lett.* 319–320, 133–145. doi: 10.1016/j.epsl.2011.12.002

Gieskes, J., Mahn, C., Day, S., Martin, J. B., Greinert, J., Rathburn, T., et al. (2005). A study of the chemistry of pore fluids and authigenic carbonates in methane seep environments: Kodiak trench, hydrate ridge, Monterey bay, and eel river basin. *Chem. Geology* 220, 329–345. doi: 10.1016/j.chemgeo.2005.04.002

Glass, J. B., Chen, S., Dawson, K. S., Horton, D. R., Vogt, S., Ingall, E. D., et al. (2018). Trace metal imaging of sulfate-reducing bacteria and methanogenic archaea at single-cell resolution by synchrotron X-ray fluorescence imaging. *Geomicrobiology J.* 35, 81–89. doi: 10.1101/087585

Glass, J. B., and Orphan, V. J. (2012). Trace metal requirements for microbial enzymes involved in the production and consumption of methane and nitrous oxide. *Front. Microbiol.* 3. doi: 10.3389/fmicb.2012.00061

Glass, J. B., Yu, H., Steele, J. A., Dawson, K. S., Sun, S., Chourey, K., et al. (2014). Geochemical, metagenomic and metaproteomic insights into trace metal utilization by methane-oxidizing microbial consortia in sulphidic marine sediments. *Environ. Microbiol.* 16, 1592–1611. doi: 10.1111/1462-2920.12314

Goetschl, K. E., Purgstaller, B., Dietzel, M., and Mavromatis, V. (2019). Effect of sulfate on magnesium incorporation in low-magnesium calcite. *Geochimica Cosmochimica Acta* 265, 505–519. doi: 10.1016/j.gca.2019.07.024

Gong, J., Sun, X., Xu, L., and Lu, H. (2017). Contribution of thermogenic organic matter to the formation of biogenic gas hydrate: Evidence from geochemical and microbial characteristics of hydrate-containing sediments in the taixinan basin, south China Sea. *Mar. Petroleum Geology* 80, 432–449. doi: 10.1016/j.marpetgeo.2016.12.019

Greinert, J., Bohrmann, G., and Suess, E. (2013). "Gas hydrate-associated carbonates and methane-venting at hydrate ridge: Classification, distribution, and origin of authigenic lithologies," in *Natural gas hydrates: Occurrence, distribution, and detection*, vol. 124 . Eds. C. K. Paull and W. P. Dillon (Washington, DC: American Geophysical Union), 99–113.

Guo, H., Du, Y., Lian, Z., Yang, J., Huang, H., Liu, M., et al. (2013). Trace and rare earth elemental geochemistry of carbonate succession in the middle gaoyuzhuang formation, pingquan section: Implications for early mesoproterozoic ocean redox conditions. *J. Palaeogeogr.* 2 (2), 209–221. doi: 10.3724/SP.J.1261.2013.00027

Haese, R. R., Meile, C., Van Cappellen, P., and De Lange, G. J. (2003). Carbon geochemistry of cold seeps: Methane fluxes and transformation in sediments from kazan mud volcano, eastern Mediterranean Sea. *Earth Planetary Sci. Lett.* 212, 361–375. doi: 10.1016/S0012-821X(03)00226-7

Hill, T. M., Kennett, J. P., and Valentine, D. L. (2004). Isotopic evidence for the incorporation of methane-derived carbon into foraminifera from modern methane seeps, hydrate ridge, northeast pacific. *Geochimica Cosmochimica Acta* 68, 4619–4627. doi: 10.1016/j.gca.2004.07.012

Hu, Y., Feng, D., Liang, Q., Xia, Z., Chen, L., and Chen, D. (2015). Impact of anaerobic oxidation of methane on the geochemical cycle of redox-sensitive elements at

cold-seep sites of the northern south China Sea. *Deep Sea Res. Part II: Topical Stud. Oceanography* 122, 84–94. doi: 10.1016/j.dsr2.2015.06.012

Jørgensen, B. B. (2021). Sulfur biogeochemical cycle of marine sediments. *Geochemical Perspect.* 10 (2), 145–307. doi: 10.7185/geochempersp.10.2

Jin, M., Feng, D., Huang, K., Peckmann, J., Li, N., Huang, H., et al. (2021). Behavior of mg isotopes during precipitation of methane-derived carbonate: Evidence from tubular seep carbonates from the south China Sea. *Chem. Geology* 567, 120101. doi: 10.1016/j.chemgeo.2021.120101

Katz, A., Sass, E., Starinsky, A., and Holland, H. D. (1972). Strontium behavior in the aragonite-calcite transformation: An experimental study at 40–98 c. *Geochimica Cosmochimica Acta* 36 (4), 481–496. doi: 10.1016/0016-7037(72)90037-3

Kennett, J. P., Cannariato, K. G., Hendy, I. L., and Behl, R. J. (2000). Carbon isotopic evidence for methane hydrate instability during quaternary interstadials. *Science* 288, 128–133. doi: 10.1126/science.288.5463.128

Kuang, Z., Fang, Y., Liang, J., and Wang, L. (2018). Geomorphological-geological-geophysical signatures of high-flux fluid flows in the eastern pearl river mouth basin and effects on gas hydrate accumulation. *Sci. China Earth Sci.* 61, 914–924. doi: 10.1007/s11430-017-9183-y

Lea, D. W. (2003). "Trace elements in foraminiferal calcite," in *Modern foraminifera*. Ed. B. K. S. Gupta (Dordrecht: Kluwer Academic Publishers), 259–277.

Liang, Q., Hu, Y., Feng, D., Peckmann, J., Chen, L., Yang, S., et al. (2017). Authigenic carbonates from newly discovered active cold seeps on the northwestern slope of the south China Sea: Constraints on fluid sources, formation environments, and seepage dynamics. *Deep Sea Res. Part I: Oceanographic Res. Papers* 124, 31–41. doi: 10.1016/j.dsr.2017.04.015

Lin, Z., Sun, X., Strauss, H., Lu, Y., Böttcher, M. E., Teichert, B. M. A., et al. (2018). Multiple sulfur isotopic evidence for the origin of elemental sulfur in an iron-dominated gas hydrate-bearing sedimentary environment. *Mar. Geology* 403, 271–284. doi: 10.1016/j.margeo.2018.06.010

Lin, Q., Wang, J., Algeo, T. J., Su, P., and Hu, G. (2016). Formation mechanism of authigenic gypsum in marine methane hydrate settings: Evidence from the northern south China Sea. *Deep Sea Res. Part I: Oceanographic Res. Papers* 115, 210–220. doi: 10.1016/j.dsr.2016.06.010

Liu, Y., Hu, Z., Gao, S., Günther, D., Xu, J., Gao, C., et al. (2008). *In situ* analysis of major and trace elements of anhydrous minerals by LA-ICP-MS without applying an internal standard. *Chem. Geology* 257, 34–43. doi: 10.1016/j.chemgeo.2008.08.004

Liu, Y., Wei, J., Li, Y., Chang, J., Miao, X., and Lu, H. (2022). Seep dynamics as revealed by authigenic carbonates from the eastern qiongdongnan basin, south China Sea. *Mar. Petroleum Geology* 142, 105736. doi: 10.1016/j.marpetgeo.2022.105736

Luff, R., and Wallmann, K. (2003). Fluid flow, methane fluxes, carbonate precipitation and biogeochemical turnover in gas hydrate-bearing sediments at hydrate ridge, cascadia margin: numerical modeling and mass balances. *Geochimica Cosmochimica Acta* 67, 3403–3421. doi: 10.1016/s0016-7037(03)00127-3

Martin, R. A., Nesbitt, E. A., and Campbell, K. A. (2007). Carbon stable isotopic composition of benthic foraminifera from pliocene cold methane seeps, cascadia accretionary margin. *Palaeogeography Palaeoclimatology Palaeoecol.* 246, 260–277. doi: 10.1016/j.palaeo.2006.10.002

Miao, X., Feng, X., Li, J., and Lin, L. (2021). Tracing the paleo-methane seepage activity over the past 20,000 years in the sediments of qiongdongnan basin, northwestern south China Sea. *Chem. Geology* 559, 119956. doi: 10.1016/j.chemgeo.2020.119956

Millo, C., Sarnthein, M., Erlenkeuser, H., and Frederichs, T. (2005a). Methane-driven late pleistocene $\delta^{13}C$ minima and overflow reversals in the southwestern Greenland Sea. *Geology* 33, 873. doi: 10.1130/G21790.1

Millo, C., Sarnthein, M., Erlenkeuser, H., Grootes, P. M., and Andersen, N. (2005b). Methane-induced early diagenesis of foraminiferal tests in the southwestern Greenland Sea. *Mar. Micropaleontology* 58, 1–12. doi: 10.1016/j.marmicro.2005.07.003

Moore, T. S., Murray, R. W., Kurtz, A. C., and Schrag, D. P. (2004). Anaerobic methane oxidation and the formation of dolomite. *Earth Planetary Sci. Lett.* 229, 141–154. doi: 10.1016/j.epsl.2004.10.015

Morley, C. K. (2012). Late Cretaceous–early palaeogene tectonic development of SE Asia. *Earth-Science Rev.* 115, 37–75. doi: 10.1016/j.earscirev.2012.08.002

Mucci, A., and Morse, J. W. (1983). The incorporation of Mg^{2+} and Sr^{2+} into calcite overgrowths: influences of growth rate and solution composition. *Mar. Geology* 47, 217–233. doi: 10.1016/0016-7037(83)90135-7

Nöthen, K., and Kasten, S. (2011). Reconstructing changes in seep activity by means of pore water and solid phase Sr/Ca and Mg/Ca ratios in pockmark sediments of the northern Congo fan. *Mar. Geology* 287, 1–13. doi: 10.1016/j.margeo.2011.06.008

Palomares, R. M., Hernández, R. L., and Frías, J. M. (2012). Mechanisms of trace metal enrichment in submarine, methane-derived carbonate chimneys from the gulf of cadiz. *J. Geochemical Explor.* 112, 297–305. doi: 10.1111/1462-2920.12314

Panieri, G., James, R. H., Camerlenghi, A., Westbrook, G. K., Consolaro, C., Cacho, I., et al. (2014). Record of methane emissions from the West Svalbard continental margin during the last 23.500yrs revealed by $\delta^{13}C$ of benthic foraminifera. *Global Planetary Change* 122, 151–160. doi: 10.1016/j.gloplacha.2014.08.014

Panieri, G., Lepland, A., Whitehouse, M. J., Wirth, R., Raanes, M. P., James, R. H., et al. (2017). Diagenetic mg-calcite overgrowths on foraminiferal tests in the vicinity of methane seeps. *Earth Planetary Sci. Lett.* 458, 203–212. doi: 10.1016/j.gloplacha.2014.08.014

Pattan, J. N. (1993). Manganese micronodules: a possible indicator of sedimentary environments. *Mar. Geology* 113, 331–344. doi: 10.1016/0025-3227(93)90026-R

Peckmann, J., Birgel, D., and Kiel, S. (2009). Molecular fossils reveal fluid composition and flow intensity at a Cretaceous seep. *Geology* 37, 847–850. doi: 10.1130/G25658A.1

Peckmann, J., Reimer, A., Luth, U., Luth, C., Hansen, B. T., Heinicke, C., et al. (2001). Methane-derived carbonates and authigenic pyrite from the northwestern black Sea. *Mar. Geology* 177, 129–150. doi: 10.1016/S0025-3227(01)00128-1

Peckmann, J., and Thiel, V. (2004). Carbon cycling at ancient methane–seeps. *Chem. Geology* 205, 443–467. doi: 10.1016/j.chemgeo.2003.12.025

Rathmann, S., Hess, S., Kuhnert, H., and Mulitza, S. (2004). Mg/Ca ratios of the benthic foraminifera *Oridorsalis umbonatus* obtained by laser ablation from core top sediments: Relationship to bottom water temperature. *Geochemistry Geophysics Geosystems* 5, Q12013. doi: 10.1029/2004GC000808

Retallack, G. J., Seyodolali, A., Krull, E. S., Holser, W., Ambers, C. P., and Kyte, F. T. (1998). Search for evidence of impact at the permian-Triassic boundary in Antarctica and Australia. *Geology* 26, 979–982. doi: 10.1130/0091-7613(1998)0262.3.CO;2

Sato, H., Hayashi, K. I., Ogawa, Y., and Kawamura, K. (2012). Geochemistry of deep sea sediments at cold seep sites in the nankai trough: insights into the effect of anaerobic oxidation of methane. *Mar. Geology* 323–325, 47–55. doi: 10.1016/j.margeo.2012.07.013

Scheller, S., Goenrich, M., Boecher, R., Thauer, R. K., and Jaun, B. (2010). The key nickel enzyme of methanogenesis catalyses the anaerobic oxidation of methane. *Nature* 465, 606–608. doi: 10.1038/nature09015

Schier, K., Himmler, T., Lepland, A., Kraemer, D., Schönenberger, J., and Bau, M. (2021). Insights into the REY inventory of seep carbonates from the northern Norwegian margin using geochemical screening. *Chem. Geology* 559, 119857. doi: 10.1016/j.chemgeo.2020.119857

Schlanger, S. O., and Douglas, R. G. (1974). "The pelagic ooze-chalk-limestone transition and its implication for marine stratigraphy," in *Pelagic sediments: on land and under the Sea*. Eds. K. J. Hsü and H. C. Jenkyns (London: Blackwell Scientific Publications), 117–148.

Schneider, A. (2018). Diagenetically altered benthic foraminifera reveal paleo-methane seepage, department of geoscience (Norway: The Arctic University of Norway).

Schneider, A., Crémière, A., Panieri, G., Lepland, A., and Knies, J. (2017). Diagenetic alteration of benthic foraminifera from a methane seep site on vestnesa ridge (NW Svalbard). *Deep Sea Res. Part I: Oceanographic Res. Papers* 123, 22–34. doi: 10.1016/j.dsr.2017.03.001

Skinner, L. C., Sadekov, A., Brandon, M., Greaves, M., Plancherel, Y., de la Fuente, M., et al. (2019). Rare earth elements in early-diagenetic foraminifer 'coatings': Pore-water controls and potential palaeoceanographic applications. *Geochimica Cosmochimica Acta* 245, 118–132. doi: 10.1016/j.gca.2018.10.027

Snyder, G. T., Dickens, G. R., and Castellini, D. G. (2007). Labile barite contents and dissolved barium concentrations on Blake ridge: New perspectives on barium cycling above gas hydrate systems. *J. Geochemical Explor.* 95, 48–65. doi: 10.1016/j.gexplo.2007.06.001

Sztybor, K., and Rasmussen, T. L. (2017). Diagenetic disturbances of marine sedimentary records from methane-influenced environments in the fram strait as indications of variation in seep intensity during the last 35 000 years. *Boreas* 46, 212–228. doi: 10.1111/bor.12202

Taylor, B., and Hayes, D. E. (1980). "The tectonic evolution of the south China basin," in *The tectonic and geologic evolution of southeast Asian seas and islands*, vol. 23. Ed. D. E. Hayes (Washington, DC: American Geophysical Union), 89–104.

Them, T. R., Gill, B. C., Caruthers, A. H., Gerhardt, A. M., Gröcke, D. R., Lyons, T. W., et al. (2018). Thallium isotopes reveal protracted anoxia during the toarcian (early Jurassic) associated with volcanism, carbon burial, and mass extinction. *Proc. Natl. Acad. Sci. (U.S.A.)* 115 (26), 6596–6601. doi: 10.1073/pnas.1803478115

Torres, M. E., Embley, R. W., Merle, S. G., Trehu, A. M., Collier, R. W., Suess, E., et al. (2009). Methane sources feeding cold seeps on the shelf and upper continental slope off central Oregon, USA. *Geochemistry Geophysics Geosystems* 10, Q11003. doi: 10.1029/2009GC002518

Torres, M. E., Martin, R. A., Klinkhammer, G. P., and Nesbitt, E. A. (2010). Post depositional alteration of foraminiferal shells in cold seep settings: New insights from flow-through time-resolved analyses of biogenic and inorganic seep carbonates. *Earth Planetary Sci. Lett.* 299, 10–22. doi: 10.1016/j.epsl.2010.07.048

Torres, M. E., McManus, J., and Huh, C. A. (2002). Fluid seepage along the San clemente fault scarp: basin-wide impact on barium cycling. *Earth Planetary Sci. Lett.* 203, 181–194. doi: 10.1016/S0012-821X(02)00800-2

Tribovillard, N., Algeo, T. J., Lyons, T., and Riboulleau, A. (2006). Trace metals as paleoredox and paleoproductivity proxies: an update. *Chem. Geology* 232, 12–32. doi: 10.1016/j.chemgeo.2006.02.012

Wan, S., Feng, D., Chen, F., Zhuang, C., and Chen, D. (2018). Foraminifera from gas hydrate-bearing sediments of the northeastern south China Sea: Proxy evaluation and application for methane release activity. *J. Asian Earth Sci.* 168, 125–136. doi: 10.1016/j.jseaes.2018.04.036

Wang, Z., Wang, J., Fu, X., Zhan, W., Armstrong-Altrin, J. S., Yu, F., et al. (2018). Geochemistry of the upper Triassic black mudstones in the qiangtang basin, Tibet: Implications for paleoenvironment, provenance, and tectonic setting. *J. Asian Earth Sci.* 76, 346–361. doi: 10.1016/j.jseaes.2018.04.022

Whiticar, M. J. (1999). Carbon and hydrogen isotope systematics of bacterial formation and oxidation of methane. *Chem. Geology* 161, 291–314. doi: 10.1016/S0009-2541(99)00092-3

Yoshinaga, M. Y., Holler, T., Goldhammer, T., Wegener, G., Pohlman, J. W., Brunner, B., et al. (2014). Carbon isotope equilibration during sulphate-limited anaerobic oxidation of methane. *Nat. Geosci.* 7, 190–194. doi: 10.1038/NGEO2069

Zhang, G., Liang, J., Lu, J. A., Yang, S., Zhang, M., Holland, M., et al. (2015). Geological features, controlling factors and potential prospects of the gas hydrate occurrence in the east part of the pearl river mouth basin, south China Sea. *Mar. Petroleum Geology* 67, 356–367. doi: 10.1016/j.marpetgeo.2015.05.021

Zhao, J., Wang, J., Cen, Y., Su, P., Lin, Q., and Liu, J. (2018). Authigenic minerals at site GMGS2-16 of northeastern south China Sea and its implications for gas hydrate evolution. *Mar. Geology Quaternary Geology* 38 (5), 144–155. doi: 10.16562/j.cnki.0256-1492.2018.05.014

Zhao, J., Wang, J., Phillips, S. C., Liang, J., Su, P., Lin, Q., et al. (2021). Non-evaporitic gypsum formed in marine sediments due to sulfate-methane transition zone fluctuations and mass transport deposits in the northern south China Sea. *Mar. Chem.* 233, 103988. doi: 10.1016/j.marchem.2021.103988

Zhu, B., Ge, L., Yang, T., Jiang, S., and Lv, X. (2019). Stable isotopes and rare earth element compositions of ancient cold seep carbonates from enza river, northern Apennines (Italy): Implications for fluids sources and carbonate chimney growth. *Mar. Petroleum Geology* 109, 434–448. doi: 10.1016/j.marpetgeo.2019.06.033

Zhu, W., Huang, B., Mi, L., Wilkins, R. W. T., Fu, N., and Xiao, X. (2009). Geochemistry, origin, and deep-water exploration potential of natural gases in the pearl river mouth and qiongdongnan basins, south China Sea. *AAPG Bull.* 93, 741–761. doi: 10.1306/02170908099

frontiers | Frontiers in Marine Science

TYPE Original Research
PUBLISHED 29 March 2023
DOI 10.3389/fmars.2023.1167578

OPEN ACCESS

EDITED BY
Wei Li,
South China Sea Institute of Oceanology (CAS), China

REVIEWED BY
Lihua Zuo,
Texas A&M University Kingsville, United States
Qing Li,
Qingdao Institute of Marine Geology (QIMG), China

*CORRESPONDENCE
Zhifeng Wan
wanzhif@mail.sysu.edu.cn
Jiujing Shang
shjj2012@126.com

SPECIALTY SECTION
This article was submitted to Marine Biogeochemistry, a section of the journal Frontiers in Marine Science

RECEIVED 16 February 2023
ACCEPTED 14 March 2023
PUBLISHED 29 March 2023

CITATION
Chen C, Wu X, Wan Z, Shang J, Huang W, Zhang W, Liang J, Xiao Z, Zhou W and Zhong L (2023) Geochemical characteristics of sediment and pore water affected by cold seeps in southern South China Sea.
Front. Mar. Sci. 10:1167578.
doi: 10.3389/fmars.2023.1167578

Geochemical characteristics of sediment and pore water affected by cold seeps in southern South China Sea

Chongmin Chen[1], Xuewan Wu[1], Zhifeng Wan[1,2]*, Jiujing Shang[3]*, Wei Huang[3], Wei Zhang[4], Jinqiang Liang[3], Zebang Xiao[1], Wei Zhou[1] and Lifeng Zhong[1]

[1]1School of Marine Sciences, Sun Yat-sen University & Southern Marine Science and Engineering Guangdong Laboratory (Zhuhai), Zhuhai, China, [2]Guangdong Provincial Key Laboratory of Marine Resources and Coastal Engineering Zhuhai, Zhuhai, China, [3]Ministry of Land and Resources (MLR) Key Laboratory of Marine Mineral Resources, Guangzhou Marine Geological Survey, Ministry of Natural Resources, Guangzhou, China, [4]Sanya Institute of South China Sea Geology, Guangzhou Marine Geological Survey, Sanya, China

Cold seep, characterized by active material circulation and methane seepage, is of great importance to reconstruct the paleo-marine environment and trace the origin of life and the occurrence of minerals. Southern South China Sea (SCS) with ample oil and gas resources is an ideal platform for cold seep study, but information and researches on cold seeps here are rather deficient. We studied the geochemical characteristics of sediment cores and pore water combined with seismic profile information in the Beikang Basin, aiming to further understand the nature of cold seeps in this area. Results show the extremely low $\delta\ ^{13}C_{DIC}$ of pore water in each core and we also found sulfate content decreases with depth, the high content of inorganic carbon (DIC) and the corresponding minimum$\delta\ ^{13}C_{DIC}$ in pore water, the kink-type depth profiles of Sr, Ba and Ni enrichment factors and Sr/Mg in the sediments of BH-CL37, the reducing sedimentary environment constrained by the features of Mo, U and REE. The extremely negative $\delta\ ^{13}C_{DIC}$ in the pore water of the sediment cores indicates strong AOM effect in cold seeps and the main biogenic origin of methane. The SO_4^{2-} depth variation trends of pore water, the high DIC content and the lowest value of $\delta\ ^{13}C_{DIC}$ can define the approximate SMTZ depth of each sediment core effectively. We thought that fluid fluxes and tectonic settings greatly influence the sedimentary environment and geochemistry, leading to the manifest regional differences in the properties and activities of cold seeps. This study of cold seep in southern SCS proves the variation of cold seep in time and space, stressing the necessity of further region-specific analysis towards different cold seeps; and the complex conditions of SCS do function well in offering multiple types of cold seeps.

KEYWORDS

geochemistry, cold seeps, sediment, pore water, southern South China Sea

1 Introduction

Cold seep commonly occurs along the continental margin, which is generated by the concentrated upward migration of dissolved hydrocarbons and/or gaseous hydrocarbons (mainly methane) (e.g. Suess, 2014; Wan et al., 2020), and functions effectively in the element circulation (Tribovillard et al., 2013; Feng D. et al., 2018; Smrzka et al., 2020). Additionally, cold seep often nurtures a unique ecosystem with a series of typical biochemical reactions (Levin, 2005; Levin and Sibuet, 2012). Cold seep is closely related to natural gas hydrate (Ingram et al., 2016; Hu et al., 2018).

Anaerobic oxidation of methane (AOM) is an important biochemical reaction in cold seep (Reeburgh, 2007; Boetius and Wenzhöfer, 2013), mainly occurring in the sulfate methane transition zone (SMTZ), carried out by a combination of anaerobic methane-oxidizing archaea and sulfate-reducing bacteria (Boetius et al., 2000; Orphan et al., 2001). AOM can generate carbonate and hydrogen sulfide and then increase the alkalinity in the surroundings, which further promotes the precipitation of some authigenic minerals, such as authigenic carbonates and pyrites etc. (Suess, 2014; Lin Q. et al., 2016; Feng D. et al., 2018). Studies on biochemistry of sediments, pore water and authigenic minerals in cold seeps can reveal the nature and history of cold seep. Sediment pore waters can offer information of modern cold seep on a short timescale of days to months (Hu et al., 2015; Feng J. et al., 2018), while sediment cores can be used as a continuous record to reconstruct the evolution of cold seep on much longer timescales (Bayon et al., 2007; Peketi et al., 2015; Li et al., 2018). In addition, authigenic minerals precipitated in cold seep sediments at a specific depth (usually SMTZ) effectively archive the formation conditions and even the dynamics of gas hydrate reservoirs (Tong et al., 2013; Bayon et al., 2015; Wang et al., 2015; Crémière et al., 2016; Liang et al., 2017).

Researches on cold seep in South China Sea (SCS) have gained increasing concern in decades and many samples such as authigenic carbonate, mussels, sediments and pore water, from more than 40 seepage in SCS have been studied so far (Feng D. et al., 2018). However, those studies mostly focused on northern SCS, which has greatly furthered the understanding of the cold seep system of northern SCS, including the fluid source and evolution etc. of cold seeps (Feng and Chen, 2015; Liang et al., 2017; Feng D. et al., 2018). In contrast, few studies have been carried out on the activities of cold seeps in southern SCS. The trough areas such as Zengmu, Wan' an, Nanwei, Nansha and Beikang in southern SCS are reported to store rich hydrocarbon gas and gas hydrate resources, and southern SCS has tectonic environment conducive to the migration of hydrocarbon-rich fluids and extensive methane outlets (Zhu et al., 2001; Wang et al., 2006; Yao, 2007; Zhang et al., 2010; Liu et al., 2011; Trung, 2012; Wei et al., 2012). In the Beikang Basin, some evidences that may indicate existence of cold seeps have been found, including some geophysical features (such as BSR) and authigenic minerals (such as authigenic pyrite) (Figure 1) (Wang et al., 2003; Su et al., 2005; Chen et al., 2009; Chen Z. et al., 2010; Liu et al., 2011). Nonetheless, till now there are only two studies focusing on the activities of cold seeps in the Beikang Basin (Yao, 2007; Li et al., 2018; Feng J. et al., 2018), their studies showed that the sulfate-methane transition zones (SMTZ) of the four sites are between 5.3 and 8.8 mbsf and the dissolved SO_4^{2-} was predominantly consumed by the anaerobic oxidation of methane (AOM) at rates between 27 and 44 mmol $m^{-2}yr^{-1}$ only by geochemical characteristics and model of porewater near our study area in the Beikang Basin(Feng J. et al., 2018). The cold seep system and its impact on the surroundings in the Beikang Basin remain vague.

In this paper, to further understand the cold seep system of southern SCS, combining the data of sediment and pore water, we studied the geochemical characteristics of pore water (concentration of Ca^{2+}, Mg^{2+}, Cl^- and SO_4^{2-}, dissolved inorganic carbon (DIC) and $\delta^{13}C_{DIC}$) and core sediments (mineralogy, total organic carbon (TOC), $\delta^{13}C_{TOC}$, $\delta^{13}C_{TIC}$, $\delta^{18}O_{TIC}$ and element contents). Moreover, the S isotope values of tubular pyrites in the sediments were analyzed to reveal the effects of cold seep activity on pyrite precipitation to a certain extent.

2 Geological settings

Located at the intersection of the Eurasian, the Pacific and the Indo-Australian plate, the South China Sea (SCS) is in complex tectonic conditions controlled by the interaction among different plates (Morley, 2012), with an average water depth of 1212 m and a total area of 350×10^4 km^2. The SCS is topographically tilted from the periphery to the center, broad in the north and south, narrow in the west and east. Diverse landscapes such as platforms, plateaus, troughs, valleys and reefs have well been developed in southern SCS.

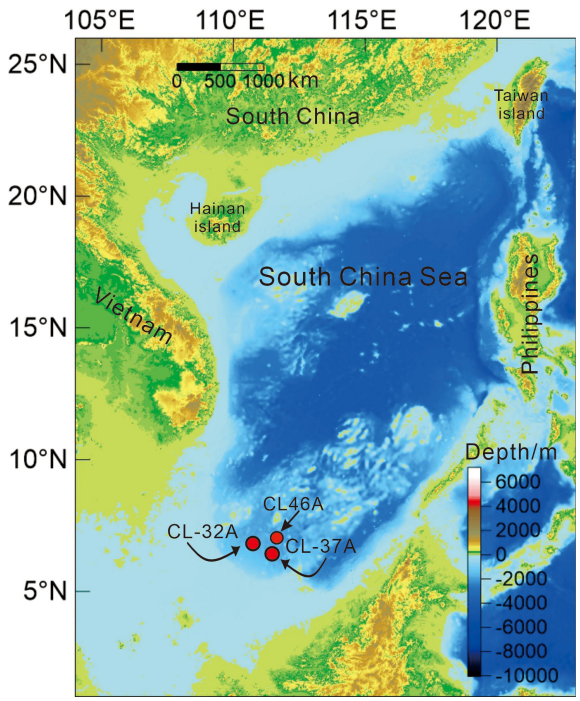

FIGURE 1
Map of the regional tectonic and sampling site locations in the Beikang basin.

The sedimentary thickness of greater than 500 m with the maximum over 10000 m, is favorable for the accumulation of sediments and the preservation of organic matter. Additionally, abundant resources of oil, gas and natural gas hydrate have been discovered in southern SCS (Fu, 2007). Gas hydrate stability zone thinned during the Last Glacial Maximum (LGM) can exhale plenty of methane, possibly promoting the formation and development of cold seeps in southern SCS (Wang et al., 2005; Yan et al., 2018).

The Beikang Basin is a Cenozoic flexural - extensional passive marginal basin in the middle of Nansha area, southern SCS (Xie et al., 2011). Its sedimentary evolution can be divided into three periods: Paleocene-Middle Eocene rift stage, Late Eocene-Middle Miocene depression stage and Late Miocene-Quaternary regional subsidence stage (Feng J. et al., 2018). Since the Palaeocene, the sedimentary environment of the Beikang Basin has gradually changed from lacustrine and littoral-neritic to a bathyal and abyssal environment (Feng J. et al., 2018). Abundant oil and gas resources have been found in the Beikang Basin. The high sedimentation rate, the deposition thickness up to 13 km and geologic structures like a large number of well-developed faults, mud diapirs and folds favoured for fluid migration, provide environment and conditions conductive to the production of oil and gas, the formation of natural gas hydrate and the migration and release of hydrocarbon (Li et al., 2018; Feng J. et al., 2018). The average value of heat flow in the Beikang Basin is 76. 8 ± 21.7 mW/m^2, which is generally higher than that of the northern SCS (Chen et al., 2017). In addition, the discovery of BSR further indicates a good potential of gas hydrate occurrences in this area.

Figures 2A, B are seismic profiles of the study area. BH-CL37 and BH-CL37A show obvious diapirs as the source of cold seep fluids, both of which are located on the same side of the fluid source, and the latter is closer to the source. There is an apparent convex phenomenon in the deep seismic profile of BH-CL37A, indicating rich fluid sources. Moreover, evident fractures, faults and other favorable fluid migration channels under the sedimentary column are present.

3 Materials and methods

The samples studied in this paper are sediment cores (BH-CL37, BH-CL37A, BH-CL32A and BH-CL46A) collected by Guangzhou Marine Geological Survey in the Beikang Basin, southern SCS, through *Haiyang IV* in 2019 (Figure 1 and Table 1). Ten cm of cores were sampled at every fifty cm, and corresponding pore water was extracted from each interval. The sediments were freezed-dried, and portions were ground to powder with an agate mortar for subsequent geochemical analysis.

3.1 Pore water

Anions (Cl^-, SO_4^{2-}) and cations (Ca^{2+}, Mg^{2+}) of pore water were measured after dilutions of 500 times with ultra-pure water by DIONEX ICS-5000 and DIONEX ICS-900 ion chromatographs respectively, with RSDs less than 3% completed at the Sun Yat-sen University Instrumental Analysis and Research Center.

In order to calculate the diffused sulfate flux, we assumed a steady-state condition and use Fick's first law (Eq. (1),(2)) for calculation:

$$J = -\varphi D_s \frac{dc}{dx} \tag{1}$$

$$D_s = \frac{D_0}{1 - ln(\varphi)^2} \tag{2}$$

Where J represents the diffusion flux of sulfate (mol m^{-2} yr^{-1}) and φ represents porosity (here we assume that the porosity of

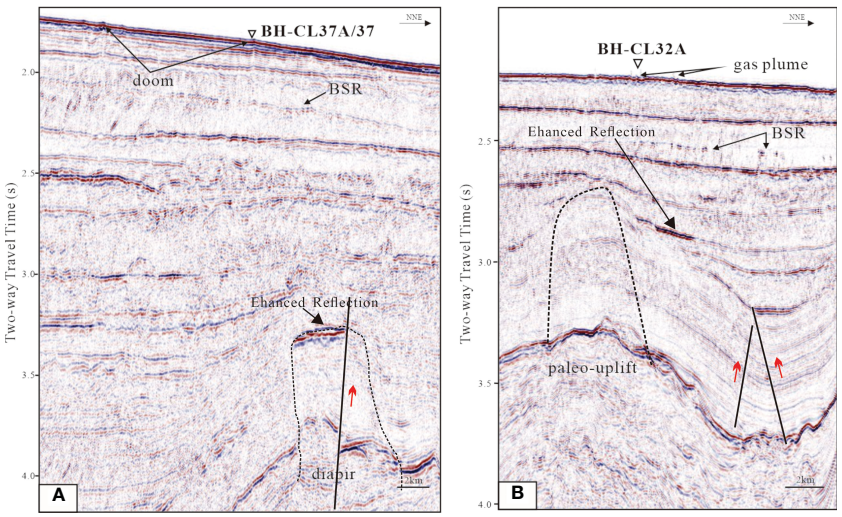

FIGURE 2
Seismic profiles of sampling sites in this study. **(A)** Seismic profile of BH-CL37, weak continuity of BSR, fault, enhanced reflection and seafloor dome; **(B)** Seismic profile of BH-CL32A, discontinuous BSR, fault, enhanced reflection and gas leakage on the seafloor.

sediments is 75%, Feng J. et al., 2018), D_0 is the diffusion coefficient of seawater ($m^2 s^{-1}$) (Boudreau, 1997), D_S is the diffusion coefficient of sediment ($m^2 s^{-1}$), C is the concentration of sulfate (mmol L^{-1}), X is the depth of sediment (m).

The contents of DIC and stable carbon isotopes in pore water were measured by a MAT253-Gasbench mass spectrometer in Beijing Createch Testing Technology Co., Ltd. 0.2 mL pore water was treated with pure H_3PO_4 in a glass vial of 25 °C, and the resulting CO_2 was transported by He to the mass spectrometer. The results were given in the standard δ-notation in per mil (‰) relative to the Vienna Peedee Belemnite Standard (V-PDB). $\delta^{13}C$ analysis precision is better than 0.1‰ V-PDB; The accuracy of DIC concentration analysis is better than 2%.

3.2 Sediments

The X-ray Diffraction (XRD) test of the samples was carried out at the Guangdong Provincial Key Laboratory of Marine Resources and Coastal Engineering, using a DMAX Rapid II Diffraction system (Mo Kα radiation) manufactured by Rigaku, Japan, with a working voltage of 50 kV and a current size of 30 mA. The diameter of the collimator (incident line spot) is 0.1 mm and the exposure time of each test is 10 minutes. Diffraction data were documented as two-dimensional images and then transformed into 2θ-intensity patterns by Rigaku's 2DP software.

The analyses of major and trace elements in sediments were carried out in the laboratory of Wuhan SampleSolution Analytical Technology Co., Ltd, Wuhan, China. The major elements were tested by Primus, Rigaku, Japan X-ray Fluorescence (XRF) and the Agilent 7700e ICP-MS was used for testing the trace elements. Detailed sample digestion process was described in Yang et al. (2019). The measurement precision of major elements of whole rocks is 2% and accuracy is 5%.The precision of trace element tests is 5% and the accuracy is 10%.

The total organic carbon (TOC) and $\delta^{13}C_{TOC}$ measurements were performed on an elemental analyzer manufactured by Thermoelectric Corporation of America combined with a MAT 253 plus in the laboratory of Beijing Createch Testing Technology Co., Ltd. Before TOC test, the samples were decalcified with 20% HCl for 12 h, washed with deionized water 5 times, and dried at 60 ° C for 12 h. The carbon isotope analytical accuracy of the standard samples could reach 0.2 ‰ V-PDB.

Carbon and oxygen stable isotopic measurements of total inorganic carbon (TIC) in sediments were performed in the laboratory of Beijing Createch Testing Technology Co., Ltd., using the MAT253-Gas Bench Mass Spectrometer of American Thermoelectric Corporation. After the reaction of the sample and phosphoric acid, the generated CO_2 was passed through a 70 °C fused silicon capillary column for impurity separation, and finally entered into a stable gas isotope mass spectrometer for measurements. The results of carbon and oxygen isotopes are all calibrated on VPDB standard, and the analytical accuracy of both $\delta^{13}C$ and $\delta^{18}O$ is better than 0.1‰ V-PDB.

The sediment samples were sifted and dried after washing by water, and tubular pyrites were sorted out under a stereomicroscope. 200 μg pyrite was weighed with a precision balance and put into a tin cup with 3 times of the combustion-supporting agent V_2O_5. The samples were put into the automatic sampler and combustioned rapidly and fully at 1020 °C to produce SO_2 gas, which were then fed into the mass spectrometer by the He carrier gas through the splitter interface. The tests were carried out by MAT253 Plus stable isotope mass spectrometer combined with elemental analyzer (EA-IRMS). The international standard used was IAEA-S1 (Ag_2S, $\delta^{34}S$=-0.30‰ V-CDT), and the analytical deviation is better than ±0.3‰. The sulfur isotopes were normalized to $\delta^{34}S$ by Vienna Canyon Diablo Troilite (V-CDT): $\delta^{34}S$ (‰, V-CDT) = $[(^{34}S/^{32}S)_{sample}/(^{34}S/^{32}S)_{V\text{-}CDT} -1]*1000$.

4 Results

BH-CL37, BH-CL37A and BH-CL32A display obvious methane leakage phenomenon, while BH-CL46A does not present significant methane leakage, which is used as the reference cores for the study of pore water in this paper.

BH-CL37, BH-CL37A and BH-CL32A core sediments are mainly gray-green silty clay, fine-grained. With the increasing depth, sediments show deeper color and stronger rotten egg smell interpreted as the apparent hydrogen sulfide contents; and deep asphalt gray organic interlayers are observed at the bottom of these cores.

4.1 Pore water

4.1.1 Main cations and anions of pore water

Cl^- and Mg^{2+} in the pore water of BH-CL37, BH-CL37A, BH-CL32A and BH-CL46A generally fluctuate between 400-900 mmol/L and 28-65 mmol/L. Ca^{2+} and SO_4^{2-} in each sediment core show a decreasing trend with depth. These ions in BH-CL37 present high concentrations at the depth of 50-60 cmbsf (102.7 mmol/L Mg^{2+}, 19.3 mmol/L Ca^{2+}, 1143.3 mmol/L Cl^-, 57.6 mmol/L SO_4^{2-}) (Table 2).

In particular, Mg^{2+}/Ca^{2+} ratios of BH-CL46A, BH-CL37A and BH-CL32A vary greatly and similarly (Figure 3), while Mg^{2+}/Ca^{2+} ratios increase slowly with depth in a minor range in BH-CL37.

In BH-CL37, BH-CL37A and BH-CL32A cores, a quasi-linear decline of sulfate concentration can be observed among the depths of 350-600 cmbsf, 170-360 cmbsf and 350-540 cmbsf. Calculated sulfate fluxes of BH-CL37A and BH-CL32A are 110 mol m^{-2} yr^{-1}, 135 mol m^{-2} yr^{-1} and 119 mol m^{-2} yr^{-1}, respectively (Figure 4).

4.1.2 DIC and $\delta^{13}C_{DIC}$ of pore water

The $\delta^{13}C_{DIC}$ values of pore water in BH-CL46A show a slight decrease trend with the increase of depth, and the variation ranges are -40.73 - -16.70‰ V-PDB, -11.8 - -55.66‰ V-PDB and -40.57 - -21.24‰ V-PDB, respectively. The $\delta^{13}C_{DIC}$ values of BH-CL37, BH-CL37A and BH-CL32A are rather stable at the top section, and then decrease to the minimum values at 530-540 cmbsf, 290- 300 cmbsf and 470-480 cmbsf, respectively. There is a good correlation between the depth profiles of DIC and $\delta^{13}C_{DIC}$ (Figure 5). DIC concentrations of the pore water in BH-CL46A show a trend of slow

TABLE 1 Details of the study sites.

Site	Water depth(m)	Core length(cmbsf)	Seafloor temperature(°C)	Geothermal gradient(°C/km)
BH-CL37	1336	660	3.23	74.80
BH-CL37A		360		
BH-CL32A	1653	730	2.73	102.00
BH-CL46A	–	730	–	–

TABLE 2 Concentration of main ions, DIC and $\delta^{13}C_{DIC}$ in pore water.

Sampling sites	Interval	Mg^{2+}	Ca^{2+}	Cl^-	SO_4^{2-}	ωDIC	$\delta^{13}C_{DIC}$
	(cmbsf)	(mmol/L)	(mmol/L)	(mmol/L)	(mmol/L)	(μg/mL)	(‰)
BH-CL37							
	50-60	102.74	19.28	1143.33	57.60	582.04	-11.60
	110-120	66.52	12.50	772.27	37.78	665.44	-15.17
	170-180	54.79	10.54	642.06	30.96	635.98	-16.86
	230-240	58.24	10.24	681.58	32.67	798.31	-19.39
	290-300	56.78	10.23	653.21	31.34	679.42	-18.97
	350-360	58.09	10.39	697.85	32.20	939.39	-25.24
	410-420	51.71	8.58	675.93	22.00	1452.52	-37.90
	470-480	45.06	7.11	625.00	13.86	1653.93	-42.58
	530-540	39.73	5.84	605.52	6.07	2367.02	-46.37
	590-600	36.74	4.87	581.06	1.22	2569.10	-44.96
	650-660	28.84	3.65	461.85	0.88	1955.68	-32.25
BH-CL37A							
	50-60	47.02	8.48	544.95	28.32	426.15	-11.18
	110-120	47.78	8.73	544.26	27.97	475.10	-11.98
	170-180	53.04	9.76	609.27	30.96	543.01	-12.75
	230-240	45.95	7.05	537.60	23.40	929.46	-35.17
	290-300	47.83	5.09	619.79	10.57	2597.94	-55.66
	350-360	37.86	2.72	531.31	3.51	2667.72	-40.62
BH-CL32A							
	50-60	50.10	9.46	562.54	29.12	2337.34	-6.76
	110-120	57.91	10.62	649.99	32.99	491.78	-6.74
	170-180	46.55	8.43	538.89	27.53	496.30	-6.52
	230-240	49.75	9.11	568.16	29.20	416.12	-7.67
	290-300	51.76	9.49	598.62	30.93	493.08	-9.61
	350-360	43.94	8.01	505.35	25.53	576.11	-16.12
	410-420	48.15	7.48	579.81	24.07	511.63	-39.72
	470-480	47.70	5.81	624.04	15.37	1190.63	-51.45
	530-540	32.30	2.45	479.55	2.79	2611.66	-41.98
	590-600	46.98	3.50	693.74	3.81	2419.39	-27.23

(Continued)

TABLE 2 Continued

Sampling sites	Interval	Mg^{2+}	Ca^{2+}	Cl^-	SO_4^{2-}	ωDIC	$\delta^{13}C_{DIC}$
	(cmbsf)	(mmol/L)	(mmol/L)	(mmol/L)	(mmol/L)	(μg/mL)	(‰)
	650-660	36.54	2.59	531.86	2.80	3230.28	-17.50
	710-720	33.43	2.37	485.34	2.23	2274.52	-14.72
BH-CL46A							
	50-60	74.51	13.06	892.71	39.54	1168.34	-21.24
	110-120	57.75	9.28	711.98	30.45	1301.05	-24.06
	170-180	56.50	9.46	691.92	29.06	1341.11	-25.45
	230-240	58.39	9.11	729.58	28.52	1682.77	-27.30
	290-300	48.04	7.07	595.56	21.14	1555.77	-29.95
	350-360	42.60	6.01	541.50	17.05	1636.88	-32.54
	410-420	43.30	5.46	563.68	14.69	1886.05	-34.05
	470-480	46.38	5.17	628.69	12.52	2383.49	-36.65
	530-540	44.02	3.88	617.88	7.38	2776.17	-38.97
	590-600	38.54	2.76	565.04	3.31	3007.67	-40.57
	650-660	38.32	2.94	565.44	1.57	3097.25	-38.06
	710-720	36.73	2.59	546.47	0.64	3355.97	-33.39

increase with depth (1168-3356 μg/mL), while DIC concentration profiles of BH-CL37, BH-CL37A and BH-CL32A show more complicated trend (Figure 5).

4.2 Sediments

4.2.1 XRD results of the sediments

The sediments of BH-CL37, BH-CL37A and BH-CL32A are mainly composed of quartz and clay minerals (such as illite and chlorite, etc). Some sediments at shallow intervals contain relatively abundant calcite (Figure 6).

4.2.2 Major and trace elements in the sediments

The contents of some major elements in the sediments are shown in Table 3. Al contents of BH-CL37, BH-CL37A and BH-CL32A are in the range of 7.69-10.06% (9.00% on average), 7.90-9.61% (8.80% on average), 7.85-9.95% (9.26% on average) respectively. Al is used to standardize the major elements considering the variation of carbonate contents (Tribovillard et al., 2006; Tribovillard et al., 2013). Both Ca/Al and Mg/Al in each sediment core show a trend of first decreasing and finally stabilizing, and Mn/Al ratios shallower than 400 cmbsf obviously are lower in each sediment core. Ti/Al and Si/Al ratios fluctuate in a small range of 0.043-0.053 and 2.48-3.15 respectively, showing

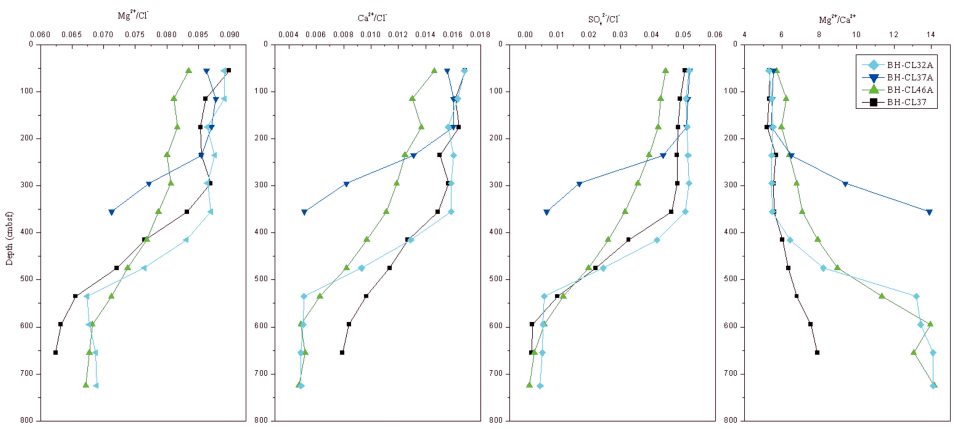

FIGURE 3
Depth profiles of Mg^{2+}/Cl^-, Ca^{2+}/Cl^-, SO_4^{2-}/Cl^- and Mg^{2+}/Ca^{2+} ratios.

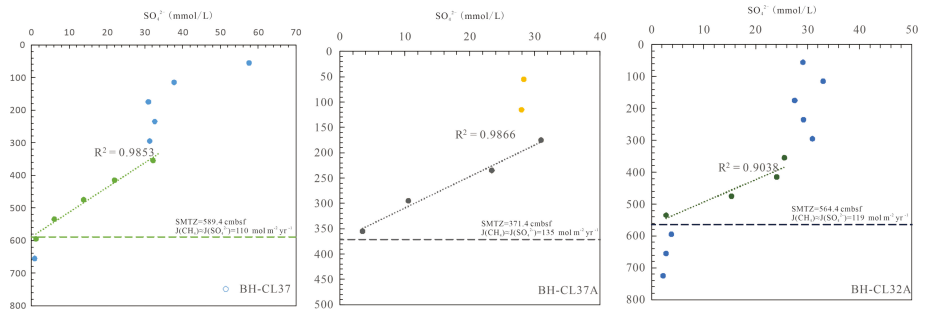

FIGURE 4
Estimated SMTZ depth and methane diffusion flux for BH-CL37, BH-CL37A and BH-CL32A cores.

relatively constant values. Fe/Al ratios have no obvious trend with depth, ranging from 0.44 to 0.52 (Figure 7).

The enrichment factor (EF) of the trace element in sediments was calculated by $X_{EF} = (X_{sample}/Al_{sample})/(X_{upper\ crust}/Al_{upper\ crust})$, where X and Al refer to the element and Al content in the sample of the upper crust (McLennan, 2001), respectively. Enrichment factor can effectively evaluate the authigenic enrichment degree of trace elements (Tribovillard et al., 2006). In general, the enrichment factor greater than 1 indicates enrichment relative to the standard (the upper crust); EF greater than 3 indicates detectable enrichment; and EF greater than 10 indicates moderate to strong enrichment (Algeo and Tribovillard, 2009).

Trace elements (Table 4) such as Mo, U, Ni, V, Co, Zn are known as redox sensitive elements and Ba content can record the activity of paleo cold seep (Dickens, 2001; Castellini et al., 2006; Riedinger et al., 2006; Joseph et al., 2013). As shown in Figure 8, except for Mo, their enrichment factors basically decrease with depth at first and then tend to be stable, and their values in the

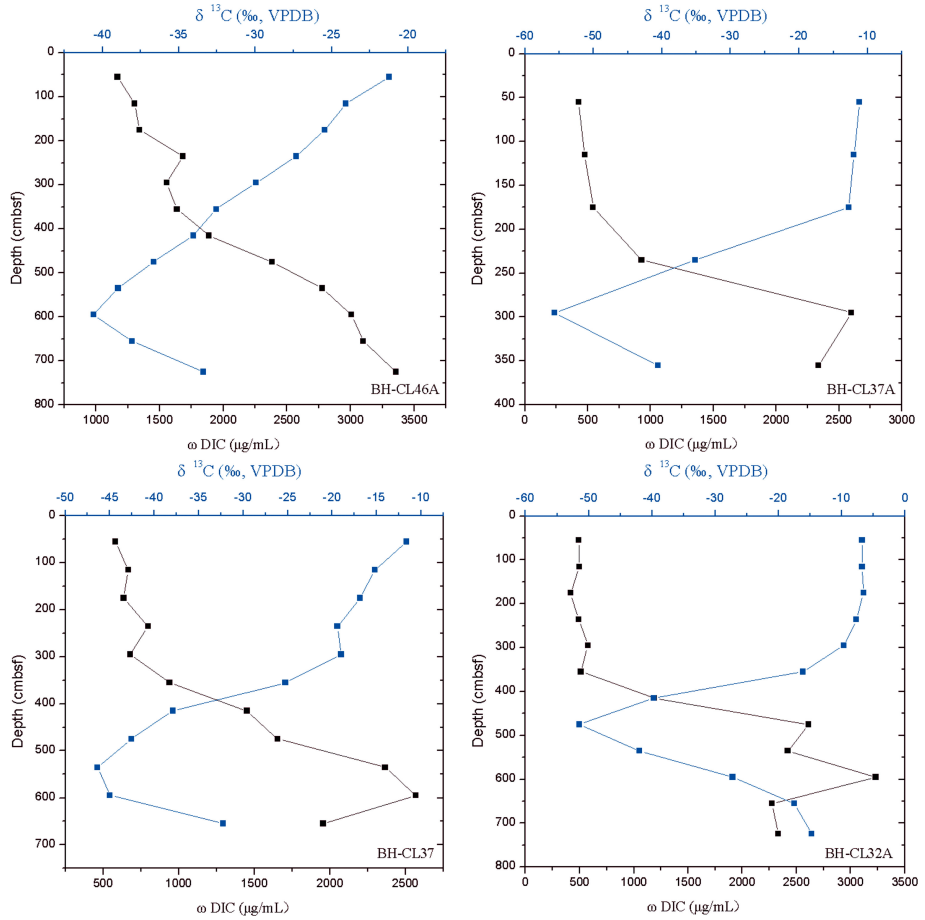

FIGURE 5
Depth profiles of DIC and $\delta^{13}C_{DIC}$ in pore water of each sediment core.

10.3389/fmars.2023.1167578

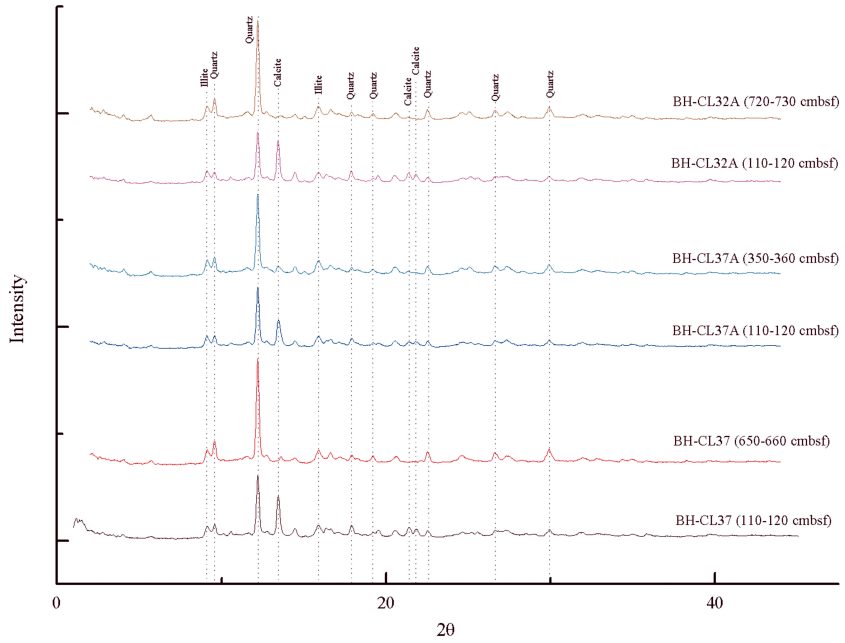

FIGURE 6
XRD results of the studied sediment cores. Shallow sediments show higher contents of calcite in each sediment core.

TABLE 3 Concentration of some major elements in sediments.

Sampling sites	Interval (cmbsf)	Al (%)	Ti (%)	Ca (%)	Mg (%)	Mn (%)	Fe (%)	Si (%)
BH-CL37								
	50-60	7.69	0.35	7.98	1.52	0.06	3.66	20.04
	110-120	7.92	0.37	7.27	1.51	0.06	4.03	20.78
	170-180	8.37	0.38	4.94	1.52	0.07	4.11	21.61
	230-240	8.88	0.39	4.17	1.46	0.05	4.33	22.72
	290-300	8.91	0.39	4.09	1.44	0.05	4.23	22.36
	350-360	9.56	0.45	1.48	1.38	0.05	4.75	25.02
	410-420	10.06	0.46	0.73	1.44	0.09	4.99	25.04
	470-480	9.28	0.47	0.56	1.31	0.08	4.57	26.91
	530-540	9.47	0.50	0.34	1.20	0.10	4.39	27.35
	590-600	9.45	0.50	0.32	1.19	0.09	4.53	27.36
	650-660	9.42	0.50	0.33	1.19	0.09	4.61	27.51
BH-CL37A								
	50-60	7.90	0.36	7.01	1.53	0.05	3.88	20.38
	110-120	8.07	0.37	6.44	1.58	0.05	3.92	21.19
	170-180	8.11	0.40	2.98	1.26	0.04	3.92	25.51
	230-240	9.53	0.43	2.30	1.44	0.05	4.53	24.25
	290-300	9.58	0.43	2.02	1.47	0.05	4.54	24.15

(Continued)

TABLE 3 Continued

Sampling sites	Interval	Al	Ti	Ca	Mg	Mn	Fe	Si
	(cmbsf)	(%)	(%)	(%)	(%)	(%)	(%)	(%)
	350-360	9.61	0.45	1.15	1.45	0.05	4.81	25.03
BH-CL32A								
	50-60	7.86	0.35	8.57	1.46	0.04	3.63	19.50
	110-120	7.96	0.36	7.63	1.48	0.04	3.81	19.98
	170-180	8.37	0.38	6.39	1.42	0.03	3.95	20.98
	230-240	9.37	0.42	2.75	1.40	0.04	4.31	23.33
	290-300	9.81	0.45	1.67	1.42	0.04	4.39	24.77
	350-360	9.76	0.47	0.58	1.30	0.05	4.78	25.78
	410-420	9.41	0.46	1.45	1.32	0.07	4.75	25.73
	470-480	9.60	0.48	0.51	1.30	0.09	4.76	26.41
	530-540	9.58	0.47	1.20	1.39	0.09	4.78	25.92
	590-600	9.95	0.48	0.42	1.40	0.09	4.77	25.64
	650-660	9.93	0.49	0.43	1.44	0.09	4.78	26.04
	710-720	9.56	0.48	0.44	1.37	0.09	4.95	26.36

shallow depths are bigger than 1. U first enriches in shallow depth, then decreases and finally tends to the equilibrium of 1 with depth in each sediment core. However, the variations of Mo enrichment factor are significantly different in the sediments: At BH-CL37, Mo_{EF} is generally less than 1, while the value as high as 12.4 suddenly appears between 350 cmbsf and 400 cmbsf; at BH-CL37A, Mo_{EF} decreases rapidly from a high value of 42.5 to a low value of about 1.4 with depth; At BH-CL32A, Mo_{EF} increases first and then decreases with depth, ranging from 0.8 to 44.8, and reaches the highest value at the depth of 410-420 cmbsf (Figure 8).

The total rare earth element (REE) contents of BH-CL37, BH-CL37A and BH-CL32A sediments range from 153.91 μg/g to 190.11 μg/g, from 151.50 μg/g to 183.24 μg/g and from 153.91 μg/g to 196.63 μg/g, respectively, generally increasing with depth (Table 5).

The studied sediments show no Eu anomaly, while most samples show no Ce anomaly, and minor show negative Ce anomaly caused by La anomaly (Figures 9 and 10).

4.2.3 TOC and $\delta^{13}C_{TOC}$ in sediments

TOC of BH-CL37 varies from 0.66% to 1.30% with an average value of 0.89%. TOC of BH-CL37A varies from 0.75% to 1.02% with an average value of 0.84%. TOC of BH-CL32A ranges from 0.69% to 1.15% with an average value of about 0.86% (Table 6).

$\delta^{13}C_{TOC}$ values of BH-CL37 greatly fluctuate at the depth of 50-420 cmbsf with a range of -23.80‰ - -21.29‰ V-PDB, and then

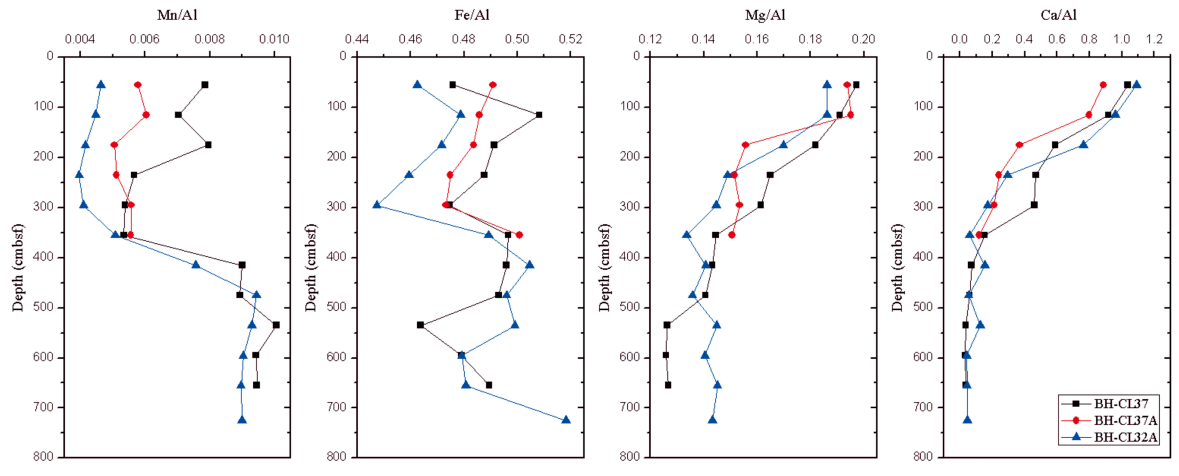

FIGURE 7
Images of the ratios of major elements to Al changing with depth.

10.3389/fmars.2023.1167578

TABLE 4 Concentration of some trace elements in sediments.

Sampling sites	Interval	Mo	U	Ni	V	Co	Zn	Ba	Cr	Cu	Sr
	(cmbsf)	(μg/g)	(μg/g)	(μg/g)	(μg/g)	(μg/g)	(μg/g)	(μg/g)	(μg/g)	(μg/g)	(μg/g)
BH-CL37											
	50-60	0.48	4.13	57.2	99.2	15.1	110	516	70.3	26.5	442
	110-120	0.70	5.06	63.9	109	17.1	118	548	76.8	29.5	419
	170-180	1.55	4.71	58.3	114	16.6	114	467	78.0	28.5	326
	230-240	1.20	5.81	51.3	114	15.6	108	478	76.8	30.4	290
	290-300	1.11	5.81	51.8	116	15.7	109	475	77.4	30.3	290
	350-360	11.1	4.28	42.6	124	16.5	104	343	80.0	21.1	142
	410-420	1.27	3.01	41.6	129	17.6	106	325	81.9	19.6	108
	470-480	0.74	3.01	36.3	118	16.0	95.2	291	77.2	17.4	94.6
	530-540	0.71	3.03	36.3	119	16.7	96.4	282	75.2	15.9	84.9
	590-600	0.68	3.09	36.5	117	16.7	96.8	283	77.2	15.9	86.9
	650-660	0.67	3.21	35.1	117	16.3	96.5	275	78.4	15.7	89.5
BH-CL37A											
	50-60	31.4	12.2	55.3	107	14.9	110	492	72.0	28.3	398
	110-120	29.7	13.6	56.2	117	15.7	111	397	77.5	28.8	366
	170-180	22.1	9.69	42.1	107	14.2	92.3	320	72.9	24.3	202
	230-240	23.4	7.67	44.0	130	17.0	103	304	80.7	21.7	160
	290-300	1.63	3.52	40.6	122	16.5	101	301	77.7	21.6	149
	350-360	1.22	3.28	40.8	126	16.7	102	309	80.4	20.5	133
BH-CL32A											
	50-60	2.43	6.44	61.2	109	15.6	124	566	74.4	31.5	483
	110-120	7.40	8.64	61.1	114	16.3	121	555	77.2	32.2	434
	170-180	15.3	8.69	56.5	120	16.2	118	517	80.0	33.4	370
	230-240	32.9	9.34	53.2	136	17.4	116	427	84.9	31.9	204
	290-300	26.0	8.94	49.9	142	17.0	116	403	88.1	29.6	151
	350-360	39.8	7.51	44.7	130	18.3	107	311	82.6	21.9	99.4
	410-420	39.4	6.32	42.9	125	17.9	100	297	81.5	20.1	112
	470-480	4.75	4.37	38.6	122	17.7	99.9	301	78.8	18.3	96.9
	530-540	1.53	3.39	38.3	118	17.2	98.0	296	76.7	18.0	122
	590-600	1.21	3.02	38.5	121	17.5	99.2	297	77.2	17.7	90.2
	650-660	0.71	3.02	38.6	126	17.5	102	294	77.9	18.3	94.8
	710-720	0.84	3.07	37.9	123	17.0	97.2	282	76.7	17.5	95.7

decrease slowly to a relatively stable value of -25.14‰ - -24.98‰ V-PDB from 530 cmbsf to 660 cmbsf with an overall mean of -23.62‰ V-PDB. $\delta^{13}C_{TOC}$ values of BH-CL37A decrease from -22.91‰ to -25.50‰ V-PDB in the depth range of 50-180 cmbsf, and then increase to -23.92‰ V-PDB with depth, finally tend to be stable gradually, with an overall mean value of -23.94‰ V-PDB. $\delta^{13}C_{TOC}$ of BH-CL32A is basically stable in the range of -22.41–21.70‰ V-PDB at the depth of 50-300cmbsf, then drops sharply to -25.88‰ V-PDB at the depth of 350-360cmbsf, and later remains relatively stable (-25.88–24.78‰ V-PDB) with an overall mean of -24.15‰ (Figure 11).

4.2.4 Carbon and oxygen isotope compositions of TIC in sediments

$\delta^{13}C_{TIC}$ values in BH-CL37, BH-CL37A and BH-CL32A are -14.15 - 0.98‰ V-PDB, -31.89 - -4.91‰ V-PDB and -29.11 - 1.26‰

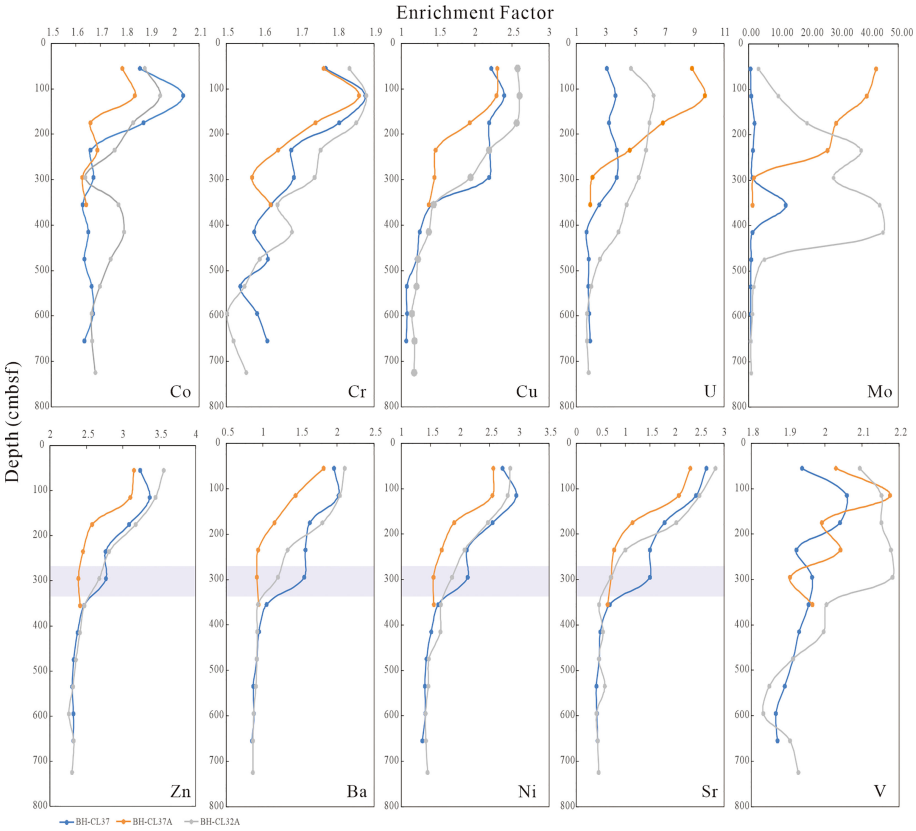

FIGURE 8
Depth profiles of trace element enrichment factors. The shadow area denotes a kink-type feature.

V-PDB, respectively, and have minimum values at 590-600 cmbsf, 230-240 cmbsf and 410-420 cmbsf. $\delta^{18}O_{TIC}$ values of BH-CL37, BH-CL37A and BH-CL32A are -2.02 - 0.15‰, -0.33 - 1.94‰ and -2.51 - 0.68‰, respectively, which are similar to the results of Li et al. (2018) (Figure 12 and Table 6).

4.2.5 Sulfur isotopes of tubular pyrites in sediments

The sulfur isotope values of pyrites in BH-CL37 sediments vary widely, ranging from -45.04‰ to 8.69‰ V-CDT. $\delta^{34}S$ fluctuates slightly at shallow depth, reaching a relatively low value at 230-240 cmbsf and 350-360 cmbsf, and a maximum value at 470-480 cmbsf. The sulfur isotopes of pyrites in BH-CL37A range from -30.58‰ to -7.81‰ V-CDT. The sulfur isotopes of pyrites in BH-CL32A vary from -27.38‰ to -15.38‰ V-CDT (Figure 13 and Table 7).

5 Discussion

5.1 AOM signals in cold seeps.

Generally, DIC in pore water in marine sediments is mainly derived from (1) DIC from overlying seawater diffusing into sediments or DIC retained during burial (usually $\delta^{13}C_{DIC}$=0 V-PDB); (2) DIC generated by degradation of organic matter; (3) DIC generated by AOM; (4) The residual DIC after methane formation (Feng D. et al., 2018; Feng J. et al., 2018). In cold seeps with active methane leakage, DIC generated by AOM often has extremely negative $\delta^{13}C$ values (usually lower than -30‰ V-PDB, Borowski et al., 2000; Claypool et al., 2006). Strong negative $\delta^{13}C_{DIC}$ values in pore water are present at the bottom of BH-CL37, BH-CL37A and BH-CL32A cores (as low as -55–35‰ V-PDB, Figure 3). In addition, considering the low content of organic matter in the sediments and the $\delta^{13}C_{TOC}$ values that vary between -25.94‰ V-PDB and -21.29‰ V-PDB (Figure 5), we infer that methane is the main source of DIC through AOM.

There are two main sources of methane in marine sediments: biogenic methane and thermogenic methane, which have different $\delta^{13}C$ characteristics. The $\delta^{13}C$ values of biogenic methane generally range from -110‰ to -50‰ V-PDB (Whiticar, 1999), while the $\delta^{13}C$ values of thermogenic methane are generally between -50‰ and -30‰ V-PDB (Sackett, 1978). Therefore, stable carbon isotopes are often used in the studies to trace the methane source in cold seeps (Feng D. et al., 2018). ^{13}C isotopes of DIC in sediment pore water can well define the source of methane (Chen Y. et al., 2010; Wang et al., 2018). Previous studies have found that the carbon fractionation between methane and DIC generated by AOM is insignificant. However, due to various mixing of different DIC sources such as seawater and organic degradation, the $\delta^{13}C$ of methane is about 10-20‰ V-PDB lighter than the $\delta^{13}C_{DIC}$ of pore water (Chen Y. et al., 2010; Feng J. et al., 2018), so the minimum value is usually used to constrain the main source of methane

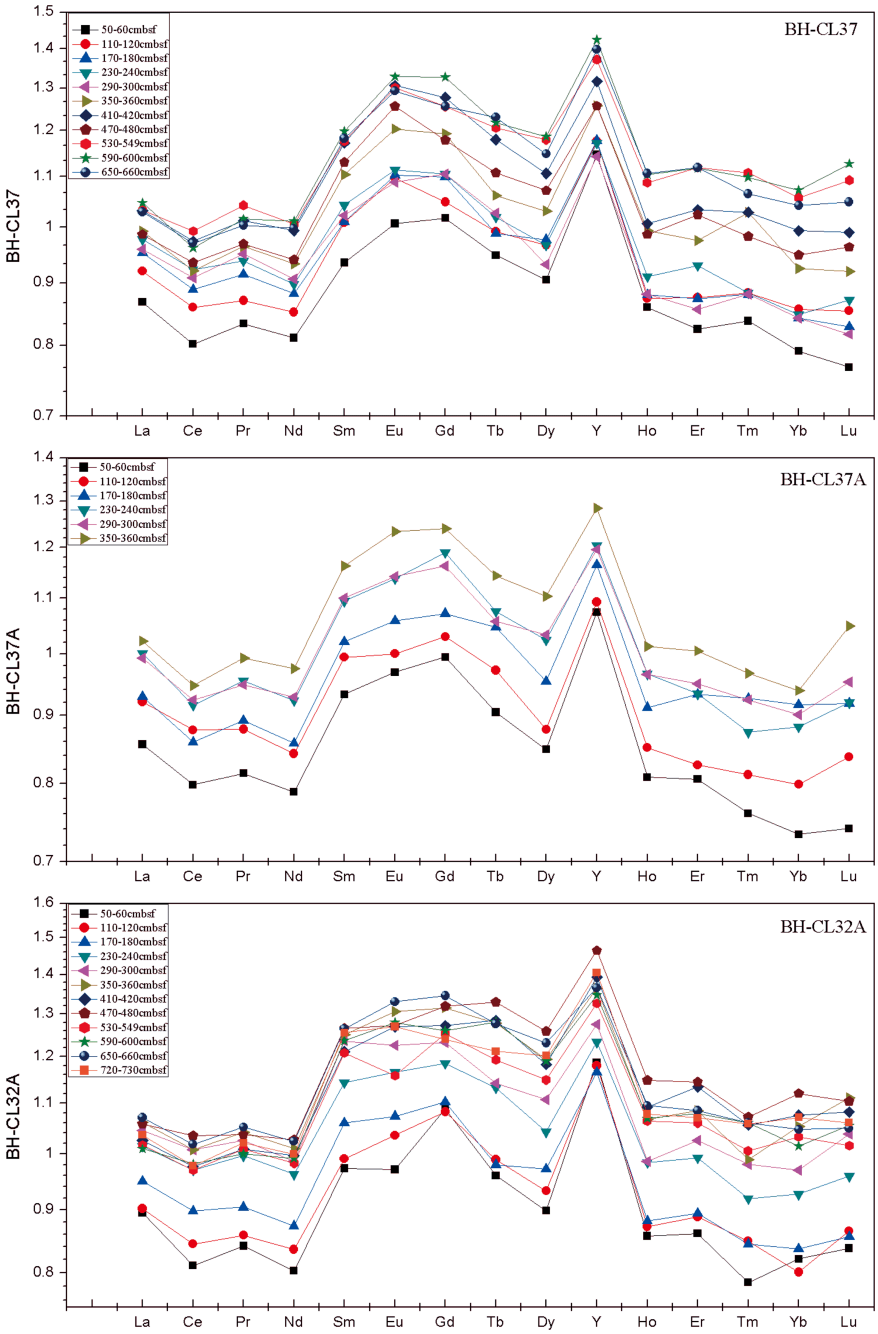

FIGURE 9
REE+Y distribution curves of BH-CL37, BH-CL37A and BH-CL32A at different depths. They are characterized as enrichment of middle rare earth element (MREE) and Y without Ce and Eu anomalies.

(Feng D. et al., 2018). The lowest $\delta^{13}C_{DIC}$ values of BH-CL37, BH-CL37A and BH-CL32A are lower than -44‰ V-PDB, indicating the microbial origin of methane in the shallow sediments of the study area. This result is consistent with that of biogenic methane obtained by Feng J. et al. (2018). Moreover, as shown in the seismic profiles of BH-CL37, BH-CL37A and BH-CL32A (Figure 2), there are obvious fluid migration channels below the sampling sites, indicating that the migration of deep fluid and thermogenic methane may play a crucial role in the sediment cores.

The sediment cores BH-CL46A show extremely negative $\delta^{13}C_{DIC}$ values as well, suggesting the abundant methane diffusion and biogenic methane. Additionally, their DIC contents increasing with depth are interpreted as the contribution of active biological reactions and methane derived from bottom (including thermogenic methane).

Based on the images of SO_4^{2-}/Cl^- (Figure 3), we infer that the approximate SMTZ depths of BH-CL37, BH-CL37A and BH-CL32A are 590-600 cmbsf, 355 cmbsf and 535-595 cmbsf,

TABLE 5 Concentration of rare earth element in sediments.

Sampling sites	Interval	La	Ce	Pr	Nd	Sm	Eu	Gd	Tb	Dy	Ho	Er	Tm	Yb	Lu	Y	TREE
	(cmbsf)	(μg/g)	(μg/g)	(μg/g)	(μg/g)	(μg/g)	(μg/g)	(μg/g)	(μg/g)	(μg/g)	(μg/g)	(μg/g)	(μg/g)	(μg/g)	(μg/g)	(μg/g)	(μg/g)
BH-CL37																	
	50-60	33.2	63.8	7.36	27.5	5.19	1.09	4.74	0.73	4.24	0.85	2.35	0.34	2.23	0.33	25.2	153.92
	110-120	35.1	68.4	7.69	28.9	5.60	1.19	4.89	0.77	4.52	0.87	2.50	0.36	2.42	0.37	25.9	163.56
	170-180	36.4	70.7	8.07	29.9	5.61	1.19	5.12	0.76	4.57	0.87	2.49	0.36	2.37	0.36	25.9	168.79
	230-240	37.3	73.4	8.29	30.4	5.78	1.20	5.15	0.79	4.52	0.90	2.65	0.36	2.39	0.38	25.8	173.60
	290-300	36.6	72.3	8.39	30.7	5.67	1.17	5.15	0.79	4.36	0.87	2.44	0.36	2.37	0.35	25.1	171.60
	350-360	37.9	73.3	8.51	31.6	6.13	1.30	5.56	0.82	4.82	0.98	2.78	0.42	2.61	0.40	27.7	177.12
	410-420	39.4	77.5	8.93	33.7	6.51	1.41	5.95	0.91	5.18	1.00	2.94	0.42	2.80	0.43	29.0	187.06
	470-480	37.7	74.4	8.55	31.9	6.27	1.36	5.49	0.86	5.01	0.98	2.92	0.40	2.68	0.42	27.6	178.88
	530-540	39.4	79.0	9.20	34.1	6.53	1.41	5.85	0.93	5.52	1.08	3.19	0.45	2.98	0.47	30.2	190.10
	590-600	40.0	76.5	8.97	34.3	6.65	1.43	6.19	0.94	5.55	1.09	3.19	0.44	3.02	0.49	31.3	188.78
	650-660	39.3	77.2	8.86	33.8	6.56	1.40	5.85	0.95	5.37	1.10	3.19	0.43	2.94	0.45	30.8	187.45
BH-CL37A																	
	50-60	32.7	63.6	7.19	26.7	5.18	1.05	4.63	0.70	3.97	0.80	2.30	0.31	2.07	0.32	23.6	151.51
	110-120	35.2	69.8	7.76	28.6	5.52	1.08	4.80	0.75	4.11	0.84	2.35	0.33	2.25	0.36	24.0	163.71
	170-180	35.5	68.4	7.87	29.1	5.66	1.14	4.99	0.81	4.46	0.90	2.66	0.38	2.58	0.40	25.6	164.86
	230-240	38.2	72.9	8.43	31.3	6.07	1.23	5.55	0.83	4.79	0.96	2.66	0.35	2.49	0.40	26.5	176.13
	290-300	37.9	73.5	8.37	31.5	6.11	1.23	5.42	0.82	4.83	0.96	2.71	0.37	2.54	0.41	26.3	176.71
	350-360	39.0	75.4	8.77	33.1	6.45	1.33	5.78	0.89	5.16	1.00	2.86	0.39	2.65	0.45	28.2	183.24
BH-CL32A																	
	50-60	34.2	64.5	7.43	27.2	5.40	1.05	5.07	0.74	4.21	0.85	2.45	0.32	2.31	0.36	26.1	156.12
	110-120	34.5	67.2	7.58	28.3	5.50	1.12	5.04	0.77	4.37	0.86	2.53	0.34	2.26	0.37	26.0	160.75
	170-180	36.3	71.5	7.99	29.6	5.88	1.16	5.14	0.76	4.55	0.87	2.55	0.34	2.36	0.37	25.6	169.34
	230-240	38.8	77.2	8.80	32.6	6.34	1.26	5.52	0.88	4.88	0.98	2.83	0.37	2.61	0.42	27.1	183.47
	290-300	39.9	80.2	9.05	33.4	6.86	1.32	5.74	0.88	5.18	0.98	2.92	0.40	2.73	0.45	28.0	190.10
	350-360	40.5	80.2	9.19	34.2	6.94	1.41	6.13	0.99	5.59	1.06	3.09	0.40	2.97	0.48	30.0	193.22

(Continued)

10.3389/fmars.2023.1167578

TABLE 5 Continued

Sampling sites	Interval (cmbsf)	La (μg/g)	Ce (μg/g)	Pr (μg/g)	Nd (μg/g)	Sm (μg/g)	Eu (μg/g)	Gd (μg/g)	Tb (μg/g)	Dy (μg/g)	Ho (μg/g)	Er (μg/g)	Tm (μg/g)	Yb (μg/g)	Lu (μg/g)	Y (μg/g)	TREE (μg/g)
	410-420	39.2	77.7	8.91	33.8	6.72	1.37	5.93	0.99	5.53	1.08	3.23	0.43	3.03	0.47	30.7	188.38
	470-480	40.4	82.4	9.15	34.8	7.02	1.37	6.14	1.03	5.89	1.14	3.26	0.43	3.16	0.48	32.2	196.63
	530-540	38.8	77.2	8.90	33.3	6.71	1.25	5.84	0.92	5.38	1.05	3.02	0.41	2.91	0.44	29.2	186.19
	590-600	38.6	78.1	8.83	33.6	6.86	1.38	5.87	0.99	5.57	1.06	3.07	0.43	2.86	0.46	29.6	187.63
	650-660	40.9	81.0	9.28	34.7	7.02	1.44	6.27	0.99	5.76	1.08	3.09	0.43	2.95	0.45	30.0	195.38
	710-720	39.6	77.8	9.02	33.9	6.97	1.37	5.78	0.94	5.63	1.07	3.05	0.43	3.02	0.46	30.9	188.99

respectively (Figure 3). Due to the intense AOM, DIC concentrations and carbon isotopic compositions of sediment pore water vary greatly in the SMTZ. The maximum DIC concentration with the corresponding minimum $\delta^{13}C_{DIC}$ value is an indicative parameter for the depth of SMTZ in cold seeps (Malinverno and Pohlman, 2011). Compared with the slow changing $\delta^{13}C_{DIC}$ values of BH-CL46A, the $\delta^{13}C_{DIC}$ depth profiles of BH-CL37, BH-CL37A and BH-CL32A all show sudden decreasing trend at a certain depth, which confirm the existence of active AOM process (Figure 5). From minimum $\delta^{13}C_{DIC}$ depth corresponding to the maximum DIC content of pore water, we infer that the SMTZ depth in each sediment core is 530-540 cmbsf for BH-CL37, 290-300 cmbsf for BH-CL37A, and 470-480 cmbsf for BH-CL32A. But for BH-CL32A site, there is a gap of 100cm between the depth of the maximum DIC concentration and the minimum $\delta^{13}C_{DIC}$ value. We think because the distance between our adjacent samples was 50cm, the accuracy was not high enough. So some key information may not be reconstructed. respectively, The depth of SMTZ is slightly shallower than the SMTZ illustrated by the minimum value of SO_4^{2-} in the depth profiles. Kim et al. (2011) explained that this deviation was related to methanogenesis reaction and other biochemical reactions in the shallow sediments. The steep reduction of Ca^{2+} and Mg^{2+} at these depths also denotes the saturation of DIC and probable precipitation of authigenic carbonates (Figure 3), confirming the strong AOM. Based on the extremely low $\delta^{13}C_{DIC}$ and positive S isotope values of the carbonates in the sediment cores, Li et al. (2018) defined the possible paleo SMTZ depths of 5.5-6.2 mbsf and 6.8-7.2 mbsf in the Beikang Basin; Feng J. et al. (2018) determined that the approximate SMTZ depth was between 5.3 mbsf and 8.8 mbsf by studying the chemical characteristics of pore water in the sediment cores in the Beikang Basin. These SMTZ depths are slightly deeper than the estimated SMTZ depths in our study area, indicating that the cold seeps studied here may have experienced more intense methane seepage activity.

In addition, considering the influence of active cold seep activity (deep fluid migration), the increase of Mg^{2+}/Ca^{2+} in the deep sediments of BH-CL37A and BH-CL32A indicates strong carbonate precipitation (Figure 3). BH-CL37, which is relatively

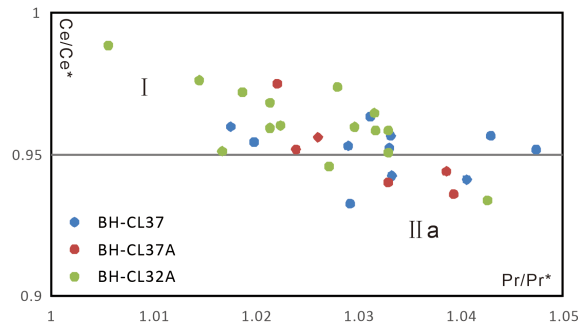

FIGURE 10
Ce/Ce* vs Pr/Pr* (Bau and Dulski, 1996; Shields and Webb, 2004) in the sediments. Zone I: no Ce and La anomaly; Zone II a: positive La anomaly, no Ce anomaly.

10.3389/fmars.2023.1167578

TABLE 6 Data of TOC, $\delta^{13}C_{TOC}$, $\delta^{13}C_{TIC}$ and $\delta^{18}O_{TIC}$ in sediments.

Sampling sites	Interval (cmbsf)	TOC (%)	$\delta^{13}C_{TOC}$ (‰)	$\delta^{13}C_{TIC}$ (‰)	$\delta^{18}O_{TIC}$ (‰)
BH-CL37					
	50-60	1.09	-23.10	0.98	-0.98
	110-120	0.80	-21.95	0.25	-1.33
	170-180	1.30	-23.80	0.71	-0.52
	230-240	0.95	-21.29	0.11	-1.04
	290-300	1.16	-23.64	-0.22	-1.29
	350-360	0.86	-23.72	-1.35	-0.75
	410-420	0.69	-22.90	-3.47	-1.84
	470-480	0.80	-24.34	-6.01	-2.02
	530-540	0.78	-25.01	-13.55	0.15
	590-600	0.72	-24.93	-14.15	-1.10
	650-660	0.67	-25.14	-13.98	-0.65
BH-CL37A					
	50-60	0.79	-22.91	-4.91	-0.33
	110-120	1.01	-24.35	-17.08	0.23
	170-180	0.83	-25.50	-13.37	0.46
	230-240	0.85	-23.92	-31.89	1.94
	290-300	0.76	-23.54	-25.34	-0.20
	350-360	0.83	-23.40	-13.27	0.08
BH-CL32A					
	50-60	0.99	-22.41	1.26	-0.81
	110-120	0.72	-21.70	0.86	-0.63
	170-180	0.76	-22.13	0.16	-1.46
	230-240	0.94	-22.60	0.30	-1.39
	290-300	0.86	-22.34	0.47	-1.17
	350-360	1.14	-25.88	-0.54	-2.51
	410-420	0.76	-25.57	-29.11	0.68
	470-480	0.86	-25.61	-11.87	-2.37
	530-540	0.78	-25.94	-15.08	0.38
	590-600	1.06	-25.77	-17.20	-0.10
	650-660	0.69	-24.78	-14.01	-1.09
	710-720	0.70	-25.10	-12.99	-0.94

close to BH-CL37A, doesn't show any similar trend, which may result from too small methane flux to induce manifest carbonate precipitation (Luff and Wallmann, 2003; Karaca et al., 2010). BH-CL46A shows high value of Mg^{2+}/Ca^{2+} at the bottom, which may be affected by deep fluid environment or horizontal fluid intrusion.

Previous studies have shown steep linear sulfate gradients under high methane fluxes and strong AOM effects (Borowski et al., 1996; Borowski et al., 1999). Here, the theoretical SMTZ calculated based on the linear extension of SO_4^{2-} is approximately 589.4 cmbsf, 371.4 cmbsf and 564.4 cmbsf (Figure 4). These are very close to the depth our observed, indicating certain reliability of our calculation.

TABLE 7 Results of sulfur isotopes of tubular pyrites in sediments.

Sampling sites	Interval (cmbsf)	$\delta^{34}S$ (‰)
BH-CL37		
	230-240	-43.64
	290-300	-37.46
	350-360	-45.05
	410-420	-37.06
	470-480	8.69
BH-CL37A		
	230-240	-28.41
	350-360	-7.81
BH-CL32A		
	110-120	-22.86
	170-180	-25.32
	230-240	-27.38
	290-300	-21.21
	350-360	-15.38
	470-480	-21.12

Besides, considering that concentration of SO_4^{2-} at SMTZ is often not zero in reality, the gap between our theoretical and observed SMTZ is reasonable. Based on the 1:1 reaction relationship between SO_4^{2-} and CH_4 in the AOM reaction and the low organic matter content in the sediments of the study area, we use the change of SO_4^{2-} to roughly define the methane diffusion flux in the SMTZ of the study area, 110 mol m^{-2} yr^{-1}, 135 mol m^{-2} yr^{-1} and 119 mol m^{-2} yr^{-1}, respectively (Figure 4), higher than that calculated in Feng J. et al. (2018), which indicates the active CH_4 leakage in the study and good gas storage potential in the Beikang Basin.

In contrast to pore water, sediment cores are formed in cumulative processes that record both current and past biochemical processes in geochemical features. In this study, $\delta^{13}C_{TIC}$ values of the sediments represent the mixture of biogenic carbonates (benthic and planktic foraminiferal shells) ($\delta^{13}C_{TIC}$ of about 1.1 ‰ V-PDB) and authigenic carbonates ($\delta^{13}C_{TIC}$ smaller than -30 ‰ V-PDB) (Figure 12) (Li et al., 2018; Wang et al., 2018). Our results show the lowest $\delta^{13}C_{TIC}$ value of the sediments near the SMTZ, which indicates that the authigenic carbonates were generated by strong AOM at SMTZ.

5.2 Response of environmental geochemical characteristics to cold seep activity

5.2.1 Sulfur isotope characteristics of tubular pyrites under the influence of AOM

Previous studies have shown that the AOM process can affect both the abundance of solid sulfide phase and its sulfur isotopic compositions in sediments (Canfield and Thamdrup, 1994; Borowski et al., 2013; Lin Z. et al., 2016). Sulfate reduction in anoxic marine sediments mainly includes organoclastic sulfate reduction (OSR; Berner, 1980), and anaerobic oxidation of

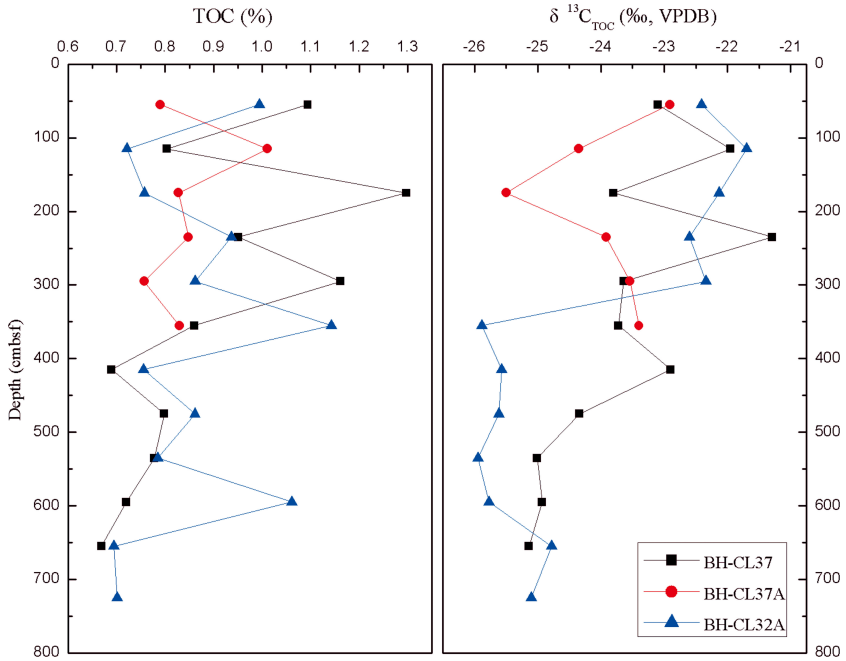

FIGURE 11
Depth profiles of TOC and $\delta^{13}C_{TOC}$ in the sediments.

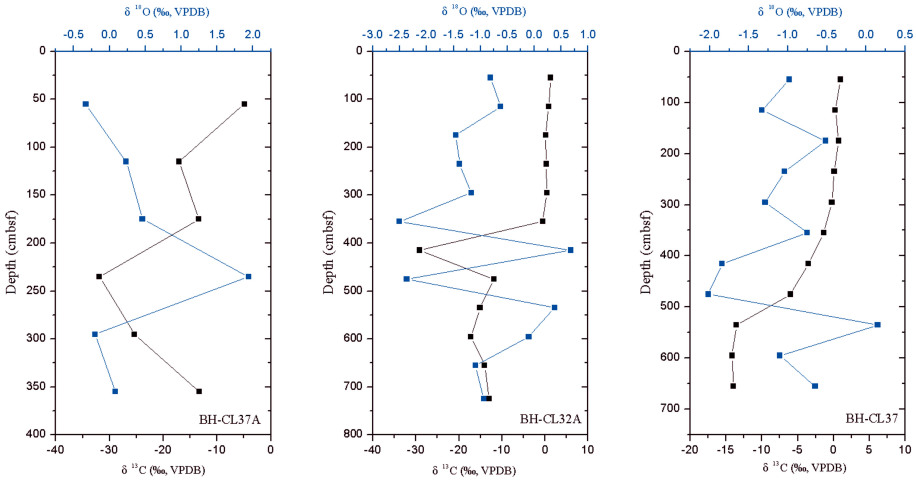

FIGURE 12
Depth profiles of the $\delta^{18}O_{TIC}$ and $\delta^{13}C_{TIC}$ in the sediments. Oxygen isotopes are shown in blue and carbon isotopes in black.

methane (AOM). The $\delta^{34}S$ value of dissolved sulfate in seawater is about 21‰ V-CDT (Rees et al., 1978), while the isotope fractionation can be as high as 60‰ V-CDT due to microbial sulfate reduction (Jørgensen et al., 2004). OSR is the main sulfate reduction process in methane-free sediments, usually leading to the production of poor ^{34}S sulfide, while ^{34}S of pyrite in methane-free sediments is often close to -50‰ to -40‰ V-CDT (Feng D. et al., 2018). In cold seeps, AOM strongly consumes sulfate under closed or semi-closed conditions, which may lead to the generation of sulfur compounds enriched in ^{34}S (Jørgensen et al., 2004; Lin et al., 2017; Feng D. et al., 2018). Although both OSR and AOM will lead to positive $\delta^{34}S$ (Feng D. et al., 2018), we think that changes of $\delta^{34}S$ at different depths at the same site can reflect the AOM process to small extent. The ^{34}S of tubular pyrites in BH-CL37, BH-CL37A and BH-CL32A have a large variation range,and present low and stable values in the shallow part, where the sulfate reduction rate is low and the fractionation is relatively thorough (Figure 13). Deeper than 350 cmbsf, all three sediment cores show high sulfur isotope values, and the values of BH-CL37A and BH-CL32A are generally bigger than -25‰ V-CDT. Both OSR and AOM will lead to positive $\delta^{34}S$, we think different ranges in sites between BH-CL37 and BH-CL32A are most likely due to the large differences in OSR rates among different sites. The values of $\delta^{34}S$ of pyrites at the bottom of BH-CL37 are even greater than 0 V-CDT, indicating that the reduction rate of sulfate is increasing. These prove the important influence of AOM on the S cycle in cold seeps, and the higher methane flux in the deeper formation also supports the AOM process. According to our results, the ^{34}S variations with depth and previous studies (Lin Z. et al., 2016; Feng D. et al., 2018), we speculate that pyrites formed near the SMTZ in the sediment core are likely to have higher ^{34}S isotope values. In addition, BH-CL37 and BH-CL37A are located at similar locations but affected by different intensities of cold seep activities, while the S isotopes of BH-CL37A are heavier in the same depth range, which may indicate a quicker sulfate consumption rate here and a stronger effect of cold seep.

5.2.2 Geochemical evidence of methane seepage variation

Cold seeps rich in methane usually have high biological abundance (Gibson et al., 2005; Campbell, 2006; Levin and Sibuet, 2012). The shallow parts of the sediment cores are abundant in the biological shells e.g. foraminifera and show a high content of Ca (Figure 7). The XRD results show that shallow sediments contain a high content of carbonates (Figure 6), mainly low magnesium calcite, which is associated with calcareous biological shells and deep fluids with low salinity.

Sr/Ca and Mg/Ca ratios in sediments have recently been used to reconstruct cold seep activities in the past in methane seepage (Yang et al., 2014; Gong et al., 2018). The images of Sr/Ca vs Mg/Ca (Figure 14) show the major calcite content with minor aragonite, which is consistent with our XRD results (Figure 6). As the depth

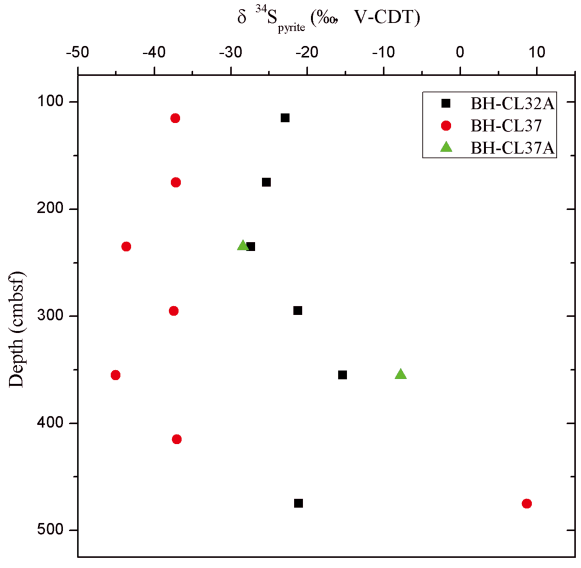

FIGURE 13
Depth profiles of sulfur isotopes of tubular pyrite in the sediment cores.

increases, the data points get closer to the reference detrital value, and there is a good correlation between Sr/Ca and Mg/Ca in the sediment cores, indicating that the influence of debris gradually increases with the increase of depth. Meanwhile, from the $\delta^{13}C_{TIC}$ and XRD results of shallow sediments, we conclude that the contents of carbonates in the sediment cores are not high enough and the carbonates in shallow sediments are mainly calcareous biological shells, which may conceal the information of authigenic carbonates. Therefore, it is difficult for Mg/Ca and Sr/Ca to directly and effectively reflect the types and formation of authigenic carbonates.

Specially, Sr, Ca/Al, Ca/Sr, Sr/Mg and Ca/Mg in the BH-CL37 sediments show a kick-type feature at depths of 290-300 cmbsf. The image of Ca^{2+}/Cl^{-} concentration in BH-CL37 pore water shows no addition of fluid from horizontal or other directions is found in this layer, and a relatively consistent Ca deposit rate is found in the corresponding depth range (Figure 3). As mentioned above, the information of elements of authigenic carbonates is easily covered by the biological shell information in the sediments, so the kick-type feature here reflects the precipitation of the authigenic carbonates with higher Ca/Sr, Sr/Mg and Ca/Mg ratios. Similar feature is also present in the depth profiles of Ba and Ni enrichment factors. Sr_{EF}, Ca concentration, Ca/Sr and Sr/Mg have a good correlation with the enrichment factors of trace elements Ba, Ni, Cu and Zn (as shown in Figure 15, Ca concentration, Ca/Sr and Sr/Mg etc. have similar relationship with these trace elements). Many studies have shown that the authigenic minerals in cold seeps may have recorded the changes of paleo cold seeps, while the Ba peak and authigenic carbonates are often considered as the indicator of paleo SMTZ (Torres et al., 1996; Dickens, 2001; Snyder et al., 2007; Vanneste et al., 2013; Gong et al., 2018; Feng D. et al., 2018). The correlations between Ni, Cu, Zn and Sr, Ca, Mg indicate that cold seep authigenic carbonates have strong enrichment and retention potential of trace elements (Smrzka et al., 2019; Smrzka et al., 2020). The good correlation between Ni and Sr is also present in our carbonate samples from southern SCS. Thus, this kick-type feature in BH-CL37 probably reflects a periodic strengthened AOM reaction, indicating the depth of the paleo SMTZ. $\delta^{34}S$ of pyrite in BH-CL37 also appears a relatively high value near the depth of 300 cmbsf, which provides evidence for the existence of paleo SMTZ.

SMTZ depth is reported to be affected by different methane fluxes (Michaelis et al., 2002; Luff et al., 2004). Generally, while the cold seep is more active, the methane flux is greater, and its SMTZ depth is shallower, and vice versa. The paleo SMTZ depth of BH-CL37 is obviously shallower than the present SMTZ depth, indicating that the methane flux of BH-CL37 was reduced and reflecting the existence of stronger methane leakage in a certain period in the past; this may be caused by the weakening of cold seep activity or the periodic decomposition of natural gas hydrate in the past, resulting in the local increase of methane. Similar feature in BH-CL37A is absent though these two cores are located closely. The reason may be that the larger and more concentrated deep fluid flow in BH-CL37A leading to a shallower SMTZ and more open condition, preventing the accumulation and preservation of authigenic carbonates and barite. Additionally, due to the limited permeability and fluid migration conditions, the locally increased methane leakage at BH-CL37 may not affect BH-CL37A.

5.2.3 cold seep influenced trace elements

The trace elements transported and ultimately enriched in seafloor sediments come from the sinking organic and inorganic particulate matter, as well as the seawater itself (Smrzka et al., 2019). Redox conditions often promote the accumulation of trace elements in sediments due to their redox sensitivity, which leads to the wide application of trace element contents as a proxy of paleo environmental conditions (Tribovillard et al., 2006).

Redox sensitive elements such as U, Mo and other trace elements are often used to trace the redox condition during the formation of cold seep carbonates (Merinero Palomares et al., 2012; Sato et al., 2012; Tribovillard et al., 2012; Hu et al., 2015). In oxidizing seawater, U and Mo are stable and persist for a long time (residence time of U and Mo is 450 kyr and 780 kyr, respectively), but U and Mo behave differently between the anoxic and euxinic

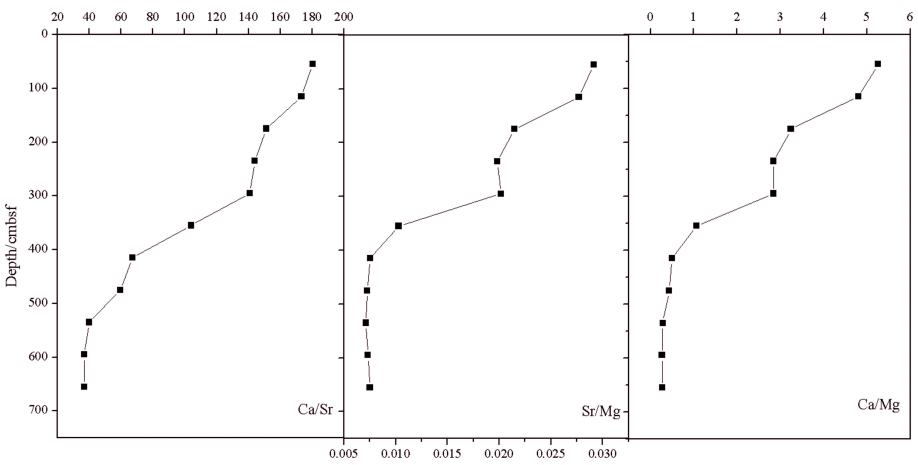

FIGURE 14
Sr/Ca vs Mg/Ca in the sediments. The values of aragonite, biological calcite, calcite and detrital fraction are derived from Yang et al.(2014).

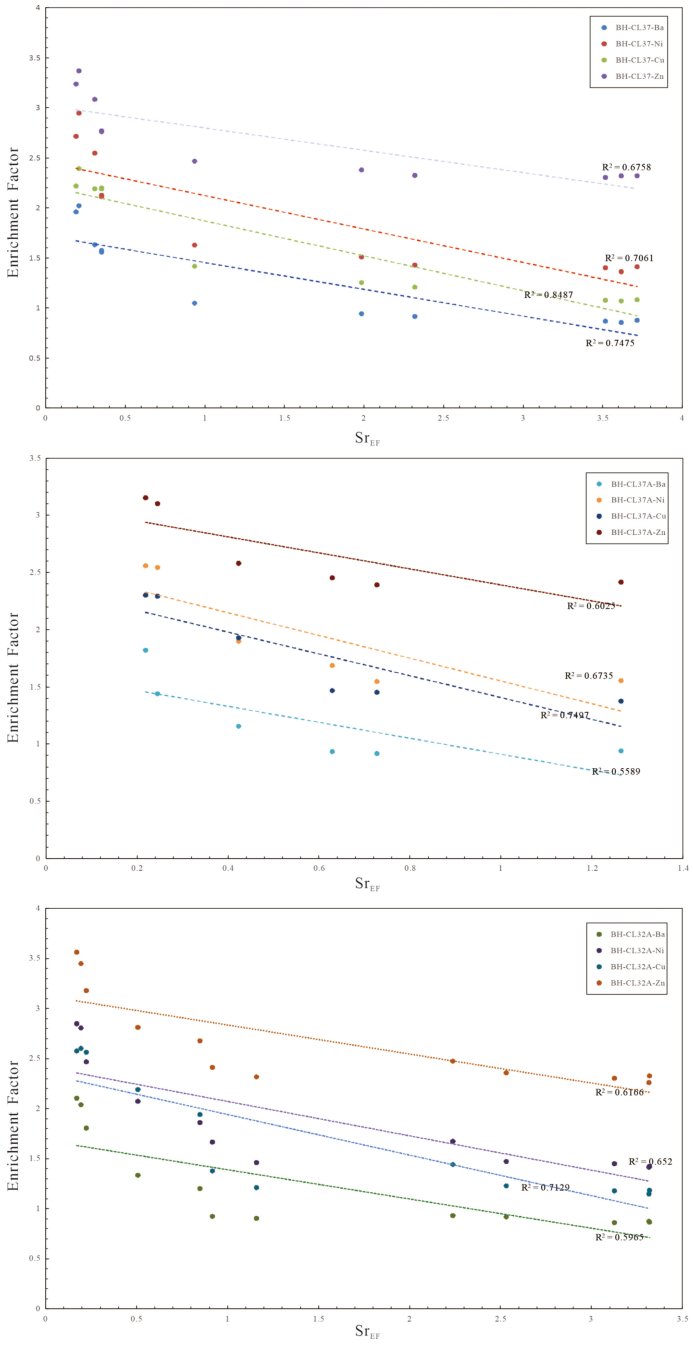

FIGURE 15
Correlations between Sr_{EF} and enrichment factors of trace elements (Ba, Ni, Cu, Zn).

environment (Algeo and Tribovillard, 2009). U exists stably in the soluble form of $UO_2(CO_3)_3^{4-}$ in oxidizing seawater; but in the iron reduction zone, the reduction of iron produces hydrogen sulfide, and U begins to form UO_2 precipitates or be absorbed by organometallic ligands and preserved in sediments (Tribovillard et al., 2006; Smrzka et al., 2019). As a result, U enrichment is stronger than Mo, resulting in the smaller $(Mo/U)_{EF}$ ratio in carbonates than the corresponding ratio in seawater (Algeo and Tribovillard, 2009). Mo mainly exists in the form of MoO_4^{2-} in oxidizing seawater, while in the euxinic environment caused by hydrogen sulfide supersaturation, Mo will transform and combine with metal ions to form a series of Molybdate thiomolybate ($MoS_{4-x}O_x^{2-}$) which is easily captured by iron sulfide or sulfur-rich organic compounds and stored in carbonates, finally resulting in the larger $(Mo/U)_{EF}$ ratio (Algeo and Tribovillard, 2009; Li et al., 2016; Smrzka et al., 2020). Therefore, the different authigenic enrichment degree of U and Mo, and $(Mo/U)_{EF}$ can help to distinguish euxinic condition from anoxic condition effectively.

U tends to enrich in the Fe-Mn reduction zone, while Mo is enriched in sulfate reduction zone (Smrzka et al., 2019; Smrzka et al.,

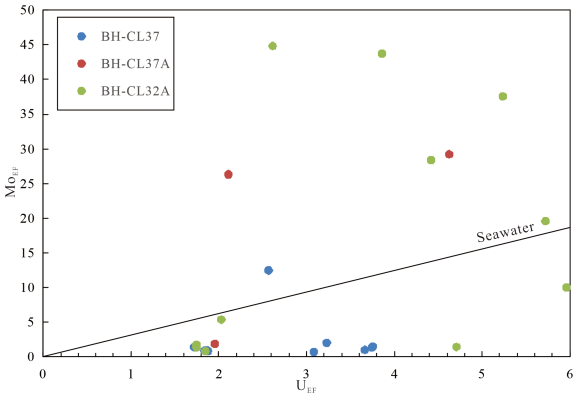

FIGURE 16
Mo_{EF} vs U_{EF}. $(Mo/U)_{EF}$ =3.1 of seawater (Algeo and Tribovillard, 2009).

2020). As shown in Figure 8, U is enriched in the shallow part of the sediments, and the enrichment depth of U varies among different sediment cores. The deeper SMTZ corresponds to the deeper Fe-Mn reduction zone. The Fe-Mn reduction zone of BH-CL37A appears narrower and shallower than that of BH-CL37 due to the stronger methane seepage found in BH-CL37A. Furthermore, the enrichment factors of U in the shallow depths of BH-CL37A are much higher than those of BH-CL37. Studies have shown that the behaviour of U varies greatly with oxygen content and it can be re-mobilized in case of post-deposition reoxygenation (Smrzka et al., 2019; Smrzka et al., 2020). BH-CL37A gains a greater cold seep effect due to the closer distance to the diapir than BH-CL37. The actively upward migration of anoxic fluid prevents the oxic seawater from diffusing into the sediments, so BH-CL37A could better preserve the enrichment of U, while seawater could diffuse downward to deeper formation in BH-CL37, harmful for the preservation of U enrichment. Moreover, considering the obvious change of methane flux in BH-CL37 in the past (discussed in section 5.2.2), the previously formed U precipitate was reactivated and dissolved in pore water due to the reoxygenation, weakening the indicator function of U enrichment. In contrast to BH-CL37, BH-CL37A has enough methane flux to maintain U enrichment even if the methane flux decreases, and the decrease of methane flux would also result in a more focused fluid seepage, protecting the original condition from fast change to some extent. Compared with the enrichment of U, the difference of V enrichment between BH-CL37 and BH-CL37A is not manifest (Figure 8), which further stresses that the decrease of cold seep fluid flow or the decrease after the sudden increase of methane flux does affect the enrichment degree of U by changing the redox conditions of sediments.

In anoxic marine sediments, Mo tends to be incorporated into pyrite by adsorbing molybdate and thiomolybdate to form stable complexes, which can be retained irreversibly (Bostick et al., 2003). Based on our Mo results, we believe that the euxinic environment in the study area is limited to pore water and does not include overlying seawater. Previous studies have shown that in areas where sulfide and thiomolybdate are present but confined to in pore water, Mo content in sediments averages 10 mg/kg and rarely exceeds 25 mg/kg, while Mo content under euxinic condition with free H_2S exceeds 60 mg/kg and can even reach 100 mg/kg in sediments (Scott and Lyons, 2012; Chen et al., 2016). Mo in our study area is significantly enriched at some depths, exceeding 30 μg/g (BH-CL37A: 50-120 cmbsf; BH-CL32A: 230-420 cmbsf) with low Mn contents, indicating euxinic environment in the pore water. OSR and AOM are two main important biochemical reactions related to the sulfate reduction that influence greatly on Mo. However, the low content of organic matter in sediments in the study area and the insignificant enrichment of redox sensitive elements such as Co, Cu, Ni, Zn and V (their enrichment factor are mostly under 3) indicate that OSR is not the main reason for the enrichment of Mo. In fact, rapid AOM reaction will create a suitable euxinic environment for Mo enrichment as a dominant process in cold seeps. It can be concluded from Figure 16 that Mo enrichment factor is greater than U enrichment factor at 350-360 cmbsf of BH-CL37, 50-120 cmbsf of BH-CL37A and 230-420 cmbsf of BH-CL32A, indicating the intense sulfate reduction. Though having the close locations and similar fluid sources, the depth profiles of Mo_{EF} vary greatly: Mo enrichment occurs only at 410-420 cmbsf in BH-CL37, while Mo is enriched significantly in shallow sediments in a wide depth range in BH-CL37A. From the difference of the methane seepage, we deduce that Mo enrichment is more likely to occur in shallow sediments with high methane flux. In methane fluid flow events or high methane flux, methane is transported to the water-sediment interface, and compresses the SMTZ into a narrow area of the topmost sediment cores where sulfate flux and hydrogen sulfide produced by rapid AOM are relatively high. However, deeper SMTZ usually appears with limited Mo availability in BH-CL37 (Figure 17). Comparing the depth profiles of U_{EF} and Mo_{EF}, high methane flux and active cold seep activity tend to compress the Fe-Mn reduction zone and sulfate reduction zone into a narrow area, so Mo and U are enriched within the same depth range (for example, in BH-CL37A, Figure 8). However, under the influence of low methane flux, the sediment core presents a wider sulfate reduction zone and a deeper SMTZ, accompanied by a lower Mo precipitation effect, such as BH-CL37.

BH-CL32A has a deep SMTZ similar as BH-CL37A and the overlap degree of Fe-Mn redox zone and sulfate reduction zone is lower than that of BH-CL37A (the area with high methane flux and high AOM reaction rate). In contrast to BH-CL37, evident Mo enrichment is present in several depth intervals of the shallow sediments here indicating the high AOM reaction rate and the relatively closed structural conditions at certain depths, indicating the high AOM reaction rate and the condition in favor of Mo diffusion.

Previous studies have shown that Mo-Fe-S can co-precipitate from pore water with the threshold of 0.1 μm H_2S, while Mo can co-precipitate with S or precipitate in granular form when H_2S is greater than 100 μm (Zheng et al., 2000; Chen et al., 2016). In other words, Mo can precipitate under the condition of 0.1 μm H_2S content in pore water with sufficient Fe, so the enrichment depth of Mo precipitation in pore water may not be consistent with the depth of H_2S maximum or SMTZ, which contributes to the inconsistent depth of the Mo enrichment and SMTZ in this study.

Other redox sensitive elements, such as Co, Cr, Cu, Zn, V, etc., generally show a relatively consistent trend of enrichment factors,

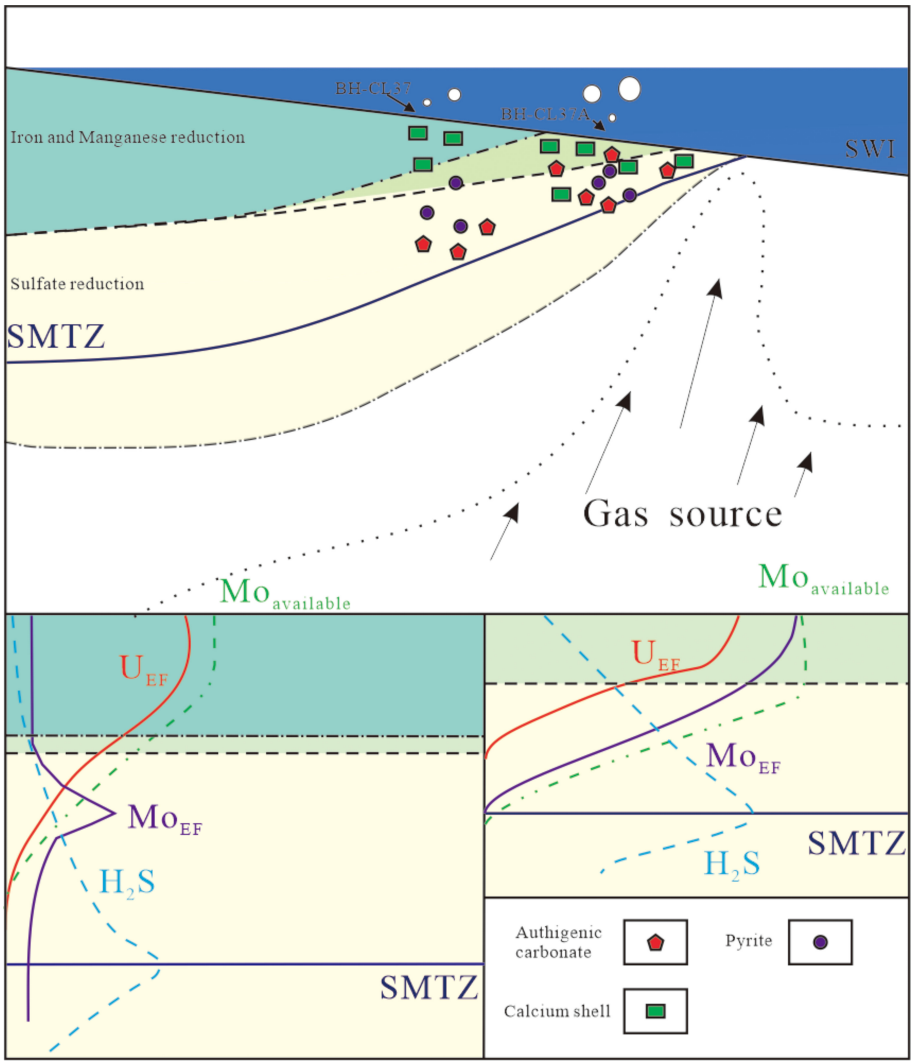

FIGURE 17
Response of different cold seep activities in BH-CL37 and BH-CL37A to geochemistry.

decreasing first and then stabilizing with the increase of depth (Figure 8). According to the Mn/Al image (Figure 7), the higher contents of trace elements in the shallow layer may be mainly from the reductive dissolution of manganese oxides or hydroxides (Tribovillard et al., 2006). Although these trace elements do not show significant enrichment factors, their changes to some extent reflect the changes of redox conditions in the sedimentary environment, and the speed of trace element removals often corresponds to the transition and transformation of iron reduction zone and sulfate reduction zone. As shown in Figure 8, compared with trace elements of BH-CL37, BH-CL37A has a shallower turning depth and a larger gradient of descent, indicating that the intense cold seep activity and large methane flux make the Fe-Mn reduction zone and sulfate reduction zone much closer, narrower and shallower. The enrichment of these trace elements in the shallow sediments reflects the relatively reductive pore water environment under the influence of cold seeps effectively.

The REE+Y distribution curves standardized by PAAS for each sediments cores show similar MREE-enriched pattern (Figure 9). MREE enrichment generally occurs in iron reduction zone and is related to anoxic pore water, indicating the anoxic sedimentary environment. The enrichment of Y shows the obvious influence of seawater. In this study, the samples generally show no Eu anomaly, and most of the samples show no Ce anomaly, while minor shows negative Ce anomaly caused by La anomaly (Figure 10), confirming the reductive condition.

5.3 Evolution and regional specificity of cold seep activity under the influence of different methane fluxes

BH-CL37 and BH-CL37A are two sites impacted by cold seeps located on the same side of the same fluid source with different distances (Figure 2). BH-CL37A closer to the fluid source, is affected

by stronger cold seep activity than BH-CL37, and has a larger methane fluid flux. Its intense AOM reaction and the relatively open environment of the shallow SMTZ may make the sulfur isotopes of pyrites in the shallow sediments larger than that of BH-CL37A at the corresponding depth, but less than that of BH-CL37 at deeper down to the bottom. Near the present SMTZ of BH-CL37, the more closed sedimentation environment is conductive to the deposits of authigenic pyrite with higher S isotopic values (>0), but impeding the Mo enrichment (Figure 17).

The seismic profile of BH-CL37 and BH-CL37A shows weak continuity of BSR and the seafloor dome (Figure 2). The low-frequency fuzzy reflection of the underlying layer on one side of the updip of the BSR may indicate the phenomenon of acoustic turbidity caused by gas in the formation and the rich source of methane in the study area, leading to the low background value of $\delta^{13}C_{DIC}$. The obvious geochemical differences between BH-CL37 and BH-CL37A in similar locations may denote the poor seepage conditions, such as low porosity or blocking effect on migration channels due to the formation of gas hydrate. Previous studies have measured that the geothermal gradient in this area is 69.8 °C/km, lower than the average geothermal gradient value of 84.5 °C/km in the Beikang Basin. Strong fluid activity is supposed to cause the change of the thermal field (Milkov, 2000; Feseker et al., 2009; Yang et al., 2018). The lower geothermal gradient indicates the more dispersed fluid diffusion, which corresponds to the wide and deep SMTZ in BH-CL37 and the smaller $\delta^{13}C_{TIC}$ fluctuation gradient (Figure 18). Meanwhile, the abnormally high ion concentrations (Cl^-, Mg^{2+},Ca^{2+}, SO_4^{2-}) in the 50-60 cmbsf of BH-CL37 are interpreted as the abnormal fluid input with high salinity, which may reflect the influence of high-salt fluid caused by the formation of natural gas hydrate, combined with previous studies and its regionally geological structures (Feng J. et al., 2018; Huang et al., 2022).

BH-CL32A has discontinuous BSR and significant submarine gas leakage (Figure 2). Figure 2B shows that BH-CL32A has a relatively isolated fluid migration channel that communicates with the deep strata and extends directly to the seafloor. Combined with its geothermal gradient as high as 102 °C/km, BH-CL32A shows obvious concentrated cold seep fluid upwelling, which is consistent with its high gradient of $\delta^{13}C_{DIC}$ with the narrow area of strong negative values(Figures 5, 18). The compositions of headspace gas in the study area further demonstrate a typical bio-methane source for BH-CL37 and mixed methane source with a significant contribution of the thermogenic gas for BH-CL32A (Huang et al., 2022), which is corresponding to our analysis of the geochemistry of pore water. BH-CL37 and BH-CL32A have similar SMTZ depths, but BH-CL37 has wider depth range of $\delta^{13}C$ strongly deficient (compared with the stable values at the top and bottom of the sediment cores). In general, the background $\delta^{13}C_{DIC}$ values (the average $\delta^{13}C_{DIC}$ of the top and bottom sediments that show stable values of $\delta^{13}C_{DIC}$) of BH-CL32A is slightly higher than that of the other sediment cores. The lower $\delta^{13}C_{DIC}$ values in BH-CL37 and BH-CL37A result from the abundant biogenic methane sources, and the higher values in BH-CL32A confirm the great influence of the thermogenous methane sources. Furthermore, the variation range of $\delta^{13}C_{DIC}$ in SMTZ is comparable to that of BH-CL37A, indicating the intense AOM in SMTZ in BH-CL32A. In BH-CL37, the lower reaction rate of AOM and the lower $\delta^{13}C_{DIC}$ here lead to a wider sulfate reduction zone, so the slope of $\delta^{13}C_{DIC}$ change is less obvious. Besides, BH-CL37 shows a shallower Fe and Mn reduction zone restricted by U enrichment and the lower AOM rate had a limited effect on Mo accumulation. By contrast, the intense and concentrated upwelling of cold seep fluid shown in BH-CL32A activates the exchange of elements between the overlying water and sediments, which is conducive to Mo enrichment.

6 Conclusion

In this paper, we combined geochemical analyses of various samples (pore water, sediments and authigenic pyrites) and the local geological structure to systematically study the cold seep phenomenon in southern SCS on the basis of previous studies. We conclude that SMTZ depth is relatively shallow compared with Feng's study.

The extremely negative $\delta^{13}C_{DIC}$ in the pore water of the sediment cores indicates strong AOM effect in cold seeps and the main biogenic origin of methane. The SO_4^{2-} depth variation trends of pore water, the high DIC content and the lowest value of $\delta^{13}C_{DIC}$ can define the approximate SMTZ depth of each sediment core effectively. In addition, paleo SMTZ depth of about 290-300 cmbsf in BH-CL37 indicates the decrease of methane flux or the sudden release of methane flux in the past.

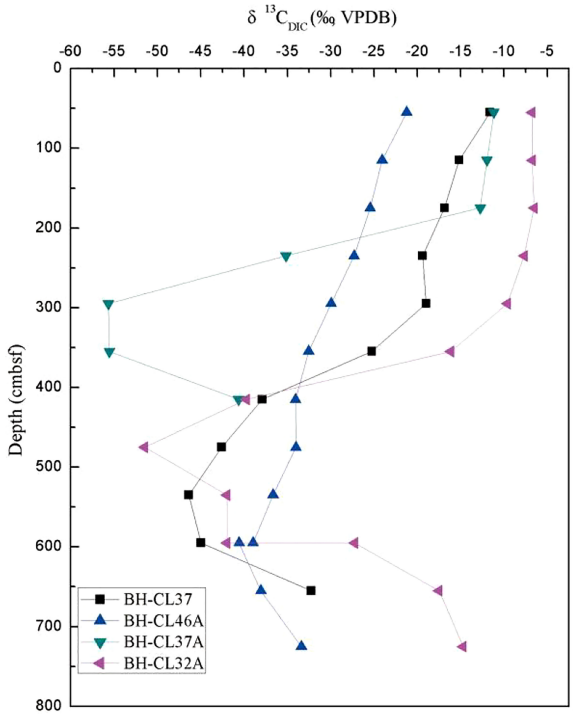

FIGURE 18
Comparison of $\delta^{13}C_{DIC}$ with depth in different sediment cores.

The strong AOM in cold seep leads to the formation of authigenic minerals (authigenic carbonates and authigenic pyrites), and affects the enrichment of trace elements, especially the redox sensitive elements.

BH-CL32A is different from BH-CL37 and BH-CL37A in fluid sources and regional geological structures. The $\delta^{13}C_{DIC}$ value of the background methane in BH-CL32A is higher, which may indicate a greater contribution of thermogenic gas. Furthermore, due to its high AOM rate, BH-CL32A shows a large and steep variation of $\delta^{13}C_{DIC}$ value in pore water, which indicates that the geochemistry in cold seep is closely related to fluid flux, methane sources and local geologic structures.

In conclusion, geologic tectonic conditions such as fluid migration channels in the study area can effectively constrain the generation and evolution of cold seeps, emphasizing the obvious regional specificity of cold seep.

Though many studies on columns and drill cores have been carried out in SCS, the complexity of geological features in the SCS aggravates differences of cold seeps. More quantities of researches on cold seeps in the SCS are inevitably requested for better understanding of cold seeps. With the Sunda continental shelf, one of the most extensive continental shelves in the world, southern SCS has great sensitivity to environmental changes and uniqueness different from northern SCS, pointing to the necessity of researches on cold seep here. Thus, we hope that this study can lay a foundation for the construction of a larger cold seep database in southern SCS and better knowledge of the cold seep system in the future.

Data availability statement

The original contributions presented in the study are publicly available. This data can be found here: https://data.mendeley.com/datasets/d7f9vt5bnt/1.

Author contributions

CC: Writing—original draft, Methodology, Data analysis. XW: Writing—original draft, Data analysis. ZW: Main idea, Methodology, Writing—review and editing. JS: Methodology, Project administration. WH: Methodology, Data analysis. WZha: Data analysis. JL: Supervision. ZX: Data analysis. WZho: Writing—review and editing. LZ: Methodology. All authors contributed to the article and approved the submitted version.

Funding

This work was supported by the Fund of National Nature Science Foundation of China (No. 4207605, 441776056), Innovation Group Project of Southern Marine Science and Engineering Guangdong Laboratory (Zhuhai) (No.311020003/311021004).

Conflict of interest

The authors declare that the research was conducted in the absence of any commercial or financial relationships that could be construed as a potential conflict of interest.

Publisher's note

All claims expressed in this article are solely those of the authors and do not necessarily represent those of their affiliated organizations, or those of the publisher, the editors and the reviewers. Any product that may be evaluated in this article, or claim that may be made by its manufacturer, is not guaranteed or endorsed by the publisher.

References

Algeo, T. J., and Tribovillard, N. (2009). Environmental analysis of paleoceanographic systems based on molybdenum-uranium covariation. *Chem. Geol.* 268, 211–225. doi: 10.1016/j.chemgeo.2009.09.001

Bau, M., and Dulski, P. (1996). Distribution of yttrium and rare-earth elements in the penge and kuruman iron-formations, Transvaal supergroup, south Africa. *Precambrian Res.* 79, 37–55. doi: 10.1016/0301-9268(95)00087-9

Bayon, G., Henderson, G. M., Etoubleau, J., Caprais, J.-C., Ruffine, L., Marsset, T., et al. (2015). U-Th Isotope constraints on gas hydrate and pockmark dynamics at the Niger delta margin. *Mar. Geol.* 370, 87–98. doi: 10.1016/j.margeo.2015.10.012

Bayon, G., Pierre, C., Etoubleau, J., Voisset, M., Cauquil, E., Marsset, T., et al. (2007). Sr/Ca and Mg/Ca ratios in Niger delta sediments: Implications for authigenic carbonate genesis in cold seep environments. *Mar. Geol.* 241, 93–109. doi: 10.1016/j.margeo.2007.03.007

Berner, R. (1980). *Early diagenesis: A theoretical approach* (Princeton: Princeton University Press). doi: 10.1515/9780691209401

Boetius, A., Ravenschlag, K., Schubert, C. J., Rickert, D., Widdel, F., Gieseke, A., et al. (2000). A marine microbial consortium apparently mediating anaerobic oxidation of methane. *Nature* 407, 623–626. doi: 10.1038/35036572

Boetius, A., and Wenzhöfer, F. (2013). Seafloor oxygen consumption fuelled by methane from cold seeps. *Nat. Geosci.* 6, 725–734. doi: 10.1038/ngeo1926

Borowski, W., Hoehler, T., Alperin, M., Rodriguez, N., and Paull, C. (2000). 9. significance of anaerobic methane oxidation in methane-rich sediments overlying the Blake ridge gas hydrates. *Proc. Ocean Drill. Progr. Sci. Results* 164, 87–99. doi: 10.2973/odp.proc.sr.164.214.2000

Borowski, W. S., Paull, C. K., and Ussler, W. (1996). Marine pore-water sulfate profiles indicate *in situ* methane flux from underlying gas hydrate. *Geology* 24, 655–658. doi: 10.1130/0091-7613(1996)024<0655:MPWSPI>2.3.CO;2

Borowski, W. S., Paull, C. K., and Ussler, W.III (1999). Global and local variations of interstitial sulfate gradients in deep-water, continental margin sediments: Sensitivity to underlying methane and gas hydrates. *Mar. Geol.* 159, 131–154. doi: 10.1016/S0025-3227(99)00004-3

Borowski, W. S., Rodriguez, N. M., Paull, C. K., and Ussler, W. (2013). Are 34S-enriched authigenic sulfide minerals a proxy for elevated methane flux and gas hydrates in the geologic record? *Mar. Pet. Geol.* 43, 381–395. doi: 10.1016/j.marpetgeo.2012.12.009

Bostick, B. C., Fendorf, S., and Helz, G. R. (2003). Differential adsorption of molybdate and tetrathiomolybdate on pyrite (FeS2). *Environ. Sci. Technol.* 37, 285–291. doi: 10.1021/es0257467

Boudreau, B. P. (1997). "Diagenetic models and their implementation: modeling transport and reactions in aquatic sediments," *Diagenetic Models and Their Implementation*, vol. 414. (New York: Springer).

Campbell, K. A. (2006). Hydrocarbon seep and hydrothermal vent paleoenvironments and paleontology: Past developments and future research directions. *Palaeogeogr. Palaeoclimatol. Palaeoecol.* 232, 362–407. doi: 10.1016/j.palaeo.2005.06.018

Canfield, D. E., and Thamdrup, B. (1994). The production of 34S-depleted sulfide during bacterial disproportionation of elemental sulfur. *Science* 266, 1973–1975. doi: 10.1126/science.11540246

Castellini, D. G., Dickens, G. R., Snyder, G. T., and Ruppel, C. D. (2006). Barium cycling in shallow sediment above active mud volcanoes in the gulf of Mexico. *Chem. Geol.* 226, 1–30. doi: 10.1016/j.chemgeo.2005.08.008

Chen, F., Hu, Y., Feng, D., Zhang, X., Cheng, S., Cao, J., et al. (2016). Evidence of intense methane seepages from molybdenum enrichments in gas hydrate-bearing sediments of the northern south China Sea. *Chem. Geol.* 443, 173–181. doi: 10.1016/j.chemgeo.2016.09.029

Chen, A., Xu, H., Luo, X., Liao, K., and Peng, D. (2017). Heat flow characteristics and controlling factors of the Baikang Basin in South China sea. *Acta Geologica Sinica* 91 (08):1720–1728. doi: 10.1007/s11430-010-0018-y

Chen, Z., Huang, C.-Y., Wu, B., and Yan, W. (2010). Discovery of native aluminum and its possible origin from prospective gas hydrate areas in the south China Sea. *Sci. China Earth Sci.* 53, 335–344. doi: 10.1007/s11430-010-0018-y

Chen, Y., Ussler, W., Haflidason, H., Lepland, A., Rise, L., Hovland, M., et al. (2010). Sources of methane inferred from pore-water δ13C of dissolved inorganic carbon in pockmark G11, offshore mid-Norway. *Chem. Geol.* 275, 127–138. doi: 10.1016/j.chemgeo.2010.04.013

Chen, Z., Yan, W., Tang, X., Liu, J., Chen, M., and Yang, H. (2009). Magnetic susceptibility in surface sediments in the southern south China Sea and its implication for sub-sea methane venting. *J. Earth Sci.* 20, 193–204. doi: 10.1007/s12583-009-0019-y

Claypool, G., Milkov, A., Lee, Y.-J., Torres, M., Borowski, W., and Tomaru, H. (2006). Microbial methane generation and gas transport in shallow sediments of an accretionary complex, southern hydrate ridge (ODP leg 204), offshore Oregon, USA. *Proc. Ocean Drill. Progr. Sci. Results* 204, 1–52. doi: 10.2973/odp.proc.sr.204.113.2006

Crémière, A., Lepland, A., Chand, S., Sahy, D., Kirsimäe, K., Bau, M., et al. (2016). Fluid source and methane-related diagenetic processes recorded in cold seep carbonates from the alvheim channel, central north Sea. *Chem. Geol.* 432, 16–33. doi: 10.1016/j.chemgeo.2016.03.019

Dickens, G. R. (2001). Sulfate profiles and barium fronts in sediment on the Blake ridge: present and past methane fluxes through a large gas hydrate reservoir. *Geochim. Cosmochim. Acta* 65, 529–543. doi: 10.1016/S0016-7037(00)00556-1

Feng, D., and Chen, D. (2015). Authigenic carbonates from an active cold seep of the northern south China Sea: New insights into fluid sources and past seepage activity. *Deep Sea Res. Part II Top. Stud. Oceanogr.* 122, 74–83. doi: 10.1016/j.dsr2.2015.02.003

Feng, D., Qiu, J. W., Hu, Y., Peckmann, J., Guan, H., Tong, H., et al. (2018). Cold seep systems in the south China Sea: An overview. *J. Asian Earth Sci.* 168, 3–16. doi: 10.1016/j.jseaes.2018.09.021

Feng, J., Yang, S., Liang, J., Fang, Y., He, Y., Luo, M., et al. (2018). Methane seepage inferred from the porewater geochemistry of shallow sediments in the beikang basin of the southern south China Sea. *J. Asian Earth Sci.* 168, 77–86. doi: 10.1016/j.jseaes.2018.02.005

Feseker, T., Dählmann, A., Foucher, J.-P., and Harmegnies, F. (2009). *In-situ* sediment temperature measurements and geochemical porewater data suggest highly dynamic fluid flow at Isis mud volcano, eastern Mediterranean Sea. *Mar. Geol.* 261, 128–137. doi: 10.1016/j.margeo.2008.09.003

Fu, S. (2007). Study on paleoclimate and paleoenvironment in the SouthernSouth China Sea since the late quaternary. *Diss. GSCAS.*

Gibson, R., Atkinson, R., Gordon, J., Editors, T., In, F., and Carney, R. (2005). Zonation of deep biota on continental margins. *Annu. Rev.* 43, 211–278. doi: 10.1201/9781420037449-8

Gong, S., Hu, Y., Li, N., Feng, D., Liang, Q., Tong, H., et al. (2018). Environmental controls on sulfur isotopic compositions of sulfide minerals in seep carbonates from the south China Sea. *J. Asian Earth Sci.* 168, 96–105. doi: 10.1016/j.jseaes.2018.04.037

Hu, Y., Feng, D., Liang, Q., Xia, Z., Chen, L., and Chen, D. (2015). Impact of anaerobic oxidation of methane on the geochemical cycle of redox-sensitive elements at cold-seep sites of the northern south China Sea. *Deep. Res. Part II Top. Stud. Oceanogr.* 122, 84–94. doi: 10.1016/j.dsr2.2015.06.012

Hu, Y., Luo, M., Chen, L., Liang, Q., Feng, D., Tao, J., et al. (2018). Methane source linked to gas hydrate system at hydrate drilling areas of the south China Sea: Porewater geochemistry and numerical model constraints. *J. Asian Earth Sci.* 168, 87–95. doi: 10.1016/j.jseaes.2018.04.028

Huang, W., Meng, M., Zhang, W., Shang, J., Liang, J., and Wan, Z. (2022). Geological, geophysical, and geochemical characteristics of deep-routed fluid seepage and its indication of gas hydrate occurrence in the beikang basin, southern south China Sea. *Mar. Pet. Geol.* 139, 105610. doi: 10.1016/j.marpetgeo.2022.105610

Ingram, W. C., Meyers, S. R., Shen, Z., Xu, H., and Martens, C. S. (2016). Manganese enrichments near a large gas-hydrate and cold-seep field: a record of past redox and sedimentation events. *Depos. Rec.* 2, 142–153. doi: 10.1002/dep2.18

Jørgensen, B. B., Böttcher, M. E., Lüschen, H., Neretin, L. N., and Volkov, I. I. (2004). Anaerobic methane oxidation and a deep H2S sink generate isotopically heavy sulfides in black Sea sediments. *Geochim. Cosmochim. Acta* 68, 2095–2118. doi: 10.1016/j.gca.2003.07.017

Joseph, C., Campbell, K. A., Torres, M. E., Martin, R. A., Pohlman, J. W., Riedel, M., et al. (2013). Methane-derived authigenic carbonates from modern and paleoseeps on the cascadia margin: Mechanisms of formation and diagenetic signals. *Palaeogeogr. Palaeoclimatol. Palaeoecol.* 390, 52–67. doi: 10.1016/j.palaeo.2013.01.012

Karaca, D., Hensen, C., and Wallmann, K. (2010). Controls on authigenic carbonate precipitation at cold seeps along the convergent margin off Costa Rica. *Geochem. Geophys. Geosyst* 11, Q08S27. doi: 10.1029/2010GC003062

Kim, J.-H., Park, M.-H., and Chun, J.-H. (2011). Molecular and isotopic signatures in sediments and gas hydrate of the central/southwestern ulleung basin: high alkalinity escape fuelled by biogenically sourced methane. *Geo-Mar Lett* 31:37–49. doi: 10.1007/s00367-010-0214-y

Levin, L. A. (2005). Ecology of cold seep sediments: Interactions of fauna with flow, chemistry and microbes. *Oceanogr. Mar. Biol.* 43, 1–46. doi: 10.1201/9781420037449.ch1

Levin, L. A., and Sibuet, M. (2012). Understanding continental margin biodiversity: A new imperative. *Ann. Rev. Mar. Sci.* 4, 79–112. doi: 10.1146/annurev-marine-120709-142714

Li, N., Feng, D., Chen, L., Wang, H., and Chen, D. (2016). Using sediment geochemistry to infer temporal variation of methane flux at a cold seep in the south China Sea. *Mar. Pet. Geol.* 77, 835–845. doi: 10.1016/j.marpetgeo.2016.07.026

Li, N., Yang, X., Peng, J., Zhou, Q., and Chen, D. (2018). Paleo-cold seep activity in the southern south China Sea: Evidence from the geochemical and geophysical records of sediments. *J. Asian Earth Sci.* 168, 106–111. doi: 10.1016/j.jseaes.2017.10.022

Liang, Q., Hu, Y., Feng, D., Peckmann, J., Chen, L., Yang, S., et al. (2017). Authigenic carbonates from newly discovered active cold seeps on the northwestern slope of the south China Sea: Constraints on fluid sources, formation environments, and seepage dynamics. *Deep. Res. Part I Oceanogr. Res. Pap.* 124, 31–41. doi: 10.1016/j.dsr.2017.04.015

Lin, Z., Sun, X., Peckmann, J., Lu, Y., Xu, L., Strauss, H., et al. (2016). How sulfate-driven anaerobic oxidation of methane affects the sulfur isotopic composition of pyrite: A SIMS study from the south China Sea. *Chem. Geol.* 440, 26–41. doi: 10.1016/j.chemgeo.2016.07.007

Lin, Z., Sun, X., Strauss, H., Lu, Y., Gong, J., Xu, L., et al. (2017). Multiple sulfur isotope constraints on sulfate-driven anaerobic oxidation of methane: Evidence from authigenic pyrite in seepage areas of the south China Sea. *Geochim. Cosmochim. Acta* 211, 153–173. doi: 10.1016/j.gca.2017.05.015

Lin, Q., Wang, J., Algeo, T. J., Sun, F., and Lin, R. (2016). Enhanced framboidal pyrite formation related to anaerobic oxidation of methane in the sulfate-methane transition zone of the northern south China Sea. *Mar. Geol.* 379, 100–108. doi: 10.1016/j.margeo.2016.05.016

Liu, H., Yao, Y., and Deng, H. (2011). Geological and geophysical conditions for potential natural gas hydrate resources in southern south China Sea waters. *J. Earth Sci.* 22, 718–723. doi: 10.1007/s12583-011-0222-5

Luff, R., and Wallmann, K. (2003). Fluid flow, methane fluxes, carbonate precipitation and biogeochemical turnover in gas hydrate-bearing sediments at hydrate ridge, cascadia margin: numerical modeling and mass balances. *Geochim. Cosmochim. Acta* 67, 3403–3421. doi: 10.1016/S0016-7037(03)00127-3

Luff, R., Wallmann, K., and Aloisi, G. (2004). Numerical modeling of carbonate crust formation at cold vent sites: significance for fluid and methane budgets and chemosynthetic biological communities. *Earth Planet. Sci. Lett.* 221, 337–353. doi: 10.1016/S0012-821X(04)00107-4

Malinverno, A., and Pohlman, J. W. (2011). Modeling sulfate reduction in methane hydrate-bearing continental margin sediments: Does a sulfate-methane transition require anaerobic oxidation of methane? *Geochem. Geophys. Geosyst.* 12, Q07006. doi: 10.1029/2011GC003501

McLennan, S. (2001). Relationships between the trace element composition of sedimentary rocks and upper continental crust. geochemistry geophys. *Geosystems - GEOCHEM Geophys GEOSYST* 2. doi: 10.1029/2000GC000109

Merinero Palomares, R., Lunar Hernández, R., and Martínez Frías, J. (2012). Mechanisms of trace metal enrichment in submarine, methane-derived carbonate chimneys from the gulf of cadiz. *J. Geochemical Explor.* 112, 297–305. doi: 10.1016/j.gexplo.2011.09.011

Michaelis, W., Seifert, R., Nauhaus, K., Treude, T., Thiel, V., Blumenberg, M., et al. (2002). Microbial reefs in the black Sea fueled by anaerobic oxidation of methane. *Science* 297, 1013–1015. doi: 10.1126/science.1072502

Milkov, A. V. (2000). Worldwide distribution of submarine mud volcanoes and associated gas hydrates. *Mar. Geol.* 167, 29–42. doi: 10.1016/S0025-3227(00)00022-0

Morley, C. K. (2012). Late Cretaceous–early palaeogene tectonic development of SE Asia. *Earth-Science Rev.* 115, 37–75. doi: 10.1016/j.earscirev.2012.08.002

Orphan, V., Hinrichs, K.-U., Ussler, B., Paull, C., Taylor, L., Sylva, S., et al. (2001). Comparative analysis of methane-oxidizing archaea and sulfate-reducing bacteria in anoxic marine sediments. *Appl. Environ. Microbiol.* 67, 1922–1934. doi: 10.1128/AEM.67.4.1922-1934.2001

Peketi, A., Mazumdar, A., Joao, H. M., Patil, D. J., Usapkar, A., and Dewangan, P. (2015). Coupled c-S-Fe geochemistry in a rapidly accumulating marine sedimentary system: diagenetic and depositional implications. *Geochem. Geophys. Geosyst.* 16, 2865–22883. doi: 10.1002/2015GC005754

Reeburgh, W. (2007). Oceanic methane biogeochemistry. *Chem. Rev.* 107, 486–513. doi: 10.1021/cr050362v

Rees, C. E., Jenkins, W. J., and Monster, J. (1978). The sulphur isotopic composition of ocean water sulphate. *Geochim. Cosmochim. Acta* 42, 377–381. doi: 10.1016/0016-7037(78)90268-5

Riedinger, N., Kasten, S., Gröger, J., Franke, C., and Pfeifer, K. (2006). Active and buried authigenic barite fronts in sediments from the Eastern cape basin. *Earth Planet. Sci. Lett.* 241, 876–887. doi: 10.1016/j.epsl.2005.10.032

Sackett, W. M. (1978). Carbon and hydrogen isotope effects during the thermocatalytic production of hydrocarbons in laboratory simulation experiments. *Geochim. Cosmochim. Acta* 42, 571–580. doi: 10.1016/0016-7037(78)90002-9

Sato, H., Hayashi, K. I., Ogawa, Y., and Kawamura, K. (2012). Geochemistry of deep sea sediments at cold seep sites in the nankai trough: Insights into the effect of anaerobic oxidation of methane. *Mar. Geol.* 323–325, 47–55. doi: 10.1016/j.margeo.2012.07.013

Scott, C., and Lyons, T. W. (2012). Contrasting molybdenum cycling and isotopicproperties in euxinic versus non-euxinic sediments and sedimentary rocks: Refining the paleoproxies. *Chem. Geol.* 324–325, 19–27. doi: 10.1016/j.chemgeo.2012.05.012

Shields, G. A., and Webb, G. E. (2004). Has the REE composition of seawater changed over geological time? *Chem. Geol.* 204, 103–107. doi: 10.1016/j.chemgeo.2003.09.010

Smrzka, D., Feng, D., Himmler, T., Zwicker, J., Hu, Y., Monien, P., et al. (2020). Trace elements in methane-seep carbonates: Potentials, limitations, and perspectives. *Earth-Science Rev.* 208. doi: 10.1016/j.earscirev.2020.103263

Smrzka, D., Zwicker, J., Bach, W., Feng, D., Himmler, T., Chen, D., et al. (2019). *The behavior of trace elements in seawater, sedimentary pore water, and their incorporation into carbonate minerals: a review, facies* (Berlin Heidelberg: Springer). doi: 10.1007/s10347-019-0581-4

Snyder, G. T., Dickens, G. R., and Castellini, D. G. (2007). Labile barite contents and dissolved barium concentrations on Blake ridge: New perspectives on barium cycling above gas hydrate systems. *J. Geochemical Explor.* 95, 48–65. doi: 10.1016/j.gexplo.2007.06.001

Su, X., Chen, F., Yu, X., and Huang, Y. (2005). A pilot study on Miocene through Holocene sediments from the continental slope of the south China Sea in correlation with possible distribution of gas hydrates. *Geoscience* 19, 1–13.

Suess, E. (2014). Marine cold seeps and their manifestations: geological control, biogeochemical criteria and environmental conditions. *Int. J. Earth Sci.* 103, 1889–1916. doi: 10.1007/s00531-014-1010-0

Tong, H., Feng, D., Cheng, H., Yang, S., Wang, H., Min, A. G., et al. (2013). Authigenic carbonates from seeps on the northern continental slope of the south China Sea: New insights into fluid sources and geochronology. *Mar. Pet. Geol.* 43, 260–271. doi: 10.1016/j.marpetgeo.2013.01.011

Torres, M. E., Brumsack, H. J., Bohrmann, G., and Emeis, K. C. (1996). Barite fronts in continental margin sediments: a new look at barium remobilization in the zone of sulfate reduction and formation of heavy barites in diagenetic fronts. *Chem. Geol.* 127, 125–139. doi: 10.1016/0009-2541(95)00090-9

Tribovillard, N., Algeo, T. J., Baudin, F., and Riboulleau, A. (2012). Analysis of marine environmental conditions based onmolybdenum–uranium covariation–applications to mesozoic paleoceanography. *Chem. Geol.* 324–325, 46–58. doi: 10.1016/j.chemgeo.2011.09.009

Tribovillard, N., Algeo, T. J., Lyons, T., and Riboulleau, A. (2006). Trace metals as paleoredox and paleoproductivity proxies: An update. *Chem. Geol.* 232, 12–32. doi: 10.1016/j.chemgeo.2006.02.012

Tribovillard, N., Du Châtelet, E. A., Gay, A., Barbecot, F., Sansjofre, P., and Potdevin, J. L. (2013). Geochemistry of cold seepage-impacted sediments: Per-ascensum or per-descensum trace metal enrichment? *Chem. Geol.* 340, 1–12. doi: 10.1016/j.chemgeo.2012.12.012

Trung, N. N. (2012). The gas hydrate potential in the south China Sea. *J. Pet. Sci. Eng.* 88–89, 41–47. doi: 10.1016/j.petrol.2012.01.007

Vanneste, H., James, R. H., Kelly-Gerreyn, B. A., and Mills, R. A. (2013). Authigenic barite records of methane seepage at the carlos ribeiro mud volcano (Gulf of cadiz). *Chem. Geol.* 354, 42–54. doi: 10.1016/j.chemgeo.2013.06.010

Wan, Z., Chen, C., Liang, J., Zhang, W., Huang, W., and Su, P. (2020). Hydrochemical characteristics and evolution mode of cold seeps in the qiongdongnan basin, south China Sea. *Geofluids*. doi: 10.1155/2020/4578967

Wang, M., Cai, F., Li, Q., Liang, J., Yan, G. J., Dong, G., et al. (2015). Characteristics of authigenic pyrite and its sulfur isotopes, influenced by methane seep at Core A, Site 79 of the middle Okinawa trough. *Sci. China: Earth Sci.* 45, 1819–1828. doi: 10.1007/s11430-015-5196-1

Wang, X., Li, N., Feng, D., Hu, Y., Bayon, G., Liang, Q., et al. (2018). Using chemical compositions of sediments to constrain methane seepage dynamics: A case study from haima cold seeps of the south China Sea. *J. Asian Earth Sci.* 168, 137–144. doi: 10.1016/j.jseaes.2018.11.011

Wang, S., Yan, W., and Song, H. (2006). Mapping the thickness of the gas hydrate stability zone in the south China Sea. *Terr. Atmos. Ocean. Sci.* 17, 815–828. doi: 10.3319/TAO.2006.17.4.815(GH

Wang, S., Yan, W., Song, H., and Fan, S. (2005). Change of gas hydrate reservoirs in the southern south China Sea from the last glacial maximum to present and its effect on the environmen. *Chin. J. Geophys* 48 (5), 1117–1124. doi: 10.1002/cjg2.764

Wang, H., Zhang, G., Yang, M., Liang, J., Liang, J., and Zhong, G. (2003). Structural circumstance of gas hydrate deposition in the continent margin, the south China Sea. *Mar. Geol. Quat. Geol* 23, 82–83. doi: CNKI:SUN:HYDZ.0.2003-01-013

Wei, W., Zhang, J., Wei, X., and Wang, Y. (2012). Resource potential analysis of natural gas hydrate in south China Sea. *Prog. Geophys* 27, 2646–2655. doi: CNKI: SUN: DQWJ.0.2012-06-044

Whiticar, M. J. (1999). Carbon and hydrogen isotope systematics of bacterial formation and oxidation of methane. *Chem. Geol.* 161, 291–314. doi: 10.1016/S0009-2541(99)00092-3

Xie, X., Zhang, C., Ren, J., Yao, B., Wan, L., Chen, H., et al. (2011). Effects of distinct tectonic evolutions on hydrocarbon accumulation in northern and southern continental marginal basins of the south China Sea. *Chin. J. Geophys* 54, 3280–3291. doi: 10.1002/cjg2.1687

Yan, W., Zhang, G., Zhang, L., Xia, B., Yang, Z., Lei, Z., et al. (2018). Focused fluid flow systems and their implications for hydrocarbon accumulations on the southern margin of south China Sea. *Geol. China* 45, 39–47. doi: 10.12029/gc20180104

Yang, K., Chu, F., Ye, L., Zhang, W., Xu, D., Zhu, J., et al. (2014). Implication of methane seeps from sedimentary geochemical proxies (Sr/Ca & Mg/Ca) in the northern south China Sea. *J. Jilin Univ. Earth Sci. Ed.* 44, 469–479. doi: 10.13278/j.cnki.jjuese.201402106

Yang, H.-T., Yang, D.-B., Mu, M.-S., Wang, A.-Q., Quan, Y.-K., Hao, L.-R., et al. (2019). Sr–Nd–Hf isotopic compositions of lamprophyres in western Shandong, China: Implications for the nature of the early cretaceous lithospheric mantle beneath the eastern north China craton. *Lithos.* 336–337, 1–13. doi: 10.1016/j.lithos.2019.03.030

Yang, X., Zhong, S., and Wan, Z. (2018). The thermodynamics of mud diapir/volcano fluidand its influence on gas hydrate occurrence. *Mar. Geology Front.* 34, 15–23. doi: 10.16028/j.1009-2722.2018.07003

Yao, B. (2007). The forming condition and distribution characteristics of the gas hydrate in the south China Sea. *Offshore Oil* 27, 1–10. doi: CNKI:SUN:HYDZ.0.2005-02-017

Zhang, G., Zhu, W., Mi, L., Zhang, H., Liang, J., and Qu, H. (2010). The theory of hydrocarbon generation controlled by source rock and heat from circle distribution of outside-oil fields and inside-gas fields in south China Sea. *Acta Sedimentol. Sin.* 28, 987–1005. doi: 10.1017/S0004972710001772

Zheng, Y., Anderson, R. F., Van Geen, A., and Kuwabara, J. (2000). Authigenic molybdenum formation in marine sediments: a link to pore water sulfide in the Santa Barbara basin. *Geochim. Cosmochim. Acta* 64, 4165–4178. doi: 10.1016/S0016-7037(00)00495-6

Zhu, Y., Zhang, G., and Lou, Z. (2001). Gas hydrate in the south China Sea: background and indicators. *Acta Petrol. Sin.* 22, 6–10. doi: 10.3321/j.issn:0253-2697.2001.05.002

frontiers | Frontiers in Marine Science

TYPE Original Research
PUBLISHED 20 April 2023
DOI 10.3389/fmars.2023.1187594

OPEN ACCESS

EDITED BY
Wei Li,
South China Sea Institute of Oceanology (CAS), China

REVIEWED BY
Xiting Liu,
Ocean University of China, China
Tao Yang,
Nanjing University, China

*CORRESPONDENCE
Xudong Wang
xd-wang@shou.edu.cn

SPECIALTY SECTION
This article was submitted to Marine Biogeochemistry, a section of the journal Frontiers in Marine Science

RECEIVED 16 March 2023
ACCEPTED 10 April 2023
PUBLISHED 20 April 2023

CITATION
Feng X, Jia Z and Wang X (2023) Uncovering the temporal carbon isotope ($\delta^{13}C$) heterogeneity in seep carbonates: a case study from Green Canyon, northern Gulf of Mexico.
Front. Mar. Sci. 10:1187594.
doi: 10.3389/fmars.2023.1187594

Uncovering the temporal carbon isotope ($\delta^{13}C$) heterogeneity in seep carbonates: a case study from Green Canyon, northern Gulf of Mexico

Xia Feng[1], Zice Jia[2] and Xudong Wang[2]*

[1]Guangdong Polytechnic of Environmental Protection Engineering, Foshan, Guangdong, China, [2]Shanghai Engineering Research Center of Hadal Science and Technology, College of Marine Sciences, Shanghai Ocean University, Shanghai, China

Authigenic carbonates that form at hydrocarbon seeps, known as seep carbonates, are direct records of past fluid flow close to the seafloor. Stable carbon isotopes of seep carbonates ($\delta^{13}C_{carb}$) have been widely used as a proxy for determining fluid sources and seepage mode. Although the spatial heterogeneity of $\delta^{13}C$ in seep carbonates is increasingly understood, the temporal heterogeneity of $\delta^{13}C$ in seep carbonates is not well studied. In this study, we report $\delta^{13}C$ values of different components (clasts, matrix, and pore-filling cements) for 124 subsamples drilled across an authigenic carbonate block from Green Canyon block 140 (GC140) of the northern Gulf of Mexico continental slope. High-Mg calcite is the dominant mineral regardless the types of components. The $\delta^{13}C_{carb}$ values range from –39.6‰ to 3.6‰, indicating multiple dissolved inorganic carbon (DIC) sources that include methane carbon (^{13}C-depleted), seawater DIC, and residual CO_2 from methanogenesis (^{13}C-enriched). Specifically, the clasts show large variability in $\delta^{13}C$ values (–39.6‰ to 2.3‰; mean: –27.6‰, n = 71), demonstrating the dominance of methane-derived fluids during formation at the initial seepage stage. The $\delta^{13}C$ values of the matrix vary between –29.4‰ and 3.4‰ (mean: –11.6‰, n = 21). The carbon isotopes of pore-filling cements that formed most recently vary narrowly, with $\delta^{13}C$ values of –3.2‰ to 3.6‰ (mean: 1.7‰, n = 28). Isotopic variations within individual samples were observed in seep carbonate. However, common trends occur across components of carbonates that formed during different seepage stages. This suggests that the temporal evolution of local fluid sources may play an important role in determining carbonate isotope geochemistry. Studies regarding seeps must take into account the highly variable fluids that leave their geochemical imprints on the seep carbonate.

KEYWORDS

hydrocarbon seep, methane, authigenic carbonate, stable carbon isotopes, Gulf of Mexico

1 Introduction

Observations of methane seepage in marine settings are common (Suess, 2020, and references therein). The seeping methane is primarily consumed by consortia of methane-oxidizing archaea and sulfate-reducing bacteria, a process known as anaerobic oxidation of methane (e.g., Boetius et al., 2000). As a result, carbonate alkalinity increase induces the precipitation of carbonate minerals close to the seafloor. These carbonates serve as an excellent archive of past seepage (Ritger et al., 1987; Bohrmann et al., 1998; Aloisi et al., 2000; Peckmann et al., 2001; Mazzini et al., 2004; Gontharet et al., 2007; Naehr et al., 2007; Haas et al., 2010; Sun et al., 2015; Himmler et al., 2019; Wang et al., 2022).

Carbon isotopes in the mineral phase of seep carbonate are derived from ambient bicarbonate and dissolved inorganic carbon (DIC). The variation of carbon isotopic composition of these carbonates (as much as 85‰) indicating an almost equally wide range of geochemical processes involved in carbonate precipitation (e.g., Naehr et al., 2007). The stable carbon isotopes of seep carbonates ($\delta^{13}C_{carb}$) have been widely used since the discovery of methane seep in 1980s for almost any carbonate-based seep studies. For instance, $\delta^{13}C$ values provided stable isotopic evidence for methane seeps in Neoproterozoic postglacial cap carbonates (Jiang et al., 2003), demonstrated the involvement of oil seepage (Smrzka et al., 2016; Sun et al., 2020), meteoric water and methogenesis during carbonate formation (Naehr et al., 2007).

Seep carbonates are known to show a wide range of carbon isotopic and variation across multiple geographic areas (Gontharet et al., 2007; Roberts et al., 2010; Zhang et al., 2023). The observed variations, spatial heterogeneity of $\delta^{13}C$ in seep carbonates, mainly reflect local controls on the sources of fluids and flux of the fluids, which have been well constrained. In contrast, carbon isotopic variation in authigenic carbonate composition within individual study samples, the temporal heterogeneity of $\delta^{13}C$ in seep carbonates is not well studied. Such temporal heterogeneity of $\delta^{13}C$ in seep carbonates can be used to constrain the evolution of the fluid sources and mode of seepage with time. Given that seep-related authigenic minerals provide an important geological archive, as they represent one of the few permanent records of an otherwise ephemeral phenomenon (Roberts et al., 2010; Smrzka et al., 2016; Chen et al., 2019).

The aim of this paper is to assess the heterogeneity of $\delta^{13}C$ in a single seep carbonate sample to reveal the evolution of seep fluids during carbonate formation. We describe different types of components of the studied carbonates including clasts, matrix, and pore-filling cements that represent archive of variation between different formation stages. We use the obtained data to constrain the conditions under which carbonate formation occurred and uncover the temporal carbon isotope heterogeneity during the precipitation.

2 Samples and methods

2.1 Samples

The Green Canyon block 140 (GC140) seep site is in the northern upper continental slope of the GOM (Figure 1; Roberts et al., 1989; Roberts and Feng, 2013). Bathymetric and high-resolution seismic profiles and side-scan sonographs indicate that the thin sedimentary sequence over the shallow salt mass of site GC140 is broken by numerous faults and that most mounded carbonates are cut due to salt deformation (Roberts and Carney, 1997; Roberts et al., 2000). Previous investigations revealed the occurrence of mound-like buildups, 20-100 m in diameter and up to 20 m in height, are composed of chaotically oriented carbonate blocks in the surrounding sediments (Roberts et al., 1990; Roberts and Aharon, 1994; Roberts et al., 2000; Roberts et al., 2010; Roberts and Feng, 2013). In terms of the seepage, the site GC140 is currently not active. However, scattered living tube worms and sponges were present at the sampling site (Roberts et al., 2010). The studied authigenic carbonate was recovered during Pisces II dive in 1989

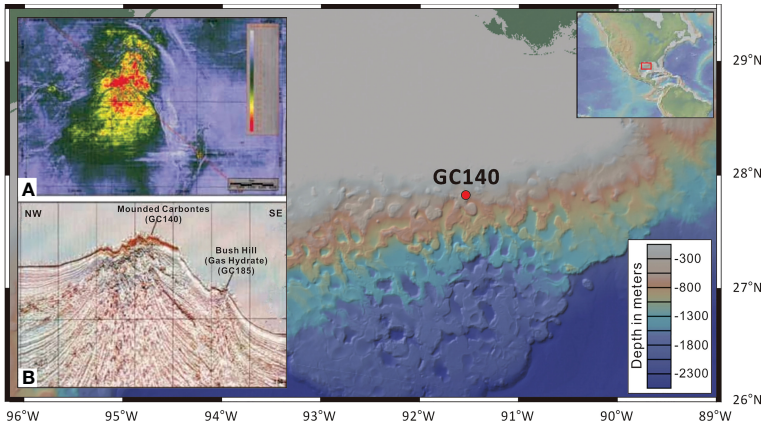

FIGURE 1
Location of the Green Canyon block 140 (GC140; 27°48′N/91°32′W) study site, northern Gulf of Mexico (from Bian et al., 2013). The inset 3-D seismic surface amplitude illustrates the extent of the hard bottom **(A)** and the profile view **(B)**, showing that the dome top has an irregular surface and that the seafloor reflector is a strong, positive reflector, indicating a hard bottom (Roberts, 2001).

(Roberts et al., 1989). The sample was collected from the seafloor. The water depth at the site was 320 m, and the bottom water temperature was about 13°C (Roberts et al., 2010).

2.2 Methods

After collection, the sample was rinsed with fresh water and left to air dry. The resulting carbonate block was photographed digitally and then cut into slabs using a water-lubricated rock saw. Each slab was also photographed. Visual examination of the rock slab used to distinguish main components of the carbonate (see Figure 2), which were determined to be clasts, matrix, and pore-filling cements. All components were collected using a dental drill to determine their mineralogy. Mineralogy was determined using x-ray diffraction (XRD) using a Rigaku DXR 3000 computer-automated diffractometer at the Guangzhou Institute of Geochemistry, Chinese Academy of Sciences (CAS). Bulk samples were powdered to less than 200 mesh. The x-ray source operated at 40 kV and 40 mA using CuKα radiation equipped with a diffracted beam graphite monochromator. Scans were made through a 5-65° using a 0.02° step at 5 sec/step.

Subsamples for carbonate carbon and oxygen isotopes were extracted from polished rock slabs using a hand-held dental drill. Clast, matrix, and pore-filling cements were selected for sampling (see Figure 2 for sampling locations). The powdered samples were processed with 100% phosphoric acid at 70°C to release CO2 for analysis using a Delta V Advantage stable isotopic mass spectrometer at Shanghai Ocean University. All isotope values are expressed using the δ-notion relative to the Vienna-Pee Dee Belemnite (V-PDB) standard. The values were reported in permil (‰) with a standard deviation of less than 0.1‰ (2σ) for both $\delta^{13}C$ and $\delta^{18}O$ values.

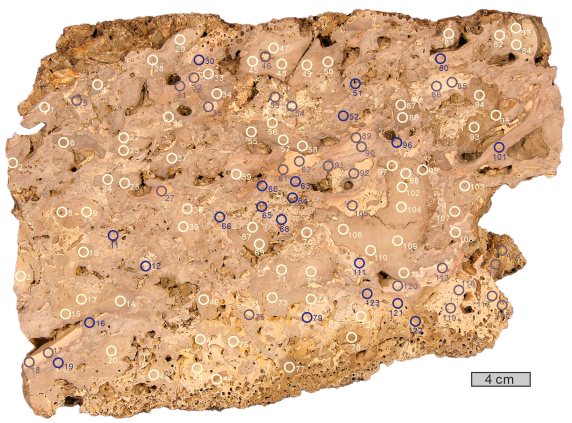

FIGURE 2
Morphology and sampling points for the carbon and oxygen isotopes of seep carbonate. Yellow dots represent clasts, blue dots represent matrix, and purple dots represent pore-filling cements. Sponge borings around the perimeter indicate exposure on the seafloor (Roberts and Aharon, 1994).

3 Results

3.1 Minerology and petrography

The carbonate sample show no obvious stratification and present as irregular structures. The mineral composition of the carbonate is summarized in Table 1. Visual examination of the rock slab revealed that the carbonate consisted mainly of clasts, carbonate mud matrix, and pore-filling cements (Figure 2). The paragenetic sequence identified in this study consisted of three stages: (1) deposition of carbonate clasts; (2) precipitation of microcrystalline matrix and (3) pore-filing cements. High-Mg calcite serves as the predominant mineral while a small amount (less than 3%) of quartz is present for all components. The clasts occur as homogeneous micrite while the matrix and pore-filling cements are characterized by a dominance of microcrystalline Mg-calcite. Geopetal structures in various orientations are common, suggesting multiple attitudes during the development (Roberts, 2001). Sponge borings around the perimeter indicate exposure on the seafloor (Roberts and Aharon, 1994).

3.2 Carbonate carbon and oxygen isotopes

The carbon and oxygen isotopic compositions of the three main types of components vary widely (Table 2; Figure 3). The $\delta^{13}C_{carb}$ values of the clasts vary between −39.6‰ to 2.3‰ (mean: −27.6‰, n = 71). The $\delta^{13}C_{carb}$ values of the matrix are from −29.4‰ to 3.4‰ (mean: −11.6‰, n = 21). The carbon isotopes of pore-filling cements vary narrowly with $\delta^{13}C_{carb}$ values between −3.2‰ and 3.6‰ (mean: 1.7‰, n = 28). In contrast, the stable oxygen isotopic compositions of these components display relatively narrow ranges, with $\delta^{18}O$ values from 1.9‰ to 4.1‰ (mean: 3.3‰, n = 71) for clasts, 1.8‰ to 3.9‰ (mean: 2.9‰, n = 21) for the matrix, and 2.4‰ to 4.1‰ (mean: 3.2‰, n = 28) for the pore-filling cements.

4 Discussion

4.1 Implications on megascopic characteristics and mineral composition of the carbonate

Seep carbonates have significant potential for preserving detailed information on the paleoenvironmental conditions of their formation (Haas et al., 2010; Oppo et al., 2017; Oppo et al., 2020). The megascopic features of the studied carbonate reflect local controls, such as the intensity and duration of seep activity at the formation site. The block is heterogeneous, up to 0.5 × 0.5 × 0.5 m (length, width and height), represent the biggest carbonate sample obtained from the Gulf of Mexico (Figure 2; Roberts and Feng, 2013). At a small scale, the carbonate consists of clasts that formed initially, followed by the matrix, these were then cemented by pore-filling cements (Figure 2), indicating multiple stages during the formation of the carbonate. A previous study on samples from the

10.3389/fmars.2023.1187594

TABLE 1 Mineral composition of the seep carbonate.

Test ID	High-Mg calcite (%)	Aragonite (%)	Quartz (%)	Comment
47	97.8		2.6	Matrix
67	98.2		1.8	
106	97.5		2.5	
60	98.9		1.1	Clast
101	98.9		1.1	
18	100			Pore-filling cement
61	99.3		0.7	
86	79.1	19.8	1.1	

Sample locations are indicated in Figure 2.

TABLE 2 Stable carbon and oxygen isotopic compositions of the seep carbonate.

Test ID	$\delta^{13}C$ (‰,VPDB)	$\delta^{18}O$ (‰,VPDB)	Comment
1	-1.3	3.6	Clast
2	-34.9	3.4	Clast
3	-18.3	3.7	Clast
4	-30.6	3.2	Clast
5	1.7	3.5	Pore-filling cement
6	-34.4	3.4	Clast
8	-25.3	3.6	Clast
9	-24.4	3.5	Clast
10	-24.2	3.8	Clast
11	-16.3	3.5	Matrix
12	-20.4	2.8	Matrix
13	-19.9	3.5	Clast
14	-32.4	2.7	Clast
15	-22.2	3.5	Clast
16	-11	3.9	Matrix
17	3.2	3.3	Pore-filling cement
18	0.4	4.1	Pore-filling cement
19	-3.1	3.5	Matrix
20	-22.3	3.3	Clast
22	-34.8	3.4	Clast
23	-33.3	3.3	Clast
24	-36.9	3.4	Clast
25	-31.6	2.3	Clast
27	3	3.6	Pore-filling cement
28	-34.2	3.3	Clast
29	-33	3.1	Clast
30	-6.5	1.8	Matrix
31	1.4	2.9	Pore-filling cement
32	3.5	3.3	Pore-filling cement
33	-29.6	3.3	Clast
34	-28.8	3.3	Clast
35	3.3	2.4	Pore-filling cement
36	-13.8	3.2	Clast
37	-32.5	3.3	Clast
38	-17.9	3.4	Clast
39	-17.4	3.4	Clast
40	-25.1	3.3	Clast
41	-32.6	2.6	Clast
42	-29.7	3.6	Clast
43	-26.7	2.8	Clast
44	-27.5	3.3	Clast
45	-34.2	3.2	Clast
46	-0.3	3.4	Pore-filling cement
47	-33.6	3.4	Clast
48	-32.2	3.2	Clast
49	-30	3.2	Clast
50	-32.6	3.2	Clast
51	-1.5	2.8	Matrix
52	-18	3	Matrix
53	0.5	3.2	Pore-filling cement
54	-2.7	3.3	Pore-filling cement
55	-35.3	3.3	Clast
56	-29.4	3.5	Clast
57	-36.7	3.3	Clast
58	-36.9	3.4	Clast
59	2.3	3.2	Clast
60	-7.7	3.1	Matrix
61	2.3	3.2	Pore-filling cement
62	3.4	3.7	Pore-filling cement
63	-0.9	3	Matrix
64	-20.7	2.4	Matrix
65	-9.9	3.7	Matrix
66	-22.6	3.7	Matrix
67	-31.3	3.9	Clast

(Continued)

(Continued)

10.3389/fmars.2023.1187594

TABLE 2 Continued

Test ID	$\delta^{13}C$ (‰,VPDB)	$\delta^{18}O$ (‰,VPDB)	Comment
68	-10.9	3	Matrix
69	-33.6	2.8	Clast
70	-34.9	3.5	Clast
71	-15.5	3.2	Clast
72	-17.3	3.5	Clast
73	-18.8	3.2	Clast
74	-33	3.7	Clast
75	-3.2	3.5	Pore-filling cement
76	-27.7	2	Clast
77	-26.7	3.2	Clast
78	-28.1	3.9	Clast
79	-10.7	3.1	Matrix
80	2.5	3.5	Matrix
81	-9.7	3.3	Clast
82	-36	2.3	Clast
83	-36	3.5	Clast
84	-34.8	3.4	Clast
85	1.8	3.5	Pore-filling cement
86	1.2	3.5	Pore-filling cement
87	-2.6	4.1	Clast
88	-4.2	3.4	Clast
89	3.6	3.8	Pore-filling cement
90	-0.3	3.6	Pore-filling cement
91	1.9	3.6	Pore-filling cement
92	3.2	2.9	Pore-filling cement
93	-38	3.5	Clast
94	-37.5	3.2	Clast
95	-32.5	4	Clast
96	2.5	1.9	Matrix
97	-27.8	3.7	Clast
98	-39.6	3.3	Clast
99	-35.3	3.6	Clast
101	3.4	2.3	Matrix
102	-37.8	3.4	Clast
103	-33.3	3	Clast
104	-37.3	3.3	Clast
105	2.1	3.4	Pore-filling cement
106	-33.4	3.4	Clast
107	-35.4	1.9	Clast

(Continued)

TABLE 2 Continued

Test ID	$\delta^{13}C$ (‰,VPDB)	$\delta^{18}O$ (‰,VPDB)	Comment
108	-3.4	3	Clast
109	-30.9	3.1	Clast
110	-34.3	2.8	Clast
111	-10.3	1.9	Matrix
112	-9.3	3	Clast
113	2.7	2.9	Pore-filling cement
114	1.9	2.7	Pore-filling cement
115	1.9	3	Pore-filling cement
116	1.9	3.1	Pore-filling cement
117	1.4	2.7	Pore-filling cement
118	1.5	2.4	Pore-filling cement
119	1.8	3.2	Pore-filling cement
120	3.4	3.3	Pore-filling cement
121	-29.4	2.2	Matrix
122	-28.8	2.8	Matrix
123	-23.7	3.3	Matrix
124	-27.9	2.7	Clast

Sample locations are indicated in Figure 2.

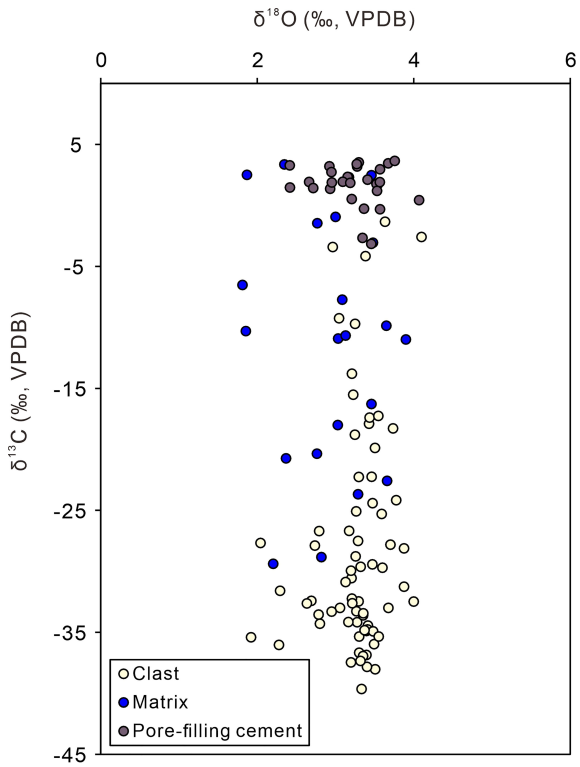

FIGURE 3
Stable carbon and oxygen isotopic compositions of seep carbonate.

same site identified three types of carbonates with ^{14}C ages from 46.5 ka to 11.7 ka BP (Bian et al., 2013). The observed geopetal structures with different orientations in the carbonate indicate multiple reworking, most likely resulting from salt tectonics in this area (Roberts, 2001; Figure 2).

The precipitation of carbonate is related to the presence of rising methane-rich fluids, which migrate upward through faults (Figure 1; Roberts and Feng, 2013). The predominance of high-Mg calcite and the negligible content of background sediment (< 3% quartz) in the seep carbonate suggests that the carbonate precipitated in sediment (Table 1; Gontharet et al., 2007). As suggested by numerous studies, high-Mg calcite formation occurs in a deep sediment column with relatively low sulfate content (Burton, 1993; Greinert et al., 2001; Bayon et al., 2007; Haas et al., 2010).

4.2 Constraints on the temporal $\delta^{13}C$ heterogeneity in seep carbonate

The authigenic minerals in cold seeps help to reveal the chemistry of the diagenetic fluids. The oxygen isotope composition of seep carbonates is commonly a convolution of multiple variables, such as temperature, fluid source, pH and growth rate (Watkins et al., 2014). In this study, the oxygen isotope compositions fall within the typical range of seep carbonate in the Gulf of Mexico (Roberts et al., 2010). The variation of carbon isotope in seep carbonate is basically controlled by the mixability of different carbon sources (Gontharet et al., 2007). The extremely large variable range of $\delta^{13}C_{carb}$ values (from −39.6‰ to 3.6‰; Figure 3) of the sample reveal that multiple DIC sources were involved during the precipitation of the carbonate. At GC140 seep site, potential carbon sources include: 1) methane ($\delta^{13}C$ = −110‰ to −30‰; Whiticar et al., 1986; Whiticar, 1999), 2) crude oil fraction ($\delta^{13}C$ = −35‰ to −25‰; Roberts and Aharon, 1994), 3) seawater ($\delta^{13}C$ = 0 ± 3‰; Anderson and Arthur, 1983), and 4) residual CO_2 from methanogenesis ($\delta^{13}C$ as high as 26‰; Paull et al., 2007). The lowest $\delta^{13}C_{carb}$ value of −39.6‰ suggest that methane is the primary carbon source, while the highest $\delta^{13}C_{carb}$ value of 3.6‰ points to the possible contribution of residual CO_2 from methanogenesis (cf. Bian et al., 2013). Although significant isotopic variations were observed within individual samples, the scattered distribution of the $\delta^{13}C_{carb}$ values makes it challenging to determine the DIC source based solely on carbon isotopes.

Nevertheless, the variation in $\delta^{13}C_{carb}$ values among different seepage stages of carbonate formation suggests a shift in dominant carbon sources. The relatively more negative carbon isotopic ratios (from −39.6‰ to 2.3‰; mean: −27.6‰, n = 71) of the clasts indicate that methane is the primary carbon source. The moderately negative $\delta^{13}C_{carb}$ values (from −29.4‰ to 3.4‰; mean: −11.6‰, n = 21) of the matrix likely reflect less incorporation of methane-derived DIC compared to clasts due to a decrease in seepage intensity. The $\delta^{13}C_{carb}$ values close to 0 of the pore-filling cement (from −3.2‰ to 3.6‰; mean: 1.7‰, n = 28) likely result from the incorporation of seawater DIC due to the cessation of seepage. The contribution of DIC from residual CO_2 from methanogenesis cannot be ruled out but the contribution should not be significant. The $\delta^{13}C_{carb}$ values of clast, matrix, and pore-filling cements that formed during different seepage stages provide insight into the temporal evolution of local fluid sources at site GC140.

4.3 A time-capsule $\delta^{13}C_{carb}$ of seep system

In the Gulf of Mexico (GOM), the deformation of salt bodies and faults results in dynamic fluid flow, leading to rapid expulsion of fluid and gas. This process creates conditions that are favorable for the formation of authigenic carbonates in close proximity to the seafloor (Roberts, 2001; Roberts, 2011). The carbonate outcropping at the seafloor provides an accessible overview to monitor the long-term dynamics of fluid and gas expulsions. By integrating mineralogical and geochemical data, a schematic model of the evolution of seep fluids at site GC140 is proposed (Figure 4; Bian et al., 2013).

During stage I, high flux fluid flow induced the formation of clasts in the subsurface sediments. The high methane flux resulted in relatively negative $\delta^{13}C$ values of the carbonates (Luff and Wallmann, 2003; Peckmann and Thiel, 2004). In stage II, low flux of fluid seepage at the studied site led to the formation of the matrix and voids. The previously formed clasts were cemented together by a surrounding matrix sediment and left voids during this stage. In stage III, fluid seepage decreased, and the formation of pore-filling cements tended to occur. At the same time, seawater was transported downwards from a minor mode to a moderate mode (Figure 4).

It is noteworthy that during all three stages, salt tectonics, such as salt bodies and salt diapirs, developed in the study site (Cook and D'Onfro, 1991; Sassen et al., 1999). Green Canyon is underlain by a Neogene salt weld (Seni, 1992). Submersible observations and high-resolution acoustic datasets show that faults are widespread in sediments as a result of tectonic activity (Roberts et al., 1990; Roberts et al., 1993; Roberts et al., 2000), suggesting that the movement of salt has been active (Bian et al., 2013).

5 Conclusions

The carbonate block obtained from site GC140 in the northern Gulf of Mexico has provided valuable insights into the significant $\delta^{13}C$ heterogeneity (over 40‰) observed in a single seep carbonate sample. The $\delta^{13}C$ values ranged from −39.6‰ to 2.3‰ (mean: −27.6‰, n = 71) for clasts, from −29.4‰ to 3.4‰ (mean: −11.6‰, n = 21) for matrix, and from −3.2‰ to 3.6‰ (mean: 1.7‰, n = 28) for the pore-filling cements. These variations suggest that multiple dissolved inorganic carbon (DIC) sources contributed to the formation of different components of the carbonate at different stages. The temporal evolution of local fluid sources may have

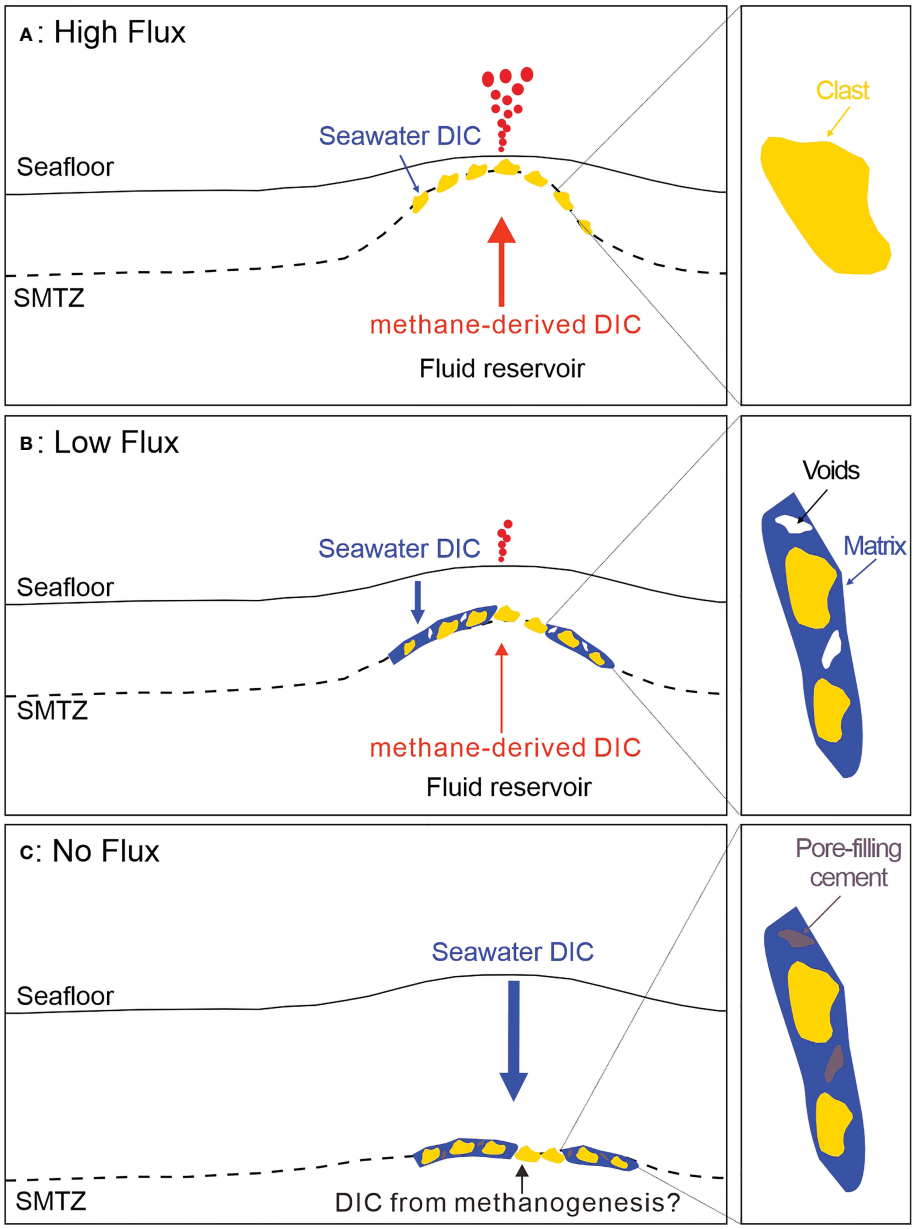

FIGURE 4
Schematic model illustrating the evolution of seep fluids and formed components of the seep carbonate (after Feng et al., 2009 and Bian et al., 2013). **(A)** High flux of the fluid seepage led to precipitation of clasts in subsurface sediment; **(B)** The clasts were being cemented together by a surrounding matrix sediment during the decrease of fluid flux. **(C)** Pore-filling cements tend to occur then the fluid flux diseased. Meantime, seawater was transported downwards from a minor mode to moderate mode. SMTZ, sulfate methane transition zone. The arrow sizes are proportional to the upward methane fluxes and downward seawater fluxes.

played a crucial role in determining the carbonate isotope geochemistry. Therefore, the highly variable fluids that leave their geochemical imprints on seep carbonate must be considered in any seep-related studies.

Data availability statement

The original contributions presented in the study are included in the article/supplementary material. Further inquiries can be directed to the corresponding author.

Author contributions

Conceptualization: XW; methodology: XF and ZJ; formal analysis: XF and ZJ; investigation: ZJ; XW; data curation: XW; writing—original draft preparation: XF; writing—review and editing: XW; visualization: XW; supervision: XW; project administration: XW; funding acquisition: XW. All authors contributed to the article and approved the submitted version.

Funding

This study was sponsored by Shanghai Sailing Program (Grant: 21YF1416800) and by the Chenguang Program of Shanghai Education Development Foundation and Shanghai Municipal Education Commission (Grant: 22CGA58).

Acknowledgments

Sample was collected during projects funded by the U.S. Bureau of Ocean Energy Management and the National Oceanic and Atmospheric Administration's National Undersea Research Program. Harry H. Roberts (Louisiana State University) and Dong Feng (Shanghai Ocean University) are thanked for providing the sample. Yang Lu (University of Oslo) is thanked for XRD mineral identification.

Conflict of interest

The authors declare that the research was conducted in the absence of any commercial or financial relationships that could be construed as a potential conflict of interest.

Publisher's note

References

Aloisi, G., Pierre, C., Rouchy, J., Foucher, J., Woodside, J., and Party, M. S. (2000). Methane-related authigenic carbonates of eastern Mediterranean Sea mud volcanoes and their possible relation to gas hydrate destabilisation. *Earth Planet. Sci. Lett.* 184, 321–338. doi: 10.1016/S0012-821X(00)00322-8

Anderson, T. F., and Arthur, M. A. (1983). "Stable isotopes of oxygen and carbon and their application to sedimentologic and paleoenvironmental problems," in *Sedimentary geology.* (Dallas: Society of economic paleontologists and mineralogists), 1–151. Available at: https://pubs.geoscienceworld.org/sepm/books/book/1147/chapter-abstract/10572697/Stable-Isotopes-of-Oxygen-and-Carbon-and-their?redirectedFrom=PDF.

Bayon, G., Pierre, C., Etoubleau, J., Voisset, M., Cauquil, E., Marsset, T., et al. (2007). Sr/Ca and Mg/Ca ratios in Niger delta sediments: implications for authigenic carbonate genesis in cold seep environments. *Mar. Geol.* 241, 93–109. doi: 10.1016/j.margeo.2007.03.007

Bian, Y., Feng, D., Roberts, H. H., and Chen, D. (2013). Tracing the evolution of seep fluids from authigenic carbonates: green canyon, northern gulf of Mexico. *Mar. Pet. Geol.* 44, 71–81. doi: 10.1016/j.marpetgeo.2013.03.010

Boetius, A., Ravenschlag, K., Schubert, C. J., Rickert, D., Widdel, F., Gieseke, A., et al. (2000). A marine microbial consortium apparently mediating anaerobic oxidation of methane. *Nature* 407, 623–626. doi: 10.1038/35036572

Bohrmann, G., Greinert, J., Suess, E., and Torres, M. (1998). Authigenic carbonates from the cascadia subduction zone and their relation to gas hydrate stability. *Geology* 26, 647–650. doi: 10.1130/0091-7613(1998)026<0647:ACFTCS>2.3.CO;2

Burton, E. A. (1993). Controls on marine carbonate cement mineralogy: review and reassessment. *Chem. Geol.* 105, 163–179. doi: 10.1016/0009-2541(93)90124-2

Chen, F., Wang, X., Li, N., Cao, J., Bayon, G., Peckmann, J., et al. (2019). Gas hydrate dissociation during sea-level highstand inferred from U/Th dating of seep carbonate from the south China Sea. *Geophys. Res. Lett.* 46, 13928–13938. doi: 10.1029/2019GL085643

Cook, D., and D'Onfro, P. (1991). Jolliet field thrust fault stucture and stratigraphy green canyon block 184, offshore Louisiana. *Trans. Gulf. Coast. Assoc. Geological. Soci.* 41, 100–121.

Feng, D., Chen, D., and Peckmann, J. (2009). Rare earth elements in seep carbonates as tracers of variable redox conditions at ancient hydrocarbon seeps. *Terra. Nova.* 21, 49–56. doi: 10.1111/j.1365-3121.2008.00855.x

Gontharet, S., Pierre, C., Blanc-Valleron, M.-M., Rouchy, J. M., Fouquet, Y., Bayon, G., et al. (2007). Nature and origin of diagenetic carbonate crusts and concretions from mud volcanoes and pockmarks of the Nile deep-sea fan (eastern Mediterranean Sea). *Deep-Sea. Res. Part II-Top. Stud. Oceanogr.* 54, 1292–1311. doi: 10.1016/j.dsr2.2007.04.007

Greinert, J., Bohrmann, G., and Suess, E. (2001). "Gas hydrate-associated carbonates and methane-venting at hydrate ridge: classification, distribution and origin of authigenic lithologies," in *Natural gas hydrates: occurrence, distribution, and detection. geophysical monographs*, vol. 124 . Eds. C. K. Paull and W. P. Dillon (Washington, DC: American Geophysical Union), 99–113.

Haas, A., Peckmann, J., Elvert, M., Sahling, H., and Bohrmann, G. (2010). Patterns of carbonate authigenesis at the kouilou pockmarks on the Congo deep-sea fan. *Mar. Geol.* 268, 129–136. doi: 10.1016/j.margeo.2009.10.027

Himmler, T., Sahy, D., Martma, T., Bohrmann, G., Plaza-Faverola, A., Bünz, S., et al. (2019). A 160,000-year-old history of tectonically controlled methane seepage in the Arctic. *Sci. Adv.* 5, eaaw1450. doi: 10.1126/sciadv.aaw1450

Jiang, G., Kennedy, M., and Christie-Blick, N. (2003). Stable isotopic evidence for methane seeps in neoproterozoic postglacial cap carbonates. *Nature* 426, 822–826. doi: 10.1038/nature02201

Luff, R., and Wallmann, K. (2003). Fluid flow, methane fluxes, carbonate precipitation and biogeochemical turnover in gas hydrate-bearing sediments at hydrate ridge, cascadia margin: numerical modeling and mass balances. *Geochim. Cosmochim. Acta* 67, 3403–3421. doi: 10.1016/S0016-7037(03)00127-3

Mazzini, A., Ivanov, M. K., Parnell, J., Stadnitskaya, A., Cronin, B., Poludetkina, E., et al. (2004). Methane-related authigenic carbonates from the black Sea: geochemical characterization and relation to seeping fluids. *Mar. Geol.* 212, 153–181. doi: 10.1016/j.margeo.2004.08.001

Naehr, T. H., Eichhubl, P., Orphan, V. J., Hovland, M., Paull, C. K., Ussler, W., et al. (2007). Authigenic carbonate formation at hydrocarbon seeps in continental margin sediments: a comparative study. *Deep-Sea. Res. Part II-Top. Stud. Oceanogr.* 54, 1268–1291. doi: 10.1016/j.dsr2.2007.04.010

Oppo, D., De Siena, L., and Kemp, D. B. (2020). A record of seafloor methane seepage across the last 150 million years. *Sci. Rep.* 10, 2562. doi: 10.1038/s41598-020-59431-3

Oppo, D., Viola, I., and Capozzi, R. (2017). Fluid sources and stable isotope signatures in authigenic carbonates from the northern Apennines, Italy. *Mar. Pet. Geol.* 86, 606–619. doi: 10.1016/j.marpetgeo.2017.06.016

Paull, C. K., Ussler, W., Peltzer, E. T., Brewer, P. G., Keaten, R., Mitts, P. J., et al. (2007). Authigenic carbon entombed in methane-soaked sediments from the northeastern transform margin of the guaymas basin, gulf of California. *Deep-Sea. Res. Part II-Top. Stud. Oceanogr.* 54, 1240–1267. doi: 10.1016/j.dsr2.2007.04.009

Peckmann, J., Reimer, A., Luth, U., Luth, C., Hansen, B. T., Heinicke, C., et al. (2001). Methane-derived carbonates and authigenic pyrite from the northwestern black Sea. *Mar. Geol.* 177, 129–150. doi: 10.1016/S0025-3227(01)00128-1

Peckmann, J., and Thiel, V. (2004). Carbon cycling at ancient methane–seeps. *Chem. Geol.* 205, 443–467. doi: 10.1016/j.chemgeo.2003.12.025

Ritger, S., Carson, B., and Suess, E. (1987). Methane-derived authigenic carbonates formed by subduction-induced pore-water expulsion along the Oregon/Washington margin. *Geol. Soc. Am. Bull.* 98, 147–156. doi: 10.1130/0016-7606(1987)98<147:MACFBS>2.0.CO;2

Roberts, H. H. (2001). "Fluid and gas expulsion on the northern gulf of Mexico continental slope: mud-prone to mineral-prone responses," in *Natural gas hydrates: occurrence, distribution, and detection*. Eds. C. K. Paull and W. P. Dillon (Washington, DC, USA: American Geophysical Union), 145–161.

Roberts, H. H. (2011). "Surficial geology of the northern gulf of Mexico continental slope: impacts of fluid and gas expulsion," in *Gulf of Mexico origin, waters, and biota. geology, 3*. Eds. N. A. Buster, W. C. Holmes and D. K. Camp (Texas: Texas A&M University Press), 209–228.

Roberts, H. H., and Aharon, P. (1994). Hydrocarbon-derived carbonate buildups of the northern gulf of Mexico continental slope: a review of submersible investigations. *Geo-Mar. Lett.* 14, 135–148. doi: 10.1007/BF01203725

Roberts, H. H., Aharon, P., Carney, R., Larkin, J., and Sassen, R. (1990). Sea Floor responses to hydrocarbon seeps, Louisiana continental slope. *Geo-Mar. Lett.* 10, 232–243. doi: 10.1007/BF02431070

Roberts, H. H., Aharon, P., and Walsh, M. W. (1993). "Cold-seep carbonates of the Louisiana continental slope to basin floor," in *Carbonate microfabrics: frontiers in sedimentary geology*. Eds. R. Rezak and D. L. Lavoie (New York, NY, USA: Springer-Verlag), 95–104.

Roberts, H. H., and Carney, R. S. (1997). Evidence of episodic fluid, gas, and sediment venting on the northern gulf of Mexico continental slope. *Econ. Geol.* 92, 863–879. doi: 10.2113/gsecongeo.92.7-8.863

Roberts, H. H., Coleman, J., Jesse Hunt, J., and Shedd, W. W. (2000). Surface amplitude mapping of 3-seismic for improved interpretations of seafloor geology and biology. *Gulf. Coast. Assoc. Geological. Soc. Trans.* 50, 495–504.

Roberts, H. H., and Feng, D. (2013). "Carbonate precipitation at gulf of Mexico hydrocarbon seeps: an overview," in *Hydrocarbon seepage: from source to surface*. Eds. M. Abrams, F. Aminzadeh, T. Berge, D. Connolly and G. O'Brien (SEG/AAPG Special Publication), 43–61. Available at: https://pubs.geoscienceworld.org/seg/books/book/2106/chapterabstract/114897131/Carbonate-Precipitation-at-Gulfof-Mexico?redirectedFrom=fulltext.

Roberts, H. H., Feng, D., and Joye, S. B. (2010). Cold-seep carbonates of the middle and lower continental slope, northern gulf of Mexico. *Deep-Sea. Res. Part II-Top. Stud. Oceanogr.* 57, 2040–2054. doi: 10.1016/j.dsr2.2010.09.003

Roberts, H. H., Sassen, R., Carney, R., and Aharon, P. (1989). ^{13}C-depleted authigenic carbonate buildups from hydrocarbon seeps, lousianna continental slope. *Gulf. Coast. Assoc. Geological. Soc. Trans.* 39, 523–530.

Sassen, R., Joye, S., Sweet, S. T., DeFreitas, D. A., Milkov, A. V., and MacDonald, I. R. (1999). Thermogenic gas hydrates and hydrocarbon gases in complex chemosynthetic communities, gulf of Mexico continental slope. *Org. Geochem.* 30, 485–497. doi: 10.1016/S0146-6380(99)00050-9

Seni, S. J. (1992). Evolution of salt structures during burial of salt sheets on the slope, northern gulf of Mexico. *Mar. Pet. Geol.* 9, 452–468. doi: 10.1016/0264-8172(92)90054-I

Smrzka, D., Zwicker, J., Klügel, A., Monien, P., Bach, W., Bohrmann, G., et al. (2016). Establishing criteria to distinguish oil-seep from methane-seep carbonates. *Geology* 44, 667–670. doi: 10.1130/G38029.1

Suess, E. (2020). "Marine cold seeps: background and recent advances," in *Hydrocarbons, oils and lipids: diversity, origin, chemistry and fate*. Ed. Wilkes, (Cham: Springer International Publishing), 747–767.

Sun, Y., Gong, S., Li, N., Peckmann, J., Jin, M., Roberts, H. H., et al. (2020). A new approach to discern the hydrocarbon sources (oil vs. methane) of authigenic carbonates forming at marine seeps. *Mar. Pet. Geol.* 114, 104230. doi: 10.1016/j.marpetgeo.2020.104230

Sun, Z., Wei, H., Zhang, X., Shang, L., Yin, X., Sun, Y., et al. (2015). A unique fe-rich carbonate chimney associated with cold seeps in the northern Okinawa trough, East China Sea. *Deep-Sea. Res. Part I-Oceanogr. Res. Pap.* 95, 37–53. doi: 10.1016/j.dsr.2014.10.005

Wang, M., Chen, T., Feng, D., Zhang, X., Li, T., Robinson, L. F., et al. (2022). Uranium-thorium isotope systematics of cold-seep carbonate and their constraints on geological methane leakage activities. *Geochim. Cosmochim. Acta* 320, 105–121. doi: 10.1016/j.gca.2021.12.016

Watkins, J. M., Hunt, J. D., Ryerson, F. J., and DePaolo, D. J. (2014). The influence of temperature, pH, and growth rate on the δ^{18}O composition of inorganically precipitated calcite. *Earth Planet. Sci. Lett.* 404, 332–343. doi: 10.1016/j.epsl.2014.07.036

Whiticar, M. J. (1999). Carbon and hydrogen isotope systematics of bacterial formation and oxidation of methane. *Chem. Geol.* 161, 291–314. doi: 10.1016/S0009-2541(99)00092-3

Whiticar, M. J., Faber, E., and Schoell, M. (1986). Biogenic methane formation in marine and fresh water environments: CO2 reduction vs acetate fermentation – isotope evidence. *Geochim. Cosmochim. Acta* 50, 693–709. doi: 10.1016/0016-7037(86)90346-7

Zhang, W., Chen, C., Su, P., Wan, Z., Huang, W., Shang, J., et al. (2023). Formation and implication of cold-seep carbonates in the southern south China Sea. *J. Asian Earth Sci.* 241, 105485. doi: 10.1016/j.jseaes.2022.105485

frontiers | Frontiers in Marine Science

TYPE Original Research
PUBLISHED 12 May 2023
DOI 10.3389/fmars.2023.1184787

OPEN ACCESS

EDITED BY
Dong Feng,
Shanghai Ocean University, China

REVIEWED BY
Yuncheng Cao,
Shanghai Ocean University, China
Duanxin Chen,
Chinese Academy of Sciences (CAS), China

*CORRESPONDENCE
Jiangxin Chen
jiangxin_chen@sina.com
Bingshou He
hebinshou@ouc.edu.cn

RECEIVED 12 March 2023
ACCEPTED 24 April 2023
PUBLISHED 12 May 2023

CITATION
Han T, Chen J, He B and Azevedo L (2023) Research on the fluid dynamics interaction between submarine sand waves and seawater by seismic oceanography. *Front. Mar. Sci.* 10:1184787. doi: 10.3389/fmars.2023.1184787

Research on the fluid dynamics interaction between submarine sand waves and seawater by seismic oceanography

Tonggang Han[1], Jiangxin Chen[2,3]*, Bingshou He[1,3]* and Leonardo Azevedo[4]

[1]Key Lab of Submarine Geosciences and Prospecting Techniques, Ministry of Education, Ocean University of China, Qingdao, China, [2]Key Laboratory of Gas Hydrate, Ministry of Natural Resources, Qingdao Institute of Marine Geology, Qingdao, China, [3]Laboratory for Marine Mineral Resources, National Laboratory for Marine Science and Technology, Qingdao, China, [4]Instituto Superior Técnico, University of Lisbon, Lisbon, Portugal

Introduction: The seafloor is an important interface between the lithosphere and the hydrosphere, where processes related to circulation and energy exchange happen along with various marine processes widely developed in the water column near the seafloor. These processes are still not yet completely understood as there are constraints of submarine detection technology and the interdisciplinary nature of these complex environments. Seismic reflection data have been a preferable tool to study and image these processes due to their characteristics in terms of spatial resolution. In seismic reflection data, submarine sand waves show hair-like reflection configurations with low continuity and wearing-hair style, appearing with an angle with the seafloor. Investigation of the relationship between the characteristics of submarine sand waves induced hair-like reflection configuration and hydrodynamics is crucial for understanding hair-like reflection configuration generation and spatiotemporal evolution.

Methods: This study combines fluid dynamics numerical simulation and seismic oceanography to discuss the seismic response characteristics and formation mechanisms of the hair-like reflection configuration. First, we create a seawater time-variant fluid-dynamical model followed by the numerical simulation of seismic oceanography data. This procedure results in seismic oceanography numerical simulation sections with hair-like reflection configurations for different constant flow conditions forced on the boundary. Optimal matching method is then applied to interpret field seismic reflection sections given the results obtained with the numerical experiments.

Results and discussion: As consequence, the fluid dynamic explanation for the formation mechanism of the hair-like reflection configuration due to differences in seawater thermohaline is proposed. The study provides additional comprehension and further insights into the dynamic process of submarine sand waves induced hair-like reflection configuration using the seismic oceanography method.

KEYWORDS

seismic oceanography, fluid dynamics, numerical simulation, hair-like reflection configuration, formation mechanism

1 Introduction

The seafloor, as interpreted as the intersection between the lithosphere and the hydrosphere, is where substance circulation and energy exchange take place (Shaw et al., 1996; Fang and Hao, 2019; Qian et al., 2022). This region is also a significant interdisciplinary research field for both physical oceanography and marine geology due to, for example, the interaction between submarine topography and multiscale ocean dynamics; the effects of turbidity and ocean bottom currents; cold seep and hydrothermal activity; biology; and marine sedimentary processes. Nevertheless, it is challenging to continuously observe and study dynamic processes happening close to or at the seafloor (Perlin et al., 2005; Jazi et al., 2020). Chen et al. (2016) defined various marine processes widely developed in the water column near the seafloor as "seafloor processes," including seabed fluid flow, sedimentary processes, tectonic processes, biological processes, and submarine dynamic processes, which cannot be studied intensively due to the constraints of submarine detection technology and interdisciplinary nature. Seafloor processes have been subject to intensive research about their horizontal scale and the location of the oceanic bottom boundary to get a systematic understanding of the evolution of the seafloor.

Compared with traditional geophysical methods of seafloor survey, seismic oceanography can image not only oceanographic phenomena in seawater, but also the important marine processes happening near the seafloor (Song et al., 2021a). Seismic oceanography (Holbrook et al., 2003) has been applied to study various oceanographic phenomena, including fronts (Holbrook et al., 2003; Tsuji et al., 2005), water mass boundaries (Nandi et al., 2004), mesoscale eddies (Biescas et al., 2008; Ménesguen et al., 2009; Song et al., 2009; Pinheiro et al., 2010; Quentel et al., 2010; Tang et al., 2014), internal waves (Holbrook and Fer, 2005; Krahmann et al., 2008; Song et al., 2009; Song et al., 2021b), submesoscale processes (Sallares et al., 2016; Tang et al., 2020; Yang et al., 2021), and seafloor processes (Vsemironva et al., 2012; Chen et al., 2016; Chen et al., 2017; Chen et al., 2018; Geng et al., 2019; Yin et al., 2021). More recently, seismic reflection studies have now been used to look at the evolution of marine processes over time (Dickinson et al., 2020; Gunn et al., 2020; Zou et al., 2021; Dickinson and Gunn, 2022). Seismic oceanography has been used to preliminarily analyze some significant images of fluid-solid interactions near the seafloor, such as submarine sand waves induced hair-like reflection configuration (Chen et al., 2016). The seismic images of submarine dynamic processes are of considerable significance, but identified phenomena have been simply analyzed and interpreted from a qualitative perspective, without detailed quantitative modeling to study the origin of the seismic response and the dynamic processes. Nevertheless, the relevant preliminary results have demonstrated that statistical models and numerical simulation can be jointly applied in the quantitative calculation of seismic oceanography (Huang et al., 2018; Chen et al., 2020). However, the currently available work, related to this topic, does not compare the results of the numerical simulation with field seismic data. Further analysis and research in this field will certainly provide a deeper understanding and further insight into not yet-known seafloor processes.

Submarine sand waves, sometimes referred to as submarine sand dunes, are simultaneously a sediment transport mechanism and a dynamic morphologic feature in subaqueous environments that are commonly found in submarine canyons and continental shelves worldwide (Flemming, 1980; Ashley, 1990; Viana et al., 1998; Wynn and Stow, 2002; Stow et al., 2009; Cukur et al., 2022; Yang et al., 2022). These sedimentary features are dynamic rhythmic bedforms with wavelengths that might have hundreds of meters and heights of several meters. Their crests are nearly perpendicular to the direction of the primary tidal current (Mccave, 1971; Terwindt, 1971; Besio et al., 2008; Campans et al., 2017). Many observations, such as the Acoustic Doppler Current Profiler (ADCP), indicate that the morphological patterns are developed in response to complex hydrodynamical conditions, sediment transport, and geomorphology (Dodd et al., 2003; Borsje et al., 2014). However, compared with other observation methods, seismic oceanography method can provide more direct images of the interaction between seafloor and seawater movement. The fluid dynamics numerical simulation is an important method to study the evolution of seafloor processes, which combined with seismic oceanography method might be used to study key dynamic parameters of the seafloor processes and the essential dynamic information reflected by the seismic dataset. Investigating the relationship between the characteristics of submarine sand waves induced hair-like reflection configuration and hydrodynamics is crucial for understanding hair-like reflection configuration generation and evolution.

Seismic events related to submarine sand waves are characterized by low continuity and wearing-hair style (Chen et al., 2016). Seismic reflection configurations of submarine sand waves had a blanket drape, higher amplitude than the surrounding seawater, and medium-high apparent frequency. The amplitude diminishes with higher height and converges with the surrounding seawater. The abnormal seismic reflection characteristic is called a hair-like reflection configuration (Chen et al., 2016), and its development characteristics are similar to those of Carr et al. (2010) and Reeder et al. (2011). The formation of the hair-like reflection configuration is significantly influenced by the submarine topography, whose dynamic process has yet to be illustrated. Additionally, the strong amplitude is due to the seawater thermohaline feature or oceanic sediment resuspension, lacking the constraint of a quantitative relationship. Chen et al. (2016) have speculated that the hair-like reflection configuration reflects the seismic response to the flow pattern and the distribution of oceanic suspended sediment caused by the interaction between the rugged seafloor, such as sand waves, and the bottom current according to simulation results of a discrete vortex model in Hansen et al. (1994). A preliminary study of the turbidity layer found that oceanic suspended sediments could be identified, and the quantitative relationships could be analyzed (Vsemironva et al., 2012), which lays a foundation for further discussion on the quantitative interpretation of the seismic response of the hair-like reflection configuration. The interaction between the bottom current and the rugged seafloor especially develops in areas with complex submarine topography and active bottom current. The seismic reflection characteristics vary with different seawater flow

velocities, possibly caused by oceanic sediment resuspension and movement (Chen et al., 2016). Under the constraint of rugged submarine topography, the following scientific questions remain unanswered: what are the reasons for the formation of diverse morphology of high-frequency small vertical offsets, high-frequency fluctuations, or hair-like reflection configurations (Song et al., 2020)? What is the correlation between the scale of submarine topography and the controlling factors such as seawater flow velocity, and is there a critical threshold to control the formation of different reflection configurations? The above questions require validation through additional observational data and numerical simulation and establishing a quantitative relationship model.

The work presented herein discusses the seismic response characteristic and the formation mechanism of hair-like reflection configuration using fluid dynamics numerical simulation and seismic oceanography method as the primary numerical tools. The optimal matching method is performed for fusion calculation to investigate the relationship between numerical simulation results and the field seismic dataset. Simultaneously, the seawater time-variant fluid-dynamical model computed from the fluid dynamics numerical simulation is compared with the seismic oceanography section to analyze the similarity between the two specific areas. If the seawater thermohaline feature, the seismic oceanography section obtained *via* numerical simulation, and the field seismic reflection section are similar in morphology at a certain time during the numerical simulation process, it is likely that the field seismic reflection section event characteristics in the region are subject to similar conditions to those set by the fluid dynamics numerical simulation. As consequence, it is possible to study the dynamic characteristics of seawater, interpret the feature of seawater reflection layers on the seismic section and the formation of the seawater seismic facies, and discuss the important parameter relations and dynamic information of the submarine sand waves induced hair-like reflection configuration, which lay a foundation for further research on the dynamic process of the hair-like reflection configuration using seismic oceanography method.

2 Materials and methods

Seawater flow near the seafloor is primarily influenced by submarine topography, such as submarine sand waves induced hair-like reflection configuration, but it has been preliminary analyzed and interpreted from a qualitative perspective, without detailed quantitative calculations about the formation mechanism and dynamic process. This study uses oceanic numerical models and seawater-related equations to construct the seismic oceanographic simulation technology, carry out the seismic oceanography mathematical modeling and numerical simulation of the hair-like reflection configuration, and apply the optimal matching method to discuss its fluid dynamic environment and formation mechanism (Figure 1).

2.1 Fluid dynamics numerical simulation

We performed numerical experiments with a two-dimensional numerical simulation of the ocean dynamics using the Massachusetts Institute of Technology general circulation model (MITgcm; Marshall et al., 1997a; Marshall et al., 1997b; Legg and Adcroft, 2003; Legg and Klymak, 2008; Klymak and Legg, 2010; Klymak et al., 2010a; Klymak et al., 2010b) to investigate the formation and dynamic process of submarine sand waves induced hair-like reflection configuration. This model solves the fully nonlinear, non-hydrostatic Navier-Stokes equations under the Boussinesq approximation for an incompressible fluid with a spatial finite-volume discretization on a curvilinear computation grid.

2.1.1 Model configuration

The study uses a two-dimensional submarine topography, with a stretched horizontal coordinate system (Klymak and Legg, 2010; Klymak et al., 2010b) of variable resolution in the horizontal direction, and a uniform vertical resolution ($\Delta z = 2m$) of 382 points. The horizontal domain was 23.5km over 1600 grid cells. The inner 850 grid cells have a horizontal width (Δx) of 10m to investigate submarine sand waves induced hair-like reflection configuration in detail, and then the grid was telescoped linearly so that for the outer cells $\Delta x = 30m$ to produce a sponge layer on each side of the domain for preventing waves from being reflected back into the interior. The simulation was run in non-hydrostatic mode as the condition for hydrostatic approximation with horizontal length scales much larger than vertical scales is violated both in model setup and observed flow response. The boundaries were forced with a constant inflow/outflow condition of U_o (U_o = 0.70, 0.75, 0.80, 0.85, 0.90, $0.95ms^{-1}$). A no-slip bottom boundary condition is used. The Coriolis frequency of $f = 5\times10^{-5}s^{-1}$ is used. Horizontal and vertical Laplacian eddy viscosity and diffusivity are set to $A_h = k_h = 2\times10^{-2}m^2s^{-1}$ and $A_v = k_v = 2\times10^{-3}m^{-2}s^{-1}$, respectively. All simulations are initialized from the state of rest and run for ~10 hours to a statistically steady state (Figure 2).

2.1.2 Bottom topography and stratification

Hair-like reflection configurations, associated with submarine sand waves, were observed on a seismic oceanography section with high spatial resolution, which was acquired from the multi-channel seismic reflection survey within a region of the northern South China Sea (Figure 2A). The northern South China Sea is part of the natural extension of the South China Sea Block to the sea. The water depth of the continental slope is generally 200-3400m, forming a gentle upper continental slope, a steep mid-continental slope, and a gentle lower continental slope (Zhang and Luan, 2012). The Dongsha Uplift is located southeast of the Pearl River estuary, the most prominent submarine topography on the continental shelf/slope of the northern South China Sea. The water depth is 0-1000m deep, mainly composed of two submarine plateaus, one is circular and the other is diamond-shaped (Chen et al., 2016). There is extensive seafloor erosion in the Dongsha Uplift, which is mainly influenced by currents of a branch of Kuroshio Current from the Luzon strait, tides, and the Pearl River, such as seafloor erosion trenches and submarine sand waves. The large amplitude internal solitary waves that appear in the form of wave packet or wave train and primarily originate from the middle Luzon Strait is able to strong tide-topography interactions (Guo and Chen, 2014; Alford et al., 2015; Huang et al., 2016). The internal solitary waves

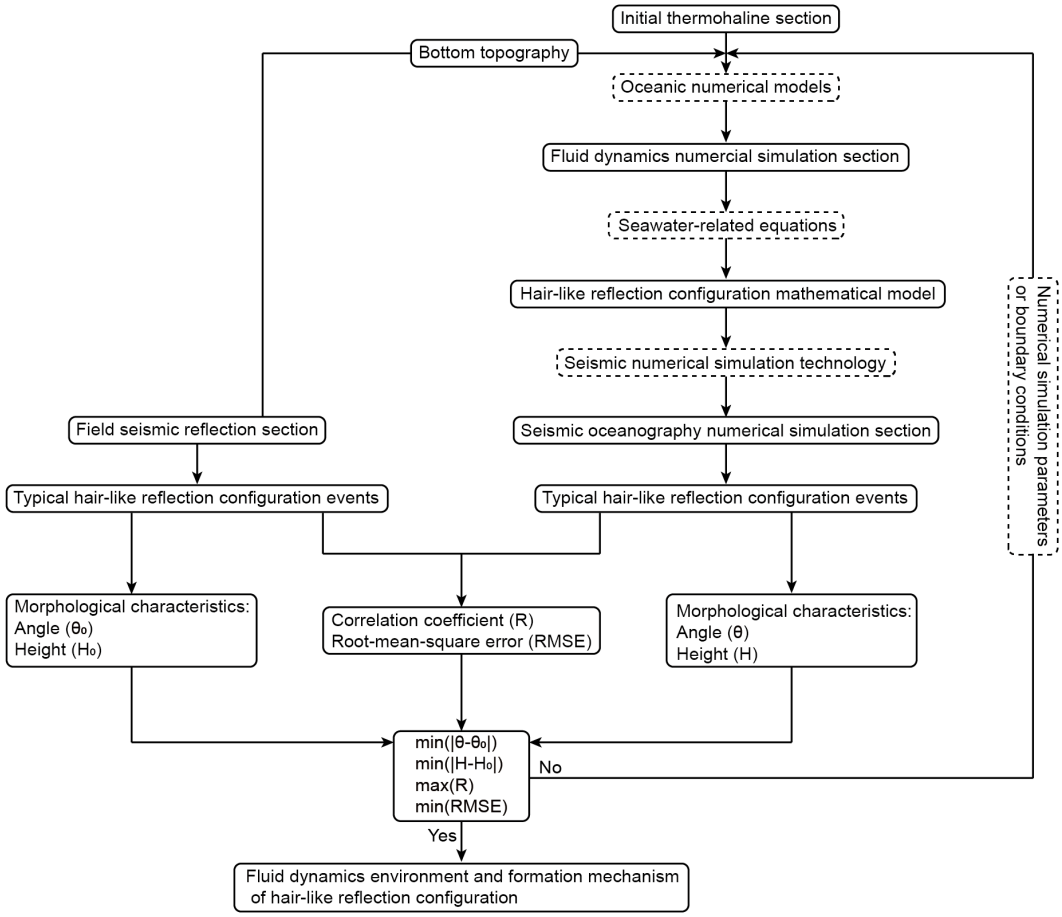

FIGURE 1
Schematic representation of the workflow followed in this work to link quantitatively hair-like reflection configuration and dynamic parameters.

are generated diurnally during an ~8 days period centered on the new and full moon in the northern South China Sea. There is approximately one internal solitary wave per day yearly during the tidal period and up to twice a day in the summer (Reeder et al., 2011; Huang et al., 2014). Here, as interval solitary waves propagate in the WNW direction from the Luzon Strait, they steepen dramatically and exhibit periodic or quasi-periodic features of internal solitary wave packets across the basin (Alford et al., 2015). The internal solitary waves are well developed around the Dongsha Uplift of the northern South China Sea. The propagation velocity of internal solitary waves in the vicinity of the Dongsha Uplift calculated by MODIS, ACDP, X-band radar, and multi-channel seismic reflection data is usually 0.55-3.0m/s, and the maximum wave height can exceed 100m (Lv et al., 2010; Fu et al., 2012; Zhao et al., 2012). Observations and analyses of oceanic sediment suspension events under various environmental conditions reveal that oceanic sediment suspension requires bottom current velocities from ~0.10m/s up to ~0.80m/s (Xu et al., 2008; Reeder et al., 2011; Tian et al., 2021) to form submarine sand waves.

The oceanic bottom boundary layer shows vertical water column features. The sheet drape seismic facies unit develops between the seafloor and the black dashed line, which indicates the turbulent bottom boundary layer. Seismic reflection presents weak amplitude, chaotic reflection characteristic on the left of the yellow dotted rectangle, and weak amplitude, turbid reflection characteristic in the middle and to the right part (Chen et al., 2016). This near-seafloor water column shows weak seismic reflections and reduced apparent frequency. Sand waves ca. 200m in wavelength develop in the zone of ca. 5km long along the seafloor, and hair-like reflection configuration grows above them, which is the research area of fluid dynamics numerical simulation in this study (Figure 2A). The model utilizes realistic bottom topography merged from Figure 2B to investigate the formation and dynamic process of submarine sand waves induced hair-like reflection configuration.

The initial stratification is horizontally uniform in the fluid dynamics numerical simulation, where the model is initialized with realistic conductivity-temperature-depth (CTD) profiles (Figures 2D, E). The seawater physical property related to seismic reflection includes density and acoustic velocity, mainly determined by seawater temperature and depth. Based on the seawater state equation, the seawater acoustic velocity and density are primarily controlled by temperature, salinity, and seawater

10.3389/fmars.2023.1184787

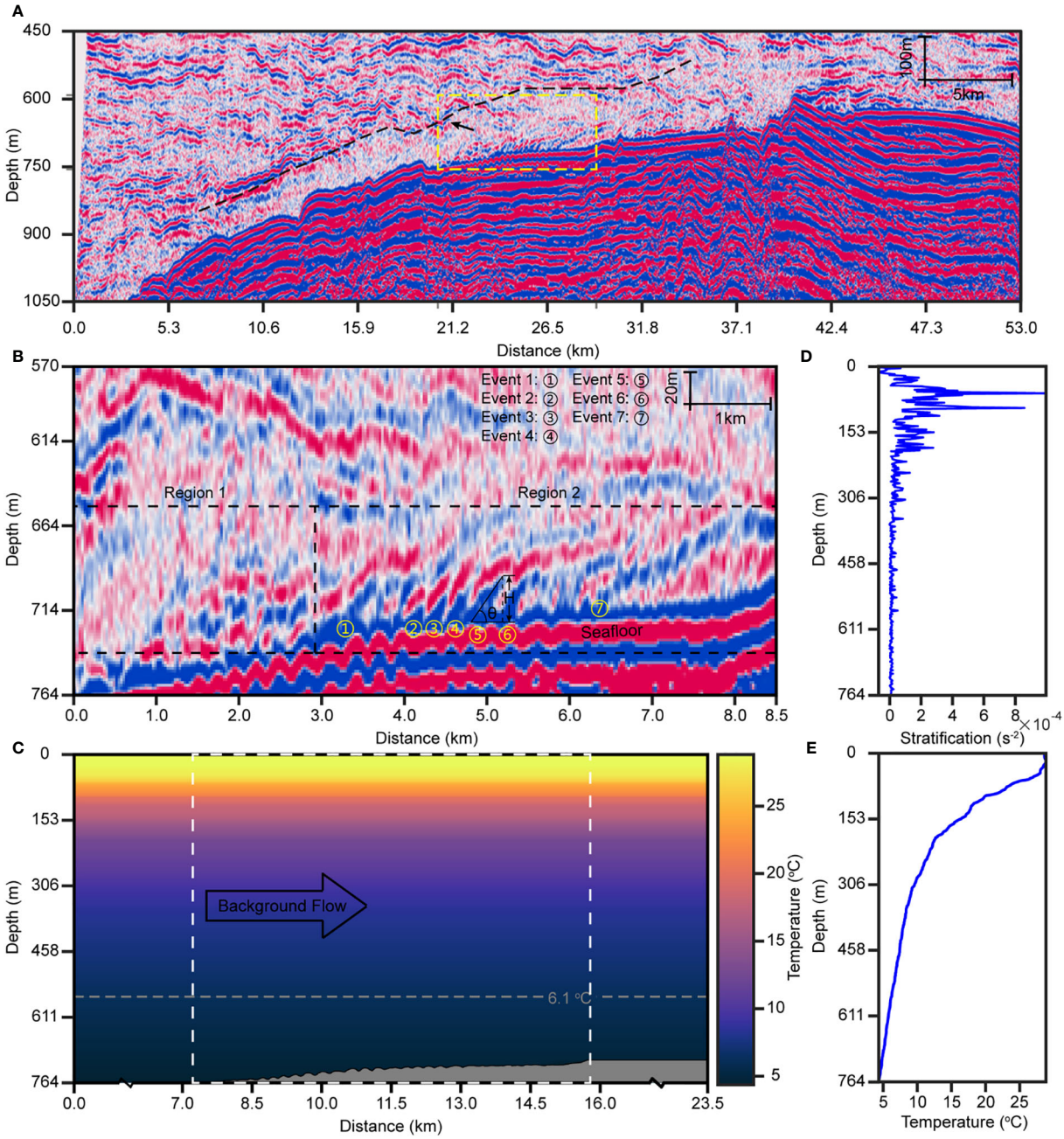

FIGURE 2
(A) The sheet drape seismic facies unit develops between the seafloor and the black dashed line, which indicates the turbulent bottom boundary layer. Black arrow indicates that there is an internal solitary wave. **(B)** Zoom-in of the yellow dashed rectangle in Figure **(A)**. Submarine sand waves develop on the seafloor and hair-like reflection configuration grows above them. Region 1: Submarine turbulent region; Region 2: The region of quantitative hair-like reflection configuration; Events 1-7: The selection of hair-like reflection configuration seismic events. **(C)** Schematic of fluid dynamics numerical simulation configuration. The depth-independent background flow interacts with the realistic bottom topography from **(B)** in initial stratification expressed in temperature. White dashed box indicates a region used for investigating the dynamics of submarine sand waves induced hair-like configuration. **(D)** The vertical profile of stratification observed in the Northern South China Sea, which were obtained from the National Centers for Environment Information (NCEI). **(E)** The vertical profile of initial temperature observed in the Northern South China Sea, which were obtained from the National Centers for Environment Information (NCEI).

pressure at different depths. Compared to salinity, the density is primarily (but not completely) associated with seawater temperature variations (Ruddick et al., 2009). The study merely discusses the changes in seawater density and acoustic velocity caused by temperature and depth and sets the seawater salinity as a constant value of 35psu.

2.2 Seismic oceanography mathematical model and numerical simulation

The field seismic reflection section is significantly different from fluid dynamics numerical simulation results in the physical meaning, reflection the seawater wave impedance contrasts and

the distribution of thermohaline, respectively. As a consequence, a mutual conversion method is required between the two as the objective of this work intends to convert fluid dynamics numerical simulation results into seismic oceanography numerical simulation sections. The seismic response characteristic of submarine sand waves induced hair-like reflection configuration is computed numerically by solving the two-dimensional acoustic wave equation with the finite-difference method (Madariaga, 1976; Frankel and Clayton, 1984; Frankel and Clayton, 1986). This numerical wave simulator models the high-order wave phenomena associated with complex velocity and density structures (Kelly et al., 1976; Swift et al., 1990). Reverse-time migration has been applied to synthetic seismic shot records of the submarine sand waves induced hair-like reflection configuration model to obtain seismic oceanography numerical simulation sections reflecting the characteristic of the water column and similar to the field seismic reflection section (Baysal et al., 1983; Chattopadhyday and McMechan, 2008; Deng and McMechan, 2008).

Based on fluid dynamics numerical simulation results, a mathematical model (acoustic velocity and density) that can be used for seismic oceanography numerical simulation is established using the seawater state equation and the acoustic velocity empirical equation (Figures 3A, B). The mathematical model is a critical data foundation for computing synthetic seismic reflection data (Kormann et al., 2010), which mimics real seismic oceanography data to analyze the seismic response characteristics of hair-like reflection configuration. Subsequently, the fluid dynamics numerical simulation parameters are adjusted appropriately according to the field seismic reflection section, and the seismic response characteristics under different numerical simulation conditions are analyzed. To simulate the source wavelet we have chosen a Ricker wavelet with a dominant frequency of 45Hz, which is close to the central frequency of the real data acquired. The space and time discretization are 2m and 0.4ms, respectively. An 8.5km-long section reaching up to 764m-depth section has been simulated (Figure 3C). The length of each shot-record simulation is 1.2s, enough to cover the model completely. The seismic line includes 340 shot records, that is, one shot every 25m.

2.3 Fusion computation and optimal matching

The seismic oceanography numerical simulation section and the field seismic reflection section are performed for fusion computation, and the key dynamic parameters of hair-like reflection configuration and the important dynamic information reflected by the seismic dataset are fitted and analyzed by the optimal matching method. The study investigates the relationship between the seismic oceanography numerical simulation section and the field seismic reflection section and analyzes the similarity between the two in a specific area. If the morphological characteristics of typical events on the seismic section are similar, it means that the ocean fluid dynamics environment in this area is consistent with the conditions set by the fluid dynamics numerical simulation, so as to deduce the seawater movement.

Based on the morphological characteristics of the hair-like reflection configuration, it is proposed to apply parameters such as the angle with the seafloor (θ) and the height from the seafloor (H) (Figure 2B) to describe it quantitatively. Two evaluation indexes, root-mean-square error (RMSE) and correlation coefficient (R), are used to quantify the similarity between the seismic oceanography numerical simulation with different fluid dynamics numerical simulation conditions and the field seismic reflection section, in order to obtain the optimization results of the dynamic parameters of hair-like reflection configuration. Under different fluid dynamics numerical simulation conditions, we

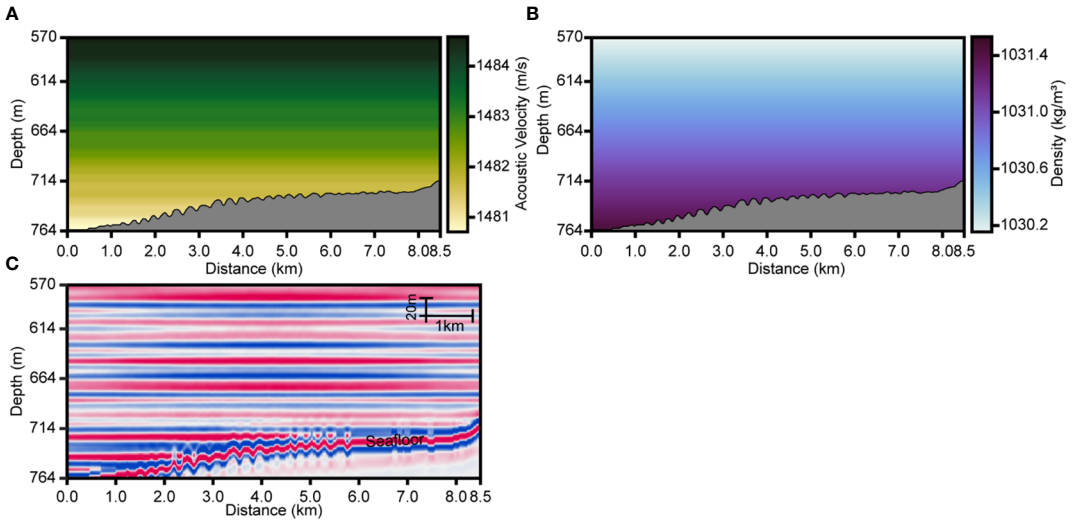

FIGURE 3
Seismic oceanography mathematical model at initial moment, **(A)** seawater acoustic velocity model, and **(B)** seawater density model. **(C)** Seismic oceanography numerical simulation section with the dominant frequency of 45Hz.

plotted the angle and height of the hair-like reflection configuration seismic events (Events 1-7) and flow conditions in a two-dimensional domain where the horizontal axis is the flow conditions, and the left vertical one is the angle, and the right vertical one is the height. In the two-dimensional domain, we plotted the height and angle of the hair-like reflection configuration seismic events (Events 1-7) obtained under different fluid dynamics numerical simulation conditions into graphs, and took the height and angle of the hair-like reflection configuration on the field seismic reflection section as the baseline. Then the optimal matching method is carried out according to the distance between the two. Based on the matching principle, the smaller the distance between the two, which illustrates that the higher the similarity. Therefore, the seismic oceanography numerical simulation section is closer to the field seismic reflection section. We developed the optimal quantitative relationship between the field seismic reflection section and the seismic oceanography numerical simulation section using the optimal matching method from these two-dimensional domains, and then the dynamic parameters and fluid dynamics environment of the hair-like reflection configuration on the field seismic reflection section are deduced from the fluid dynamics numerical simulation. Suppose the difference of angle and height between the seismic oceanography numerical simulation section and the field seismic reflection section is minimum, the root-mean-square error is minimum, and the correlation coefficient is maximum, which means that the matching between the two is optimal and the similarity is the highest (Figure 1). To improve the accuracy, the morphological characteristics of the submarine sand waves induced hair-like reflection configuration is the average value of the multiple calculation results.

3 Results

3.1 Seismic oceanography numerical simulation section of hair-like reflection configuration

The morphological characteristics of the hair-like reflection configuration can be identified on the synthetic seismic oceanography section resulting from numerical simulation (Figure 4). The thickness of the area affected by the interaction between seawater movement and submarine topography can reach a height of 120m, which is consistent with the characteristics of the field seismic reflection section (Figure 2B). Region 1 (0-3km) is a submarine turbulent region with relatively chaotic internal reflections, and the seismic reflection characteristics vary with different seawater flow velocities. The polarity of the seismic

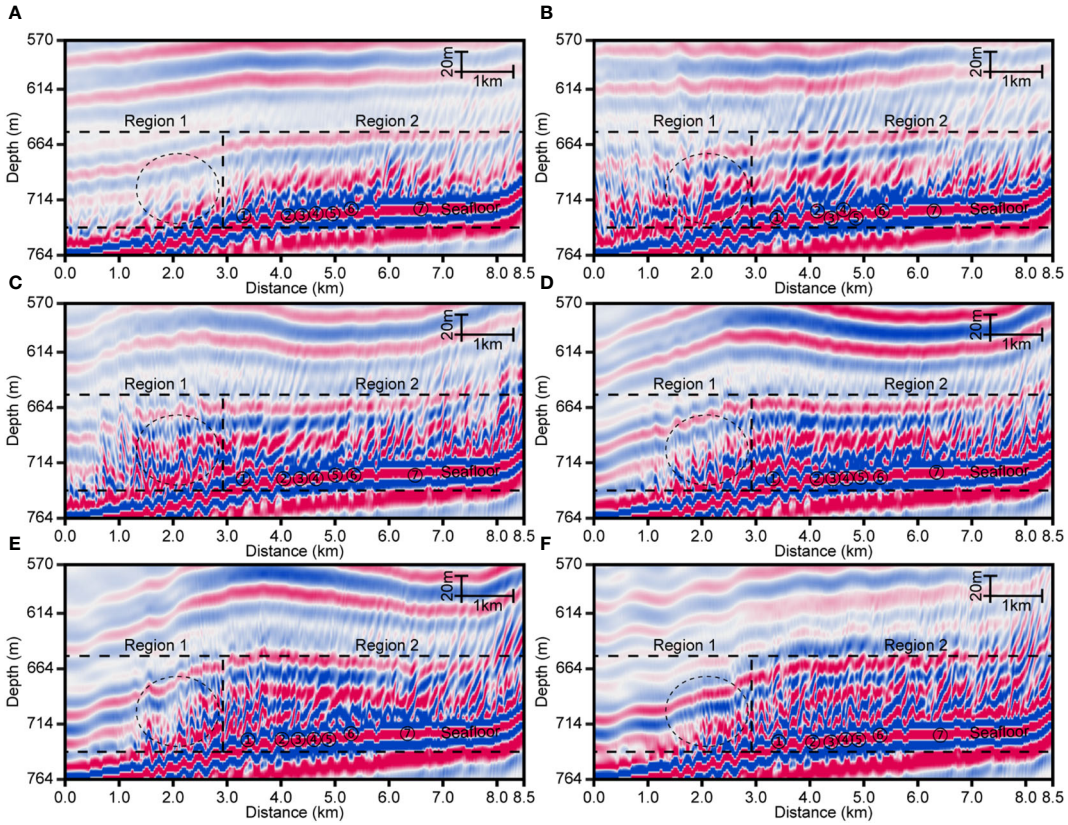

FIGURE 4
Seismic oceanography numerical simulation section of hair-like reflection configuration with the flow conditions of **(A)** 0.70m/s, **(B)** 0.75m/s, **(C)** 0.80m/s, **(D)** 0.85m/s, **(E)** 0.90m/s and **(F)** 0.95m/s. Region 1: Submarine turbulent region; Region 2: The region of quantitative hair-like reflection configuration; ①-⑦: The selection of hair-like reflection configuration seismic events with the same meaning as that in Figure 2B.

reflection event matches well with the field seismic reflection section, and the turbulent region (Region 1 in Figure 4) gradually decreases with the increase of seawater flow velocity. Moreover, when the boundary force with a constant flow condition of U_0 is less than 0.70m/s or greater than 0.90m/s, the submarine turbulent characteristics in Region 1 are not obvious. The hair-like reflection configuration generally develops above submarine sand waves in Region 2, with low continuity of seismic events and at an angle with the seafloor. The vertical thickness is about 30m, and the polarity variation is consistent with the field seismic reflection section. The characteristics of hair-like reflection configuration in the range of 4.0-5.5km are more distinct and easier to distinguish than those in other areas.

Submarine topography plays a crucial role in seawater flow near the seafloor. Therefore, it is essential to investigate the impact of deviations in submarine topography on the numerical simulation results. To this end, we smoothed the realistic bottom topography to obtain the submarine sand wave topography whose morphology characteristics are similar and amplitude is approximately half that of the realistic submarine sand wave topography (Figure 5A). The fluid dynamics numerical simulation was carried out with a constant flow condition of 0.80m/s, and other parameters were consistent, with the only variable being the difference in submarine topography. Comparing Figure 4C and Figure 5B, it is found that the differences in the thickness of the area affected by the interaction between seawater movement and submarine topography and the submarine turbulent region of Region 1 (0-3km) are slightly small. However, there are significant differences in hair-like reflection configuration in Region 2, making it difficult to identify their events, especially in Events 4-7.

3.2 Morphological characteristics parameters of hair-like reflection configuration

By comparing the hair-like reflection configuration seismic event on the field seismic reflection section and the seismic oceanography numerical simulation section, it is found that the morphological characteristics between the two have good correspondence (Figure 6). Hair-like reflection configuration seismic events tilt to the right, appearing with an angle with the seafloor and gradually decreasing with the direction of the seawater flow. There is a greater horizontal continuity, with a thickness of 30m, and submarine topography plays a crucial role in the development of hair-like reflection configuration. The difference between the hair-like reflection configuration seismic event on the field seismic reflection section and the seismic oceanography numerical simulation section of Event 1 is larger than that of other events. The angle and height can be used to describe the development scale of the hair-like reflection configuration quantitatively. The analysis shows that the angle of the hair-like reflection configuration on the field seismic reflection section is between 49.31° and 69.22°, and the height is between 9.46m and 31.43m. In comparison, the angle of the hair-like reflection configuration on the seismic oceanography numerical simulation section is 47.26-79.50°, and the height is 13.00-31.73m. The correlation coefficient between the hair-like reflection configuration seismic events (Events 1-7) on the field seismic reflection section and the seismic oceanography numerical simulation section under different fluid dynamics numerical simulation conditions is greater than 0.96, and the root-mean-square error between the two is 0.6391-7.9294.

4 Discussion

4.1 Model validation

The simulated results are validated by comparing with the field seismic reflection section. The two-dimensional model utilizes realistic bottom topography merged from the field seismic reflection section and nearby hydrological information to investigate the fluid dynamics environment and formation mechanism of submarine sand waves induced hair-like reflection configuration. Although the physical meaning of the fluid dynamics numerical simulation section (seawater thermohaline distribution) differs from that of the field seismic reflection section (seawater wave impedance), it can conduct a comparative analysis simply through conversion due to the same research objectives. The conversion of the fluid dynamics numerical simulation section into the seismic oceanography numerical simulation section is similar to the principle of high-frequency acoustics in oceanography (Reeder et al., 2011). Therefore, the simulated results can be verified on the basis of the field seismic reflection section, and the degree of

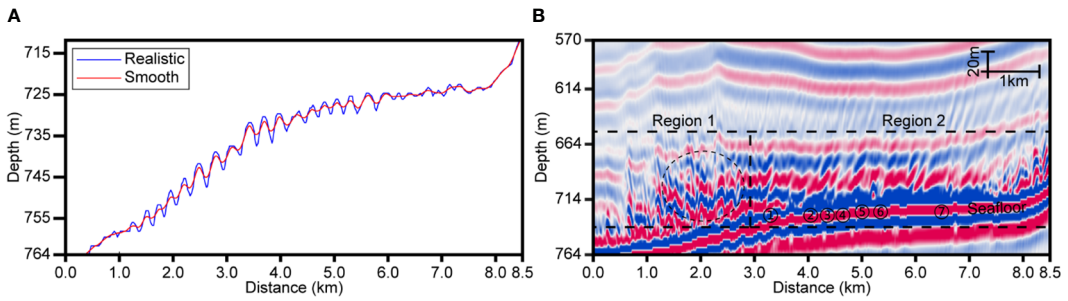

FIGURE 5
(A) The realistic submarine sand wave topography (blue line) and smooth submarine sand wave topography (red line). **(B)** Seismic oceanography numerical simulation section of hair-like reflection configuration with the flow conditions of 0.80m/s for smooth submarine sand wave topography.

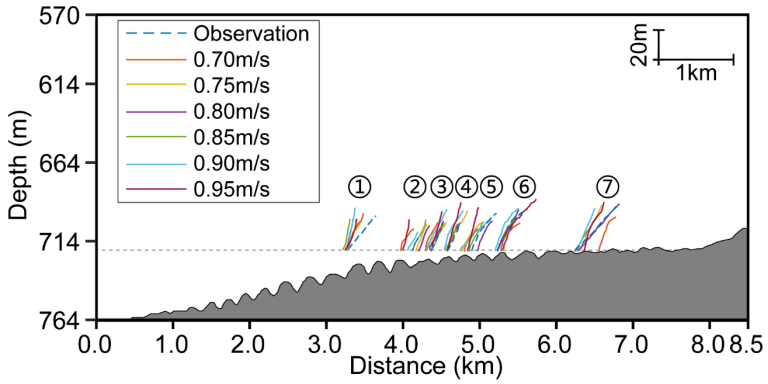

FIGURE 6
Interpretation diagram of the hair-like reflection configuration seismic events on the field seismic reflection section (Observation) and the seismic oceanography numerical simulation section under different fluid dynamics numerical simulation conditions of 0.70m/s, 0.75m/s, 0.80m/s, 0.85m/s, 0.90m/s and 0.95m/s. ①-⑦: The selection of hair-like reflection configuration seismic events with the same meaning as that in Figure 2B.

matching between the two is related to the accuracy of the two-dimensional model. It is found that the seismic oceanography numerical simulation section has similar structural characteristics to the field seismic reflection section (Figure 2B and Figure 4) according to the seismic oceanography mathematical model and numerical simulation, which implies the accuracy of fluid dynamics numerical simulation results.

The simulated background flow currents are validated by comparing with those from the morphological characteristics of seismic events on the field seismic reflection section. As shown in Figure 2B, according to the slope of submarine topography, the tendency of hair-like reflection configurations, and the morphological characteristics of submarine sand waves, it can be determined that the direction of seawater flow on the field seismic reflection section is from left to right. Consequently, the two-dimensional model we constructed with the direction of seawater flow for fluid dynamics numerical simulation is from left to right (Figure 2C), and the seismic oceanography numerical simulation section agrees well with the field seismic reflection section. Cacchione and Drake (1986) demonstrated theoretically that linear internal waves of 5m amplitude propagating over a typical continental slope could generate bottom current velocities of more than 0.5m/s. An internal solitary wave with an amplitude of approximately 30m was identified near the research area of submarine sand waves induced hair-like reflection configuration (black arrow in Figure 2A), so it indicates that the bottom boundary layer has a strong bottom current velocity and the flow conditions used in this study are reasonable. Based on the above results, we believe the simulated results are reasonable and can be used to investigate the fluid dynamics environment and formation mechanism of hair-like reflection configuration.

4.2 Fluid dynamics environment of hair-like reflection configuration

Submarine sand waves induced hair-like reflection configuration develops above the seafloor, where fluid dynamics processes are extremely complicated. There is no matching seismic model of fluid dynamics for interpreting and analyzing seafloor processes, and the seismic reflection characteristics vary with different seawater flow velocities. In our numerical examples of the fluid dynamics, when the boundary force with a constant flow condition of U_0 is less than 0.70m/s or greater than 0.90m/s, the submarine turbulent characteristics in Region 1 are not obvious. The reason is that when the boundary force with a constant flow condition of U_0 is less than 0.70m/s, the flow field intensity generated by the interaction with the submarine topography is insufficient to cause the turbulence process to occur (Figure 4A). When the boundary force with a constant flow condition of U_0 is greater than 0.90m/s, the quasi-steady stratified flow dominates, making the oceanic stratification characteristics obvious (Figures 4E, F).

Under different fluid dynamics numerical simulation conditions, there is diversity in the hair-like reflection configuration seismic event characteristics on the seismic oceanography numerical simulation section, which can reflect the distinct fluid dynamic environment in the region. Through comparative analysis of Figures 7A-G, it is found that under the different fluid dynamics numerical simulation conditions, the hair-like reflection configuration computed from fluid dynamics numerical simulation and seismic oceanography method are significantly different, indicating that the vital dynamic information reflected by the field seismic dataset is sensitive enough to be used to invert the flow field characteristics. And it can be inferred that there is a coincident position between the graph and the baseline, so the seawater flow velocity corresponding to this position is the optimization result of the dynamic parameters of the ocean environment (Figures 7A–G). Under different fluid dynamics numerical simulation conditions used in this study, the minimum height error of each hair-like reflection configuration seismic event is 0.08m, and the minimum angle error is 0.23°, which is in good agreement with a constant flow condition of U_0 is 0.80m/s. It is reasonable to use the flow condition of 0.70-0.95m/s for fluid dynamics numerical simulation from the relationship between the graph and the baseline in Figures 7A–G. It is found that when the boundary force with a constant flow condition of U_0 is 0.80m/s, the

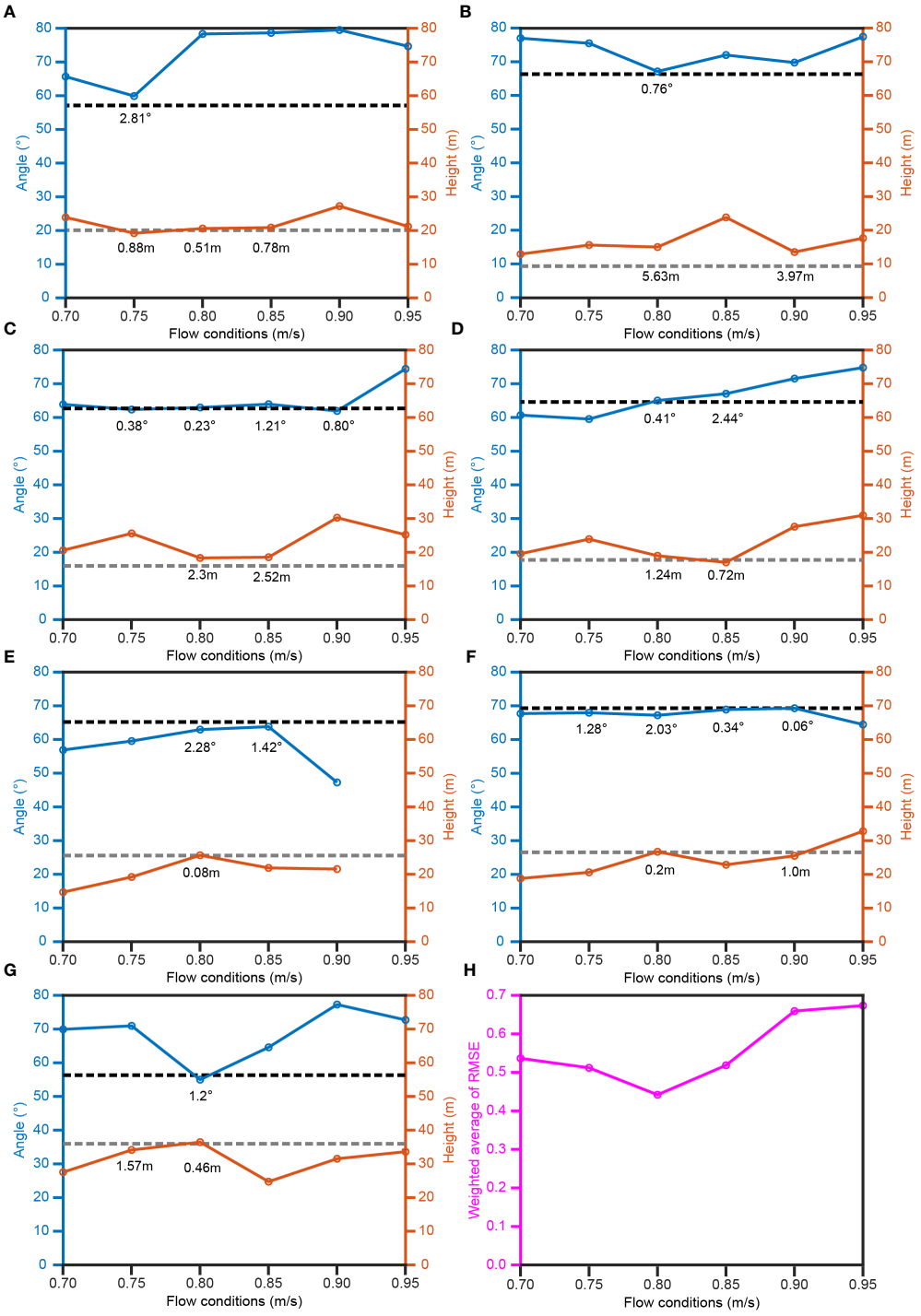

FIGURE 7
The angle and height of the typical seismic event of **(A)** Event 1, **(B)** Event 2, **(C)** Event 3, **(D)** Event 4, **(E)** Event 5, **(F)** Event 6, **(G)** Event 7 on the field seismic reflection section and the seismic oceanography numerical simulation section under different fluid dynamics numerical simulation conditions of 0.70m/s, 0.75m/s, 0.80m/s, 0.85m/s, 0.90m/s and 0.95m/s. **(H)** Relationship between seismic events on the field seismic reflection section and the seismic oceanography numerical simulation section under different fluid dynamics numerical simulation conditions. The black dashed line indicates the angle of the seismic event on the field seismic reflection section, and the gray dashed line indicates the height of the seismic event on the field seismic reflection section. The text inside the figure represents the absolute value of the error between the field seismic reflection section and the seismic oceanography numerical simulation section under different fluid dynamics numerical simulation conditions. When the boundary force with a constant condition of U_0 is 0.95m/s, the continuity of Event 5 is low, so the height and angle at 0.95m/s are not plotted in **(E)**.

angle and height of the hair-like reflection configuration on the field seismic reflection section match well with the seismic oceanography numerical simulation section, which demonstrates that the development scale of the hair-like reflection configuration obtained by numerical simulation under this flow condition is similar to that on the filed seismic reflection section. Simultaneously, comparing the weighted average of root-mean-square error between the hair-like reflection configuration computed under different fluid dynamics numerical simulation conditions and that on the field seismic reflection section, it is found that when the boundary force with a constant flow condition of U_0 is 0.80m/s, the weighted average of root-mean-square error is the smallest, indicating that the fitting between the two is optimal (Figure 7H). Consequently, it can be inferred that the seawater flow velocity here is about 0.80m/s. Simultaneously, interval solitary waves are well developed in the Dongsha Uplift of the northern South China Sea and the hydrodynamics conditions are sufficient, resulting in strong bottom current velocities in this area. One more piece of evidence for our numerical simulation results is that interval solitary waves induced the bottom current velocity reached 0.596-0.793m/s (Jia et al., 2019), even exceeding 1.0m/s (Lien et al., 2014) and reached a maximum of 2.0m/s (Geng et al., 2017). It is found that submarine sand waves primarily develop in the hydrodynamics environment with a bottom current velocity of 0.2-1.0m/s, and the best development is under the condition of a bottom current velocity of 0.4-0.8m/s (Zhuang et al., 2004). When the bottom current velocity exceeds the critical incipient velocity, the submarine sandy sediments begin to move and form small sand ripples, which gradually increase to form submarine sand waves. The calculation and analysis of the formation mechanism and mathematical model of submarine sand waves show that the incipient velocity of medium sand forming submarine sand waves is 0.507m/s. Therefore, the bottom current velocity in this area is sufficient to shape the seabed topography by forming submarine sand waves (Reeder et al., 2011; Belde et al., 2015; Ribó et al., 2016). Consequently, based on previous studies of the hydrodynamic environment around the Dongsha Uplift of the northern South China Sea and the development of submarine sand waves, it is reasonable to estimate the seawater flow velocity of 0.80m/s by fluid dynamics numerical simulation and seismic oceanography method. Inversely, the difference between the hair-like reflection configuration seismic event on the field seismic reflection section and the seismic oceanography numerical simulation section of Event 1 is larger than that of other events. It is inferred that Event 1 is located at the boundary of the submarine turbulent region and is greatly affected by turbulence. Additionally, the slope of the submarine topography at Event 1 is larger than that of others, resulting in a more obvious interaction between seawater movement and submarine topography, which is another reason for poor stability and drastic changes in the morphological characteristics of the seismic event.

The fluid dynamics numerical simulation can provide abundant information on the kinematics of seawater layers and obtain the comprehensive fluid dynamics environment characteristics of submarine sand waves induced hair-like reflection configuration, that is, the flow field section, which can accurately describe its dynamic evolution process. When the boundary force with a constant flow condition of U_0 is 0.80m/s, the flow field characteristics distribution of the oceanic bottom boundary layer is shown in Figure 8. The horizontal velocity presents a wavy variation similar to that of submarine sand waves (Figure 8A). Due to the non-hydrostatic effect and the friction between seawater movement and submarine topography, the vertical velocity appears in the seawater layer, with the upwelling and downwelling alternating (Figure 8B), which affects the characteristics of ocean stratification. Additionally, the vertical velocity within the range of 0-3.5km and 5.0-8.5km can affect the larger area above the seafloor. It is speculated that it is related to the slope of the submarine topography, which in turn causes the horizontal velocity to change at the same location.

4.3 Formation mechanism analysis of hair-like reflection configuration

Based on the fluid dynamics environment of the hair-like reflection configuration, we can investigate its formation mechanism and dynamically analyze the fluid dynamics origin of the seismic event characteristics near the oceanic bottom boundary layer. Under the constraints of the submarine sand wave topography, the seafloor of Region 1 (0-3.0km) does not develop a hair-like reflection configuration, but forms a turbulent region. The phenomenon can be explained by the temperature field, which shows the apparent vortex shape in the temperature field near the position (Hu et al., 2021), destroying the seawater layer feature. The hair-like reflection configuration within the range of 4.0-5.5km in Region 2 is better as well for this reason. The overlying water column of the submarine sand waves does not form a vortex shape, which enables the hair-like reflection configuration to develop normally (Figure 9).

The deviations in submarine sand wave topography have little effect on the thickness of the area affected by the interaction between seawater movement and submarine topography and the submarine turbulent region of Region 1 (0-3km) (Figure 4C and Figure 5B). It is speculated that the reason for its formation is mainly restricted by the slope of submarine topography, and is independent of the scale of submarine sand waves. There are significant differences in the hair-like reflection configuration of Region 2 (Figure 4C and Figure 5B). The reason is that with the decrease of the amplitude of submarine sand waves, the interaction between seawater movement and submarine topography cannot form vortex shapes at the position of submarine sand waves troughs, resulting in limited development of hair-like reflection configuration. The amplitude of the smooth submarine sand waves corresponding to Events 4-7 is approximately 1m, indicating that the hair-like reflection configuration cannot develop above submarine sand waves at this scale. Consequently, we can determine whether the overlying water column develops hair-like reflection configurations by the scale of submarine sand waves.

The interaction between seawater movement and submarine topography results in the formation of vortex shapes at the position of submarine sand wave troughs (Carr et al., 2010), which destroy

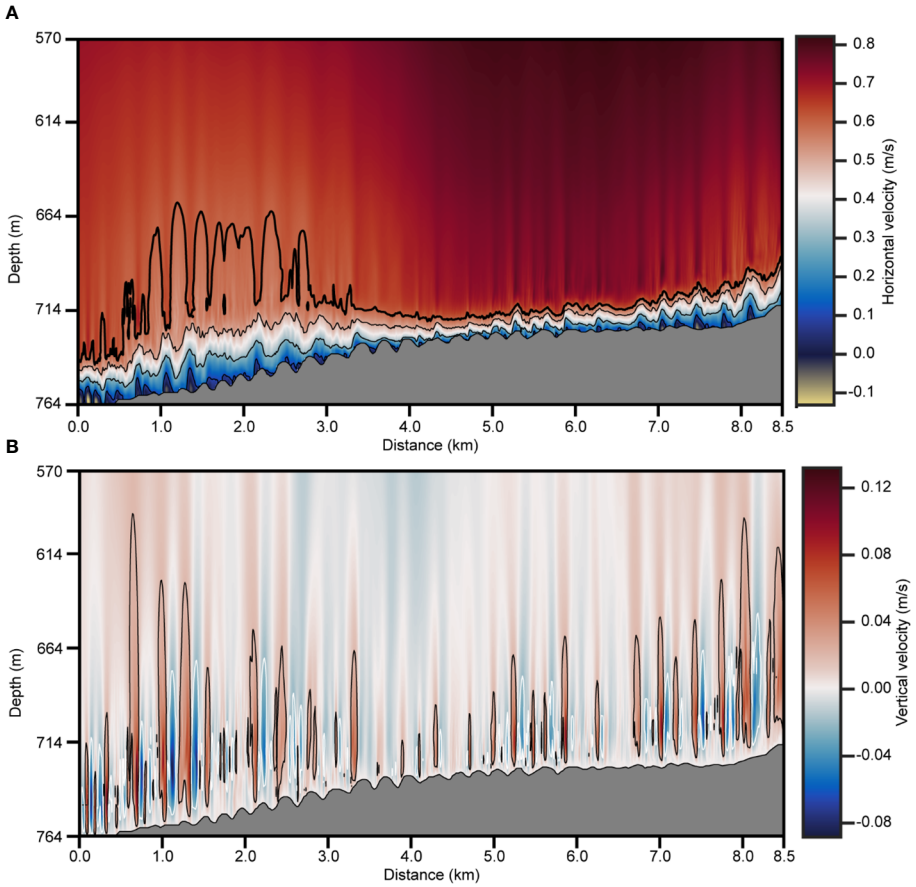

FIGURE 8
Fluid dynamics environment of hair-like reflection configuration with a constant flow condition forced on the boundary of 0.80m/s. **(A)** Horizontal velocity field section. Velocity is contoured in 0.2m/s intervals starting at 0.1m/s. Thicker contour shows the 0.6m/s isovelocity. **(B)** Vertical velocity field section. The white contour isovelocity is -0.02m/s and the black isovelocity is 0.02m/s.

the ocean stratification feature, leads to the redistribution of seawater thermohaline, and then develops a hair-like reflection configuration. The range between the isoline of 0.5m/s and the seafloor in the horizontal velocity section is the area where seawater movement interacts with submarine topography, and the hair-like reflection configuration is also developed in this range (Figure 8). Within the range of 6.5-8.5km in Region 2, the amplitude of submarine sand waves is small, whose trough position does not form a vortex shape. Consequently, there is no hair-like reflection configuration in this area, and the seawater layer seismic event presents chaotic reflection characteristics due to the vortex shape of the overlying water column at the height of approximately 3m above the seafloor. There are vortex shapes in the overlying water column above the seafloor of Region 1 and Region 2 (6.5-8.5km), while there is no vortex shape in the overlying water column above the seafloor of Region 2 (4.5-5.5km). It is speculated that it is caused by changes in the slope of the submarine topography. Due to the topographic acceleration effect, the flow field intensity in the overlying water column at this position is greater than that at other positions. It can be concluded that under the same seawater flow velocity, the change of submarine topography scale also affects the development of hair-like reflection configuration. It is found that the slope of the submarine topography in Region 1 is about 13°, while that in Region 2 (4.0-5.0km) is about 3° in the study. Consequently, we demonstrated that as the slope of the submarine topography varies, under the constraint of the submarine sand wave topography, the oceanic bottom boundary layer will also develop different morphological characteristics of reflection configuration. With the increase of submarine topography slope, the morphological characteristics of submarine sand waves induced hair-like reflection configuration will be affected. For instance, when the slope of the submarine topography increases to 13°, the hair-like reflection configuration will not develop above the submarine sand waves, but the submarine turbulent region will be formed. When the boundary force with a constant condition of U_0 is 0.95m/s, the flow field intensity generated by the interaction between seawater movement and submarine topography is large enough to produce vortex shapes in the overlying water column of Region 2 (4.0-5.5km), which will affect the development of the hair-like reflection configuration under this seawater flow velocity. It is concluded that the change in the temperature field is consistent with the change in the seawater flow field according to comprehensive analysis. Consequently, it is inferred that without the influence of oceanic suspended sediments, the change of seawater layer features caused only by the interaction between seawater movement and

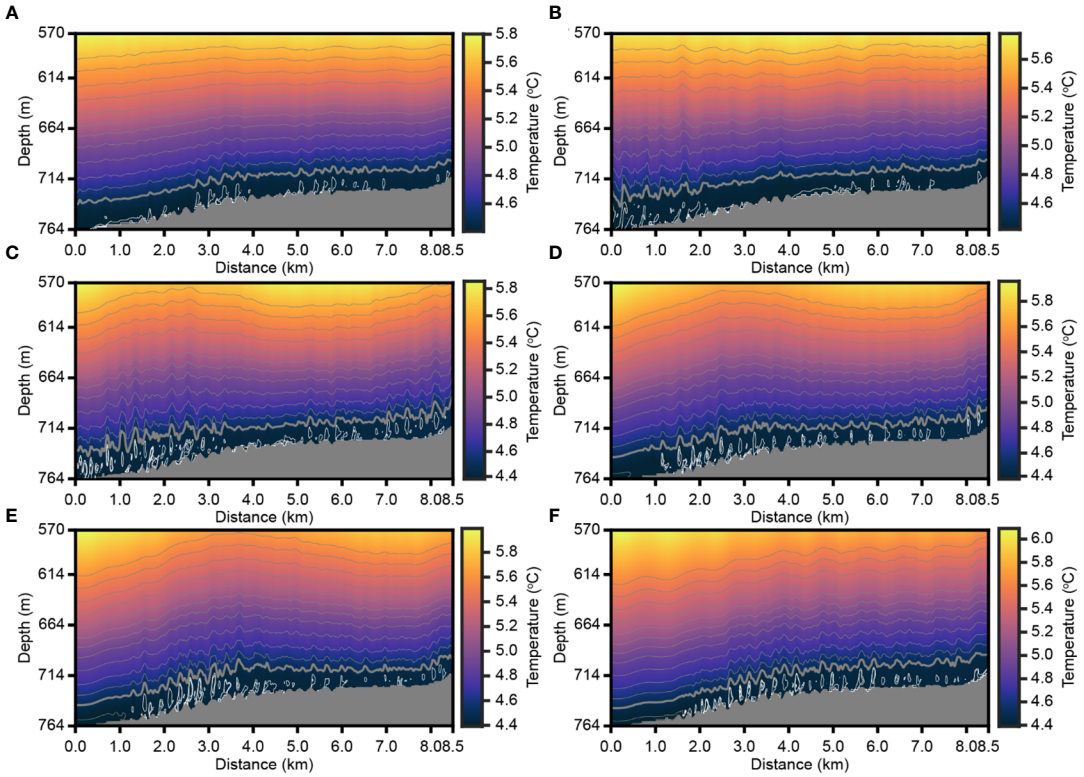

FIGURE 9
Temperature field section of hair-like reflection configuration with constant flow conditions forced on the boundary of **(A)** 0.70m/s, **(B)** 0.75m/s, **(C)** 0.80m/s, **(D)** 0.85m/s, **(E)** 0.90m/s and **(F)** 0.95m/s. Temperature is contoured in 0.1°C intervals starting at 4.39°C with grey isotherms. Thicker contour shows the 4.39°C isotherm. The white isotherms are below 4.39°C.

submarine topography, that is, the difference of seawater thermohaline, can form hair-like reflection configuration.

5 Conclusions

This study proposes a method to discuss the fluid dynamics environment and formation mechanism of hair-like reflection configuration by using fluid dynamics numerical simulation and seismic oceanography technology. The fluid dynamics numerical simulation provides a basis for the dynamic analysis of the evolution process of the hair-like reflection configuration. Combined with the seismic oceanography numerical simulation and the optimal matching method, the seawater flow velocity in this study is estimated to be approximately 0.80m/s. Simultaneously, we obtain the flow field characteristics of the water column above submarine sand waves and deeply understand the fluid dynamics environment. Moreover, the deviations in submarine topography (amplitude of submarine sand waves) have significant impact on the development of the hair-like reflection configuration. Based on the constructed fluid dynamics seismic reflection model, the fluid dynamics formation mechanism of the submarine sand waves induced hair-like reflection configuration is proposed. Without the influence of oceanic suspended sediments, the change of seawater layer features caused only by the interaction between seawater movement and submarine topography, that is, the difference of seawater thermohaline, can form a hair-like reflection configuration.

Consequently, it is possible to discuss the fluid dynamics environment and formation mechanism of submarine sand waves induced hair-like reflection configuration, which lays a foundation for further research on dynamic processes of hair-like reflection configuration using the seismic oceanography method. This work provides a new research perspective for interpreting complex seismic oceanography images, deepens understanding of the interaction process between multiscale ocean dynamics and submarine bottom topography, and can further quantify the dynamic process.

Data availability statement

The raw data supporting the conclusions of this article will be made available by the authors, without undue reservation.

Author contributions

TH performed the numerical simulation and wrote the manuscript. JC contributed to the conception of the study. BH

and LA contributed significantly to analysis and manuscript preparation. All authors contributed to the article and approved the submitted version.

Funding

This work is financially supported by the National Natural Science Foundation of China [Grant No. 42274149]. JC is funded by the Shandong Province "Taishan Scholar" Construction Project.

Acknowledgments

The CTD data used in this study were provided by the National Centers for Environment Information (https://www.ncei.noaa.gov/products/world-ocean-database).

Conflict of interest

The authors declare that the research was conducted in the absence of any commercial or financial relationships that could be construed as a potential conflict of interest.

Publisher's note

References

Alford, M. H., Peacock, T., MacKinnon, J. A., Nash, J. D., Buijsman, M. C., Centuroni, L. R., et al. (2015). The formation and fate of internal waves in the south China Sea. *Nature* 521 (7550), 65–69. doi: 10.1038/nature14399

Ashley, G. M. (1990). Classification of large-scale subaqueous bedforms: a new look at an old problem. SEPM bedforms and bedding structure research symposium. *J. Sediment. Petrology* 60 (1), 160–172. doi: 10.2110/jsr.60.160

Baysal, E., Kosloff, D. D., and Sherwoods, J. W. C. (1983). Reverse time migration. *Geophysics* 48 (11), 1514–1524. doi: 10.1190/1.1441434

Belde, J., Back, S., and Reuning, L. (2015). Three-dimensional seismic analysis of sediment waves and related geomorphological features on a carbonate shelf exposed to large amplitude internal waves. *Sedimentology* 62 (1), 87–109. doi: 10.1111/sed.12141

Besio, G., Blondeaux, P., Brocchini, M., Hulscher, S. J. M. H., Idier, D., Knaapen, M. A. F., et al. (2008). The morphodynamics of tidal sand waves: a model overview. *Coast. Eng.* 55 (7-8), 657–670. doi: 10.1016/j.coastaleng.2007.11.004

Biescas, B., Sallarès, V., Pelegrí, J. L., Machín, F., Carbonell, R., Buffett, G., et al. (2008). Imaging meddy finestructure using multichannel seismic reflection data. *Geophys. Res. Lett.* 35 (11), L11609. doi: 10.1029/2008GL033971

Borsje, B. W., Kranenburg, W. M., Roos, P. C., Matthieu, J., and Hulscher, J. M. H. (2014). The role of suspended load transport in the occurrence of tidal sand waves. *J. Geophys. Res. Earth Surface* 119, 701–716. doi: 10.1002/2013JF002828

Cacchione, D. A., and Drake, D. E. (1986). Nepheloid layers and internal waves over continental shelves and slopes. *Geo-Mar. Lett.* 6, 147–152. doi: 10.1007/BF02238085

Campans, G. H. P., Roos, P. C., de Vriend, H. J., and Hulshcher, S. J. M. H. (2017). Modeling the influence of storms on sand wave formation: a linear stability approach. *Cont. Shelf Res.* 137 (1), 103–116. doi: 10.1016/j.csr.2017.02.002

Carr, M., Stastna, M., and Davies, P. A. (2010). Internal solitary wave-induced flow over a corrugated bed. *Ocean Dynam.* 60, 1007–1025. doi: 10.1007/s10236-010-0286-2

Chattopadhyday, S., and McMechan, G. A. (2008). Imaging conditions for prestack reverse-time migration. *Geophysics* 73 (3), S81–S89. doi: 10.1190/1.2903822

Chen, J., Bai, Y., Guan, Y., Yang, S., Song, H., and Liu, B. (2016). Geophysical analysis of abnormal seismic (oceanography) reflection characteristics of ocean bottom boundary layer. *Chin. J. Geophys.* 59 (5), 573–586. doi: 10.6038/cjg20160620

Chen, J., Song, H., Guan, Y., Pinheiro, L. M., and Geng, M. (2018). Geological and oceanographic controls on seabed fluid escape structures in the northern zhongjiannan basin, south China Sea. *J. Asian Earth Sci.* 168, 38–47. doi: 10.1016/j.jseaes.2018.04.027

Chen, J., Song, H., Guan, Y., Yang, S., Bai, Y., and Geng, M. (2017). A preliminary study of submarine cold seeps by seismic oceanography techniques. *Chin. J. Geophys. (in Chin. English abstract)* 60 (1), 117–129. doi: 10.1002/cjg2.30032

Chen, J., Tong, S., Han, T., Song, H., Pinheiro, L., Xu, H., et al. (2020). Modelling and detection of submarine bubble plumes using seismic oceanography. *J. Mar. Syst.* 209, 103375. doi: 10.1016/j.jmarsys.2020.103375

Cukur, D., Kong, G. S., Buchs, D. M., Lee, G. S., Kim, S. P., Um, I. K., et al. (2022). Upslope migrating sand waves on sediment-starved shelves: an example from the southeastern continental margin of the Korean peninsula. *Mar. Geol.* 444, 106728. doi: 10.1016/j.margeo.2021.106728

Deng, F., and McMechan, G. A. (2008). Viscoelastic true-amplitude prestack reverse-time depth migration. *Geophysics* 73 (4), S143–S155. doi: 10.1190/1.2938083

Dickinson, A., and Gunn, K. L. (2022). The next decade of seismic oceanography: possibilities, challenges and solutions. *Front. Mar. Sci.* 9. doi: 10.3389/fmars.2022.736693

Dickinson, A., White, N. J., and Caulfield, C. P. (2020). Time-lapse acoustic imaging of mesoscale and fine-scale variability within the faroe-Shetland channel. *J. Geophys. Res. Oceans* 125, e2019JC015861. doi: 10.1029/2019JC015861

Dodd, H., Blondeaux, P., Calvete, D., Swart, H. E. D., Falqués, A., Hulscher, S. J. M. H., et al. (2003). Understanding coastal morphodynamics using stability methods. *J. Coast. Res.* 19 (4), 849–865.

Fang, C., and Hao, J. (2019). Research progress of turbulence characteristic parameters in bottom boundary layer. *IOP Conf. Series: Earth Environ. Sci.* 330, 32005. doi: 10.1088/1755-1315/330/3/032005

Flemming, B. W. (1980). Sand transport and bedform patterns on the continental shelf between Durban and port Elizabeth (southeast African continental margin). *Sediment. Geol.* 26 (1-3), 179–205. doi: 10.1016/0037-0738(80)90011-1

Frankel, A., and Clayton, R. W. (1984). A finite-difference simulation of wave propagation in two-dimensional random media. *B. Seismol. Soc Am.* 74 (6), 2167–2186. doi: 10.1785/bssa0740062167

Frankel, A., and Clayton, R. W. (1986). Finite difference simulations of seismic scattering: implications for the propagation of short-period seismic waves in the crust and models of crustal heterogeneity. *J. Geophys. Re. Sol. Ea.* 91 (B6), 6465–6489. doi: 10.1029/JB091iB06p06465

Fu, K. H., Wang, Y., Laurent, L. S., Simmons, H., and Wang, D. (2012). Shoaling of large amplitude nolinear internal waves at dongsha atoll in the northern south China Sea. *Cont. Shelf Res.* 37, 1–7. doi: 10.1016/j.csr.2012.01.010

Geng, M., Song, H., Guan, Y., and Bai, Y. (2019). Analyzing amplitudes of internal solitary waves in the northern south China Sea by use of seismic oceanography data. *Deep-Sea Res. I Oceanogr. Res. Pap.* 146, 1–10. doi: 10.1016/j.dsr.2019.02.005

Geng, M., Song, H., Guan, Y., Bai, Y., Liu, S., and Chen, Y. (2017). The distribution and characteristics of very large subaqueous sand dunes in the dongsha region of the northern south China Sea. *Chin. J. Geophys. (in Chin. English abstract)* 60 (2), 628–638. doi: 10.6038/cjg20170217

Gunn, K. L., White, N., and Caulfield, C. P. (2020). Time-lapse seismic imaging of oceanic fronts and transient lenses within south Atlantic ocean. *J. Geophys. Res. Oceans* 125, e2020JC016293. doi: 10.1029/2020JC016293

Guo, C., and Chen, X. (2014). A review of internal solitary wave dynamics in the northern south China Sea. *Prog. Oceanogr.* 121, 7–23. doi: 10.1016/j.pocean.2013.04.002

Hansen, E. A., Fredsøe, F., and Deigaard, R. (1994). Distribution of suspended sediment over wave-generated ripples. *J. Waterw. Port Coast.* 120 (1), 37–55. doi: 10.1061/(ASCE)0733-950X(1994)120:1(37)

Holbrook, W. S., and Fer, I. (2005). Ocean internal wave spectra inferred from seismic reflection transects. *Geophys. Res. Lett.* 32, L15604. doi: 10.1029/2005GL023733

Holbrook, W. S., Páramo, P., Pearse, S., and Schmitt, R. W. (2003). Thermohaline fine structure in an oceanographic front from seismic reflection profiling. *Science* 301, 821–824. doi: 10.1126/science.1085116

Hu, X., Zhang, X., Lin, L., Zhang, L., and Wang, S. (2021). Effects of a two-equation turbulence model on the simulation of the internal lee waves. *Atmos. Ocean. Sci. Lett.* 14, 100020. doi: 10.1016/j.aosl.2020.100020

Huang, X., Chen, Z., Zhao, W., Zhang, Z., Zhou, C., Yang, Q., et al. (2016). An extreme internal solitary wave event observed in the northern south China Sea. *Sci. Rep.* 6 (1), 30041. doi: 10.1038/srep30041

Huang, X., Song, H., Guan, Y., Geng, M., and Wang, Y. (2018). Study of seawater seismic facies based on computational fluid dynamics. *Chin. J. Geophys. (in Chin. English abstract)* 61 (7), 2892–2904. doi: 10.6038/cjg2018L0382

Huang, X., Zhao, W., Tian, J., and Yang, Q. (2014). Mooring observations of internal solitary waves in the deep basin west of Luzon strait. *Acta Oceanol. Sin.* 33 (3), 82–89. doi: 10.1007/s13131-014-0417-7

Jazi, S. D., Wells, M. G., Peakall, J., Dorrell, R. M., Thomas, R. E., Keevil, G. M., et al. (2020). Influence of Coriolis force upon bottom boundary layers in a large-scale gravity current experiment: implications for evolution of sinuous deep-water channel systems. *J. Geophys. Res. Oceans* 125, e2019JC015284. doi: 10.1029/2019JC015284

Jia, Y., Tian, Z., Shi, X., Liu, J. P., Chen, J., Liu, X., et al. (2019). Deep-sea sediment resuspension by internal solitary waves in the northern south China Sea. *Sci. Rep.* 9, 12137. doi: 10.1038/s41598-019-47886-y

Kelly, K. R., Ward, R. W., and Treitel, S. (1976). Synthetic seismograms: a finite-difference approach. *Geophysics* 41 (1), 2–27. doi: 10.1190/1.1440605

Klymak, J. M., and Legg, S. M. (2010). A simple mixing scheme for models that resolve breaking internal waves. *Ocean Modell.* 33, 224–234. doi: 10.1016/j.ocemod.2010.02.005

Klymak, J. M., Legg, S. M., and Pinkel, R. (2010a). A simple parameterization of turbulent tidal mixing near supercritical topography. *J. Phys. Oceanogr.* 40, 2059–2074. doi: 10.1175/2010jpo4396.1

Klymak, J. M., Legg, S. M., and Pinkel, R. (2010b). High-mode stationary waves in stratified flow over large obstacles. *J. Fluid Mech.* 644, 321–336. doi: 10.1017/S0022112009992503

Kormann, J., Cobo, P., Biescas, B., Sallarés, V., Papenberg, C., Recuero, M., et al. (2010). Synthetic modelling of acoustic propagation applied to seismic oceanography experiments. *Geophys. Res. Lett.* 37, L00D90. doi: 10.1029/2009GL041763

Krahmann, G., Brandt, P., Klaeschen, D., and Reston, T. (2008). Mid-depth internal wave energy off the Iberian peninsula estimated from seismic reflection data. *J. Geophys. Res.* 113 (C12), C12016. doi: 10.1029/2007JC004678

Legg, S., and Adcroft, A. (2003). Internal wave breaking at concave and convex continental slopes. *J. Phys. Oceanogr.* 33, 2224–2246. doi: 10.1175/1520-0485(2003)033<2224:iwbaca>2.0.co;2

Legg, S., and Klymak, J. M. (2008). Internal hydraulic jumps and overturning generated by tidal flow over a tall steep ridge. *J. Phys. Oceanogr.* 38, 1949–1964. doi: 10.1175/2008JPO3777.1

Lien, R. C., Henyey, F., Ma, B., and Yang, Y. J. (2014). Large-Amplitude internal solitary waves observed in the northern south China Sea: properties and energetics. *J. Phys. Oceanogr.* 44 (4), 1095–1115. doi: 10.1175/JPO-D-13-088.1

Lv, H., He, Y., Shen, H., Cui, L., and Dou, C. (2010). "The propagation speed of internal solitary waves investigated by X-band radar near dongsha island," in *Proceedings of the 2010 IEEE International Geoscience and Remote Sensing Symposium*. Honolulu, HI, USA: IEEE 4705–4708. doi: 10.1109/IGARSS.2010.5654467

Madariaga, R. (1976). Dynamics of an expanding circular fault. *B. Seismol. Soc Am.* 66 (3), 639–666. doi: 10.1785/BSSA0660030639

Marshall, J., Adcroft, A., Hill, C., Perelman, L., and Heisey, C. (1997a). A finite-volume, incompressible navier stokes model for studies of the ocean on parallel computers. *J. Geophys. Res. Oceans* 103, 5753–5766. doi: 10.1029/96JC02775

Marshall, J., Hill, C., Perelman, L., and Adcroft, A. (1997b). Hydrostatic, quasi-hydrostatic, and nonhydrostatic ocean modeling. *J. Geophys. Res. Oceans* 102, 5733–5752. doi: 10.1029/96JC02776

Mccave, I. N. (1971). Sand waves in the north Sea off the coast of Holland. *Mar. Geol.* 10 (3), 199–225. doi: 10.1016/0025-3227(71)90063-6

Ménesguen, C. L., Hua, B. L., Papenberg, C., Klaeschen, D., Géli, L., and Hobbs, R. (2009). Effect of bandwith on seismic imaging of rotating stratified turbulence surrounding an anticyclonic eddy from field data and numerical simulations. *Geophys. Res. Lett.* 36, L00D05. doi: 10.1029/2009GL039951

Nandi, P., Holbrook, W. S., Pearse, S., Páramo, P., and Schmitt, R. W. (2004). Seismic reflection imaging of water mass boundaries in the Norwegian Sea. *Geophys. Res. Lett.* 31, 345–357. doi: 10.1029/2004GL021325

Perlin, A., Moum, J. N., and Klymak, J. M. (2005). Response of the bottom boundary layer over a sloping shelf to variations in alongshore wind. *J. Geophys. Res.* 110, C10S09. doi: 10.1029/2004JC002500

Pinheiro, L. M., Song, H., Ruddick, B., Dubert, J., Ambar, I., Mustafa, K., et al. (2010). Detailed 2-d imaging of the Mediterranean outflow and meddies off wiberia from multichannel seismic data. *J. Mar. Syst.* 79, 89–100. doi: 10.106/j.jmarsys.2009.07.004

Qian, S., Zhang, J., Wang, D., and Wang, Y. (2022). Observational study on drag reduction of continental-shelf bottom boundary layer. *Phys. Fluids* 34, 055127. doi: 10.1063/5.0091335

Quentel, E., Carton, X., Gutscher, M. A., and Hobbs, R. (2010). Detecting and characterizing mesoscale and submesoscale structures of Mediterranean water from joint seismic and hydrographic measurements in the gulf of cadiz. *Geophys. Res. Lett.* 37 (6), L06604. doi: 10.1029/2010GL042766

Reeder, D. B., Ma, B. B., and Yang, Y. J. (2011). Very large subaqueous sand waves on the upper continental slope in the south China Sea generated by episodic, shoaling deep-water internal solitary waves. *Mar. Geol.* 279, 12–18. doi: 10.1016/j.margeo.2010.10.009

Ribó, M., Puig, P., Muñoz, A., Lo lacono, C., Masque, P., Palanques, A., et al. (2016). Morphobathymetric analysis of the large fine-grained sediment waves over the gulf of Valencia continental slope (NW Mediterranean). *Geomorphology* 253, 22–37. doi: 10.1016/j.geomorph.2015.09.027

Ruddick, B., Song, H., Dong, C., and Pinheiro, L. (2009). Water column seismic images as map of temperature gradient. *Oceanography* 22 (1), 192–205. doi: 10.5670/oceanog.2009.19

Sallares, V., Mojica, J. F., Biescas, B., Klaeschen, D., and Gràcia, E. (2016). Characterization of the submesoscale energy cascade in the alboran Sea thermocline from spectral analysis of high-resolution MCS data. *Geophys. Res. Lett.* 43, 6461–6468. doi: 10.1002/2016GL069782

Shaw, W. J., Williams, A. J.III, and Trobridge, J. H. (1996)Measurement of turbulent sound speed fluctuations with an acoustic travel-time meter (Accessed OCEANS 96 MTS/IEEE Conference Proceedings. The Coastal Ocean - Prospects for the 21st Century).

Song, H., Chen, J., Pinheiro, L. M., Ruddick, B., Fan, W., Gong, Y., et al. (2021a). Progress and prospects of seismic oceanography. *Deep-Sea Res. Part I* 177, 103631. doi: 10.1016/j.dsr.2021.103631

Song, H., Fan, W., Sun, S., Guan, Y., Zhang, K., Gong, Y., et al. (2020)Features of internal solitary waves revealed by seismic oceanography data (Accessed EGU General Assembly 2020 EGU2020).

Song, H., Gong, Y., Yang, S., and Guan, Y. (2021b). Observations of interval structure changes in shoaling internal solitary waves based on seismic oceanography method. *Front. Mar. Sci.* 8. doi: 10.3389/fmars.2021.733959

Song, H., Pinheiro, L. M., Wang, D., Dong, C., Song, Y., and Bai, Y. (2009). Seismic images of ocean meso-scale eddies and internal waves. *Chin. J. Geophys.* 52 (6), 1251–1257. doi: 10.1002/cjg2.1451

Stow, D. A. W., Hernández-Molina, F. J., Llave, E., Sayago-Gil, M., del Río, V. D., and Branson, A. (2009). Bedform-velocity matrix: the estimation of bottom current velocity from bedform observations. *Geology* 37 (4), 327–330. doi: 10.1130/G25259A.1

Swift, S. A., Dougherty, M. E., and Stephen, R. A. (1990). Finite difference seismic modeling of axial magma chambers. *Geophys. Res. Lett.* 17 (12), 2105–2108. doi: 10.1029/GL017i012p02105

Tang, Q., Gulick, S. P., and Sun, L. (2014). Seismic observations from a yakutat eddy in the northern gulf of Alaska. *J. Geophys. Res. Oceans* 119 (6), 3535–3547. doi: 10.1002/2004JC009938

Tang, Q., Gulick, S. P. S., Sun, J., Sun, L., and Jing, Z. (2020). Submesoscale features and turbulent mixing of an oblique anticyclonic eddy in the gulf of Alaska investigated by marine seismic survey data. *J. Geophys. Res. Oceans* 125 (1), e2019JC015393. doi: 10.1029/2019JC015393

Terwindt, J. H. J. (1971). Sand waves in the southern bight of the north Sea. *Mar. Geol.* 10 (1), 51–67. doi: 10.1016/0025-3227(71)90076-4

Tian, Z., Jia, Y., Chen, J., Liu, J. P., Zhang, S., Ji, C., et al. (2021). Internal solitary waves induced deep-water nepheloid layers and seafloor geomorphic changes on the continental slope of the northern south China Sea. *Phys. Fluids* 33, 053312. doi: 10.1063/5.0045124

Tsuji, T., Noguchi, T., Niino, H., Matsuoka, T., Nakamura, Y., Tokuyama, H., et al. (2005). Two-dimensional mapping of fine structures in the kuroshio current using seismic reflection data. *Geophys. Res. Lett.* 32, L14609. doi: 10.1029/2005g1023095

Viana, A. R., Faugeres, J. C., and Stow, D. A. V. (1998). Bottom-current-controlled sand deposits - a review of modern shallow- to deep-water environments. *Sediment. Geol.* 115 (1-4), 53–80. doi: 10.1016/s0037-0738(97)00087-0

Vsemironva, E. A., Hobbs, R. W., and Housegood, P. (2012). Mapping turbidity layers using seismic oceanography methods. *Ocean Sci.* 8, 11–18. doi: 10.5194/os-8-11-2012

Wynn, R. B., and Stow, D. A. (2002). Classification and characterization of deep-water sediment waves. *Mar. Geol.* 193 (1-3), 7–22. doi: 10.1016/S0025-3227(02)00547-9

Xu, J., Wong, F., Kvitek, R., Smith, D. P., and Paull, C. K. (2008). Sandwave migration in Monterey submarine canyon, central California. *Mar. Geol.* 248, 193–212. doi: 10.1016/j.margeo.2007.11.005

Yang, Y., Liu, M., Xu, J., and Xu, W. (2022). Migrating sandwaves riding on relict dunes of Taiwan shoal, northern south China Sea. *Front. Earth Sc.* 10. doi: 10.3389/feart.2022.975220

Yang, S., Song, H., Fan, W., and Wu, D. (2021). Submesoscale features of a cyclonic eddy in the gulf of papagayo, central America. *Chin. J. Geophys. (in Chin. English abstract)* 64 (4), 1328–1340. doi: 10.6038/cjg2021O02024

Yin, S., Hernández-Molina, F. J., Lin, L., Chen, J., Ding, W., and Li, J. (2021). Isolation of the south China sea from the north pacific subtropical gyre since the latest Miocene due to formation of the Luzon strait. *Sci. Rep.* 11 (1), 1562. doi: 10.1038/s41598-020-79941-4

Zhang, L., and Luan, X. (2012). Quantitative analysis of submarine slope stability on the northern slooe of the south China Sea. *Prog. Geophys. (in Chin. English abstract)* 27 (4), 1443–1453. doi: 10.6038/j.issn.1004-2903.2012.04.019

Zhao, W., Huang, X., and Tian, J. (2012). A new method to estimate phase speed and vertical velocity of internal solitary waves in the south China Sea. *J. Geophys. Res.* 68 (5), 761–769. doi: 10.1007/s10872-012-0132-x

Zhuang, Z., Lin, Z., Zhou, J., Liu, Z., and Liu, Y. (2004). Environment conditions for the formation and development of sand dunes (waves) in the continental shelf. *Mar. Geol. Lett. (in Chin. English abstract)* 20 (4), 5–10. doi: 10.16028/j.1009-2722.2004.04.002

Zou, Z., Rad, P. B., Macelloni, L., and Zhang, L. (2021). Temporal and spatial variations in three-dimensional seismic oceanography. *Ocean Sci.* 17, 1053–1066. doi: 10.5194/os-17-1053-2021

frontiers | Frontiers in Marine Science

TYPE Original Research
PUBLISHED 12 May 2023
DOI 10.3389/fmars.2023.1147843

OPEN ACCESS

EDITED BY
Min Luo,
Shanghai Ocean University, China

REVIEWED BY
Chuanwei Zhu,
Chinese Academy of Sciences (CAS), China
Huichao Zhang,
Hohai University, China

*CORRESPONDENCE
Jingfang Lu
lujingfangcug@126.com

RECEIVED 19 January 2023
ACCEPTED 20 April 2023
PUBLISHED 12 May 2023

CITATION
Huang W, Liang J, Lu J, Hou F, Li P and Cui R (2023) Distribution of gold derived from hydrothermal fluids on the modern seafloor and its impact on the gold budget of seawater.
Front. Mar. Sci. 10:1147843.
doi: 10.3389/fmars.2023.1147843

Distribution of gold derived from hydrothermal fluids on the modern seafloor and its impact on the gold budget of seawater

Wei Huang[1,2], Jin Liang[3], Jingfang Lu[1]*, Fanghui Hou[1,2], Panfeng Li[1] and Ruyong Cui[1]

[1]Qingdao Institute of Marine Geology, China Geological Survey, Qingdao, China, [2]Laboratory for Marine Mineral Resources, Laoshan Laboratory, Qingdao, China, [3]Key Laboratory of Submarine Geosciences, Second Institute of Oceanography, Ministry of Natural Resources, Hangzhou, China

The modern seafloor hydrothermal system plays a significant role in the cycling of energy and mass between the internal and external layers of the oceanic crust and upper mantle. It continues to supply hydrothermal fluids containing three to five orders of magnitude more gold into the ocean than the amount typically present in deep seawater. It has a considerable impact on the distribution and budget of gold with respect to the large geological inventory of the ocean along with other input sources such as river water. The large amount of various types of data compiled for this study reveals that only about 0.3% of the annual hydrothermal flux of gold (2618.3 kg/a) injected into the overlying seawater column as a dissolved phase is eventually trapped in sulfide deposits near vent sites on the seafloor, while about 0.8% is trapped in metalliferous sediments that fall out from the distal nonbuoyant plume. The remaining ~98.9% of gold is delivered into the depths of the global open ocean. The global budget of gold in seawater (about 1.4×10^7 kg), the annual flux of hydrothermal fluids at the seafloor (about 2.6×10^3 kg/a), the amount delivered by river water (about 7.2×10^4 kg/a), and significant estuarine removal (15%) allows us to estimate the residence time of gold in the modern ocean to be about 220 years. This value is 70% shorter than that (~1000 years) reported previously. In the future, the use of appropriate artificial means to achieve more efficient precipitation of gold from the hydrothermal system at the seafloor could increase the level of enrichment of gold to obtain gold-rich hydrothermal deposits, yielding greater economic benefits.

KEYWORDS

gold, hydrothermal fluids, sulfides, metalliferous sediments, budget, residence time

1 Introduction

Gold (Au) belongs to the group of precious metals, and it occurs in nature as the monoisotopic element ^{197}Au, having an abundance of 100%. Owing to the reputation of Au as the most noble of the metals in human history and motivated by hopes of financial gain, many investigators have estimated the content and distribution of Au in the large volume of seawater and have attempted to recover it (Koide et al., 1988; Falkner and Edmond, 1990, and references therein). However, these studies were hampered by inadequately precise analyses and sample-contamination problems. The Au content associated with the vertical profiles of open-ocean seawater were not available until the end of the last century (Falkner and Edmond, 1990). In general, the distribution of Au in the principal layers of the Earth is heterogeneous, with its content in the shallow crust being extremely low compared to that in the deep mantle and core (Palme and O'Neill, 2014). Among the many ways for Au to be exchanged between the inner and outer layers of the oceanic crust and upper mantle, one of the most important is the seafloor hydrothermal system. Hydrothermal fluids predominantly occur along global mid-ocean ridges, volcanic arcs, and back-arc basin spreading centers, where Au is transported from sources deep within the oceanic crust and upper mantle to the seafloor. The Au content in hydrothermal fluids at the modern seafloor is generally three to five orders of magnitude and one to two orders of magnitude higher than those in the overlying seawater and river water, respectively (McHugh, 1988; Falkner and Edmond, 1990; Cidu et al., 1994; Lucas et al., 2015; Gartman et al., 2018; Fuchs et al., 2019). Therefore, hydrothermal processes at the modern seafloor can affect the cycle and budget of Au in the ocean. The average concentration and total quantity of Au delivered to the ocean from various origins must be collected and recalculated as they may reveal the ultimate fate and destination of Au derived from hydrothermal fluids in the ocean as well as the contribution of hydrothermal Au to the Au budget of ocean.

Using extensive analytical datasets that have recently be published for Au in the marine environment, in this work, we attempt to quantify the Au content and distribution in the ocean as well as the associated contribution of the seafloor hydrothermal system, including the annual flux of Au transported by hydrothermal fluids at the seafloor and the proportion of Au derived from the hydrothermal fluids and trapped in seafloor sulfide deposits that have great economic prospects as well as in metalliferous sediments that are difficult to utilize. The distributions of Au in the open ocean, river water, and hydrothermal fluids are assumed to remain approximately constant over timescales less than a million years. We consider additional input sources to the open ocean—such as aeolian dust, cosmic material, aerosols, rain, snow, and groundwater—to be negligible. Finally, using the mass-balance equation, we infer the residence time of Au in the deep modern seawater from the total quantity of Au in global seawater, the contributions of Au delivered into the open ocean from seafloor hydrothermal fluids and river water in supplying Au to the open ocean and the proportion of riverine Au trapped in estuaries and on the continental shelves. The results of this study provide significant quantitative insights regarding the trapping efficiency of Au during the formation of hydrothermal sulfide deposits at the seafloor and place constraints on the behavior of Au in the hydrothermal circulation system.

2 Contribution of Au from hydrothermal fluids onto the modern ocean seafloor

An enormous volume of seawater is required to percolate downward through fractured oceanic crust every year to cool newly formed volcanic zones at plate boundaries on the global seafloor. The estimated annual flux of seawater involved in the circulation of hydrothermal fluids at the seafloor is between 7×10^{12} and 1.5×10^{14} kg/a, based on the geochemical mass balance of elements in the ocean (Hannington, 2013). Alternatively, if the temperature of the downwelling seawater reaches 350°C, the annual flux of seawater required to cool the newly formed seafloor crust is 3×10^{13} to 6×10^{13} kg/a (Elderfield and Schultz, 1996; Schultz and Elderfield, 1997). Although the eruption of high-temperature fluids on the modern seafloor is very spectacular, their flux represents a small fraction of the total flux of the hydrothermal fluids circulating in new volcanic zones on the global seafloor. Elderfield and Schultz (1996) and Hannington et al. (2011) have argued that the flux of such high-temperature flows accounts for only about 10% of the total flux of hydrothermal fluids at the seafloor, which is dominated by diffuse flows at much lower temperatures. Subsequent works (Nielsen et al., 2006; German and Seyfried, 2014) have suggested that a proportion of 20% may be more accurate.

Few works have tested and analyzed the Au content in hydrothermal fluids at the modern seafloor due to sampling and measurement difficulties. These results have demonstrated that the Au content differs for high-temperature fluids from different areas of the seafloor (Falkner and Edmond, 1990; Gartman et al., 2018; Fuchs et al., 2019). Toward the end of the 1980s, the first measurements of the Au content were performed for two fluid samples collected at 332°C by two submersible dives at the same hydrothermal vent in the Hanging Gardens hydrothermal field at 21°N in the East Pacific Rise (EPR); the obtained results were considerably different: 7.3×10^{-12} and 4.9×10^{-11} (Falkner and Edmond, 1990). Recent investigations at the Niua South hydrothermal field in the Tonga volcanic arc exhibited Au content ranging from 3.2×10^{-10} to 1.1×10^{-9}, with an average of 5.5×10^{-10}, for nine fluid samples recovered by a remotely operated vehicle from six vents with temperatures of 278°C–325°C (Gartman et al., 2018). This value is similar to the average content of Au (7.0×10^{-10}) obtained from 27 hydrothermal fluid samples with temperatures of 285°C–358°C in the Manus back-arc basin (Fuchs et al., 2019). As the Au content of all these high-temperature fluid samples is much lower than the saturated solubility of Au and because these ascending hydrothermal fluids tend to attain equilibrium with the surrounding rocks (German and Seyfried, 2014; Pokrovski Gleb et al., 2014), small changes in the fluid temperature around 350°C do not considerably affect the Au

content in these fluids. Thus, the average Au content (6.3×10^{-10}) in all the high-temperature fluid samples obtained from the Tonga volcanic arc and the Manus back-arc basin can be considered representative of the global Au content in hydrothermal fluids with temperatures of 350°C derived from volcanic arcs and back-arc basin spreading centers.

Very few high-temperature fluid samples were collected to analyze the Au content within the 21°N hydrothermal field in the EPR. This hydrothermal field formed at a fast-spreading ridge, where intense magmatic activity occurs and hydrothermal fluids with wide ranges of chemical composition and temperature circulate (Falkner and Edmond, 1990; German and Seyfried, 2014). This contrasts significantly with the hydrothermal fields along slow- and ultraslow-spreading mid-ocean ridges, which account for more than half of the global ridge lengths (Hannington et al., 2005; Hannington et al., 2011; German and Seyfried, 2014). Therefore, the measured Au content in the two high-temperature fluid samples from the EPR cannot be used directly to represent the Au content in hydrothermal fluids from the global mid-ocean ridges. In this paper, we assume that the ratio of the Au content in high-temperature hydrothermal fluids from mid-ocean ridges to those from back-arc basins and volcanic arcs is equal to the ratio of the seafloor hydrothermal sulfides formed in these tectonic settings (1.2/9.5; see below). Thus, we obtain the average Au content in seafloor hydrothermal fluids with temperatures of 350°C from the global mid-ocean ridges by multiplying 6.3×10^{-10} with this ratio. The result is about 7.9×10^{-11}, which is similar to the high value of the Au content in the two fluid samples from the 21°N hydrothermal field in the EPR (Falkner and Edmond, 1990).

The global plate boundaries have a total strike length of 8.9×10^4 km in the ocean, which includes 6.4×10^4 km for the mid-ocean ridges and 2.5×10^4 km for the volcanic arcs and back-arc basin spreading centers (Bird, 2003; Hannington et al., 2011). Since low-temperature hydrothermal fluids at the seafloor are considered to be a mixture of the high-temperature vent fluids and the recharging cold seawater (German and Seyfried, 2014), we assume that all the Au transported by the high-temperature hydrothermal fluids is either leached from the surrounding rocks or supplied directly by sub-seafloor magma. In this paper, we adopt the recently recommended annual flux of 5.6×10^{13} kg/a (German and Seyfried, 2014) for hydrothermal fluids with temperatures of 350°C, which is of the same order of magnitude as that used by Hannington 2013. Furthermore, we considered that 20% of the circulating hydrothermal fluids can be directly injected into the water column above the seafloor (Nielsen et al., 2006; German and Seyfried, 2014). We assume that these high-temperature fluids erupt uniformly along the mid-ocean ridges, volcanic arcs, and back-arc basin spreading centers. Accordingly, we calculate the annual flux of Au transported to the global ocean by high-temperature fluids at the seafloor to be about 636.3 kg/a through the mid-ocean ridges and to be about 1982.0 kg/a through the volcanic arcs and back-arc basin spreading centers (Supplementary Table 1).

3 Discussion

3.1 Distribution and quantity of Au in the modern seafloor hydrothermal products

3.1.1 Au in seafloor sulfide deposits

Hannington et al. (2011) estimated that about 6×10^{11} kg of hydrothermal sulfide deposits exist at the seafloor along global mid-ocean ridges, volcanic arcs, and back-arc basin spreading centers. This is similar to the result estimated *via* Monte Carlo simulations combined with probabilistic numbers for the seafloor sulfide deposits (Singer, 2014). We assume that the global distribution of these sulfide deposits on the mid-ocean ridges, volcanic arcs, and back-arc basin spreading centers is uniform. Based on their respective aforementioned strike lengths, the amounts of sulfide deposits in these tectonic settings are about 4.3×10^{11} kg and 1.7×10^{11} kg. The hydrothermal sulfides on the seafloor have heterogeneous Au distributions, i.e., the Au content in these sulfides varies by factors of thousands, but most of the values lie in between 0.1×10^{-6} and 20×10^{-6} (Hannington et al., 1986; Hannington et al., 1993; Hannington et al., 2005; D. Knight et al., 2018; Fuchs et al., 2019). Based on these statistical data, the average Au content in sulfide samples from the seafloor at the mid-ocean ridges (n = 1354) is calculated as 1.2×10^{-6}, while that from the volcanic arcs and back-arc basin spreading centers (n = 415) is 9.5×10^{-6}. These values are consistent with the results from several detailed reviews on the mean Au content in hydrothermal sulfides in various tectonic settings on the global seafloor (Herzig and Hannington, 1995; Petersen et al., 2016; Cherkashov, 2017). Finally, we quantify the total Au present in hydrothermal sulfide deposits from new volcanic zones on the global seafloor to be about 2.1×10^6 kg (Supplementary Table 2).

Hannington (2013) hypothesized that all hydrothermal sulfide deposits occur within a 10-km width of the axis of a seafloor spreading center. Thus, at a full-spreading rate of 4 cm/a, it would require 0.25 Ma of continuous spreading to form the current seafloor morphology. In comparison, the hundreds of sulfide samples from different hydrothermal fields on the seafloor range from several years to more than 0.2 Ma in age (Tarasov et al., 2005; Cherkashev et al., 2013; Jamieson, 2013; Jamieson et al., 2013; Cherkashov et al., 2017). The oldest known seafloor sulfide sample, with an age of 0.223 Ma, is located in the Petersburgskoye hydrothermal field at 19°52'N along the Mid-Atlantic Ridge (Cherkashov et al., 2017). An assumed spreading time of 0.25 Ma can therefore develop sulfide deposits with all the known ages of new volcanic zones on the global seafloor. The annual amount of Au accumulated in hydrothermal sulfides on the seafloor is about 8.5 kg, which accounts for about 0.3% of the annual flux of Au derived from hydrothermal fluids at the seafloor (Supplementary Table 2).

The sulfide deposits formed in association with modern hydrothermal mineralization are some of the most economically important ore deposits on the seafloor. However, the percentage of the total quantity of Au trapped in sulfide deposits with respect to

the amount transported by the hydrothermal fluids circulating in the sub-seafloor hydrothermal system is only 0.33%. This value agrees with the results obtained from Hole 1256D of the Ocean Drilling Program and from the Troodos ophiolite in Cyprus reported by Patten et al. (2016; 2017). These works indicate that the trapping efficiency of Au is extremely low under the natural conditions prevailing during modern hydrothermal mineralization on the seafloor. Based on the ongoing extraction of active geothermal fluids in Reykjanes, Iceland, Hardardóttir et al. (2009) and Hannington et al. (2016) demonstrated that the Au content in the geothermal fluids has increased about fourfold in the seven years prior and that it can produce sizable high-grade Au deposits. The continuous extraction of fluids causes pressure reduction, which increases the probability of boiling or phase separation and creates an imbalance between the surrounding rock and the hydrothermal fluids (Pokrovski Gleb et al., 2014; Hannington et al., 2016; Petrella et al., 2020). If this method can be applied effectively to the hydrothermal fields on the modern seafloor, more Au can be precipitated from the colloidal suspensions in the vent fluids, like those in the active Reykjanes geothermal system, and become trapped in the sulfide deposits. In the future, this may be an important artificial methodology for enhancing the economic potential of the hydrothermal sulfide deposits on the seafloor.

3.1.2 Au in metalliferous sediments on the seafloor

Metalliferous sediments on the seafloor predominantly comprise fine-grained particles that were formed by hydrothermal plumes that settled on the seafloor. The metalliferous sediments represent an important dispersal mechanism for the abundant chemical materials derived from the hydrothermal fluids as they diffuse into the ocean. The accumulation age of the metalliferous component of the first meter of basal sediments in the EPR (corresponding to about 0.1 Ma) multiplied by the accumulation rate of Fe (95.9 mg/cm^2/ka) at the same location and by the formation rate of new areas of global oceanic crust, 2.56 × 10^6 m^2/a, and then divided by the average Fe content (32.7%) in the metalliferous sediments (Barrett et al., 1987; Hannington, 2013), yields 7.5 × 10^8 kg/a, which we adopt in this paper as the total annual flux of metalliferous sediment deposition on the seafloor of the new volcanic zones of the mid-ocean ridges. If the ratio of the deposition flux of metalliferous sediments from mid-ocean ridges to volcanic arcs and back-arc basin spreading centers is consistent with the ratio (4.3/1.7) of their strike lengths, then we estimate 1.04 × 10^9 kg/a as the deposition flux of metalliferous sediments in new global volcanic zones, which is two to three orders of magnitude higher than that of the sulfide deposits. The hydrothermal fields in the EPR are the modern-day areas that have been investigated most extensively for the Au content of the metalliferous sediments on the seafloor. A detailed statistical study has shown that after removing their carbonate components, the average Au content in metalliferous sediments from the EPR is about 2.03 × 10^{-8} (Gurvich, 2006), which is one order of magnitude higher than that in pelagic sediments not affected by seafloor hydrothermal processes (Li and Schoonmaker, 2014). The annual flux of Au in the global seafloor metalliferous sediments is about 21.2 kg/a when the average Au content in the metalliferous sediments on the global seafloor is the same as in the EPR, which accounts for about 0.8% of the annual flux of Au derived from the seafloor hydrothermal fluids (Supplementary Table 3).

3.1.3 Delivery of remaining Au into the ocean

Subtracting the annual flux of Au in the global seafloor sulfide deposits and metalliferous sediments yields the remaining annual flux of Au of about 2588.6 kg/a, which is about 98.9% of the annual flux of Au derived from hydrothermal fluids at the seafloor. The distribution and quantity of Au in hydrothermal products on the modern seafloor is summarized in Supplementary Figure 1. The Au transported by the rising hydrothermal fluids is distributed to different places once it reaches the seafloor; a small portion of Au is trapped directly in near-vent sulfide deposits, slightly more Au is carried by hydrothermal plumes and falls out into the distal metalliferous sediments, whereas an enormous proportion of Au transported by the hydrothermal fluids from deep within the oceanic crust and upper mantle is finally injected into the overlying column of seawater.

3.2 Global ocean budget of Au and the riverine flux

3.2.1 Total quantity of Au in modern ocean seawater

The modern ocean is a vast body of saline water that covers most of the Earth's surface; it thus becomes a huge natural repository of Au. The concentration of dissolved Au varies with depth in the vertical profile of seawater, and the content of Au in a column of open seawater ranges from 2 × 10^{-15} to 6 × 10^{-14} (Koide et al., 1988; Falkner and Edmond, 1990). In addition, the distribution of Au varies globally, with the Au content in open seawater generally being lower than that in coastal and marginal seawater, which may be affected by terrestrial materials and tailing sewage (Large et al., 2015). The total mass of the global seawater is a staggering 1.41 × 10^{21} kg (Garrison, 2016). If the most common content of Au (1 × 10^{-14}) obtained from seawater profiles from the Atlantic and Pacific Oceans is taken as the average value for seawater globally (Falkner and Edmond, 1990), which is also similar to the values given in a recent work (Bruland et al., 2014), the total quantity of Au dissolved in seawater globally is about 1.4 × 10^7 kg.

3.2.2 Annual riverine flux of Au into the ocean

Rivers around the globe also majorly determine the quantity and chemical composition of a column of seawater as they annually discharge about 3.6 × 10^{16} kg of freshwater into the oceans (Milliman and Farnsworth, 2013). Although the distribution of Au within river water samples is heterogeneous, most of the Au content ranges from 1 × 10^{-12} to 5 × 10^{-12}, with an average of 2 × 10^{-12}, based on analyses of dozens of river-water samples recovered from North America,

Europe, and Australia (McHugh, 1988; Cidu et al., 1994; Lucas et al., 2015). The content of Au in some rivers and in the groundwater around Au mines that were contaminated by mine sewage is one to two orders of magnitude higher than that in normal river water (McHugh, 1988; Lucas et al., 2014; Large et al., 2015; Myagkaya et al., 2016), but the flux of such sewage into the rivers is too small to affect the Au content in river water globally. Consequently, in this paper we adopt 2×10^{-12} to be the average Au content in river water globally, which yields an annual flux of Au transported by river water of about 7.2×10^{4} kg/a (Supplementary Figure 2).

Nekrasov et al. (1996); Leybourne et al. (2000), and Large et al. (2015) have demonstrated that Au is present in a higher proportion in river water as suspended particles or in a colloidal state than as the predominant dissolved species, which consist of a mixture of colloids, nanoparticles, aqueous clusters, or Au absorbed onto detrital clays and Au–organic complexes in the ocean. Therefore, a significant portion of the Au delivered to the ocean is more likely to be deposited in estuaries and on continental shelves than be extended into the open ocean. This conclusion is in agreement with the work from the Swan River estuary in Western Australia, which shows that the content of Au in the estuary water ranges from 1.1×10^{-11} to 3.7×10^{-11} and that it is about one order of magnitude higher than that in the upriver water (Lucas et al., 2015). Assuming that the percentage of Au removed by the estuaries and continental shelves is the same as that of Os, which is also an immobile precious metal, and that about 15% of the total riverine Os is deposited in estuaries and on continental shelves (Turekian et al., 2007), we observe that the annual flux of Au transported by river water is reduced to about 6.1×10^{4} kg/a (Supplementary Table 4).

3.3 Impact of Au derived from seafloor hydrothermal fluids on the Au budget of the global ocean

3.3.1 Residence time of Au in modern open-ocean seawater

The input of aeolian dust, cosmic material, aerosols, rain, snow, and groundwater can be considered to provide additional fluxes of Au into the ocean, in excess of those derived from river water and hydrothermal fluids. However, some of these sources have negligible Au content, some have very small input fluxes, and others are difficult to dissolve in seawater and eventually settle onto the seafloor. Thus, these input sources barely affect the input flux of Au into modern seawater (Falkner and Edmond, 1990; Love and Brownlee, 1993; Oxburgh, 2001; Jickells et al., 2005; Lucas et al., 2014). The residence time (T) of Au in the ocean is defined at steady state by its mass balance. The equation is T = I/F, where I (about 1.4×10^{7} kg) is the inventory of the Au in the global seawater, and F is the net riverine and hydrothermal fluid input fluxes (about 6.4×10^{3} kg) to the ocean. Therefore, from existing datasets of hydrothermal fluids at the seafloor and river water flowing into the open ocean, we estimate the residence time of Au in the ocean to be about 220 years, 70% lower than that estimated in a previous work (Falkner and Edmond, 1990). This residence time is much shorter than the turnover time of the deep ocean (Bruland et al., 2014), and it indicates that Au has the obvious behavioral characteristics of a non-conservative element in the ocean.

3.3.2 Seafloor hydrothermal eruptions and the formation of Au-rich deposits in geological history

The net impact of Au associated with the venting of fluids at the seafloor is similar to the relationship with river water and the ocean because the Au has markedly higher concentrations in the vent fluids and river water than in the seawater. This implies that sediment deposition and authigenic mineral formation in the marine environment can remove a large amount of dissolved Au from the seawater, significantly and continuously altering the Au budget of the global ocean. However, the contribution of Au delivered to the ocean from hydrothermal fluids at the modern seafloor is less than that delivered by river water. Nevertheless, larger episodic volcanic eruptions at the seafloor may have transported larger fluxes of hydrothermal fluids and, consequently, a higher average Au content into the ocean earlier in the Earth's history, i.e., during the Mesoarchean, the Neoarchean, and the end of the Proterozoic Eras, during which the average content of Au in seawater was several times higher than the present values (Large et al., 2015). The input of Au delivered into the ocean by hydrothermal fluids at the seafloor during these times has gained tremendous importance because it not only affected the total quantity and economic prospects of the hydrothermal sulfide deposits at the seafloor but also may have reduced the residence time of Au in the global seawater significantly.

4 Conclusions

The annual flux of Au derived from hydrothermal fluids at the modern seafloor is about 2618.3 kg/a. About 0.3% of this (8.5 kg/a) is first trapped in near-vent hydrothermal sulfide deposits, and another ~0.8% (21.2 kg/a) diffuses with hydrothermal plumes and falls out into the distal metalliferous sediments. The remaining ~98.9% (2588.6 kg/a) is eventually delivered to the seawater column.

From the total quantity of Au in seawater globally (1.4×10^{7} kg) and from the input fluxes of Au derived from hydrothermal fluids at the seafloor (2588.6 kg/a) and river water (6.1×10^{4} kg/a), we estimate the residence time of Au in the modern open ocean to be about 220 years, which is about 70% lower than the previous value and considerably shorter than the turnover time of the deep ocean. In the future, more efficient mechanisms to precipitate Au from the seafloor hydrothermal system, such as the use of appropriate artificial means like continuous extraction from hydrothermal fluids or breaking the buffer balance between the fluids and the surrounding rock, may be used to increase the enrichment of Au in seafloor hydrothermal systems to form Au-rich deposits and obtain increased economic benefits.

Data availability statement

The original contributions presented in the study are included in the article/Supplementary Material. Further inquiries can be directed to the corresponding author.

Author contributions

WH and JLu contributed to conception, methodology and design of the study. WH and JLi organized the data and performed the statistical analysis. WH wrote the first draft of the manuscript. FH, PL, and RC made revisions of the manuscript. All the authors contributed to the article and approved the submitted version.

Funding

This research was supported by the Project of Laoshan Laboratory of China (Grant No. LSKJ202203602), the National Natural Science Foundation of China (Grant No. 41506074, 41806076), and the China Geological Survey Project (DD20221720, DD20230647).

Acknowledgments

The authors would like to thank two reviewers for their constructive comments and suggestions.

Conflict of interest

The authors declare that the research was conducted in the absence of any commercial or financial relationships that could be construed as a potential conflict of interest.

Publisher's note

Supplementary material

The Supplementary Material for this article can be found online at: https://www.frontiersin.org/articles/10.3389/fmars.2023.1147843/full#supplementary-material

References

Barrett, T. J., Taylor, P. N., and Lugoqski, J. (1987). Metalliferous sediments from DSDP leg 92: the East pacific rise transect. *Geochimica Cosmochimica Acta* 51 (9), 2241–2253. doi: 10.1016/0016-7037(87)90278-X

Bird, P. (2003). An updated digital model of plate boundaries. *Geochemistry Geophysics Geosystems* 4 (3) 1-52. doi: 10.1029/2001GC000252

Bruland, K. W., Middag, R., and Lohan, M. C. (2014). "8.2 - controls of trace metals in seawater," in *Treatise on geochemistry (Second edition)*. Eds. H. D. Holland and K. K. Turekian (Oxford: Elsevier), 19–51. doi: 10.1016/B978-0-08-095975-7.00602-1

Cherkashev, G. A., Ivanov, V. N., Bel'tenev, V. I., Lazareva, L. I., Rozhdestvenskaya, I. I., Samovarov, M. L., et al. (2013). Massive sulfide ores of the northern equatorial mid-Atlantic ridge. *Oceanology* 53 (5), 607–619. doi: 10.1134/S0001437013050032

Cherkashov, G. (2017). "Seafloor massive sulfide deposits: distribution and prospecting," in *Deep-Sea mining: resource potential, technical and environmental considerations*. Ed. R. Sharma (Cham: Springer International Publishing), 143-164).

Cherkashov, G., Kuznetsov, V., Kuksa, K., Tabuns, E., Maksimov, F., and Bel'tenev, V. (2017). Sulfide geochronology along the northern equatorial mid-Atlantic ridge. *Ore Geology Rev.* 87, 147–154. doi: 10.1016/j.oregeorev.2016.10.015

Cidu, R., Fanfani, L., Shand, P., Edmunds, W. M., Van't dack, L., and Gijbels, R. (1994). Determination of gold at the ultratrace level in natural waters. *Analytica Chimica Acta* 296 (3), 295–304. doi: 10.1016/0003-2670(94)80249-1

D. Knight, R., Roberts, S., and Webber, A. P. (2018). The influence of spreading rate, basement composition, fluid chemistry and chimney morphology on the formation of gold-rich SMS deposits at slow and ultraslow mid-ocean ridges. *Mineralium Deposita* 53 (1), 143–152. doi: 10.1007/s00126-017-0762-4

Elderfield, H., and Schultz, A. (1996). Mid-ocean ridge hydrothermal fluxes and the chemical composition of the ocean. *Annu. Rev. Earth Planetary Sci.* 24 (1), 191–224. doi: 10.1146/annurev.earth.24.1.191

Falkner, K., and Edmond, J. M. (1990). Gold in seawater. *Earth Planetary Sci. Lett.* 98 (2), 208–221. doi: 10.1016/0012-821X(90)90060-B

Fuchs, S., Hannington, M. D., and Petersen, S. (2019). Divining gold in seafloor polymetallic massive sulfide systems. *Mineralium Deposita* 54 (6), 789–820. doi: 10.1007/s00126-019-00895-3

Garrison, T. S. (2016). *Oceanography: an invitation to marine science* (Toronto, Canada: nelson education).

Gartman, A., Hannington, M., Jamieson, J. W., Peterkin, B., Garbe-Schönberg, D., Findlay, A. J., et al. (2018). Boiling-induced formation of colloidal gold in black smoker hydrothermal fluids. *Geology* 46 (1), 39–42. doi: 10.1130/G39492.1 %J Geology

German, C. R., and Seyfried, W. E. (2014). "8.7 - hydrothermal processes," in *Treatise on geochemistry (Second edition)*. Eds. H. D. Holland and K. K. Turekian (Oxford: Elsevier), 191–233. doi: 10.1016/B978-0-08-095975-7.00607-0

Gurvich, E. G. (2006). *Metalliferous sediments of the world ocean: fundamental theory of deep-sea hydrothermal sedimentation* (Berlin: Springer).

Hannington, M. D. (2013). The role of black smokers in the Cu mass balance of the oceanic crust. *Earth Planetary Sci. Lett.* 374, 215–226. doi: 10.1016/j.epsl.2013.06.004

Hannington, M. D., De Ronde, C. E. J., Petersen, S., Hedenquist, J. W., Thompson, J. F. H., Goldfarb, R. J., et al. (2005). "Sea-Floor tectonics and submarine hydrothermal systems," in *Geochemistry, Mineralogy and Genesis of Gold Deposits* (Society of Economic Geologists). https://oceanrep.geomar.de/id/eprint/6271/

Hannington, M., Harðardóttir, V., Garbe-Schönberg, D., and Brown, K. L. (2016). Gold enrichment in active geothermal systems by accumulating colloidal suspensions. *Nat. Geosci.* 9 (4), 299–302. doi: 10.1038/ngeo2661

Hannington, M. D., Herzig, P. M., and Scott, S. D. (1993). "Auriferous hydrothermal precipitates on the modern seafloor," in *Gold metallogeny and exploration*. Ed. R. P. Foster (Dordrecht: Springer Netherlands), 249–282.

Hannington, M., Jamieson, J., Monecke, T., Petersen, S., and Beaulieu, S. (2011). The abundance of seafloor massive sulfide deposits. *Geology* 39 (12), 1155–1158. doi: 10.1130/G32468.1 %J Geology

Hannington, M. D., Peter, J. M., and Scott, S. D. (1986). Gold in sea-floor polymetallic sulfide deposits. *Economic Geology* 81 (8), 1867–1883. doi: 10.2113/gsecongeo.81.8.1867 %J Economic Geology

Hardardóttir, V., Brown, K. L., Fridriksson, T., Hedenquist, J. W., Hannington, M. D., and Thorhallsson, S. (2009). Metals in deep liquid of the reykjanes geothermal system, southwest Iceland: implications for the composition of seafloor black smoker fluids. *Geology* 37 (12), 1103–1106. doi: 10.1130/G30229A.1 %J Geology

Herzig, P. M., and Hannington, M. D. (1995). Polymetallic massive sulfides at the modern seafloor a review. *Ore Geology Rev.* 10 (2), 95–115. doi: 10.1016/0169-1368(95)00009-7

Jamieson, J. W. (2013). *Size, age, distribution and mass accumulation rates of seafloor hydrothermal sulfide deposits* (University of Ottawa (Canada: Doctoral degree).

Jamieson, J. W., Hannington, M. D., Clague, D. A., Kelley, D. S., Delaney, J. R., Holden, J. F., et al. (2013). Sulfide geochronology along the endeavour segment of the Juan de fuca ridge. *Geochemistry Geophysics Geosystems* 14 (7), 2084–2099. doi: 10.1002/ggge.20133

Jickells, T. D., An, Z. S., Andersen, K. K., Baker, A. R., Bergametti, G., Brooks, N., et al. (2005). Global iron connections between desert dust, ocean biogeochemistry, and climate. *Science* 308 (5718), 67–71. doi: 10.1126/science.1105959

Koide, M., Hodge, V., Goldberg, E. D., and Bertine, K. (1988). Gold in seawater: a conservative view. *Appl. Geochemistry* 3 (3), 237–241. doi: 10.1016/0883-2927(88)90103-5

Large, R. R., Gregory, D. D., Steadman, J. A., Tomkins, A. G., Lounejeva, E., Danyushevsky, L. V., et al. (2015). Gold in the oceans through time. *Earth Planetary Sci. Lett.* 428, 139–150. doi: 10.1016/j.epsl.2015.07.026

Leybourne, M. I., Goodfellow, W. D., Boyle, D. R., and Hall, G. E. M. (2000). Form and distribution of gold mobilized into surface waters and sediments from a gossan tailings pile, Murray brook massive sulphide deposit, new Brunswick, Canada. *Appl. Geochemistry* 15 (5), 629–646. doi: 10.1016/S0883-2927(99)00068-2

Li, Y. H., and Schoonmaker, J. E. (2014). "9.1 - chemical composition and mineralogy of marine sediments," in *Treatise on geochemistry (Second edition)*. Eds. H. D. Holland and K. K. Turekian (Oxford: Elsevier), 1–32. doi: 10.1016/B978-0-08-095975-7.00701-4

Love, S. G., and Brownlee, D. E. (1993). A direct measurement of the terrestrial mass accretion rate of cosmic dust. *Science* 262 (5133), 550–553. doi: 10.1126/science.262.5133.550

Lucas, A. R., Reid, N., Salmon, S. U., and Rate, A. W. (2014). Quantitative assessment of the distribution of dissolved au, as and Sb in groundwater using the diffusive gradients in thin films technique. *Environ. Sci. Technol.* 48 (20), 12141–12149. doi: 10.1021/es502468d

Lucas, A. R., Salmon, S. U., Rate, A. W., Larsen, S., and Kilminster, K. (2015). Spatial and temporal distribution of au and other trace elements in an estuary using the diffusive gradients in thin films technique and grab sampling. *Geochimica Cosmochimica Acta* 171, 156–173. doi: 10.1016/j.gca.2015.08.025

McHugh, J. B. (1988). Concentration of gold in natural waters. *J. Geochemical Explor.* 30 (1), 85–94. doi: 10.1016/0375-6742(88)90051-9

Milliman, J. D., and Farnsworth, K. L. (2013). *River discharge to the coastal ocean: a global synthesis* (Cambridge, United Kingdom: Cambridge University Press).

Myagkaya, I. N., Lazareva, E. V., Gustaytis, M. A., and Zhmodik, S. M. (2016). Gold and silver in a system of sulfide tailings. part 1: migration in water flow. *J. Geochemical Explor.* 160, 16–30. doi: 10.1016/j.gexplo.2015.10.004

Nekrasov, I. Y., Rao, P. M., and Majithia, M. (1996). *Geochemistry, mineralogy and genesis of gold deposits* (London: Routledge).

Nielsen, S. G., Rehkämper, M., Teagle, D. A. H., Butterfield, D. A., Alt, J. C., and Halliday, A. N. (2006). Hydrothermal fluid fluxes calculated from the isotopic mass balance of thallium in the ocean crust. *Earth Planetary Sci. Lett.* 251 (1), 120–133. doi: 10.1016/j.epsl.2006.09.002

Oxburgh, R. (2001). Residence time of osmium in the oceans. *Geochemistry Geophysics Geosystems* 2 (6), 1-17. doi: 10.1029/2000GC000104

Palme, H., and O'Neill, H. S. C. (2014). "3.1 - cosmochemical estimates of mantle composition," in *Treatise on geochemistry (Second edition)*. Eds. H. D. Holland and K. K. Turekian (Oxford: Elsevier), 1–39. doi: 10.1016/B978-0-08-095975-7.00201-1

Patten, C. G. C., Pitcairn, I. K., and Teagle, D. A. H. (2017). Hydrothermal mobilisation of au and other metals in supra-subduction oceanic crust: insights from the troodos ophiolite. *Ore Geology Rev.* 86, 487–508. doi: 10.1016/j.oregeorev.2017.02.019

Patten, C. G. C., Pitcairn, I. K., Teagle, D. A. H., and Harris, M. (2016). Mobility of au and related elements during the hydrothermal alteration of the oceanic crust: implications for the sources of metals in VMS deposits. *Mineralium Deposita* 51 (2), 179–200. doi: 10.1007/s00126-015-0598-8

Petersen, S., Krätschell, A., Augustin, N., Jamieson, J., Hein, J. R., and Hannington, M. D. (2016). News from the seabed – geological characteristics and resource potential of deep-sea mineral resources. *Mar. Policy* 70, 175–187. doi: 10.1016/j.marpol.2016.03.012

Petrella, L., Thébaud, N., Fougerouse, D., Evans, K., Quadir, Z., and Laflamme, C. (2020). Colloidal gold transport: a key to high-grade gold mineralization? *Mineralium Deposita* 55 (7), 1247–1254. doi: 10.1007/s00126-020-00965-x

Pokrovski Gleb, S., Akinfiev Nikolay, N., Borisova Anastassia, Y., Zotov Alexandre, V., and Kouzmanov, K. (2014). Gold speciation and transport in geological fluids: insights from experiments and physical-chemical modelling. *Geological Society London Special Publications* 402 (1), 9–70. doi: 10.1144/SP402.4

Schultz, A., and Elderfield, H. (1997). Controls on the physics and chemistry of seafloor hydrothermal circulation. *Philos. Trans. R. Soc. London A: Mathematical Phys. Eng. Sci.* 355 (1723), 387–425. doi: 10.1098/rsta.1997.0014

Singer, D. A. (2014). Base and precious metal resources in seafloor massive sulfide deposits. *Ore Geology Rev.* 59, 66–72. doi: 10.1016/j.oregeorev.2013.11.008

Tarasov, V. G., Gebruk, A. V., Mironov, A. N., and Moskalev, L. I. (2005). Deep-sea and shallow-water hydrothermal vent communities: two different phenomena? *Chem. Geology* 224 (1), 5–39. doi: 10.1016/j.chemgeo.2005.07.021

Turekian, K. K., Sharma, M., and Gordon, G. W. (2007). The behavior of natural and anthropogenic osmium in the Hudson river–long island sound estuarine system. *Geochimica Cosmochimica Acta* 71 (17), 4135–4140. doi: 10.1016/j.gca.2007.05.020

frontiers | Frontiers in Marine Science

TYPE Original Research
PUBLISHED 15 May 2023
DOI 10.3389/fmars.2023.1184397

OPEN ACCESS

EDITED BY
Wei Li,
South China Sea Institute of Oceanology (CAS), China

REVIEWED BY
Shumin Gao,
Hainan Tropical Ocean University, China
Yuyang Xie,
Shandong University, China
Marek Stastna,
University of Waterloo, Canada

*CORRESPONDENCE
Chaoqi Zhu
zhuchaoqi@ouc.edu.cn
Yonggang Jia
yonggang@ouc.edu.cn

RECEIVED 11 March 2023
ACCEPTED 28 April 2023
PUBLISHED 15 May 2023

CITATION
Feng X, Wang L, Ji C, Wang H, Zhu C and Jia Y (2023) The impact of internal solitary waves on deep-sea benthic organisms on the continental slope of the northern South China Sea.
Front. Mar. Sci. 10:1184397.
doi: 10.3389/fmars.2023.1184397

The impact of internal solitary waves on deep-sea benthic organisms on the continental slope of the northern South China Sea

Xuezhi Feng[1,2], Linsen Wang[1], Chunsheng Ji[1,3], Hui Wang[1], Chaoqi Zhu[1,2,4]* and Yonggang Jia[1,2]*

[1]Shandong Provincial Key Laboratory of Marine Environment and Geological Engineering, Ocean University of China, Qingdao, China, [2]Laboratory for Marine Geology, Qingdao National Laboratory for Marine Science and Technology, Qingdao, China, [3]Sanya Institute of South China Sea Geology, Guangzhou Marine Geological Survey, China Geological Survey, Sanya, China, [4]Key Laboratory of Submarine Geosciences and Prospecting Techniques, Ministry of Education, Ocean University of China, Qingdao, China

Internal solitary waves (ISWs) exert a significant influence on the deep-sea floor, yet little research has been conducted on their impact on benthic organisms. The objective of this study was to investigate the propagation characteristics of ISWs on the Shenhu continental slope in the northern South China Sea, as well as their mechanisms of influence on benthic activity. *In-situ* observation was performed at the head of the Shenhu Canyon (water depth 655m) to determine the physical characteristics of ISWs and the changes in benthic organisms. The study revealed that the abundance and density of benthic organisms were positively correlated with the time and intensity of ISWs. The abundance of benthic organisms affected by ISWs is 3-5 times that without ISWs, and the density of benthic organisms is 3-9 times. The impact induced by ISWs, including resuspension of bottom sediments, formation of marine snow, changes in the bottom boundary layer environment, and vertical transfer of seawater environmental factors, played a crucial role in the impact on benthic activity. To our limited knowledge, this is the first *in-situ* long-term observation study on the effects of ISWs on deep-sea benthic organisms on the continental slope of the northern South China Sea deeper than 600m, providing new insights for exploring the environmental impact of ISWs on the deep-sea bottom boundary layer.

KEYWORDS

internal solitary waves, benthic organisms, the Shenhu continental slope, in-situ observation, the bottom boundary layer

1 Introduction

Internal solitary waves (ISWs) are a type of nonlinear internal wave characterized by short periods, large amplitudes, and strong flow velocities that remain relatively constant during propagation (Bogucki and Redekopp, 1999; Helfrich et al., 2006; Alford et al., 2015). They are widely distributed in various terrains such as large lakes and marginal seas (Boegman and Stastna, 2019; Syamsudin et al., 2019) and can cause interactions between seawater and the seafloor, becoming a major driving force for perturbing the deep-sea benthic environment (Holligan et al., 1985; Jia et al., 2019). ISWs enhance material transport and vertical mixing processes on the continental slope and shelf. From a biological perspective, ISWs affect benthic biomass and activity on the continental slope and shelf (van Haren, 2020).

The distribution and dynamics of benthic communities depend on different hydrodynamic conditions (Shimeta et al., 2003). ISWs induce shear stress and turbulence, which promote vertical mixing and exchange of heat and nutrients, thereby increasing primary productivity (Chen et al., 2016b; Zhang et al., 2019; Hung et al., 2021). Marine snow, a major source of food for mobile organisms (Trudnowska et al., 2021), can enhance the feeding and survival of mobile organisms (MacKenzie, 2000; MacKenzie and Kiorboe, 2000). ISWs can affect overall biomass changes on a relatively small spatial scale (Pineda, 1991; Broitman et al., 2008), and this movement from deep to shallow waters can transport larvae and organisms to their adult habitats, thus altering population density (Roder et al., 2010). Flood et al. (2021) found that fish habitat locations change with the vertical movement of the thermocline induced by internal wave disturbances, and the time scale of fish response to physical environmental changes corresponds to the period of internal waves. Currently, the impact of ISWs on biological activity is mainly reported in shallow water areas, and their effects on deep water areas are unknown.

ISWs generated in the Luzon Strait of the South China Sea propagate northwestward, with a significant amount of energy dissipated on the continental slope and shelf (Cai et al., 2012; Fu et al., 2012). Reid et al. (2019) observed that ISWs caused a four-fold increase in instantaneous nitrate flux in the Dongsha Atoll in the northern South China Sea compared to periods without ISWs. The shoaling of ISWs transports nutrient-rich water to the shelf and coast, increasing nutrient concentrations and biological productivity, thereby improving the coral ecosystem of the Dongsha Atoll (Reid et al., 2019; Hung et al., 2021). The enhancement of biological activity by ISWs is not limited to shallow waters on the continental shelf, as ISWs can cause vertical mixing at depths of 600m and transfer nutrient-rich cold water to promote biological productivity (Pan et al., 2012). However, *in situ* observations of ISWs are mainly concentrated in the Dongsha Sea, and observations of the impact of ISWs on the marine environment and biological activity are lacking. The Shenhu Canyon is located in the central Pearl River Mouth Basin, where sediments and nutrients transported by the Pearl River greatly enrich the benthic ecosystem of the canyon (Yin et al., 2019; Zhang et al., 2022). There are many canyons and steep ridges on the Shenhu continental slope (Su et al., 2020), and the interaction between ISWs and steep terrain can increase the bottom flow velocity and shear stress (Lamb, 2014; Tian et al., 2021b), enhancing disturbances to the deep-sea benthic environment.

This study aimed to investigate the physical characteristics of ISWs and changes in benthic biological activity on the Shenhu continental slope in the northern South China Sea using long-term *in situ* observations. We explored the environmental impact of ISWs on the water column and deep-sea bottom boundary layer and analyzed the relevant mechanisms of the impact of ISWs on benthic biological activity.

2 Materials and methods

2.1 Geological setting

The Shenhu continental slope, located in the northern South China Sea, is comprised of 17 submarine canyons oriented in NW-SE direction (Ding et al., 2013; Chen et al., 2016a). The canyons' heads are affected by large-amplitude internal solitary waves (ISWs), which result in erosive turbidity currents (Yin et al., 2019), as depicted in Figures 1A, B, Observation station SH_1 is situated at the head of the canyon at a depth of approximately 655m. Satellite data show the presence of numerous internal solitary waves during the observation period (Figure 1C). During the cruise, sediment samples were collected using a gravity corer, and the sediment's physical properties were determined in the laboratory. As shown in Table 1, the sediment's median particle size was 0.01 mm, and it exhibited high water content, high porosity, and high saturation. The surface sediment in the Shenhu region contained biogenic particles, such as foraminifera and algae, as well as flocculent material (Kuang et al., 2019). The Shenhu canyon's topography results in more frequent and energetic internal solitary waves due to refraction, reflection, and interaction with the topography (Ma et al., 2016; Bai et al., 2019). These strong and frequent hydrodynamic phenomena are likely to affect changes in the seafloor environment (Zhu et al., 2023a; Zhu et al., 2023b).

W is the water content, ρ_s is the sediment natural density, n is the porosity, S is the specific weight of the particle, Sr is the sediment saturation, and D_{50} is the mean particle size.

2.2 Observation methods

The scientific research vessel "Dongfanghong 3" deployed a deep-sea *in-situ* observation system for the bottom boundary layer at observation station SH_1. Continuous underwater observations were conducted from August 20 to September 2, 2020. As shown in Figures 2A, B, The observation system was equipped with a 75 kHz acoustic Doppler current profiler (75k-ADCP), a Nortek Vector Acoustic Doppler Velocimeter (ADV), RBR concerto3a Multi-Channel Logger, and a deep-sea camera. Using the ship-borne CTD profiling system, we measured the changes in environmental parameters in the vertical direction of the water column for 24 hours from 5:00 pm on September 1 to 5:00 pm on September 2. We

10.3389/fmars.2023.1184397

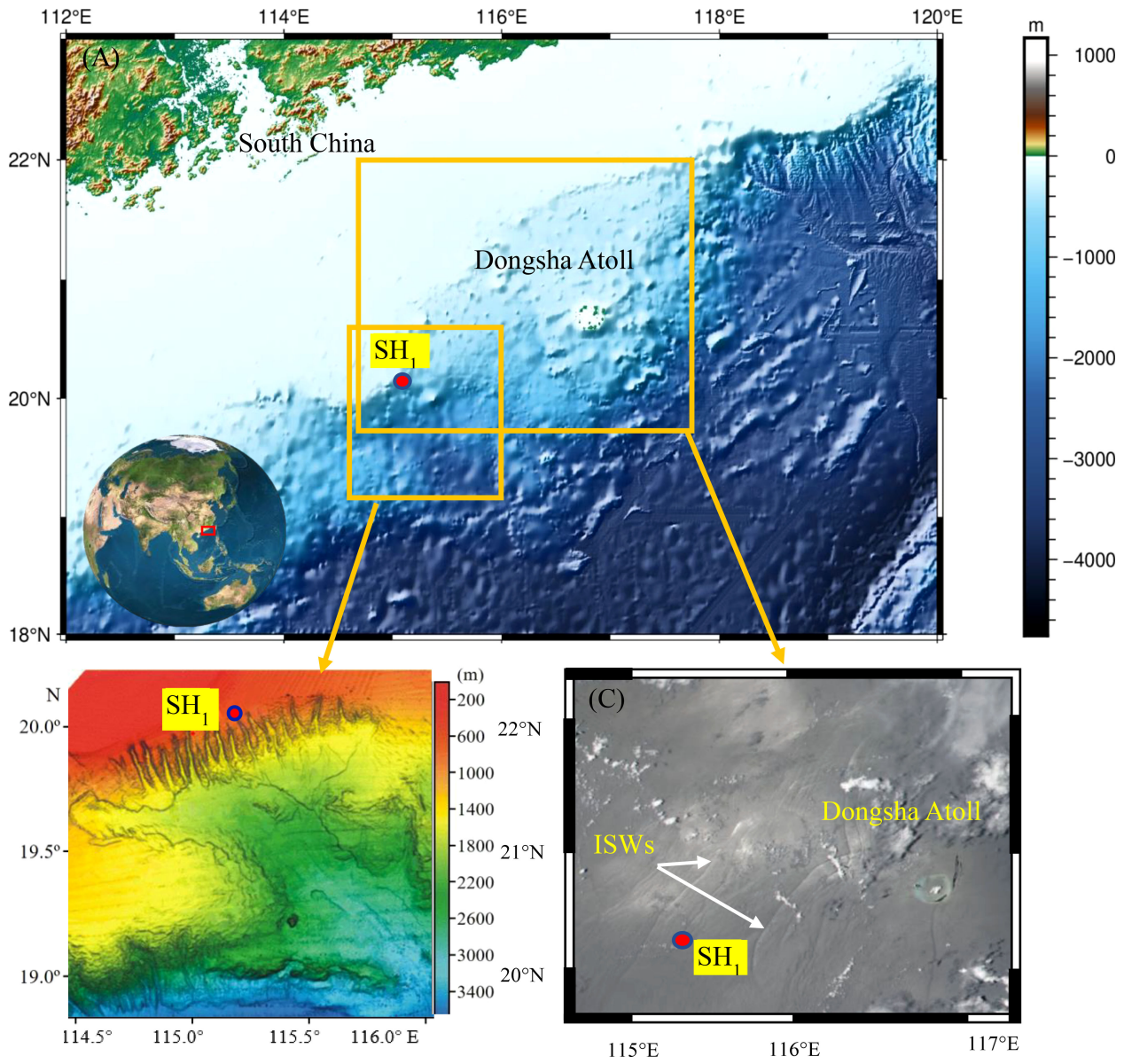

FIGURE 1
(A) Location of the Shenhu Canyon System and study area in the Northern South China Sea, **(B)** The multi-beam geomorphology shadow map was modified from Ding et al. (2013), **(C)** Moderate-resolution Imaging Spectroradiometer (MODIS) image of the northern South China Sea on Aug 25, 2020, data source https://worldview.earthdata.nasa.gov.

TABLE 1 Physical characteristics of the surface sediments in the study area.

Depth (cm)	W (%)	ρ_s (g/cm^3)	n (%)	S	Sr (%)	D_{50} (mm)
0-5	111.34	1.39	76	2.71	97	0.01
5-10	99.83	1.41	75	2.79	94	0.009
10-20	101.00	1.39	75	2.75	93	0.011
20-30	106.51	1.43	75	2.77	98	0.008

collected water samples and transformed the instrument's observed turbidity into suspended particulate matter concentration using filtration experimental methods (Wang et al., 2022). The turbidity and suspended particulate matter concentration conversion equation was SPM=5.64×Turbidity+0.12.

2.3 Data analytics

2.3.1 Instrument data

Observations of the dynamics of ISWs were conducted using a 75k-ADCP (Huang et al., 2022). Profile data were recorded every 1

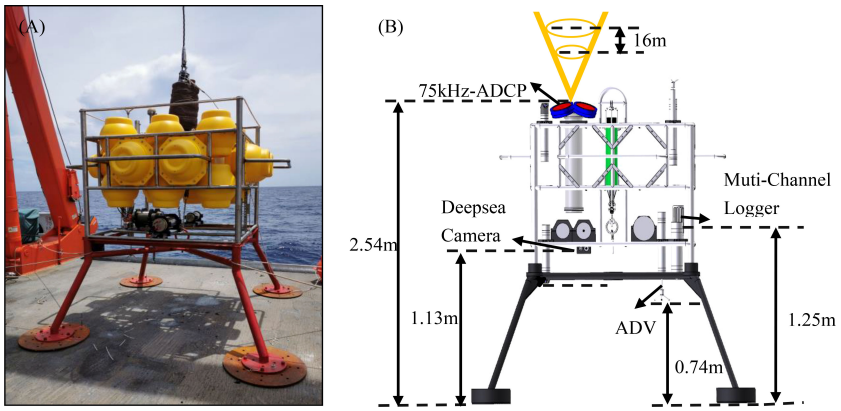

FIGURE 2
(A) Field working diagram of the observation system, **(B)** Schematic illustration of the observation instrument.

minute, with unreasonable extreme points excluded, and vertically interpolated every 8 meters. The Multi-Channel Logger collected data every 10 seconds, recording changes in temperature, salinity, dissolved oxygen, and turbidity in the bottom boundary layer (Dato et al., 2021; Du et al., 2021; Kheili et al., 2021). The ADV had a sampling frequency of 64Hz and was continuously sampled.

2.3.2 Images of benthic organisms

Video images captured by the deep-sea camera were taken every 3 minutes for 7 seconds. Each image was an RGB image stored in a three-dimensional matrix with pixel values of "1080×1920" and dimensions of 378×672 mm. Although some shadows and micro-benthic organisms were not identified as biological species due to fixed camera observation, they were used for statistical calculations of biological abundance and density. Changes in biological abundance (A) and density (D) were characterized using formula (1).

$$A = \frac{n}{N}, D = \frac{s}{S} \tag{1}$$

where n is the number of individuals per hour, N is the total number of individuals in a certain time, s is the area occupied by the organism, and S is the image area.

2.3.3 Calculation of shear stresses

In the bottom boundary layer, shear stress (τ_c) caused by velocity was calculated using the Turbulent Kinetic Energy (TKE) method, Covariance method (COV), and Logarithmic Velocity (RL) method. The TKE method (Stapleton and Huntley, 1995; Zhang et al., 2018), which does not require consideration of the height of the ADV above the seabed, was used (Pope et al., 2006). Velocity data in the three directions were averaged every minute, with the total average value subtracted from all the velocity data, and calculated the velocity fluctuations in the three directions were as follows:

$$u' = u - \bar{u}, v' = v - \bar{v}, w' = w - \bar{w} \tag{2}$$

shear stress τ_c was calculated by

$$\tau_c = C_1 \rho \left[(\overline{u'})^2 + (\overline{v'})^2 + (\overline{w'})^2 \right] /2 \tag{3}$$

where C_1 is the empirical coefficient, generally taking a value of 0.19-0.2 (Stapleton and Huntley, 1995), and ρ is the seawater density.

The sediment in the study area was fine-grained cohesive sediments, and we used the equation applicable to cohesive sediments to determine the critical shear stress (τ_{ce}) of the bottom sediment (Shi et al., 2012).

$$\tau_{ce} = 0.05 + \beta \left\{ \frac{1}{[(\pi/6)(1 + sW)]^{1/3} - 1} \right\}^2 \tag{4}$$

$$s = \rho_s / \rho - 1 \tag{5}$$

where β is a dimensionless coefficient, s is the specific weight of the particle, W is the water content, and ρ_s is the sediment particle density. When the particle size of the bottom sediment is less than a few tens of microns and the water content of the bottom sediment is relatively high, β is 0.3 (Taki, 2000).

3 Results

3.1 The characteristics of the hydrodynamics

Figure 3 shows the velocity profile for a total of 3 days from 8/21 00:00 to 8/24 12:00. The velocity profile (25-628 mab) observed by 75k-ADCP shows strong velocity at the study area, with a maximum velocity exceeding 0.5 m/s in both the u and v directions (Figures 3A, B). From an analysis of the entire water column, the horizontal velocity exhibits a three-layer structure with the same flow direction between the sea surface and the sea floor. In addition, the horizontal current exhibits an obvious diurnal variation cycle, showing internal tidal characteristics. The maximum vertical velocity (w) exceeds 0.1 m/s and exhibits clear

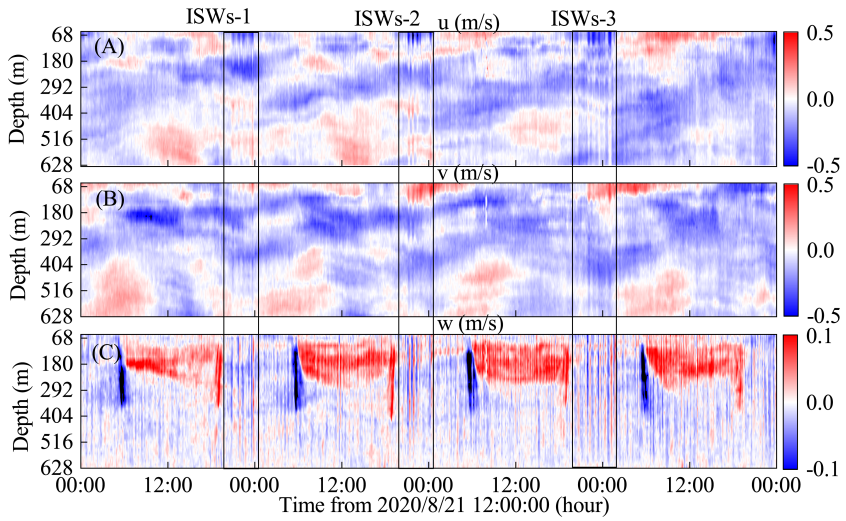

FIGURE 3
Velocity profiles measured by 75 k-ADCP. **(A)** zonal velocity u, **(B)** meridional velocity v, **(C)** vertical velocity w.(ISWs-1, ISWs-2, and ISWs-3 indicate ISW packets. The black line indicates the time scale for the ISW packet).

diel vertical migration characteristics, with organisms migrating to a depth of around 400 m around 6:00 and returning to the surface around 18:00. ISWs exists in the form of wave packets, with one ISW packet arriving at the study area around 20:00 each day. The current is northwest with a maximum velocity of 0.5 m/s at the surface. In the bottom boundary layer deeper than 600 m, The current is southeast with a maximum velocity of 0.2 m/s.

As shown in Figure 4, the profile of velocity indicates the ISWs-2 includes five distinct ISWs of depression, which lasted for about 4 hours with each individual ISW lasting around 20 minutes. Combining with Figure 3, ISW-1 contains four distinct ISWs of depression with a duration of about 3 hours, and ISW-3 contains six distinct ISWs of depression with a duration of around 5 hours. Figures 4A, B indicates that the horizontal velocity profile presents an obvious two-layered structure in which the dividing depth is approximately 130 m. In the upper layer, the zonal current is westward and the meridional current is northward, the horizontal velocity caused by ISWs can reach up to 0.6 m/s. In the lower layer, the zonal current is eastward and the meridional current is southward, and the horizontal velocity caused by ISWs exceeds 0.2 m/s. Figure 4C shows that there are strong upwelling and downwelling flows before and after the arrival of each ISW, with the highest flow velocity reaching 0.1 m/s, and such flow can act on the seafloor. It is worth noting that the time scales of the downwelling and upwelling flows are not consistent. For example, the time scale of the downwelling flow of the first ISW is 12 minutes, while the time scale of the upwelling flow is 10 minutes, and the strength of the downwelling flow is higher than the upwelling flow.

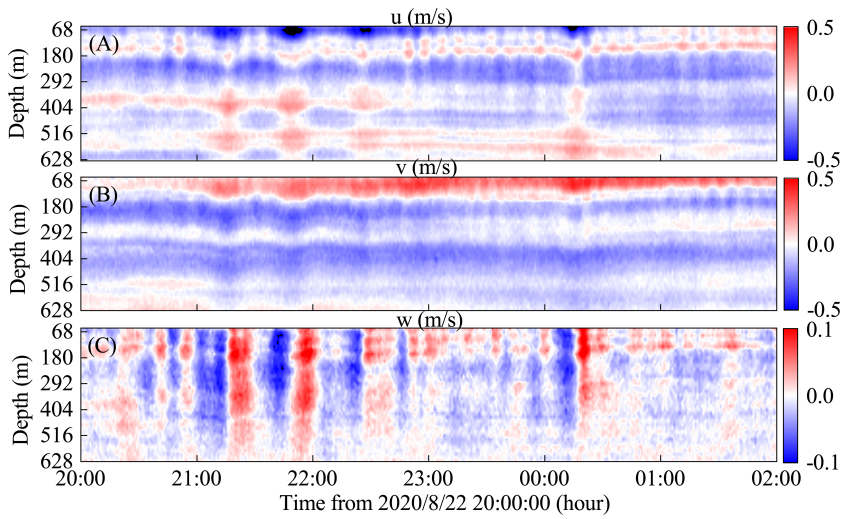

FIGURE 4
The velocity results when the ISWs-2 passed. **(A)** zonal velocity u, **(B)** meridional velocity v, **(C)** vertical velocity w.

This asymmetry enhances the transport of heat and energy in the water column, which has an important impact on the marine ecological environment (Chen et al., 2019; Hu et al., 2023).

3.2 Benthic organism activity

Video images captured by the deep-sea camera demonstrate there are a variety of benthic organisms in the study area (Figure 5). A total of 6,320 video sequences were captured, and 890 of them contained biological specimens. According to the method of Li (2017), The analysis identified 23 different species of benthic organisms from six phyla, including *Cnidaria*, *Arthropoda*, *Chordata*, *Nematoda*, *Mollusca*, and *Annelida*.

Figure 6 shows the changes in benthic abundance and density for 3 days from 8/21 00:00 to 8/24 12:00. Because the undersea camera is fixed to the observation system, there were many times when no identifiable benthic organisms were captured, so the abundance and density of the organisms were 0 at such times. The abundance and density of benthic organisms showed three peak stages. The first peak occurred around 1:00-2:30 on August 22, the maximum values of abundance and density are 0.043 and 0.78, respectively. The second peak occurred from around 22:00 on August 22 to 2:00 on August 23, the maximum values of abundance and density are 0.044 and 1.2, respectively. The third peak occurred from around 22:00 on August 23 to 2:30 on August 24, the maximum values of abundance and density are 0.053 and 1.3, respectively. Combined with Figure 4, we can find that the increase in abundance and density of benthic organisms is closely related to the passage of ISWs, and the abundance and density of benthic organisms are positively correlated with the strength and period of ISWs. The abundance of benthic organisms affected by ISWs is 3-5 times that without ISWs, and the density of benthic organisms is 3-9 times.

4 Discussions

4.1 Sediment resuspension and marine snow formation induced by ISWs

The resuspension of sediment inevitably leads to an increase in suspended particulate matter in the water column. In some canyon trench terrains, the increase in organic matter sedimentation has led to a doubling of oxygen consumption by organisms (Muacho et al., 2013). *In-situ* observation results indicated that the suspended particulate matter in the bottom boundary layer was mainly marine snow (Figures 7A, B), which are sticky particles with a

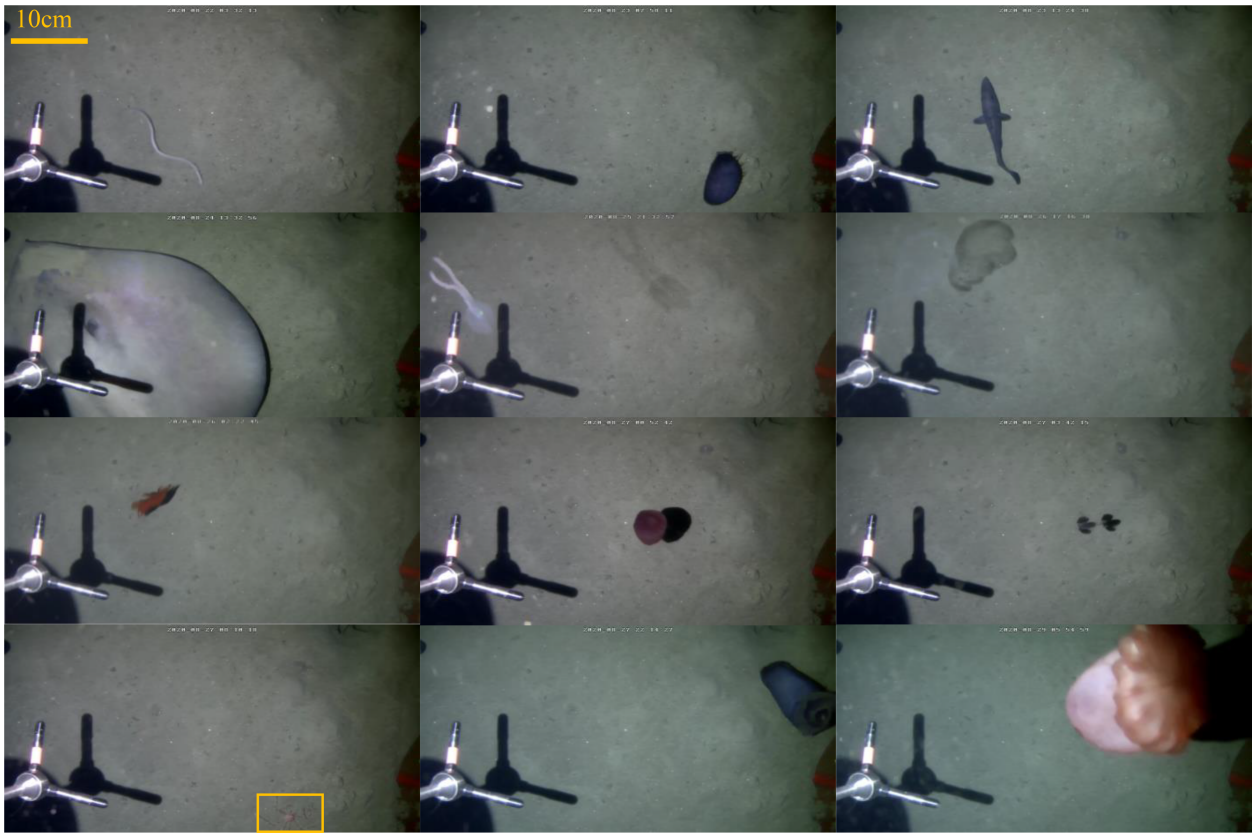

FIGURE 5
Some of the mega-benthic organisms captured by underwater cameras.

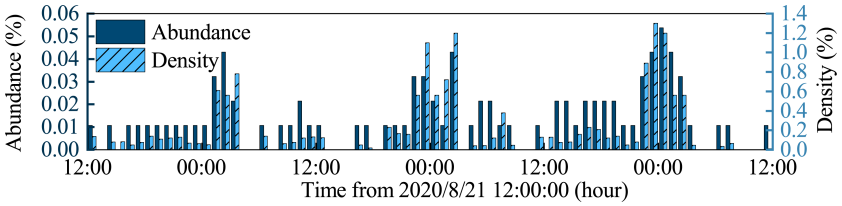

FIGURE 6
Changes in benthic abundance and density over time.

negative charge (Alldredge et al., 2002; Taucher et al., 2018). These particles can combine with sediment particles, mainly composed of diatoms, animal feces or debris, and mineral particles (Möller et al., 2012). Bottom water samples were collected using a CTD, and the suspended particle composition was mainly analyzed in the laboratory using a microscope, which revealed that diatoms and organic particles are the main components of flocculent particles (Figures 7C, D). The accumulation of marine snow in persistent, density-discontinuous nepheloid layer leads to environmental zoning in the water column area, which affects the distribution and interaction of planktonic organisms and the intensity of biological processes in the water column, and helps to maintain species diversity (Alldredge et al., 2002; Turner, 2015). Marine snow is the primary carrier of the biological carbon pump and has a significant impact on the settlement and feeding of planktonic organisms (Trudnowska et al., 2021). Therefore, the presence of suspended particles such as marine snow has become an important mechanism affecting biological activity.

In the continental slope region of the deep sea, large-amplitude ISWs of depression can cause sediment resuspension through shear stress (Lamb, 1997; Boegman and Stastna, 2019; Jia et al., 2019). Figure 8A depicts the changes in the velocity of the bottom boundary layer during the passage of ISWs-2, as recorded by ADV. For each ISW of depression, the u and v velocities are almost symmetrical, with an average velocity of 0.1 m/s. The v-direction velocity is relatively higher, with a maximum velocity of 0.22 m/s. The variation in the w-direction velocity is not significant. The incipient flow velocity of deep-sea marine snow

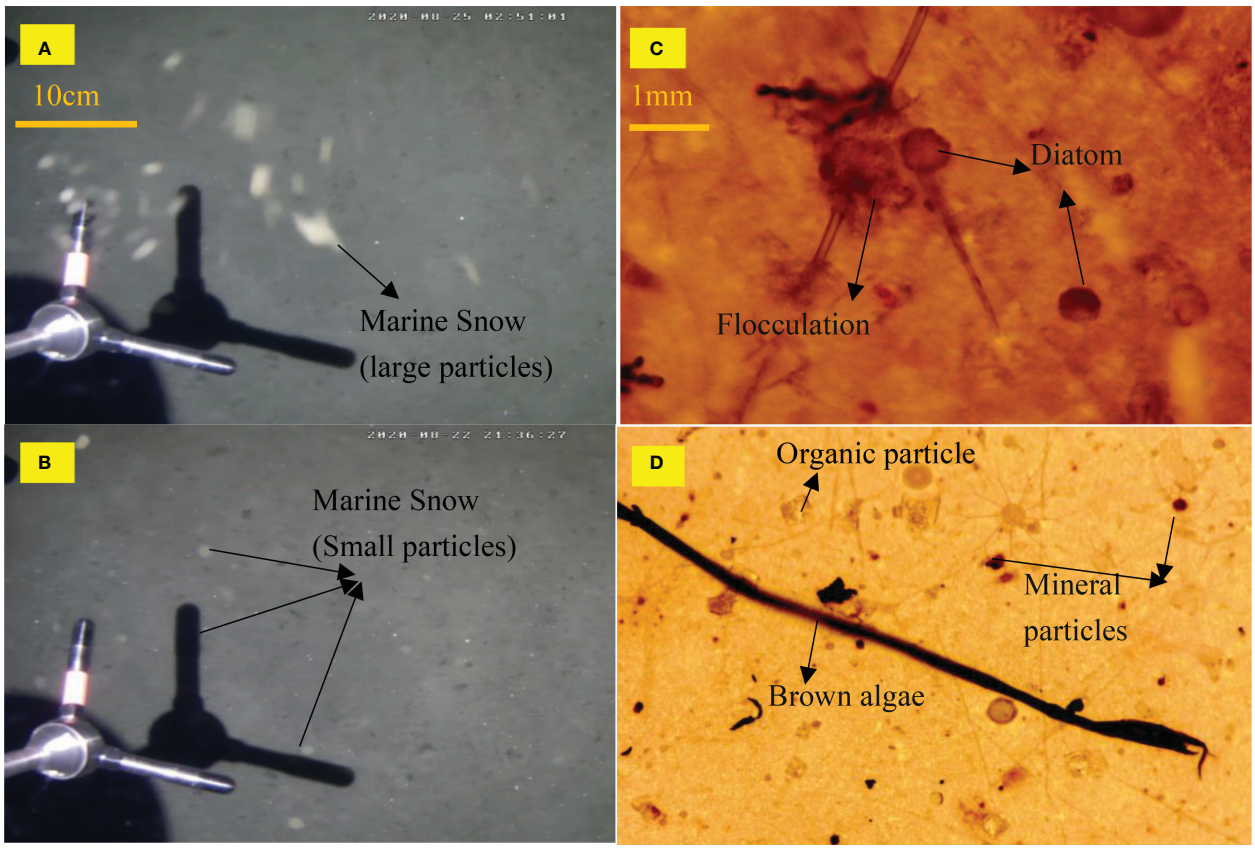

FIGURE 7
(A, B) marine snow particles captured by underwater cameras, **(C, D)** show suspended particles observed under a microscope.

particles ranges between 0.06-0.08 m/s, while a velocity of approximately 0.1-0.2 m/s can suspend most clayey sands (Camenen, 2009; Gardner et al., 2017). Therefore, ISWs can cause large-scale suspension and transport of marine snow at a depth of around 655 m. The maximum bottom shear stress generated by ISWs is 1.48 Pa, while the critical bed shear stress of the seafloor sediment is 0.2 Pa (Figure 8B). The bottom shear stress produced by ISWs surpasses the critical bed shear stress of sediment, which is the condition for sediment erosion and resuspension (Quaresma et al., 2007; Valipour et al., 2017). Figure 8C illustrates that the average suspended particulate matter concentration caused by the ISWs is 4.1 mg/l, which is 2-3 times higher than the background concentration.

4.2 Implications of shoaling on ISWs

During the propagation of ISWs from the deep sea to the continental slope and shelf regions, they play a crucial role in transporting materials and delivering heat (or cold) energy and nutrients to the benthic communities (Pan et al., 2012; Li et al., 2018; Navarro et al., 2018). Additionally, ISWs can cause small-scale physical changes in the benthic environment (Leichter et al., 2003; Hung et al., 2021) In addition, ISWs can lead to the accumulation of surface organic films, phytoplankton, and zooplankton (Macías et al., 2010), which can alter benthic organism activity. To estimate nitrate concentration (NO_3^-), a linear fit between nitrate concentration and water temperature is used (Reid et al., 2019). Although this method does not consider biotransformation of the nutrient field, such as uptake or remineralization, it can reflect trends in nutrient changes. In this study, the passage of ISWs resulted in a change in bottom temperature of approximately 0.2 °C (Figure 9A) and a change in nitrate (NO_3^-) concentration of 0.18 μM (Figure 9D). The bottom temperature and dissolved oxygen concentration decreased and then increased (Figures 9A, C), while salinity and nitrate concentration increased and then decreased (Figures 9B, D), indicating that ISWs can bring nutrient-rich cold water to the continental slope, thus impacting benthic organism activity.

4.3 The vertical structure of the water column affected by ISWs

ISWs play a crucial role in enhancing vertical mixing and modifying the thermocline structure (Wang et al., 2001; Wang et al., 2007). ISWs of depression can transfer dissolved substances (CO_2 and O_2) and water containing biological particles from the upper layer to the benthic system, affecting benthic biological activity (Pan et al., 2012; Muacho et al., 2013). In this study, to understand the impact of ISWs on the water column environment in the study area, we conducted continuous CTD observations from 17:30 on September 1, 2020 to 17:30 on September 2, 2020, tracking the environmental impact of a single internal solitary wave on the water column (Figure 10). Similar observations have been made by Hung et al. (2021) with a water depth of 200 m on the Dongsha shoal.

Figures 10A, B, and C show that a single ISW arrived around 19:10 on September 1st, with a maximum velocity in the u and v directions of 0.3 m/s and a vertical velocity w of no more than 0.05 m/s. The duration of its action was approximately 20 minutes, and compared with the other observed ISWs, the energy of this single ISW was relatively weak. However, this single ISW still can force the surface water to move downward, causing vertical mixing outside of the thermocline, with a maximum displacement distance of 50 m (Figure 10D). The ISW of depression discovered by Huang et al. (2016) caused the maximum temperature to increase by over 6°C at the trough at a depth of 300m, and even at 1000 m depth, the

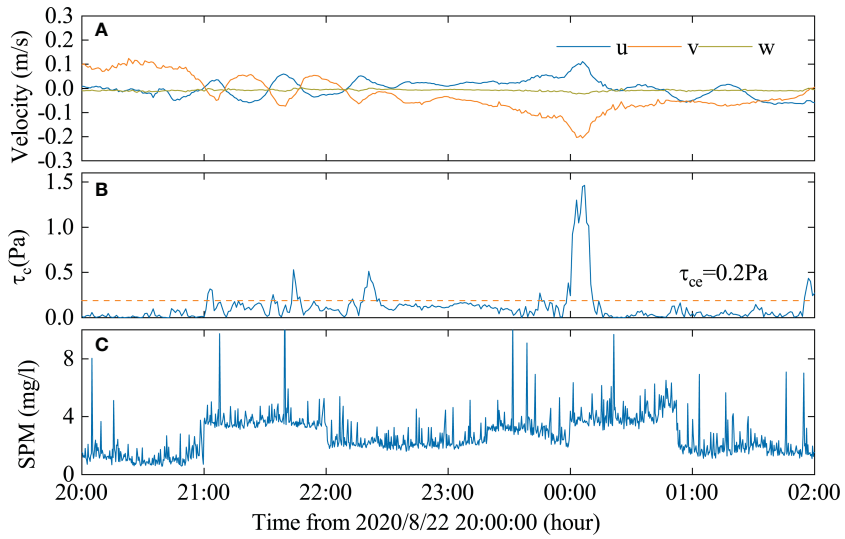

FIGURE 8
(A) Velocity characteristics of ISWs in the submarine boundary layer, **(B)** The bed shear stresses (τ_c)due to ISWs and the critical shear stress for erosion of the bottom sediment (τ_{ce}), **(C)** Suspended particulate matter (SPM).

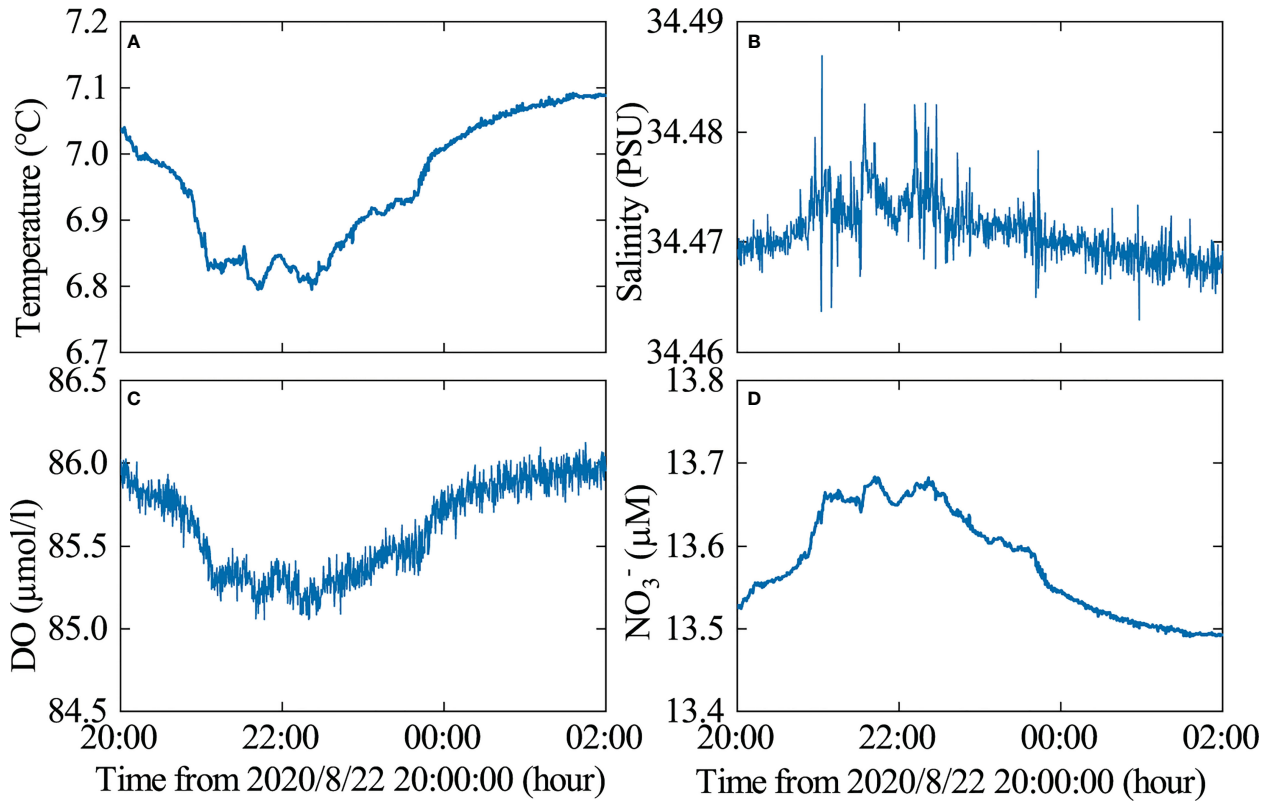

FIGURE 9
The variability of bottom environmental elements when the ISWs passed. **(A)** temperature, **(B)** salinity, **(C)** dissolved oxygen, **(D)** nitrate (NO_3^-).

temperature increase exceeded 0.5°C, which is likely to have a significant impact on benthic biological activity. Figure 10E shows an increase in turbidity at depths of 70 m, 300 m, and 600 m, indicating the presence of surface, middle, and bottom nepheloid layers (Masunaga et al., 2015). ISWs elevate the thickness of the surface nepheloid layer and increased the concentration of the middle and bottom nepheloid layers.

4.4 Mechanisms of ISW impact on benthic organism activity

We summarize three main mechanisms of benthic organism activity affected by ISWs (Figure 11): (1) In steep terrain or shallow water, ISWs mainly break and form local vortices (Bogucki and Redekopp, 1999; Puig et al., 2001), resuspending a large amount of sediment and continuously migrating these suspended sediments to the deep sea, forming nepheloid layer (Zhang et al., 2019; Tian et al., 2021a). During migration, suspended sediment particles aggregate to form marine snow and other flocs that settle to the seafloor. In the deep-sea bottom boundary layer, ISWs cause sediment resuspension through large bottom shear forces, with marine snow being the dominant suspended particle type that serves as a food source for benthic organisms on the continental slope. This represents an important mechanism for impacting benthic organism activity. (2) During the propagation of ISWs from the open ocean to the continental slope, the transport of nutrient-rich cold water to benthic communities on the seafloor impacts benthic organism activity. Strong hydrodynamics also transport some larvae and organisms to the continental slope and shelf (Roder et al., 2010), thereby affecting changes in benthic organism abundance. (3) In the vertical direction, ISWs can enhance the vertical mixing of seawater, alter thermocline structure, and impact the habitat of upper-level organisms (Flood et al., 2021). Additionally, ISWs transfer heat and bioparticles from the upper layer to the benthic system, thereby affecting benthic organism activity.

5 Conclusions

In this study, we investigated the impact of ISWs on the deep-sea bottom boundary layer environment and benthic organisms through *in-situ* long-term observations for the first time on the continental slope of the northern South China. The results are summarized as follows:

(1) ISWs of depression with a period of one day were observed in the Shenhu continental slope, arriving at the study area around 19:00 to 21:00 each day. ISWs consisted of 5-6 individual wave groups in a wave packet form, with a maximum horizontal velocity exceeding 0.5m/s and vertical velocity exceeding 0.1m/s. ISWs induced velocity changes exceeding 0.2m/s in the bottom boundary layer.

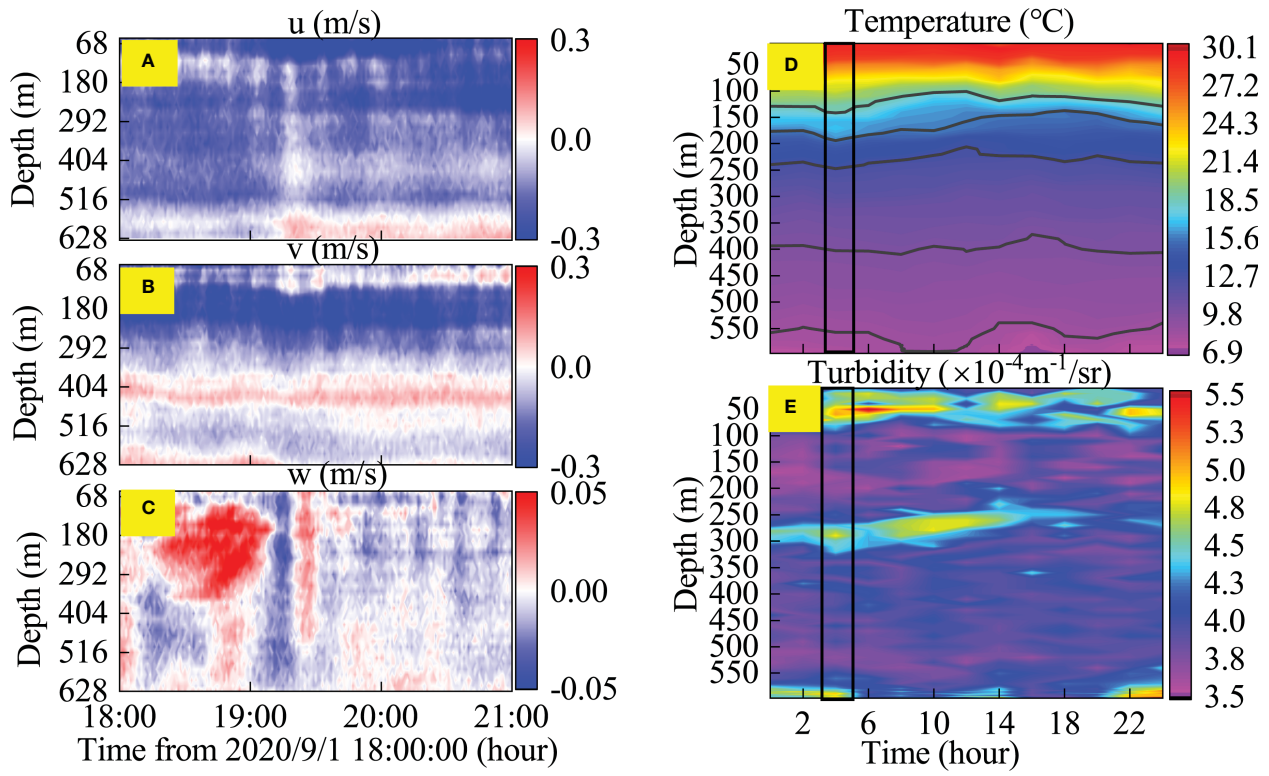

FIGURE 10
Impact of single ISW on the vertical structure of the water column. **(A–C)** velocity profiles single ISW passage measured by 75 k-ADCP, **(D)** Temperature variation, **(E)** Turbidity variation (black boxes indicate the time scale for a single ISW).

(2) The abundance and density of benthic organisms were positively correlated with the duration and intensity of ISWs. The abundance of benthic organisms affected by ISWs was found to be 3-5 times higher than that in the absence of ISWs, while the density was 3-9 times higher.

(3) ISWs generated significant shear stress in the bottom boundary layer at a depth of 655m, causing sediment resuspension on the Shenhu continental slope and increasing the aggregation and transport of marine snow and other nutrients. This provided a food source for benthic organisms. The shoaling effect of ISWs on the continental slope also introduced cold nutrient-rich water, larvae, and organisms, which affected changes in benthic biomass. In the vertical direction, ISWs were found to move temperature, salinity, dissolved oxygen, and nutrients of surface water toward deeper layers, thereby influencing the position of benthic organisms in the water column. These factors collectively influenced changes in benthic organism activity.

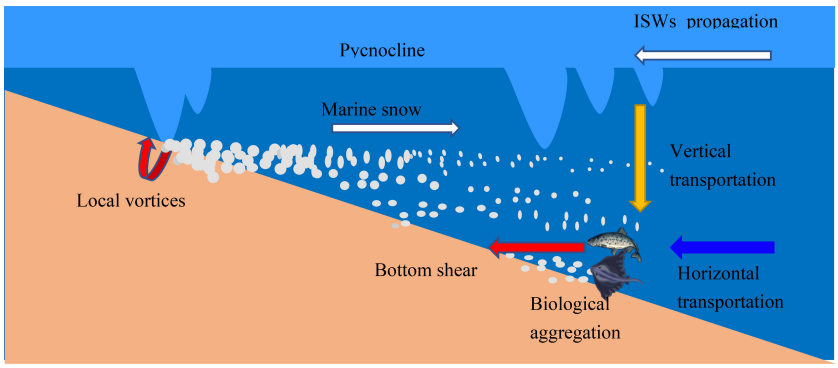

FIGURE 11
Schematic diagram of the impact of ISWs on deep-sea benthic organisms.

Data availability statement

The original contributions presented in the study are included in the article/supplementary material. Further inquiries can be directed to the corresponding authors.

Author contributions

XF took part in the *in-situ* observations, analyzed, and interpreted the data, and wrote the manuscript. LW revised the manuscript and provided suggestions for the manuscript. CJ took part in the *in-situ* observations and analyzed some of the data. HW revised part of the manuscript and provided suggestions for the manuscript. CZ presented the central ideas, revised the manuscript, discussed the results, and approved the submitted version. YJ presented the central idea, discussed the results, provided advice to the manuscript, and approved the submitted version. All authors contributed to the article and approved the submitted version.

Funding

This research was funded by the National Natural Science Foundation of China (No. 41831280, 42207173), the Natural Science Foundation of Shandong Province (No. ZR2022QD002, 2022RZB07052), the Shandong Provincial and Qingdao Postdoctoral Foundation (No. SDCX-ZG-202203089), and the Key Laboratory of Submarine Geosciences and Prospecting Techniques (MoE) (No. SGPT-2022OF-03).

Acknowledgments

We thank the Natural Science Foundation of China for the Open Research Cruise of the northern South China Sea (NORC2019-05, NORC2022-05). We appreciate all members for their efforts in the collection of the data in this study.

Conflict of interest

The authors declare that the research was conducted in the absence of any commercial or financial relationships that could be construed as a potential conflict of interest.

Publisher's note

References

Alford, M. H., Peacock, T., MacKinnon, J. A., Nash, J. D., Buijsman, M. C., Centurioni, L. R., et al. (2015). The formation and fate of internal waves in the south China Sea. *Nature* 521 (7550), 65–69. doi: 10.1038/nature14399

Alldredge, A. L., Cowles, T. J., MacIntyre, S., Rines, J. E. B., Donaghay, P. L., Greenlaw, C. F., et al. (2002). Occurrence and mechanisms of formation of a dramatic thin layer of marine snow in a shallow pacific fjord. *Mar. Ecol. Prog. Ser.* 233, 1–12. doi: 10.3354/meps233001

Bai, X., Liu, Z., Zheng, Q., Hu, J., Lamb, K. G., and Cai, S. (2019). Fission of shoaling internal waves on the northeastern shelf of the south China Sea. *J. Geophysical Research: Oceans* 124 (7), 4529–4545. doi: 10.1029/2018jc014437

Boegman, L., and Stastna, M. (2019). Sediment resuspension and transport by internal solitary waves. *Annu. Rev. Fluid Mechanics* 51 (1), 129–154. doi: 10.1146/annurev-fluid-122316-045049

Bogucki, D. J., and Redekopp, L. G. (1999). A mechanism for sediment resuspension by internal solitary waves. *Geophysical Res. Lett.* 26 (9), 1317–1320. doi: 10.1029/1999gl900234

Broitman, B. R., Blanchette, C. A., Menge, B. A., Lubchenco, J., Krenz, C., Foley, M., et al. (2008). Spatial and temporal patterns of invertebrate recruitment along the West coast of the united states. *Ecol. Monogr.* 78 (3), 403–421. doi: 10.1890/06-1805.1

Cai, S., Xie, J., and He, J. (2012). An overview of internal solitary waves in the south China Sea. *Surveys Geophysics* 33 (5), 927–943. doi: 10.1007/s10712-012-9176-0

Camenen, B. (2009). Estimation of the wave-related ripple characteristics and induced bed shear stress. *Estuarine Coast. Shelf Sci.* 84 (4), 553–564. doi: 10.1016/j.ecss.2009.07.022

Chen, T. Y., Tai, J. H., Ko, C. Y., Hsieh, C. H., Chen, C. C., Jiao, N., et al. (2016b). Nutrient pulses driven by internal solitary waves enhance heterotrophic bacterial growth in the south China Sea. *Environ. Microbiol.* 18 (12), 4312–4323. doi: 10.1111/1462-2920.13273

Chen, D., Wang, X., Völker, D., Wu, S., Wang, L., Li, W., et al. (2016a). Three dimensional seismic studies of deep-water hazard-related features on the northern slope of south China Sea. *Mar. Petroleum Geology* 77, 1125–1139. doi: 10.1016/j.marpetgeo.2016.08.012

Chen, L., Zheng, Q., Xiong, X., Yuan, Y., Xie, H., Guo, Y., et al. (2019). Dynamic and statistical features of internal solitary waves on the continental slope in the northern south China Sea derived from mooring observations. *J. Geophysical Research: Oceans* 124 (6), 4078–4097. doi: 10.1029/2018jc014843

Dato, J. F., Fiore, M. M. E., Donofrio, E. E., Oreiro, F. A., and Grismeyer, W. H. (2021). Comparison of the extreme surge estimation with the generalized extreme value distribution, using the maximum of positive storm surge and skew surge in two port areas with different hydrodynamic and tidal characteristics. *J. Mar. Environ. Eng.* 10 (4), 281–290.

Ding, W., Li, J., Li, J., Fang, Y., and Tang, Y. (2013). Morphotectonics and evolutionary controls on the pearl river canyon system, south China Sea. *Mar. Geophysical Res.* 34 (3-4), 221–238. doi: 10.1007/s11001-013-9173-9

Du, X., Sun, Y., Song, Y., and Zhu, C. (2021). In-situ observation of wave-induced pore water pressure in seabed silt in the yellow river estuary of China. *J. Mar. Environ. Eng.* 10 (4), 305–317.

Flood, B., Wells, M., Dunlop, E., and Young, J. (2021). Vertical oscillations of the thermocline caused by internal waves modify coldwater pelagic fish distribution: results from a large stratified lake. *J. Great Lakes Res.* 47 (10), 1386–1399. doi: 10.1016/j.jglr.2021.06.010

Fu, K.-H., Wang, Y.-H., St. Laurent, L., Simmons, H., and Wang, D.-P. (2012). Shoaling of large-amplitude nonlinear internal waves at dongsha atoll in the northern south China Sea. *Continental Shelf Res.* 37, 1–7. doi: 10.1016/j.csr.2012.01.010

Gardner, W. D., Tucholke, B. E., Richardson, M. J., and Biscaye, P. E. (2017). Benthic storms, nepheloid layers, and linkage with upper ocean dynamics in the western north Atlantic. *Mar. Geology* 385, 304–327. doi: 10.1016/j.margeo.2016.12.012

Helfrich, K. R., Melville, W. K., and Miles, J. W. (2006). On interfacial solitary waves over slowly varying topography. *J. Fluid Mechanics* 149 (-1), 305–317. doi: 10.1017/s0022112084002664

Holligan, P. M., Pingree, R. D., and Mardell, G. T. (1985). Oceanic solitons, nutrient pulses and phytoplankton growth. *Nature* 314 (6009), 348–350. doi: 10.1038/314348a0

Hu, C., Li, X., Ji, C., Jiao, X., and Jia, Y. (2023). In-situ observation of seabed vertical deformation inYellow River Delta under storm surges. *Mar. Pet. Geol.* 152, 106250. doi: 10.1016/j.marpetgeo.2023.106250

Huang, X., Chen, Z., Zhao, W., Zhang, Z., Zhou, Q., and Yang,, J. (2016). An extreme internal solitary wave event observed in the northern South China Sea. *Sci Rep* 6, 30041. doi: 10.1038/srep30041

Huang, X., Huang, S., Zhao, W., Zhang, Z., Zhou, C., and Tian, J. (2022). Temporal variability of internal solitary waves in the northern south China Sea revealed by long-term mooring observations. *Prog. Oceanography* 201, 102716. doi: 10.1016/j.pocean.2021.102716

Hung, J. J., Wang, Y. H., Fu, K. H., Lee, I. H., Tsai, S. S., Lee, C. Y., et al. (2021). Biogeochemical responses to internal-wave impacts in the continental margin off dongsha atoll in the northern south China Sea. *Prog. Oceanography* 199, 102689. doi: 10.1016/j.pocean.2021.102689

Jia, Y., Tian, Z., Shi, X., Liu, J. P., Chen, J., Liu, X., et al. (2019). Deep-sea sediment resuspension by internal solitary waves in the northern south China Sea. *Sci. Rep.* 9 (1), 12137. doi: 10.1038/s41598-019-47886-y

Kheili, A. G. K., Shafieefar, M., Rezaei, A., Nemati, M. H., and Bagheri, M. (2021). Contributing factors to ocean currents modelling in the makran coastal region. *J. Mar. Environ. Eng.* 10 (4), 261–280.

Kuang, Y., Yang, L., Li, Q., Lv, X., Li, Y., Yu, B., et al. (2019). Physical characteristic analysis of unconsolidated sediments containing gas hydrate recovered from the shenhu area of the south China sea. *J. Petroleum Sci. Eng.* 181, 106173. doi: 10.1016/j.petrol.2019.06.037

Lamb, K. G. (1997). Particle transport by nonbreaking, solitary internal waves. *J. Geophysical Research: Oceans* 102 (C8), 18641–18660. doi: 10.1029/97jc00441

Lamb, K. G. (2014). Internal wave breaking and dissipation mechanisms on the continental Slope/Shelf. *Annu. Rev. Fluid Mechanics* 46 (1), 231–254. doi: 10.1146/annurev-fluid-011212-140701

Leichter, J. J., Stewart, H. L., and Miller, S. L. (2003). Episodic nutrient transport to Florida coral reefs. *Limnology Oceanography* 48 (4), 1394–1407. doi: 10.4319/lo.2003.48.4.1394

Li, X. (2017). Taxonomic research on deep-sea macrofauna in the south China Sea using the Chinese deep-sea submersible jiaolong. *Integr. Zool* 12 (4), 270–282. doi: 10.1111/1749-4877.12254

Li, D., Chou, W. C., Shih, Y. Y., Chen, G. Y., Chang, Y., Chow, C. H., et al. (2018). Elevated particulate organic carbon export flux induced by internal waves in the oligotrophic northern south China Sea. *Sci. Rep.* 8 (1), 2042. doi: 10.1038/s41598-018-20184-9

Ma, X., Yan, J., Hou, Y., Lin, F., and Zheng, X. (2016). Footprints of obliquely incident internal solitary waves and internal tides near the shelf break in the northern south China Sea. *J. Geophysical Research: Oceans* 121 (12), 8706–8719. doi: 10.1002/2016jc012009

Macías, D., Somavilla, R., González-Gordillo, J. I., and Echevarría, F. (2010). Physical control of zooplankton distribution at the strait of Gibraltar during an episode of internal wave generation. *Mar. Ecol. Prog. Ser.* 408, 79–95. doi: 10.3354/meps08566

MacKenzie, B. R. (2000). Turbulence, larval fish ecology and fisheries recruitment: a review of field studies. *Oceanologica Acta* 23 (4), 357–375. doi: 10.1016/S0399-1784(00)00142-0

MacKenzie, B. R., and Kiorboe, T. (2000). Larval fish feeding and turbulence: a case for the downside. *Limnology Oceanography* 45 (1), 1–10. doi: 10.4319/lo.2000.45.1.0001

Masunaga, E., Homma, H., Yamazaki, H., Fringer, O. B., Nagai, T., Kitade, Y., et al. (2015). Mixing and sediment resuspension associated with internal bores in a shallow bay. *Continental Shelf Res.* 110, 85–99. doi: 10.1016/j.csr.2015.09.022

Möller, K. O., St John, M., Temming, A., Floeter, J., Sell, A. F., Herrmann, J. P., et al. (2012). Marine snow, zooplankton and thin layers: indications of a trophic link from small-scale sampling with the video plankton recorder. *Mar. Ecol. Prog. Ser.* 468, 57–69. doi: 10.3354/meps09984

Muacho, S., da Silva, J. C. B., Brotas, V., and Oliveira, P. B. (2013). Effect of internal waves on near-surface chlorophyll concentration and primary production in the nazaré canyon (west of the Iberian peninsula). *Deep Sea Res. Part I: Oceanographic Res. Papers* 81, 89–96. doi: 10.1016/j.dsr.2013.07.012

Navarro, G., Vicent, J., Caballero, I., Gómez-Enri, J., Morris, E. P., Sabater, N., et al. (2018). Improving the analysis of biogeochemical patterns associated with internal waves in the strait of Gibraltar using remote sensing images. *Estuarine Coast. Shelf Sci.* 204, 1–13. doi: 10.1016/j.ecss.2018.02.009

Pan, X., Wong, G. T. F., Shiah, F.-K., and Ho, T.-Y. (2012). Enhancement of biological productivity by internal waves: observations in the summertime in the northern south China Sea. *J. Oceanography* 68 (3), 427–437. doi: 10.1007/s10872-012-0107-y

Pineda, J. (1991). Predictable upwelling and the shoreward transport of planktonic larvae by internal tidal bores. *Science* 253 (5019), 548–549. doi: 10.1126/science.253.5019.548

Pope, N. D., Widdows, J., and Brinsley, M. D. (2006). Estimation of bed shear stress using the turbulent kinetic energy approach–a comparison of annular flume and field data. *Continental Shelf Res.* 26 (8), 959–970. doi: 10.1016/j.csr.2006.02.010

Puig, P., Palanques, A., and Guillen, J. (2001). Near-bottom suspended sediment variability caused by storms and near-inertial internal waves on the ebro mid continental shelf (NW Mediterranean). *Mar. Geology* 178 (1-4), 81–93. doi: 10.1016/S0025-3227(01)00186-4

Quaresma, L. S., Vitorino, J., Oliveira, A., and da Silva, J. (2007). Evidence of sediment resuspension by nonlinear internal waves on the western Portuguese mid-shelf. *Mar. Geology* 246 (2-4), 123–143. doi: 10.1016/j.margeo.2007.04.019

Reid, E. C., DeCarlo, T. M., Cohen, A. L., Wong, G. T. F., Lentz, S. J., Safaie, A., et al. (2019). Internal waves influence the thermal and nutrient environment on a shallow coral reef. *Limnology Oceanography* 64 (5), 1949–1965. doi: 10.1002/lno.11162

Roder, C., Fillinger, L., Jantzen, C., Schmidt, G. M., Khokiattiwong, S., and Richter, C. (2010). Trophic response of corals to large amplitude internal waves. *Mar. Ecol. Prog. Ser.* 412, 113–128. doi: 10.3354/meps08707

Shi, B. W., Yang, S. L., Wang, Y. P., Bouma, T. J., and Zhu, Q. (2012). Relating accretion and erosion at an exposed tidal wetland to the bottom shear stress of combined current–wave action. *Geomorphology* 138 (1), 380–389. doi: 10.1016/j.geomorph.2011.10.004

Shimeta, J., Amos, C. L., Beaulieu, S. E., and Katz, S. L. (2003). Resuspension of benthic protists at subtidal coastal sites with differing sediment composition. *Mar. Ecol. Prog. Ser.* 259, 103–115. doi: 10.3354/meps259103

Stapleton, K. R., and Huntley, D. A. (1995). Seabed stress determinations using the inertial dissipation method and the turbulent kinetic energy method. *Earth Surface Processes Landforms* 20 (9), 807–815. doi: 10.1002/esp.3290200906

Su, M., Lin, Z., Wang, C., Kuang, Z., Liang, J., Chen, H., et al. (2020). Geomorphologic and infilling characteristics of the slope-confined submarine canyons in the pearl river mouth basin, northern south China Sea. *Mar. Geology* 424, 106166. doi: 10.1016/j.margeo.2020.106166

Syamsudin, F., Taniguchi, N., Zhang, C., Hanifa, A. D., Li, G., Chen, M., et al. (2019). Observing internal solitary waves in the lombok strait by coastal acoustic tomography. *Geophysical Res. Lett.* 46 (17-18), 10475–10483. doi: 10.1029/2019gl084595

Taki, K. (2000). Critical shear stress for cohesive sediment transport. *Coast. Estuar. Fine Sediment Processes* 3, 53–61. doi: 10.1016/s1568-2692(00)80112-6

Taucher, J., Stange, P., Algueró-Muñiz, M., Bach, L. T., Nauendorf, A., Kolzenburg, R., et al. (2018). *In situ* camera observations reveal major role of zooplankton in modulating marine snow formation during an upwelling-induced plankton bloom. *Prog. Oceanography* 164, 75–88. doi: 10.1016/j.pocean.2018.01.004

Tian, Z., Jia, Y., Chen, J., Liu, J. P., Zhang, S., Ji, C., et al. (2021a). Internal solitary waves induced deep-water nepheloid layers and seafloor geomorphic changes on the continental slope of the northern south China Sea. *Phys. Fluids* 33 (5), 053312. doi: 10.1063/5.0045124

Tian, Z., Jia, Y., Du, Q., Zhang, S., Guo, X., Tian, W., et al. (2021b). Shearing stress of shoaling internal solitary waves over the slope. *Ocean Eng.* 241, 110046. doi: 10.1016/j.oceaneng.2021.110046

Trudnowska, E., Lacour, L., Ardyna, M., Rogge, A., Irisson, J. O., Waite, A. M., et al. (2021). Marine snow morphology illuminates the evolution of phytoplankton blooms and determines their subsequent vertical export. *Nat. Commun.* 12 (1), 2816. doi: 10.1038/s41467-021-22994-4

Turner, J. T. (2015). Zooplankton fecal pellets, marine snow, phytodetritus and the ocean's biological pump. *Prog. Oceanography* 130, 205–248. doi: 10.1016/j.pocean.2014.08.005

Valipour, R., Boegman, L., Bouffard, D., and Rao, Y. R. (2017). Sediment resuspension mechanisms and their contributions to high-turbidity events in a large lake. *Limnology Oceanography* 62 (3), 1045–1065. doi: 10.1002/lno.10485

van Haren, H. (2020). Challenger deep internal wave turbulence events. *Deep Sea Res. Part I: Oceanographic Res. Papers* 165, 103400. doi: 10.1016/j.dsr.2020.103400

Wang, B. J., Bogucki, D. J., and Redekopp, L. G. (2001). Internal solitary waves in a structured thermocline with implications for resuspension and the formation of thin particle-laden layers. *J. Geophysical Research: Oceans* 106 (C5), 9565–9585. doi: 10.1029/2000jc900101

Wang, Y.-H., Dai, C.-F., and Chen, Y.-Y. (2007). Physical and ecological processes of internal waves on an isolated reef ecosystem in the south China Sea. *Geophysical Res. Lett.* 34 (18), L18609. doi: 10.1029/2007gl030658

Wang, H., Jia, Y., Ji, C., Jiang, W., and Bian, C. (2022). Internal tide-induced turbulent mixing and suspended sediment transport at the bottom boundary layer of the south China Sea slope. *J. Mar. Syst.* 230, 103723. doi: 10.1016/j.jmarsys.2022.103723

Yin, S., Lin, L., Pope, E. L., Li, J., Ding, W., Wu, Z., et al. (2019). Continental slope-confined canyons in the pearl river mouth basin in the south China Sea dominated by erosion, 2004–2018. *Geomorphology* 344, 60–74. doi: 10.1016/j.geomorph.2019.07.016

Zhang, W., Didenkulova, I., Kurkina, O., Cui, Y., Haberkern, J., Aepfler, R., et al. (2019). Internal solitary waves control offshore extension of mud depocenters on the NW Iberian shelf. *Mar. Geology* 409, 15–30. doi: 10.1016/j.margeo.2018.12.008

Zhang, Q., Gong, Z., Zhang, C., Lacy, J. R., Jaffe, B. E., and Xu, B. (2018). Bed shear stress estimation under wave conditions using near-bottom measurements: comparison of methods. *J. Coast. Res.* 85, 241–245. doi: 10.2112/si85-049.1

Zhang, S., Zhu, J., Jia, Y., Li, S., Chen, R., Chen, X., et al. (2022). Submarine small-scale features of cyclic steps in the penghu canyon: implications for the migration of canyon. *J. Mar. Sci. Eng.* 10 (9), 1301. doi: 10.3390/jmse10091301

Zhu, C., Li, S., Chen, J., Wang, D., Song, X., Li, Z., et al. (2023b). Nepheloid layer generation by gas eruption: unexpected experimental results. *J. Oceanology Limnology.* 41(2). doi: 10.1007/s00343-022-2108-z

Zhu, C., Li, Q., Li, Z., Duan, M., Li, S., Zhou, Q., et al. (2023a). Seabed fluid flow in the China seas. *Front. Mar. Sci.* 10. doi: 10.3389/fmars.2023.1158685

frontiers | Frontiers in Marine Science

TYPE Original Research
PUBLISHED 11 August 2023
DOI 10.3389/fmars.2023.1204182

OPEN ACCESS

EDITED BY
Min Luo,
Shanghai Ocean University, China

REVIEWED BY
Peter Feldens,
Leibniz Institute for Baltic Sea Research (LG), Germany
Hiroyuki Matsumoto,
Japan Agency for Marine-Earth Science and Technology (JAMSTEC), Japan

*CORRESPONDENCE
Jasper J. L. Hoffmann
jasper.hoffmann@awi.de

RECEIVED 11 April 2023
ACCEPTED 24 July 2023
PUBLISHED 11 August 2023

CITATION
Hoffmann JJL, Mountjoy JJ, Spain E, Gall M, Tait LW, Ladroit Y and Micallef A (2023) Fresh submarine groundwater discharge offshore Wellington (New Zealand): hydroacoustic characteristics and its influence on seafloor geomorphology. *Front. Mar. Sci.* 10:1204182. doi: 10.3389/fmars.2023.1204182

Fresh submarine groundwater discharge offshore Wellington (New Zealand): hydroacoustic characteristics and its influence on seafloor geomorphology

Jasper J. L. Hoffmann[1,2]*, Joshu J. Mountjoy[3], Erica Spain[3], Mark Gall[3], Leigh W. Tait[4], Yoann Ladroit[3] and Aaron Micallef[1,5]

[1]Marine Geology and Seafloor Surveying Group, Department of Geosciences, University of Malta, Msida, Malta, [2]Alfred-Wegener-Institute, Helmholtz Centre for Polar and Marine Research, Wadden Sea Station, List, Germany, [3]National Institute for Water and Atmospheric Research (NIWA), Wellington, New Zealand, [4]National Institute for Water and Atmospheric Research (NIWA), Christchurch, New Zealand, [5]Monterey Bay Aquarium Research Institute, Moss Landing, CA, United States

Fresh submarine groundwater discharge (FSGD) influences the biogeochemistry of coastal areas and can be a proxy for potential untapped resources of offshore freshened groundwater (OFG). In most areas however, the onshore-offshore connection and the recharge characteristics of offshore aquifers are poorly constrained, making a potential exploitation of this resource challenging. Offshore Wellington (New Zealand), a well-defined onshore aquifer system extends beneath the harbour, where substantial amounts of freshwater seep out from the ocean floor. The aquifer system has been studied in detail and recently the first attempts worldwide have been made here to use the offshore groundwater as a future source of drinking water. However, the locations and extent of FSGD as well as its influence on seafloor morphology are still poorly understood. Exact localisation of FSGD sites is essential to sample and quantify discharging waters but remains challenging due to a lack of robust and appropriate measurement procedures. Novel sensing strategies, such as the influence of seeping groundwater on hydroacoustic water column reflectivity could greatly improve the identification of groundwater discharge locations worldwide. Therefore, we use a multidisciplinary dataset and evaluate different methodologies to map the spatial extent of FSGD sites and determine their geomorphologic expressions on the seafloor of Wellington Harbour. In this study, single and multibeam hydroacoustics and towfish (temperature, salinity and turbidity) transects were combined with remotely operated vehicle (ROV) dives and sediment cores to better characterise FSGD sites. We observed several hundred seafloor depressions (pockmarks) that we attribute to continuous seepage of gas and groundwater from the seafloor. Different pockmark morphologies indicate different fluid flow regimes and the persistent flow

allows even small pockmarks to remain unchanged over time, while the geomorphologic expressions of anchor scours on the seafloor diminish in the same region. Enhanced hydroacoustic reflections in the water column within and above the pockmarks indicate suspended sediment particles, which are likely kept in suspension by discharging groundwater and density boundaries.

KEYWORDS

Waiwhetu Aquifer, Wellington Harbour, offshore freshened groundwater, pockmarks, fluid seepage, gas escape

1 Introduction

Submarine groundwater discharge (SGD) is a common global phenomenon that describes the flow of fresh or saline waters from the subsurface into the ocean. Fresh submarine groundwater discharge (FSGD) generally occurs in regions where onshore aquifers with higher terrestrial hydraulic heads compared to the sea-level are hydraulically connected to the ocean (Moore, 1996). Where confined aquifers extend beneath the ocean, offshore freshened groundwater systems (OFGs) can form. The latter have increasingly gained scientific interest in the past decade due to their potential to mitigate freshwater scarcity in coastal areas (Post et al., 2013; Berndt and Micallef, 2019; Micallef et al., 2020a). With the advance of climate change and an expected increase in global droughts, coastal populations and pollution, coastal aquifers are under increasing pressure (Seager et al., 2007; IPCC and Core Writing Team, 2014; Neumann et al., 2015). Generally, onshore aquifer systems are well constrained by wells, geochemical groundwater characterisation and monitoring, while the offshore component remains hidden beneath the ocean. SGD is often the only available insight into the OFG compartment. Since the global volume of SGD supplies the same amount or even more nutrients to coastal areas compared to global rivers (Seitzinger and Harrison, 2008; Knee and Paytan, 2011; Santos et al., 2021), SGD locally drives primary productivity (Rocha et al., 2015), influences marine ecological systems (Starke et al., 2020) and can trigger harmful algal blooms (Hu et al., 2006; Lee et al., 2010; Luo and Jiao, 2016). Additionally, SGD not only influences the local submarine geomorphology (Rousakis et al., 2014; Purkamo et al., 2022) but is also thought to create mechanical instabilities in continental margins, potentially shaping submarine landscapes at regional scale (Saadatkhah et al., 2023). Although SGD has been intensively investigated worldwide, the sources and locations of discharge often remain unknown due to the discrete nature of point measurements generally used in geochemical characterisations. Therefore, robust monitoring techniques and a better understanding of the onshore-offshore connectivity between OFG systems are urgently required to assess the potential of OFG as an unconventional future resource (Arévalo-Martínez et al., 2023).

In Aotearoa/New Zealand, OFG bodies have been identified offshore Canterbury by Micallef et al., (2020b) whereas the likelihood of OFG around New Zealand's coasts was further investigated by Morgan and Mountjoy (2022). Groundwater is an important source of potable water in the Te Whanganui-a-Tara/Wellington Region at the bottom of the North Island, where the Hutt Valley supplies about a third of Wellington's water supply from alluvial deposits (Jones and Baker, 2005). Although the onshore and offshore part of the confined aquifers in the Lower Hutt Valley is well constrained, the FSGD into the harbour is still poorly understood.

Here we improve the general understanding of offshore confined aquifer systems by investigating the spatial and temporal characteristics of FSGD from a well-defined and spatially constrained aquifer system offshore Wellington, New Zealand (Figure 1). We focus on naturally occurring groundwater seepage sites within Wellington Harbour and aim to: 1) use a combination of hydroacoustic and towfish data for rapid mapping of FSGD; 2) characterise the spatial distribution of FSGD; 3) evaluate influences of FSGD on seafloor morphology; and 4) develop a conceptual model of the aquifer and FSGD system.

2 Study site

The Lower Hutt Valley evolved as a result of movement along the Wellington Fault. Sediments in the basin accumulated to thicknesses of a few meters in the north near Taita Gorge, and to over 600 m in the harbour, since the middle to late Quaternary period (Jones and Baker, 2005). The sediments are confined in the east by the Wellington Fault and onlap toward the west on the basement rock. They mainly consist of gravel, sands and silts sourced from the southern Tararua Range and deposited by the Hutt River. These alluvial sediments are interbedded with fine-grained marine sediments that were deposited within the last 350 ka during eustatic sea-level high stands (Mildenhall, 1994). While the alluvial gravel deposits form the high-yielding aquifers of the region, the repeated marine sequences act as aquicludes and confining units. The first bore discovering the artesian waters in the Lower Hutt valley was drilled in 1883 (Hughes and Morgan, 2001). Since then, the artesian aquifer has been intensively investigated and today supplies the majority of Lower Hutt and Wellingtons potable water. The aquifers remain unconfined in the higher elevated regions in the north of the Hutt Valley (north of Kennedy Good Bridge) and become confined in the southwest

(Figures 1, 2). Recharge occurs predominantly by the Hutt River in the unconfined parts, while rainfall recharge comprises a minor component (Donaldson and Campbell, 1977).

Two main confined aquifer systems extend down the Valley: the Waiwhetu and Moera gravels, which are separated by the low permeable marine Wilford Shell Beds (Figure 2). The Waiwhetu aquifer is further sub-divided by a continuous fine-grained layer into upper and lower units. The Upper Waiwhetu is the primary aquifer, with transmissivity values up to 25000 m²/day, while the Moera and Lower Waiwhetu are less productive (Brown and Jones, 2000; Jones and Baker, 2005). The aquifers extend offshore beneath the Wellington Harbour and are thought to extend southward as far as the harbour entrance at Flacon Shoals (Stevens, 1974). In the northeast of the harbour, a horst structure subaerially exposes the basement rock, forming Matiu/Somes Island. The Waiwhetu aquifer forms around this island and is confined at the top by the

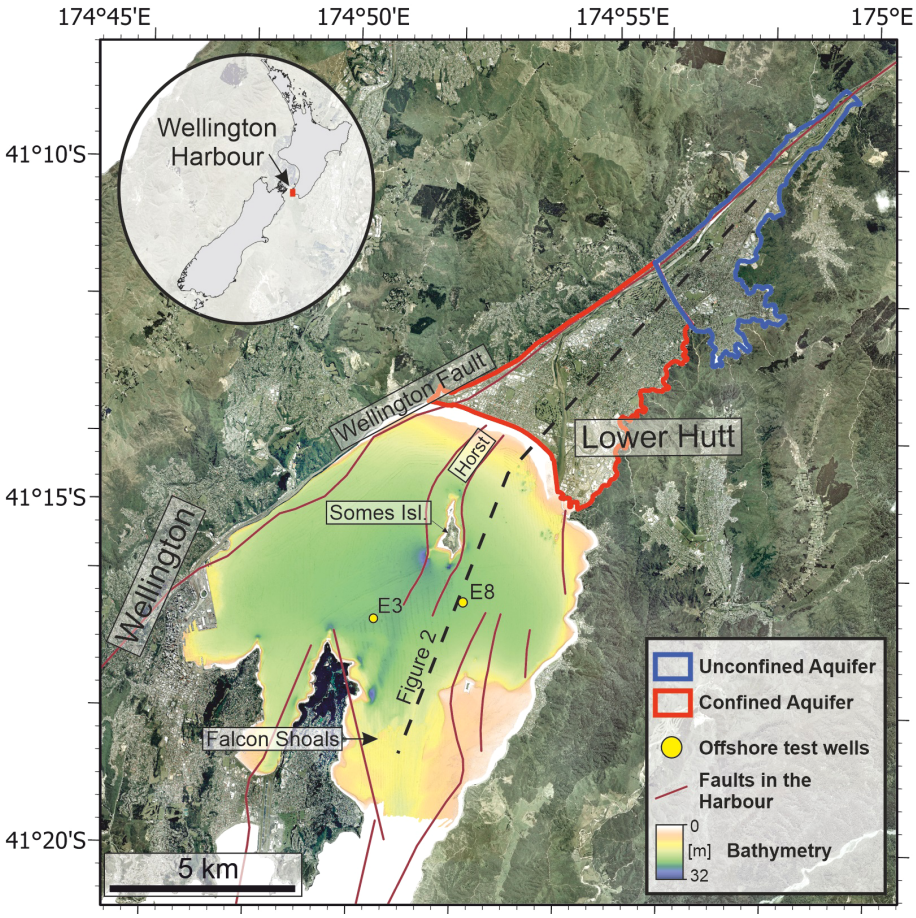

FIGURE 1
Bathymetry of the Wellington Harbour with the Lower Hutt aquifer system and groundwater test wells.

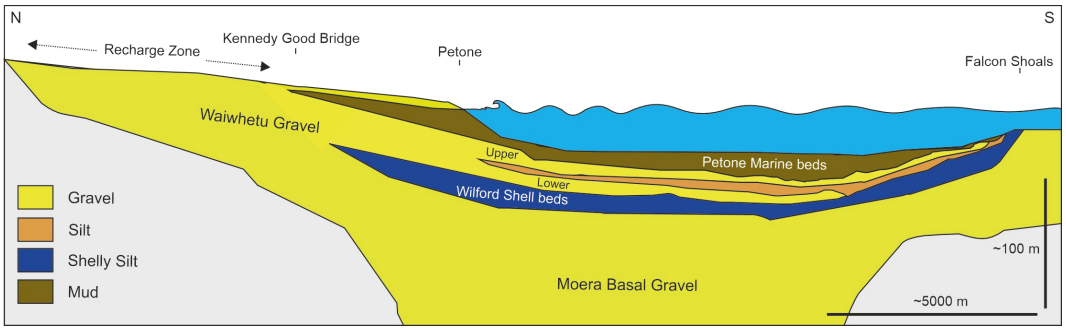

FIGURE 2
Conceptual cross section through the harbour based on well and seismic interpretations from Stevens (1974); Donaldson and Campbell (1977); Wood and Davy (1992); Brown and Jones (2000), and Gyopari et al. (2018).

Petone Marine Beds, which form the upper aquiclude and present-day seafloor in the Wellington Harbour.

Acoustic blanking, likely associated to shallow free gas within the sediment, occurs extensively in the harbour, especially in water depths greater than 18 m (Lewis and Mildenhall, 1985; Nodder et al., 2018; Barnes et al., 2019). The gas is thought to be of microbial origin forming due to the decomposition of the organic rich mud (Barnes et al., 2019). The gas mainly occurs in the north, south and west of Somes Island, while no blanking is observed in the east (Nodder et al., 2018). Seafloor depressions, so called pockmarks, were previously identified in single beam echosounder data and described by Harding (2000). Pockmarks generally form due to fluid seepage (e.g. gas or groundwater) from the seafloor (Judd and Hovland, 2009). These features are abundant around New Zealand (mostly in deeper waters on the continental slopes), but often their origin remains unknown (Davy et al., 2010; Greinert et al., 2010; Hillman et al., 2015; Hoffmann et al., 2019; Stott et al., 2019; Maier et al., 2021; Micallef et al., 2022).

Two offshore wells E3 and E8 were drilled into the harbour aquifers with depths below the seafloor of 79.3 m and 71.15 m respectively (Gyopari et al., 2018)(Figure 1). The aim was to explore the use of offshore freshwater as a supply for drinking water and thereby improving the resilience of Wellingtons water supply to natural hazards such as a rupture of the Wellington Fault and associated rupture of water pipelines (Rowan and Pipe, 2019). This pioneering work was the first attempt worldwide to use OFG as a source for significant drinking water supply. The required treatment (to reduce elevated arsenic, iron and manganese concentrations) of the offshore groundwater to meet drinking water standards meant the resource is likely not economically viable (Rowan and Pipe, 2019). Isotopic analysis of wells on Somes Island indicate residence times of 18-20 years in the Upper Waiwhetu aquifer, while groundwater from the E3 and E8 bores (Figure 1) have an average age of at least 100 years (Rowan and Pipe, 2019). This shows how flow velocities within the offshore component of the harbour decrease with distance from land.

3 Methods

3.1 Multibeam echosounder

Two different multibeam echosounder (MBES) datasets, covering two different time periods, were used within this study to examine morphological changes over time. The first dataset was acquired in 2009 by Pallentin et al. (2009). The data were acquired using a 300 kHz Kongsberg EM3000 and processed at 1 m resolution to create a bathymetric grid of the Wellington Harbour seafloor. The second dataset was acquired on the RV *Ikatere* during cruise IKA2011 in 2020. A Kongsberg EM2040 was deployed through RV *Ikatere's* moonpool and operated at a constant frequency of 300 kHz. The EM2040 was motion compensated and calibrated over a ship wreck (South Seas). Sound velocity profiles of the water column were collected using an AML Base X2 sound velocity probe to correct the bathymetric and water column data. The 2020 dataset resurveyed pockmarks around the Petone foreshore and Somes Island (Figure 3).

Both datasets were postprocessed and visualized using QPS Qimera, FMMidwater and FMGeocoder. Although tide gauges within the harbour were made available and all bathymetry data were tide-corrected, vertical inaccuracies and differences in vessel configurations make an exact vertical comparison between the datasets difficult. Therefore, only morphological changes were considered for the comparison of the two datasets.

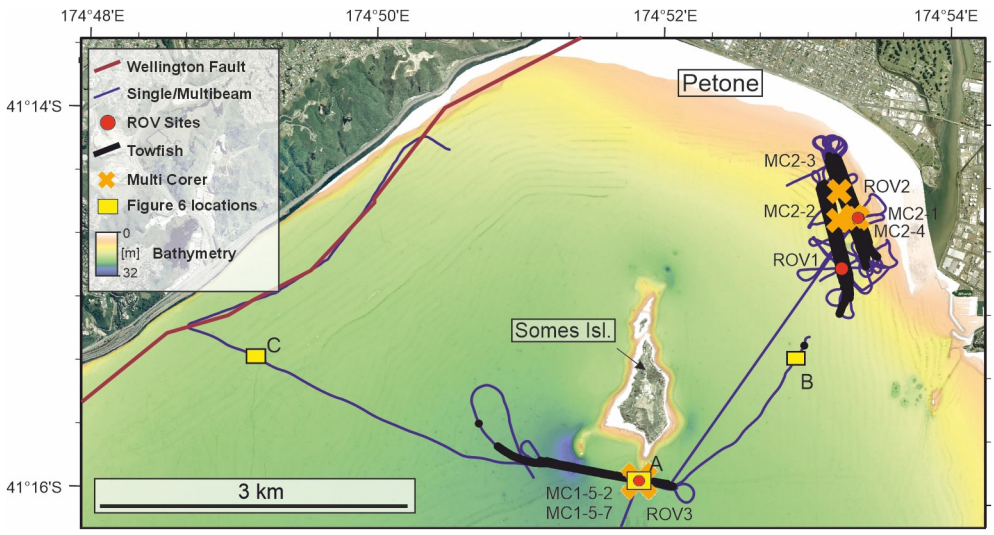

FIGURE 3
Locations and areas investigated during IKA2011 cruise with sediment cores, ROV dives, towfish transects, acoustic data coverage and locations of Figure 6.

3.2 Single beam echosounder

Two individual Kongsberg Simrad EK80 fisheries echosounders were operated in chirp mode. The two sounders simultaneously emitted wideband frequency sweep signals of 55-90 kHz (70 kHz primary frequency) and 90-170 kHz (120 kHz primary frequency) respectively. This setup allowed us to determine the wideband frequency response of specific targets in the water column. The sounders were calibrated for target strength prior to the survey using a calibrated sphere and the data were analysed using ESP3 software (Ladroit et al., 2020).

3.3 Towfish

"BIO-FISH" (ADM Elektronik) is a towed multi-parameter system which measured pressure, temperature, conductivity (salinity), and turbidity of the water column at a 1 Hz interval while underway. The depth of the towfish is manually controlled using a joystick to adjust the control fins (wings), with the aim of "flying" the instrument in transects about 1 m above the seafloor. An acoustic transducer, mounted to the vessel transom, provided an upcoming seafloor morphology trace to allow for fine scale adjustments in towfish depth with changes in bathymetry. Towfish transects were measured in conjunction with single and MBES transects to provide comparative temperature, salinity, and turbidity observations with hydroacoustic data.

3.4 Sediment cores

We collected 8 sediment cores in different regions of the harbour using a multi- and gravity-corer. Sediment recovery ranged between 17 and 80 cm (Figures 3–5). In the muddy deeper regions within the harbour, a multi corer provided good core recoveries, ranging between 17 and 53 cm, while a gravity corer, with 1.5 m long barrels, was necessary to extract sediment cores in the shelly and hard seafloor habitats around the harbour entrance at Falcon Shoals. We used Rhizon samplers with a diameter of 2.5 mm (Rhizosphere Research Products) to extract porewaters from all collected cores. Intervals for porewater extraction increased with depth of the core from 2 cm at the top to 8 cm at the bottom. The Rhizon samplers were inserted into predrilled holes in the core tubes (2 cm interval), which were sealed off with adhesive tape prior to subsampling. We used Rhizon Samplers CSS, 5 cm porous, 12 cm tubing, female luer with male luer 10 ml syringes and wood bricks to hold syringes open. The samples were filtered through Sartorius minisart syringe filters (45 µm) and subsequently analysed by a Dionex ICS 2000 ion chromatograph. Due to insufficient sample yield through the Rhizons and resulting measuring issues, 4% of the analysed samples showed unrealistically high salinity values of up to 125 PSU. These samples were excluded from Figure 5. All measured samples including the erroneous data are provided in the Supplementary Figure 1.

3.5 Remotely operated vehicle

To further investigate the nature of the seafloor and the occurrence of FSGD, we used a small remotely operated vehicle (ROV), which delivered uncompressed 4K video in real-time via a fibre-optic tether. The Boxfish™ (Boxfish Research Ltd) ROV was equipped with a Sony© RX100V camera, high-powered LED lighting and four parallel scaling lasers. In the sheltered harbour with comparatively little currents, the ROV was easily deployed and recovered by hand. We equipped the ROV with a RBRconcerto³, measuring conductivity, temperature, depth, and turbidity. In total the ROV was deployed four times in different locations (Figure 3). During initial exploratory dives, only video was recorded, however, upon finding visible evidence for FSGD, the CTD was attached to the ROV for close inspection of FSGD characteristics at two sites ROV3 and ROV4. While no USBL positioning system was used in this study, the shallow depths and position holding of the research vessel allowed the ROV to navigate to the pockmarks identified by MBES.

4 Results

4.1 Geomorphology of the Wellington Harbour

The Wellington Harbour seafloor is dominated by Holocene mud, the Petone marine beds. Circular to complex seafloor depressions, or pockmarks, occur throughout the harbour basin, varying in size from 3 m up to 500 m in diameter. Morphologies were highly diverse ranging from perfectly circular to halfmoon shaped and other irregular forms. We separate the pockmarks into three classes depending on their morphological expression, size, and location within the harbour (Figure 4).

Class 1 pockmarks are characterised by complex morphologies caused by the coalescence of individual depressions and extend over a region of about 0.3 km^2. These are located in the northeast of the harbour, approximately 1 km from the coast, in water depths between 7 m and 14 m. They occur on a seafloor slope of approximately 1°, from the shallow shore into the deeper part of the harbour. Within the intermingled pockmarks, that are about 100 m wide individually, smaller depressions of about 5 to 20 m form in their centre and on their sides. They are often asymmetric, with the eastern landward side of the pockmark being much steeper compared to the western downslope side.

Class 2 pockmarks are the largest within the harbour and located on the edges of Somes Island. The pockmarks wrap around the hard, outcropping triangular basement rock and especially in the south of the island form halfmoon shaped depressions (Figure 4). The pockmarks are up to 500 m in diameter and are up to 10 m deep compared to the surrounding seafloor. These pockmarks form the deepest part of the harbour at 32 m. Similar to Class 1 pockmarks, smaller depressions form in the centre and on their slopes. While the pockmarks on the southwestern side and in the north show outcropping rocks in

10.3389/fmars.2023.1204182

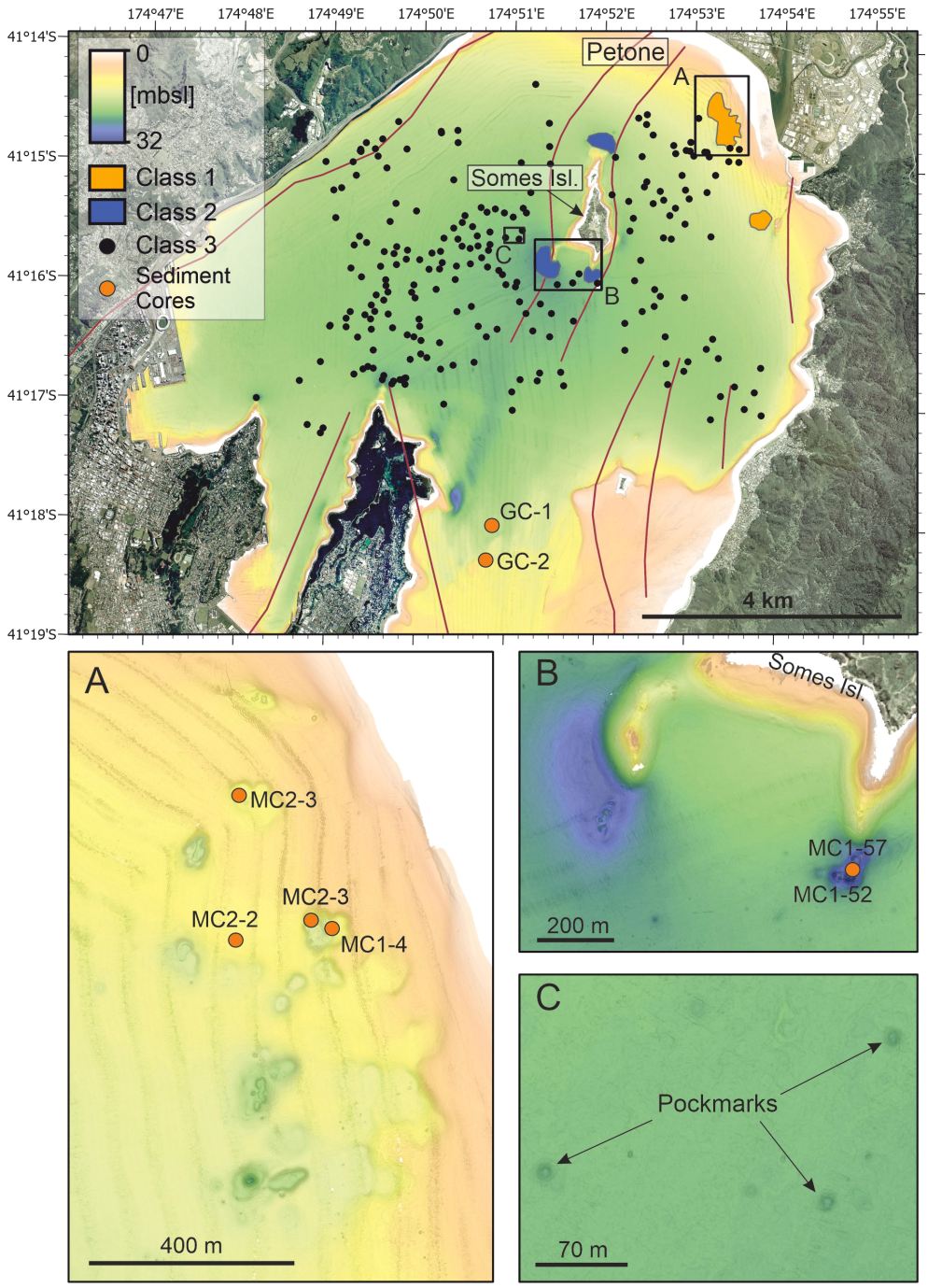

FIGURE 4
Overview of pockmark locations and classifications [Class 1 – **(A)**, Class 2 – **(B)**, Class 3 – **(C)**] in the Wellington Harbour with the distribution of sediment cores shown in Figure 5C.

their centre, the southeastern pockmark (Figure 6A) has no elevated objects in its centre.

Pockmarks of Class 3 are the smallest and most abundant features and are distributed throughout the deeper parts of the harbour floor in water depth between 10 m and 22 m. They range in size from 3 to 25 m. The pockmarks are characterised by perfectly circular shapes with depth of 0.5 m to 1 m compared to the surrounding seafloor.

We also observe various scours in the sediment caused by anchors and their associated chains in the western part of the Wellington Harbour (Watson et al., 2022). These scours show incision depths of around 60-70 cm into the sediment and reach lengths of over 1.5 km. We find linear scours associated with anchor emplacement or recovery as well as zones of abrasion, which are attributed to the anchor chain and the swinging of the vessel while on anchor.

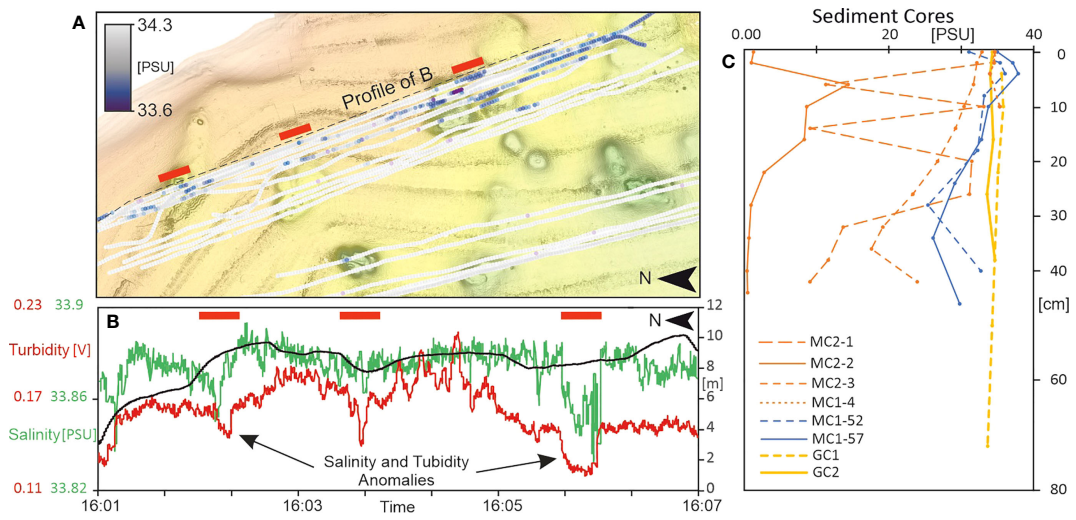

FIGURE 5
Salinity distribution within and around Class 1 pockmarks (Figure 4A). **(A)** Bathymetric features with overlaid towfish salinity transects (grey high and blue lower salinities). **(B)** Towfish transect across the pockmarks showing several salinity and turbidity anomalies indicated by red bars. **(C)** Sediment cores show a general decrease of salinity with depth within as well as outside (MC2-2) of the pockmarks (locations in Figure 4).

A comparison of the data acquired in 2009 and the 2020 shows that the pockmark locations and morphologies remain unchanged over time. In contrast, most of the observed anchor scours in the 2009 bathymetric dataset either completely vanished or were significantly diminished in the newly acquired data. Multiple new scours were observed in the 2020 dataset in the same region, but the remains of previous scours and zones of abrasion have largely disappeared (Figure 6). The new scours show similar characteristics to the previously observed ones with incision depth of about 60 cm compared to the surrounding seafloor.

4.2 Salinity and turbidity

The salinity distribution in the water column and the sediments of the harbour were investigated using the towfish and sediment porewater samples. The towfish captured strong vertical salinity gradients in the water column, with lower saline waters in the upper (about 31 - 33.6 PSU) and higher salinity waters in the deeper part (about 34 -34.3 PSU). This is the result of low-density freshwater inputs from the Hutt River discharges that freshen the upper water column while denser higher saline ocean waters flow in at the bottom through the harbour entrance (Gall and Davies-Colley, 2021).

Keeping the towfish at a constant height (1 m) above the seafloor, we were able to investigate the lateral spatial salinity distribution rather than vertical profiles. Using this technique, we were able to cover large areas and detect several salinity anomalies in the bottom waters that do not correspond to the vertical salinity gradient. Around the northern Class 1 pockmarks, salinity decreases in several locations associated with low turbidity values (Figure 5B). Groundwater is generally well-filtered by the sediments of the aquifer and is likely to be less turbid compared to the surrounding seawater (Karpen et al., 2004). It is apparent, that low turbidity and salinity values do not always coincide with pockmarks on the seafloor, but also occur in the relatively flat areas between the pockmarks. This is supported by sediment core MC2-2, which was acquired in the space between individual pockmarks (Figures 4, 5) and shows the lowest salinities of all cores. Salinity within Class 2 pockmarks, south of Somes Island, decrease from 34.15 PSU outside of the pockmarks near the seafloor to about 33.9 PSU within the pockmark. Porewaters within the cores from these pockmarks show a distinct decrease from 35 PSU at the sediment-water interface down to about 24 PSU at about 30 cm depth (MC1, Figure 5).

4.3 Water column reflectivity

We used the two EK60 fisheries echosounders to investigate the water column reflectivity across the harbour. We identified several vertical strong reflectivity anomalies that are generally indicative of gas escape (gas flares, Supplementary Figure 2A). Isolated smaller non-vertical high reflectance anomalies generally correspond to the presence of fish (Figure 7). Although gas escape is apparent within the pockmarks, high reflectance anomalies, indicative of gas, are also found in other areas of the harbour. We could not find a direct correlation between gas escape features from the seafloor and the pockmarks.

In addition to the high energy backscatter from gas and fish, we also find enhanced, hazy reflectivity within and above pockmarks (Figure 7, Supplementary Figures 2B, C). Reflection strengths of these features are small compared to the gas bubbles and fish, and the reflections are less localized but distributed over larger areas. They generally occur closer to the seafloor and only rise up 5 to 10 m above the seafloor into the water column. Within the Category 2 pockmarks (shown in Figure 7) the hazy reflections fill out the entire pockmark and extend well above the surrounding flat

seafloor. In Category 1 pockmarks we find more localised regions within individual pockmarks that show hazy reflections in the centre or on the side of the depressions (Supplementary Figure 2B). Turbidity values measured by the ROV during its descent down into the Category 2 pockmark show a sharp increase in turbidity where the hazy reflections start. The increase in turbidity in the Category 2 pockmark correspond to an increase in salinity that follows the general trend in the harbour where salinities increase with depth in the harbour.

4.4 Visual inspection of FSGD

We used a Boxfish ROV to visually inspect the seafloor within the pockmarks. In numerous locations, we were able to visually identify blurry zones (so called 'schlieren') where groundwater was seeping from the seafloor and changes the refractive index (Figure 8). The CTD readings of the ROV confirm the freshwater seepage that we visually inspected (Figure 8). Rather than a confined single spring on the seafloor we find that many small individual

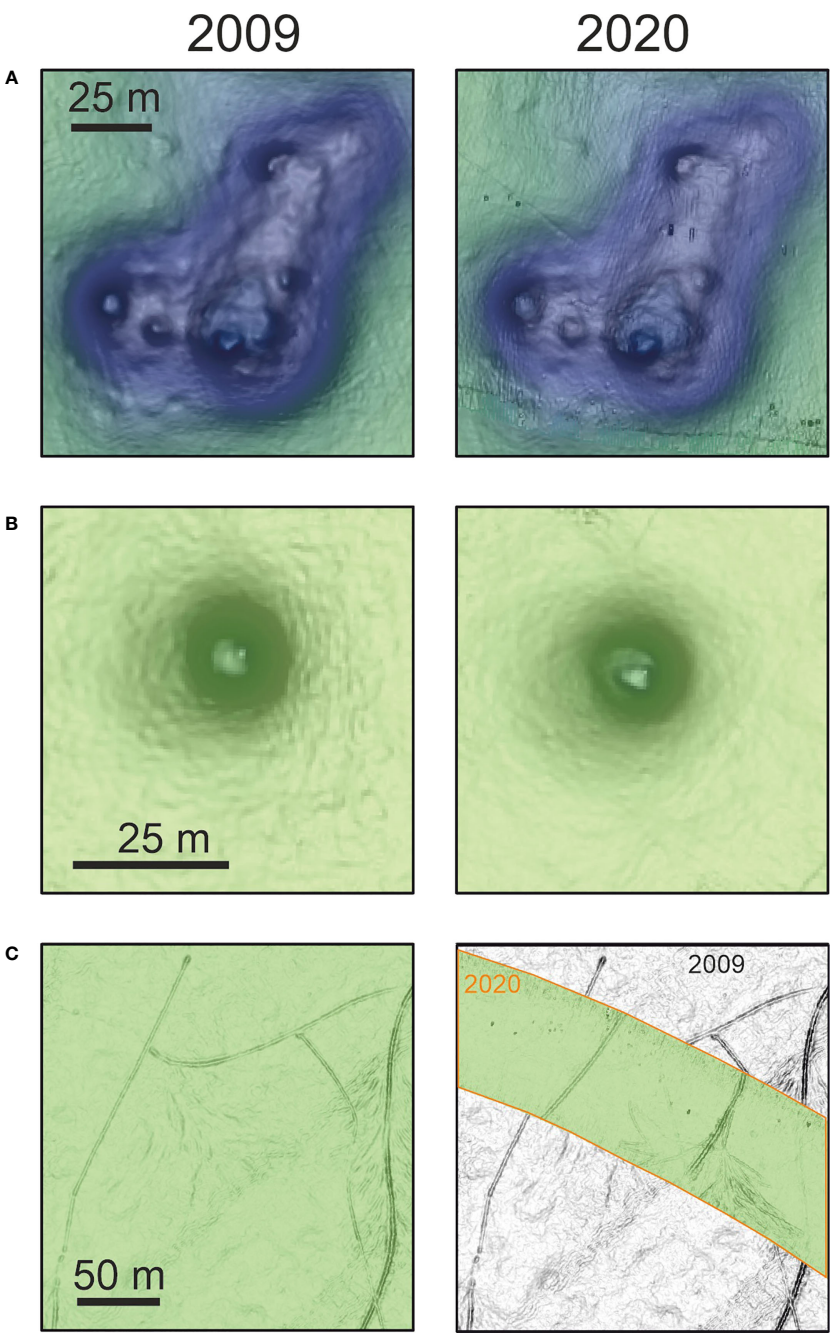

FIGURE 6
Comparison of bathymetric surveys conducted in 2009 and 2020. While the pockmarks show no or only minor changes in morphology **(A, B)**, anchor scours **(C)** disappear over time (orange inner region shows new data overlain on top of the grey scaled slope data from 2009). Locations are shown in Figure 3.

10.3389/fmars.2023.1204182

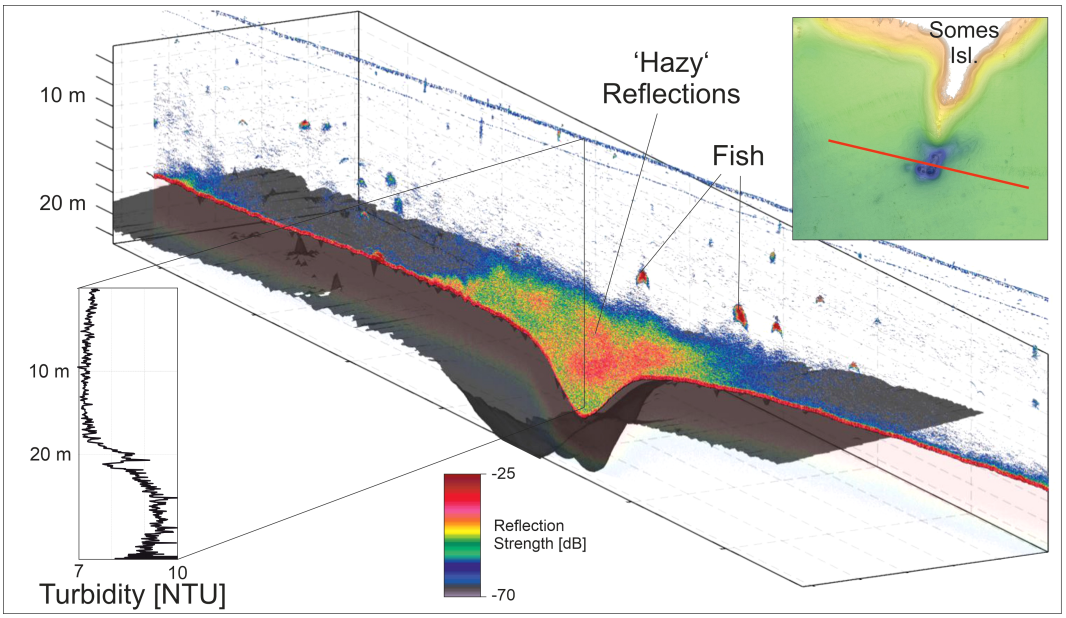

FIGURE 7
Profile over a Class 2 pockmark shows hazy reflectivity in the water column above the depression corresponding to high turbidity values measured with the ROV during the descent to the bottom.

discharge sites exist within each pockmark. Salinities in the water column at about 50 cm above the seafloor seeps decrease to 32.5 PSU from the surrounding 34.4 PSU. The water temperature within the pockmark remains approximately the same around 14.8°C. The lack of seepage meters prevented a quantification of discharge at specific locations. Therefore, discharge was only qualitatively examined, with the amount of blurred zone observed in the videos giving us the best indication of large or low discharge rates. We find that the Class 2 pockmarks on the south-eastern end of Somes Island experiences many zones of groundwater discharge. Based on the visual data, we find that seepage in all pockmark classes inspected does not occur preferentially from the deepest part of the pockmarks but rather from many small discrete locations situated on the sidewalls as well as in the central parts. No visual discharges were observed in the region around Falcon Shoals.

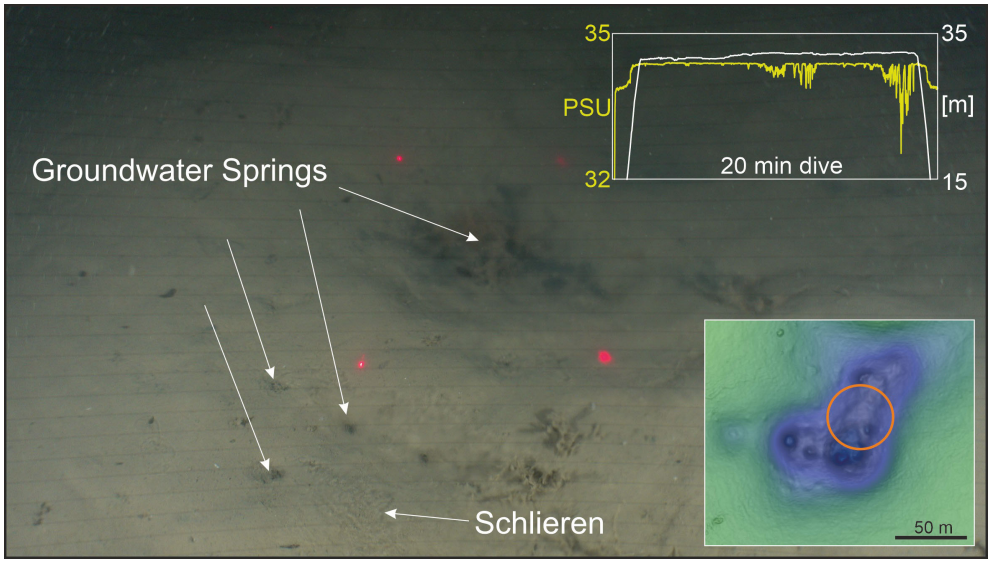

FIGURE 8
Photo of schlieren in the seawater where groundwater discharges from the seafloor at the Class 2 pockmark south of Somes Island (location of ROV3 in Figure 3). Salinities drop from over 34 to nearly 32 PSU at about 50 cm above the seafloor.

5 Discussion

5.1 Pockmark formation mechanisms

Pockmarks on the seafloor are frequently attributed to fluid venting, however their formation mechanism or the fluid involved in the venting often remains unknown (Paull et al., 2002; Judd and Hovland, 2009). In Wellington Harbour, our results show the three classes of pockmarks identified have distinct distributions. Class 1 and 2 pockmarks show freshwater seepage, as determined from sediment cores, salinity readings in the water column and, ROV video footage. We do not have any data to confirm if Class 3 pockmarks are associated with freshwater seepage. We infer that the formation of Class 1 and 2 pockmarks is mainly associated with FSGD weakening the surface sediments and localising erosion by bottom currents. Although we associate both classes to the same process, significant geomorphological differences exist related to the environment in which they have formed. Class 1 pockmarks occur nearest to the foreshore and therefore where aquifer pressure is potentially higher. They formed within shallow harbour sediments near the shore, which are likely to be more spatially heterogeneous than deep water sediments thereby potentially influencing pockmark geometry, leading to intermingled pockmarks. In contrast, Class 2 pockmarks occur on the edges of Somes Island where the aquifer onlaps against basement rock, resulting in a more halfmoon shaped pockmark geometry wrapping around the tips of the island. We interpret that groundwater migrates upwards along the sediment-rock interface and that tidal current speeds are exacerbated around the island headlands, enhancing scouring and thereby enlarging the Class 2 pockmarks.

Class 3 pockmarks are much smaller and more widely distributed within the bay and were not directly sampled due to positioning inaccuracies of the vessel and the deployed gear in the water. Hydroacoustic water column reflectivity data suggest not only groundwater, but also gas seepage in the harbour. We could not associate any of the pockmark classes directly to gas seepage, which appears to occur not only from the pockmarks but also in other areas of the harbour. Albert et al. (1998) and Hoffmann et al. (2020) show that upward migrating groundwater within the sediment can enhance gas concentrations close to the seafloor by shifting the sulfate methane transition zone upwards. This can lead to gas saturation of the porewater and free gas in the pore spaces, which induce additional sediment instabilities and subsequent sediment erosion. While the Class 3 pockmarks extend throughout the harbour, seismic data interpreted by Nodder et al. (2018) show that acoustic blanking associated to shallow gas occurs primarily in the west of the harbour and is absent to the east of Somes Island. Wood and Davy (1992) suggest a thickening of the Waiwhetu aquifer towards the Wellington Fault which suggests that freshwater likely occurs in most regions of the harbour. Since Class 3 pockmarks are widely distributed throughout the harbour and also occur to the west of Somes Island, where no acoustic blanking is observed, it seems likely that freshwater is the main driving factor for these pockmarks as well. SGD might not only shift the sulfate methane transition zone closer to the seafloor, but additionally enhance upward migration of dissolved methane in the groundwater. This may locally increase methane concentrations close to the seafloor to levels exceeding the saturation without causing widespread acoustic blanking. We therefore cannot attribute a specific fluid to the formation process of Class 3 pockmarks but distributed freshwater expulsion is a plausible factor in their genesis.

5.2 Extent of freshwater seepage

Assuming that all three classes of pockmarks are associated with FSGD, our results suggest that the areal extent of FSGD is much larger than previously thought. The southern extent of the aquifers is still under debate. The two gravity cores we acquired at the harbour entrance around Falcon shoals consisted mainly of unconsolidated shell fragments with high permeabilities. Stevens (1974) suggests that the Waiwhetu aquifer extends approximately down to this point, where the confining Petone Marine Beds and gravel beds run out. Strong tidal currents around the harbour entrance prevent smaller sediment particles from accumulating at the bottom in this area. Within the coarse-grained sediments no morphological indications for freshwater seepage, such as pockmarks, occur. Porewater samples from the two gravity cores acquired in this region show only a minor decrease of salinity with depth. This may result from high permeabilities of the shells, where mixing of upward migrating freshwater and seawater from above occurs deeper within the sbusurface. The best evidence for leakage from the Waiwhetu Aquifer at Falcon Shoals is still the measurements made by Harding (2000). Groundwater expulsion in the harbour, and associated loss of freshwater, results in a decreasing hydraulic head in the aquifer towards the harbour entrance. Although our indications for FSGD are limited, we assume that the remaining water pressure at Falcon Shoals is generally still high enough to push the water up to the seabed.

5.3 Persistence of seafloor disturbances

The persistence of seafloor irregularities and disturbances depends on many factors, but mainly the hydrodynamic system (Bruns et al., 2020; Hoffmann et al., 2022), sedimentation rates (Gilkinson et al., 2015) and sediment type (Roberts et al., 2000; Mérillet et al., 2018). While the morphological expression of anchor scours or trawl marks in exposed shallow regions generally disappears within several months, these disturbances can persist over decades in fine-grained sheltered regions (Bruns et al., 2020). In the western part of Wellington Harbour towards the port area, anchor scours were previously described by Watson et al. (2022). We found that most of the morphology of the described scours on the muddy seafloor of Wellington Harbour had vanished within a decade, or were barely visible in the newly acquired dataset compared to 2009. In contrast to the anchor scours, we find that pockmarks in the harbour did not significantly change over the observed time period of 11 years. Even Class 3 pockmarks with similar incision depth to the trawl marks remain unchanged over

time. Since the pockmarks and anchor scours occur in close proximity to one another and therefore in the same hydrodynamic and sedimentary environment, we infer that the longevity of the pockmarks compared to the anchor scours results from ongoing fluid seepage. Gas and groundwater seepage into the harbour seem to continuously occur through the same pathways and prevent the pockmarks from being infilled by sediment. It seems likely that upward migrating groundwater and gases influence settling particles and keep them buoyant in the water column rather than settling down in the pockmarks.

5.4 Water column reflectivity as an indirect indicator for FSGD

Hydroacoustic water column imaging is widely used to investigate marine biology, such as fish or plankton, to locate marine gas seeps, and to measure sediment particle distribution in the water column (Reine et al., 2002; Simmonds and MacLennan, 2008; Schneider von Deimling et al., 2013). Gas bubbles show a characteristic narrow and sub-vertical acoustic signature also called 'flare'. The acoustic response of fish is generally less vertically aligned and often more isolated and distributed throughout the water column without a connection to the seabed. Since acoustic reflections associated with fish mainly result from the fish's air bladder they have similar reflection strength to gas bubbles. In contrast, sediment particles have a smaller impedance contrast to the surrounding water than gas and therefor result in lower reflected energies. Multiple gas flares were identified within the harbour but not always related to pockmarks on the seafloor. We characterised the water column reflectivity within the Wellington Harbour, observing fish schools and free gas bubbles escaping the gaseous sediments, along with wider areas of enhanced 'hazy' reflections within and above pockmarks. These reflections appeared most pronounced in the Class 2 pockmarks of Somes Island (Figure 7). The ROV video observations indicated the highest abundance of groundwater discharge sites within these pockmarks. The enhanced hazy reflectivity within the pockmarks can be clearly distinguished from gas flares and fish by their reflection strength, distribution, and characteristics. The turbidity sensor mounted on the ROV suggests that these enhanced reflections are caused by suspended sediment particles in the water column within and above the pockmark. Generally, groundwater shows relatively low turbidity values compared to surface waters as it is naturally filtered during percolation through the soil. This is also observed by the towfish data, where we find much lower turbidity values compared to the surrounding ocean water, in the water column directly above FSGD sites (Figure 5). Therefore, it seems unlikely that the high turbidity values are caused by an enhanced sediment load of the discharging groundwater. Sediment resuspension from the seafloor by upward migrating freshwater similarly seems unlikely since the turbidity directly above the seep sites was low during our field measurements. Although not directly observed during our campaign, high discharge events might still locally resuspend sediments from the seafloor.

Several other mechanisms might play a role in the elevated sediment load in the water column within and above the pockmarks. The Hutt River is the primary source of sediment accumulating in the Wellington Harbour and observed discoloured freshwater movements at the water surface within the harbour suggest that parts of the sediments are supplied in suspension (van der Linden, 1967). This suspended matter will slowly settle in the deeper parts of the harbour to form the present-day silty mud. The depressions in the seafloor

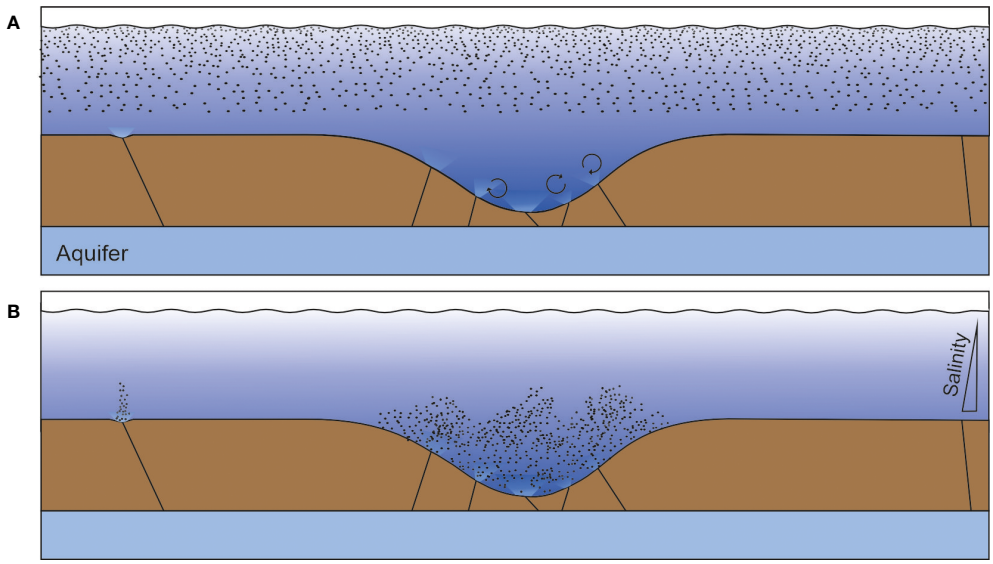

FIGURE 9
Conceptual model of FSGD and increased turbidity above pockmark sites. **(A)** Particle settling after sediment was supplied by a river plume. **(B)** Particles settle uniformly outside of the pockmarks but are kept in suspension by enhanced turbulence within the depressions induced by freshwater input and current interactions.

themselves likely act as sinks for small particles during calm weather periods where particulate matter can accumulate. The stratification of the water column, with an increased salinity with depth, will also affect the vertical particle distribution where particles tend to settle on boundary layers (MacIntyre et al., 1995; Prairie et al., 2015). These mechanisms could partly explain elevated turbidity especially within the Category 2 pockmarks but do not account for the more localised and flare like enhanced particle concentrations above and within the Category 1 pockmarks (Supplementary Figure 2). Pau et al. (2014) show how the interaction of bottom currents with the pockmark geometry can result in enhanced water turbulence in the depressions. We assume that the particles that should uniformly settle to the seafloor are kept in suspension and are prevented from settling by discharging and upward migrating freshwater that further enhances the turbulence in the water column (Figure 9). Although the general increase in salinity with depth is also apparent through the pockmarks and the discharging freshwater is quickly mixed and diluted by the seawater, the hydrodynamic impulse and related turbulence of the water column could reach much further than the salinity anomalies. It seems likely that the particles are kept in suspension by this enhanced turbulence within pockmarks and are subsequently transported away by currents during the next storm event. This is supported by the persistence and unchanged morphological expression of the pockmarks. The sediment plumes might therefore give indirect indications for isolated groundwater seepage sites.

6 Conclusions

In this study we employed a multidisciplinary approach to investigate FSGD into Wellington Harbour, providing geochemical, geomorphological, and geophysical evidence for widespread discharge locations connected to an offshore aquifer system that is recharged from land. As the onshore groundwater system, as well as its offshore component and discharge, is an important resource to Wellington City, our approach and data provide further monitoring options and an improved understanding that can assist proper management of this valuable resource.

Three different classes of pockmarks, likely related to groundwater discharge, are evident in the harbour. The upward migrating groundwater might locally enhance gas concentrations close to the seafloor and thereby trigger gas escape into the water column especially from Class 3 pockmarks. Although it appears like the seafloor morphology would be the most indicative parameter to determine discharge locations, towfish and sediment core porewater samples show that FSGD also occurs in proximity to but outside of pockmarks, potentially indicating newly developing spring sites. ROV dives within the pockmarks show that the groundwater discharge is not solely occurring from one location at the bottom of the depressions but from many individual small sites that are distributed throughout the depression; this points to many small rather than one large fluid conduit in the subsurface. In a comparison with previous surveys (11 years apart), the pockmarks did not seem to change considerably, although anchor scours in the same region diminished or disappeared. This shows that fluid flow persistently occurs through the same conduits, permitting sediments to accumulate. We assume that in these regions the rising freshwater induces turbulence and stirs up the water column which prevent sediment particles from settling. These particles are identified in hydroacoustic data as a plume of sediment above the pockmarks, which in turn can indicate FSGD.

Data availability statement

The raw data supporting the conclusions of this article will be made available by the authors, without undue reservation.

Author contributions

JH and JM contributed to the conception and design of the study. JH, MG, ES, YL and LT contributed to data acquisition in the field and subsequent analysis. JH wrote the first draft of the manuscript and JM, MG, ES, LT and AM contributed sections to the manuscript. All authors contributed to the article and approved the submitted version.

Funding

Funding for this work has been provided by the New Zealand Ministry of Business, Innovation and Employment (MBIE) through the Strategic Science Investment Fund (SSIF) administered by NIWA's Oceans Centre. This research was also supported by the Marie Curie action KARST, under the EU H2020 program, project number 101027303 and from CA21112 - Offshore freshened groundwater: An unconventional water resource in coastal regions? – OFF-SOURCE", supported by COST (European Cooperation in Science and Technology).

Acknowledgments

We are grateful to the skipper and crew of RV Ikatere for managing the vessel during the survey. We thank Steven Harding for interesting discussions about his unpublished Master's Thesis work. Wellington Water Ltd. are thanked for discussion and provision of data and reports. I acknowledge support by the Open Access Publication Funds of Alfred-Wegener-Institut Helmholtz-Zentrum für Polar- und Meeresforschung.

Conflict of interest

The authors declare that the research was conducted in the absence of any commercial or financial relationships that could be construed as a potential conflict of interest.

Publisher's note

All claims expressed in this article are solely those of the authors and do not necessarily represent those of their affiliated organizations, or those of the publisher, the editors and the reviewers. Any product that may be evaluated in this article, or claim that may be made by its manufacturer, is not guaranteed or endorsed by the publisher.

Supplementary material

The Supplementary Material for this article can be found online at: https://www.frontiersin.org/articles/10.3389/fmars.2023.1204182/full#supplementary-material

References

Albert, D. B., Martens, C. S., and Alperin, M. J. (1998). Biogeochemical processes controlling methane in gassy coastal sediments—Part 2: groundwater flow control of acoustic turbidity in Eckernförde Bay Sediments. *Cont. Shelf Res.* 18, 1771–1793. doi: 10.1016/S0278-4343(98)00057-0

Arévalo-Martínez, D. L., Haroon, A., Bange, H. W., Erkul, E., Jegen, M., Moosdorf, N., et al. (2023). Ideas and perspectives: Land–ocean connectivity through groundwater. *Biogeosciences* 20, 647–662. doi: 10.5194/bg-20-647-2023

Barnes, P. M., Nodder, S. D., Woelz, S., and Orpin, A. R. (2019). The structure and seismic potential of the Aotea and Evans Bay faults, Wellington, New Zealand. *New Zeal. J. Geol. Geophys.* 62, 46–71. doi: 10.1080/00288306.2018.1520265

Berndt, C., and Micallef, A. (2019). Could offshore groundwater rescue coastal cities? *Nature* 574, 36. doi: 10.1038/d41586-019-02924-7

Brown, L. J., and Jones, A. (2000). *Moera Gravel Aquifer Investigation Bore* (Wellington Regional Council). Publication No. WRC/RINV-T-00/30, Wellington, New Zealand.

Bruns, I., Holler, P., CapPerucci, R. M., Papenmeier, S., and Bartholomä, A. (2020). Identifying trawl marks in north sea sediments. *Geosci* 10, 1–31. doi: 10.3390/geosciences10110422

Davy, B., Pecher, I. A., Wood, R., Carter, L., and Gohl, K. (2010). Gas escape features off New Zealand: Evidence of massive release of methane from hydrates. *Geophys. Res. Lett.* 37, 1–5. doi: 10.1029/2010GL045184

Donaldson, I. G., and Campbell, D. G. (1977). *Groundwater of the Hutt Valley-Port Nicholson Alluvial Basin - A Resource Evaluation.* (DSIR Infor. Lower Hutt: New Zeland: Department of Scientific and Industrial Research).

Gall, M., and Davies-Colley, R. (2021). A portable underway flow-through sampler for rapid survey of contaminated river plumes in coastal waters. *Limnol. Oceanogr. Methods* 19, 67–80. doi: 10.1002/lom3.10405

Gilkinson, K., King, E. L., Li, M. Z., Roddick, D., Kenchington, E., and Han, G. (2015). Processes of physical change to the seabed and bivalve recruitment over a 10-year period following experimental hydraulic clam dredging on Banquereau, Scotian Shelf. *Cont. Shelf Res.* 92, 72–86. doi: 10.1016/j.csr.2014.11.006

Greinert, J., Lewis, K. B., Bialas, J., Pecher, I. A., Rowden, A., Bowden, D. A., et al. (2010). Methane seepage along the Hikurangi Margin, New Zealand: Overview of studies in 2006 and 2007 and new evidence from visual, bathymetric and hydroacoustic investigations. *Mar. Geol.* 272, 6–25. doi: 10.1016/j.margeo.2010.01.017

Gyopari, M., Grant, K., Begg, J., Nodder, S., Knowling, M., and van der Raaij, R. (2018). *Wellington Harbour Exploration Bores Project - Hydrogeological Analysis of SP1a Exploration Phase: Abstraction Feasibility Assessment & Recommendations* (Wellington, New Zealand: Wellington Water Limited).

Harding, S. J. (2000). *The characteristics of the waiwhetu artesian aquifer beneath wellington harbour including the spatial distribution and causes of submarine spring discharge.* Marster Thesis, Victoria University, Wellington.

Hillman, J. I. T., Gorman, A. R., and Pecher, I. A. (2015). Geostatistical analysis of seafloor depressions on the southeast margin of New Zealand's South Island - Investigating the impact of dynamic near seafloor processes on geomorphology. *Mar. Geol.* 360, 70–83. doi: 10.1016/j.margeo.2014.11.016

Hoffmann, J. J. L., Gorman, A. R., and Crutchley, G. J. (2019). Seismic evidence for repeated vertical fluid flow through polygonally faulted strata in the Canterbury Basin, New Zealand. *Mar. Pet. Geol.* 109, 317–329. doi: 10.1016/j.marpetgeo.2019.06.025

Hoffmann, J. J. L., Michaelis, R., Mielck, F., Bartholomä, A., and Sander, L. (2022). Multiannual seafloor dynamics around a subtidal rocky reef habitat in the north sea. *Remote Sens.* 14. doi: 10.3390/rs14092069

Hoffmann, J. J. L., Schneider von Deimling, J., Schröder, J. F., Schmidt, M., Held, P., Crutchley, G. J., et al. (2020). Complex eyed pockmarks and submarine groundwater discharge revealed by acoustic data and sediment cores in Eckernförde bay, SW Baltic Sea. *Geochem. Geophys. Geosys.* 21. doi: 10.1029/2019GC008825

Hu, C., Muller-Karger, F. E., and Swarzenski, P. W. (2006). Hurricanes, submarine groundwater discharge, and Florida's red tides. *Geophys. Res. Lett.* 33, 1–5. doi: 10.1029/2005GL025449

Hughes, B., and Morgan, M. (2001). "Wellington," in *Groundwaters of New Zealand*. Eds. M. R. Rosen and P. A. White (Wellington: New Zealand Hydrological Society Inc), 397–410.

IPCC and Core Writing Team (2014). *Climate Change 2014: Synthesis Report. Contribution of Working Groups I, II and III to the Fifth Assessment Report of the Intergovernmental Panel on Climate Change.* Eds. R. K. Pachauri and L. A. Meyer (Geneva, Switz.: IPCC), 151.

Jones, A., and Baker, T. (2005). *Groundwater monitoring technical report* (Greater Wellington Regional Council publication). GW/RINV-T-05/86, Wellington, New Zealand

Judd, A. G., and Hovland, M. (2009). *Seabed fluid flow: the impact on geology, biology and the marine environment.* (Cambridge, England: Cambridge University Press).

Karpen, V., Thomsen, L., and Suess, E. (2004). A new 'schlieren' technique application for fluid flow visualization at cold seep sites. *Mar. Geol.* 204, 145–159. doi: 10.1016/S0025-3227(03)00370-0

Knee, K. L., and Paytan, A. (2011). "Submarine Groundwater Discharge: A Source of Nutrients, Metals, and Pollutants to the Coastal Ocean," in *Treatise on Estuarine and Coastal Science* (Elsevier), 205–233. doi: 10.1016/B978-0-12-374711-2.00410-1

Ladroit, Y., Escobar-Flores, P. C., Schimel, A. C. G., and O'Driscoll, R. L. (2020). ESP3: An open-source software for the quantitative processing of hydro-acoustic data. *SoftwareX* 12, 100581. doi: 10.1016/j.softx.2020.100581

Lee, Y.-W., Kim, G., Lim, W.-A., and Hwang, D.-W. (2010). A relationship between submarine groundwater borne nutrients traced by Ra isotopes and the intensity of dinoflagellate red-tides occurring in the southern sea of Korea. *Limnol. Oceanogr.* 55, 1–10. doi: 10.4319/lo.2010.55.1.0001

Lewis, K. B., and Mildenhall, D. C. (1985). The late quaternary seismic, sedimentary and palynological stratigraphy beneath evans bay, wellington harbour. *New Zeal. J. Geol. Geophys.* 28, 129–152. doi: 10.1080/00288306.1985.10422281

Luo, X., and Jiao, J. J. (2016). Submarine groundwater discharge and nutrient loadings in Tolo Harbor, Hong Kong using multiple geotracer-based models, and their implications of red tide outbreaks. *Water Res.* 102, 11–31. doi: 10.1016/j.watres.2016.06.017

MacIntyre, S., Alldredge, A. L., and Gotschalk, C. C. (1995). Accumulation of marines now at density discontinuities in the water column. *Limnol. Oceanogr.* 40, 449–468. doi: 10.4319/lo.1995.40.3.0449

Maier, K., Orpin, A., and Neil, H. (2021). Seafloor pockmarks on the South Westland margin of the South Island/Te Waipounamu, Aotearoa New Zealand. *New Zeal. J. Geol. Geophys.* 66 (1), 42–58. doi: 10.1080/00288306.2021.2011328

Mérillet, L., Méhault, S., Rimaud, T., Piton, C., Morandeau, F., Morfin, M., et al. (2018). Survivability of discarded Norway lobster in the bottom trawl fishery of the Bay of Biscay. *Fish. Res.* 198, 24–30. doi: 10.1016/j.fishres.2017.10.019

Micallef, A., Averes, T., Hoffmann, J., Crutchley, G., Mountjoy, J. J., Person, M., et al. (2022). Multiple drivers and controls of pockmark formation across the Canterbury Margin, New Zealand. *Basin Res.* 34 (4), 1–26. doi: 10.1111/bre.12663

Micallef, A., Person, M., Berndt, C., Bertoni, C., Cohen, D., Dugan, B., et al. (2020a). Offshore freshened groundwater in continental margins. *Rev. Geophys.* 59, 1–54. doi: 10.1029/2020RG000706

Micallef, A., Person, M., Haroon, A., Weymer, B. A., Jegen, M., Schwalenberg, K., et al. (2020b). 3D characterisation and quantification of an offshore freshened groundwater system in the Canterbury Bight. *Nat. Commun.* 11, 1372. doi: 10.1038/s41467-020-14770-7

Mildenhall, D. C. (1994). Palynostratigraphy and paleoenvironments of Wellington, New Zealand, during the last 80 ka, based on palynology of drillholes. *New Zeal. J. Geol. Geophys.* 37, 421–436. doi: 10.1080/00288306.1994.9514631

Moore, W. S. (1996). Large groundwater inputs to coastal waters revealed by 226Ra enrichments. *Nature* 380, 612–614. doi: 10.1038/380612a0

Morgan, L. K., and Mountjoy, J. J. (2022). Likelihood of offshore freshened groundwater in New Zealand. *Hydrogeol. J.* 30, 2013–2026. doi: 10.1007/s10040-022-02525-1

Neumann, B., Vafeidis, A. T., Zimmermann, J., and Nicholls, R. J. (2015). Future coastal population growth and exposure to sea-level rise and coastal flooding - A global assessment. *PloS One* 10. doi: 10.1371/journal.pone.0118571

Nodder, S., Begg, J., Gyopari, M., Woelz, S., Lamarche, G., and Gerring, P. (2018). *Geological and geophysical summary, Te Whanganui a Tara/Wellington Harbour - Development of the Geological Model for hydrogeological investigations*, NIWA Client Report prepared for Stantec MWH/Wellington Water Ltd (March 2018). NIWA Client Report 201841WN. Wellington: National Institute of Water and Atmospheric Research (NIWA).

Pallentin, A., Verdier, A. L., and Mitchell, J. (2009). *Beneath the waves: Wellington Harbour* (Wellington: National Institute of Water and Atmospheric Research (NIWA)).

Pau, M., Gisler, G., and Hammer, Ø. (2014). Experimental investigation of the hydrodynamics in pockmarks using particle tracking velocimetry. *Geo-Marine Lett.* 34, 11–19. doi: 10.1007/s00367-013-0348-9

Paull, C., Ussler, W., Maher, N. M., Greene, H. G., Rehder, G., Lorenson, T. D., et al. (2002). Pockmarks off Big Sur, California. *Mar. Geol.* 181, 323–335. doi: 10.1016/S0025-3227(01)00247-X

Post, V. E. A., Groen, J., Kooi, H., Person, M., Ge, S., and Edmunds, W. M. (2013). Offshore fresh groundwater reserves as a global phenomenon. *Nature* 504, 71–78. doi: 10.1038/nature12858

Prairie, J. C., Ziervogel, K., Camassa, R., McLaughlin, R. M., White, B. L., Dewald, C., et al. (2015). Delayed settling of marine snow: Effects of density gradient and particle properties and implications for carbon cycling. *Mar. Chem.* 175, 28–38. doi: 10.1016/j.marchem.2015.04.006

Purkamo, L., von Ahn, C. M. E., Jilbert, T., Muniruzzaman, M., Bange, H. W., Jenner, A.-K., et al. (2022). Impact of submarine groundwater discharge on biogeochemistry and microbial communities in pockmarks. *Geochim. Cosmochim. Acta* 334, 14–44. doi: 10.1016/j.gca.2022.06.040

Reine, K. J., Clarke, D. G., and Dickerson, C. (2002). "*Acoustic characterization of suspended sediment plumes resulting from barge overflow*," Army Engineer Research and Development Center, Vicksburg, MS. Available at: www.wes.army.mil/el/dots/doer.

Roberts, J. M., Harvey, S. M., Lamont, P. A., Gage, J. D., and Humphery, J. D. (2000). Seabed photography, environmental assessment and evidence for deep-water trawling on the continental margin west of the Hebrides. *Hydrobiologia* 441, 173–183. doi: 10.1023/A:1017550612340

Rocha, C., Wilson, J., Scholten, J., and Schubert, M. (2015). Retention and fate of groundwater-borne nitrogen in a coastal bay (Kinvara Bay, Western Ireland) during summer. *Biogeochemistry* 125, 275–299. doi: 10.1007/s10533-015-0116-1

Rousakis, G., Karageorgis, A. P., and Georgiou, P. (2014). Geological structure and seabed morphology of the Stoupa submarine groundwater discharge system, Messinia, Greece. *Environ. Earth Sci.* 71, 5059–5069. doi: 10.1007/s12665-013-2910-1

Rowan, O., and Pipe, H. (2019). *Wellington Harbour Bores – Exploratory Drilling Findings* (Hamilton, New Zealand: Water, New Zealand Conference & Expo).

Saadatkhah, N., Kassim, A., Siat, Q. A., and Micallef, A. (2023). Salt leaching by freshwater and its impact on seafloor stability: An experimental investigation. *Mar. Geol.* 455, 106959. doi: 10.1016/j.margeo.2022.106959

Santos, I. R., Chen, X., Lecher, A. L., Sawyer, A. H., Moosdorf, N., Rodellas, V., et al. (2021). Submarine groundwater discharge impacts on coastal nutrient biogeochemistry. *Nat. Rev. Earth Environ.* 2, 307–323. doi: 10.1038/s43017-021-00152-0

Schneider von Deimling, J., Weinrebe, W., Tóth, Z., Fossing, H., Endler, R., Rehder, G., et al. (2013). A low frequency multibeam assessment: Spatial mapping of shallow gas by enhanced penetration and angular response anomaly. *Mar. Pet. Geol.* 44, 217–222. doi: 10.1016/j.marpetgeo.2013.02.013

Seager, R., Ting, M., Held, I., Kushnir, Y., Lu, J., Vecchi, G., et al. (2007). Model projections of an imminent transition to a more arid climate in Southwestern North America. *Science* 316, 1181–1184. doi: 10.1126/science.1139601

Seitzinger, S. P., and Harrison, J. A. (2008). "Land-Based Nitrogen Sources and Their Delivery to Coastal Systems," in *Nitrogen in the Marine Environment* (Elsevier), 469–510. doi: 10.1016/B978-0-12-372522-6.00009-8

Simmonds, J., and MacLennan, D. N. (2008). *Fisheries acoustics: theory and practice.* (New York, USA: John Wiley & Sons).

Starke, C., Ekau, W., and Moosdorf, N. (2020). Enhanced productivity and fish abundance at a submarine spring in a coastal lagoon on Tahiti, French Polynesia. *Front. Mar. Sci.* 6. doi: 10.3389/fmars.2019.00809

Stevens, G. R. (1974). *Rugged Landscape: The Geology of Central New Zeland. including Wellington, Wairarapa, Manawatu, and the Marlborough Sounds* (Wellington). Wellington: Reed.

Stott, L., Davy, B., Shao, J., Coffin, R., Pecher, I., Neil, H., et al. (2019). CO2 release from pockmarks on the chatham rise-bounty trough at the glacial termination. *Paleoceanogr. Paleoclimatol.* 32(11), 1726–1743. doi: 10.1029/2019pa003674

van der Linden, W. J. M. (1967). A textural analysis of Wellington Harbour sediments. *New Zeal. J. Mar. Freshw. Res.* 1, 26–37. doi: 10.1080/00288330.1967.9515189

Watson, S. J., Ribó, M., Seabrook, S., Strachan, L. J., Hale, R., and Lamarche, G. (2022). The footprint of ship anchoring on the seafloor. *Sci. Rep.* 12, 1–11. doi: 10.1038/s41598-022-11627-5

Wood, R., and Davy, B. (1992). *Interpretation of Geophysical Data Collected in Wellington Harbour* (Wellington, New Zealand). Client report no. 1992/78.

Frontiers in Marine Science

Explores ocean-based solutions for emerging global challenges

The third most-cited marine and freshwater biology journal, advancing our understanding of marine systems and addressing global challenges including overfishing, pollution, and climate change.

Discover the latest Research Topics

See more →

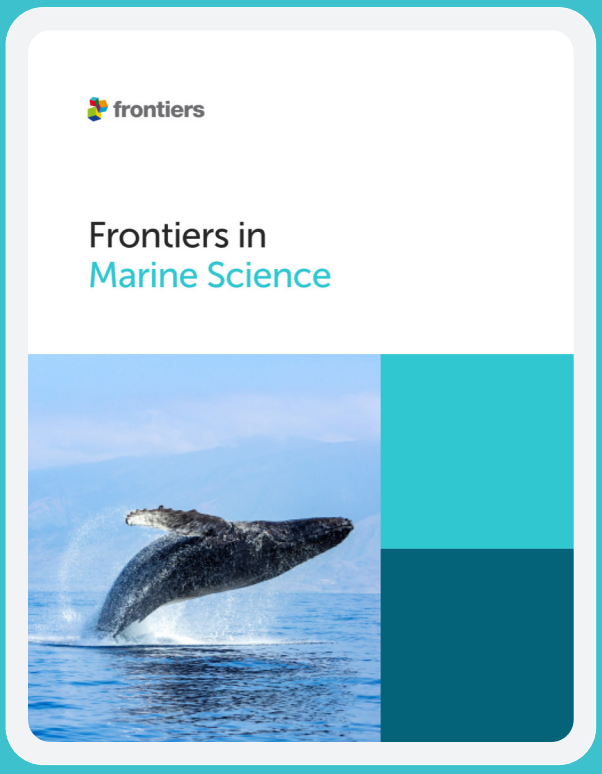

Frontiers

Avenue du Tribunal-Fédéral 34
1005 Lausanne, Switzerland
frontiersin.org

Contact us

+41 (0)21 510 17 00
frontiersin.org/about/contact